Methods for Direct Laser Cooling of Polyatomic Molecules

A DISSERTATION PRESENTED
BY
BENJAMIN LEE AUGENBRAUN
TO
THE DEPARTMENT OF PHYSICS

IN PARTIAL FULFILLMENT OF THE REQUIREMENTS
FOR THE DEGREE OF
DOCTOR OF PHILOSOPHY
IN THE SUBJECT OF
PHYSICS

HARVARD UNIVERSITY
CAMBRIDGE, MASSACHUSETTS

NOVEMBER 2021

©2021 – Benjamin Lee Augenbraun
all rights reserved.

Thesis advisor: Professor John M. Doyle Benjamin Lee Augenbraun

Methods for Direct Laser Cooling of Polyatomic Molecules

Abstract

Molecules controlled at the single-quantum-state level offer wide-ranging applications spanning many of the frontiers of modern physics. Within the past decade, simple diatomic molecules have been brought under full quantum control both via assembly from pre-cooled atoms and by direct laser cooling. Polyatomic molecules[1] have attracted focus as novel quantum resources providing distinct advantages (and challenges) compared to both atoms and diatomic molecules. For example, nearly all polyatomic molecules have long-lived states that can be fully polarized at low applied electric fields. These and other features generic to polyatomic molecules can be applied to quantum simulation, quantum chemistry, and tests of fundamental physics beyond the Standard Model. While these structural features of polyatomic molecules are highly promising for applications, they complicate the process of bringing molecules under full quantum control.

In this thesis, we describe a series of experimental and theoretical advances toward the production of ultracold complex polyatomic molecules. We demonstrate the first laser cooling of the polyatomic radical ytterbium monohydroxide (YbOH), a promising candidate to search for particles and interactions beyond the Standard Model of particle physics. We develop a novel deceleration technique ("Zeeman-Sisyphus deceleration") capable of slowing molecular beams to trappable velocities while scattering fewer than 10 optical photons. This deceleration method is demonstrated using CaOH molecules, a lighter analog of YbOH. In order to determine a viable pathway to full three-dimensional cooling and trapping of YbOH, we develop a spectroscopic technique to measure vibrational branching ratios with relative intensity sensitivity around 1 part in

[1] Molecules that contain three or more atoms.

10^5, approximately two orders of magnitude beyond the previous state of the art. We also perform the first spectroscopic observations and characterizations of the related molecule ytterbium monomethoxide, $YbOCH_3$, a promising species to probe beyond-the-Standard-Model physics. In addition, we show theoretically that an entire class of asymmetric top molecules can be laser cooled using essentially the same techniques used for much simpler species. Measurements of the vibrational branching ratios for a few prototypical asymmetric to molecules (CaSH and $CaNH_2$) are presented to confirm these predictions.

Contents

Abstract **iv**

Citations to Previous Work **xii**

Acknowledgments **xv**

1 Introduction **1**
- 1.1 Electron electric dipole moment measurements . . . 2
- 1.2 Further applications of polyatomic molecules . . . 9
- 1.3 Methods to produce cold molecules . . . 13
- 1.4 Thesis overview . . . 19

2 Molecular Structure **22**
- 2.1 Born-Oppenheimer approximation . . . 23
- 2.2 Electronic structure . . . 26
- 2.3 Vibrational structure . . . 29
- 2.4 Rotational Structure . . . 35
- 2.5 Born-Oppenheimer approximation breakdown and perturbations . . . 38
- 2.6 Forming a closed optical cycle: linear molecules . . . 41

3 Molecule Production, Slow Beams, and ^{3}He Pot **47**
- 3.1 Initial buffer-gas cell characterizations . . . 48
- 3.2 Pumped He-3 refrigerator . . . 57
- 3.3 ^{3}He-pot-cooled buffer-gas beams . . . 63
- 3.4 Potential improvements . . . 69

4 High-Sensitivity Branching Ratio Measurements **71**
- 4.1 Dispersed fluorescence spectroscopy . . . 73
- 4.2 YbOH measurements . . . 78
- 4.3 CaOH measurements . . . 84
- 4.4 Vibronic coupling effects in linear polyatomic molecules . . . 89
- 4.5 $CaOCH_3$ measurements . . . 92
- 4.6 Limitations of DLIF spectra . . . 96

5 YbOH Spectroscopy and Photon Cycling **98**
- 5.1 Production of YbOH . . . 99
- 5.2 High-resolution YbOH spectroscopy . . . 103
- 5.3 YbOH optical cycling . . . 114

6 Laser Cooling of YbOH Molecules **117**
- 6.1 Laser cooling theory . . . 118
- 6.2 Laser cooling apparatus . . . 123

6.3 Laser cooling results . . . 126
6.4 Conclusion . . . 134

7 Zeeman-Sisyphus Deceleration **136**
7.1 Overview of Zeeman-Sisyphus deceleration . . . 138
7.2 CaOH optical pumping spectroscopy . . . 144
7.3 CaOH deceleration . . . 155
7.4 Progress toward Zeeman-Sisyphus deceleration of YbOH . . . 161
7.5 Zeeman-Sisyphus apparatus . . . 163

8 Observation and Spectroscopy of $YbOCH_3$ **175**
8.1 Why symmetric top molecules? . . . 176
8.2 Low-resolution excitation and DLIF spectroscopy . . . 178
8.3 High-resolution spectroscopy . . . 192
8.4 Conclusion . . . 195

9 Asymmetric Top Molecules for Laser Cooling **197**
9.1 Electronic transitions . . . 199
9.2 Vibrational branching: theory . . . 203
9.3 Vibrational branching: measurements . . . 210
9.4 Rotational branching . . . 220

10 Conclusion and Outlook **224**
10.1 Microwave Zeeman-Sisyphus decelerator . . . 225
10.2 Microwave-Optical Stark-Sisyphus deceleration . . . 226
10.3 Large molecules . . . 230

Appendix A Stark Shifts, Parity Doubling, and eEDM Sensitivity **232**
A.1 Diatomic molecules without parity doublets . . . 233
A.2 Molecules with parity doublets . . . 234
A.3 Stark shifts in a linear molecule $\ell = 1$ state . . . 239
A.4 Electron spin projection . . . 240
A.5 The ℓ-doubling matrix elements . . . 242
A.6 Spin-rotation matrix elements . . . 243

Appendix B Labeling Vibrational States and Transitions **245**

Appendix C ^{3}He Gas Handling System **248**

Appendix D Franck-Condon Factor Calculations **250**
D.1 Analytical formula for two modes . . . 251
D.2 Application to YbOH . . . 258

Appendix E YbOH Lines **259**

Appendix F Coherent 699 Ring Dye Laser **262**
F.1 Useful part numbers . . . 263
F.2 Observed output powers . . . 263
F.3 Alignment tricks . . . 264

Appendix G Excited-State Zeeman Structure and g'_ℓ **266**
G.1 Zeeman Hamiltonian and matrix elements 267
G.2 Curl-type relationships and the meaning of g'_ℓ 269
G.3 Measurement of g'_ℓ for CaOH 271

References **273**

Listing of figures

1.1 Generation of magnetic and electric dipole moments . . . 3
1.2 Molecular polarization for molecules with and without parity doublets . . . 6
1.3 Optical cycling in a two-level system . . . 16
1.4 Sequence of typical laser cooling experiment . . . 18

2.1 Orbital mixing in alkaline-earth pseudohalides . . . 27
2.2 Molecular energy levels under various degrees of symmetry breaking . . . 28
2.3 Wavefunction overlap in one-dimensional harmonic oscillator model . . . 33
2.4 Angular momentum coupling in Hund's cases (a) and (b) . . . 37
2.5 Level diagrams of CaOH/YbOH $\tilde{X}\,^2\Sigma^+$ and $\tilde{A}\,^2\Pi$ states . . . 43

3.1 Diagram of typical buffer-gas cell . . . 49
3.2 Effect of second-stage cell mesh on Yb beam velocities . . . 50
3.3 Effect of second-stage cell length on Yb atomic beam velocities . . . 52
3.4 Yb velocity boosting measured outside a 40 mm long second-stage cell . . . 53
3.5 Speedup of Yb atomic beams due to methanol "icing" . . . 53
3.6 Velocity distributions between cells and after second cell vs. methanol flow . . . 55
3.7 Comparison between forward velocities of Na, Ca, and Yb . . . 56
3.8 Schematic of ^{3}He fridge . . . 58
3.9 Evaporator base and housing prior to brazing . . . 59
3.10 Liquid ^{3}He remaining after cooling down . . . 61
3.11 ^{3}He pot heat loads and hold time . . . 62
3.12 Ca atomic beams with ^{3}He pot at 3.2 K and 0.7 K . . . 64
3.13 Ca velocities and boosting vs. buffer-gas flow . . . 65
3.14 Na velocities and boosting vs. buffer-gas flow . . . 66
3.15 Yb atomic beam velocities with ^{3}He pot at 3.2 K and 0.7 K . . . 67
3.16 CaOH molecular beam with ^{3}He pot at 3.2 K and 0.7 K . . . 68

4.1 Beam line for DLIF spectroscopy . . . 75
4.2 Spectrometer relative intensity response measurements . . . 78
4.3 YbOH $\tilde{A}\,^2\Pi_{1/2}(000)$ DLIF measurements . . . 79
4.4 YbOH $\tilde{A}\,^2\Pi_{1/2}(100)$ DLIF measurements . . . 81
4.5 CaOH $\tilde{A}\,^2\Pi_{1/2}(000)$ DLIF measurements . . . 85
4.6 CaOH $\tilde{B}\,^2\Sigma^+(000)$ DLIF measurements . . . 87
4.7 Vibronic components involved in quadrupolar Renner-Teller perturbation . . . 91
4.8 $CaOCH_3$ $\tilde{A}\,^2E_{1/2}(v=0)$ DLIF measurements . . . 93

5.1 Enhancing YbOH production through excited state chemistry . . . 101
5.2 YbOH enhancement vs. laser power for reaction with water . . . 102
5.3 Repumper spectroscopy setup . . . 104
5.4 $\tilde{X}\,^2\Sigma^+(100)$ repumper spectroscopy . . . 106
5.5 $\tilde{X}\,^2\Sigma^+(200)$ repumper spectroscopy . . . 107

5.6 $\tilde{X}\,^2\Sigma^+(02^00)$ repumper spectroscopy . . . 108
5.7 Spectroscopy of YbOH A(100)-X(020) and A(100)-X(200) bands . . . 111
5.8 Depletion pumping the $(17.73)\leftarrow \tilde{X}\,^2\Sigma^+(000)$ transition . . . 112
5.9 Demonstrations of optical cycling . . . 114
5.10 Scan over repumping transition showing photon cycling . . . 115

6.1 Sisyphus laser cooling mechanism for $F'' = 1 \rightarrow F' = 0$ transition . . . 122
6.2 Schematic of Sisyphus cooling apparatus . . . 124
6.3 Photograph of UHV chamber used for laser cooling . . . 125
6.4 EMCCD images of molecular beam with Sisyphus cooling/heating. . . . 127
6.5 Integrated Sisyphus cooling/heating traces and comparison to simulations. . . . 128
6.6 Sisyphus-cooled molecular beams vs. detuning . . . 129
6.7 Laser cooling performance vs. intensity. . . . 131
6.8 B-field dependence of Sisyphus cooling . . . 132
6.9 Comparison of Doppler and Sisyphus cooling vs. detuning . . . 133

7.1 Schematic overview of Zeeman-Sisyphus deceleration. . . . 138
7.2 Rendering of decelerator beamline. . . . 141
7.3 Input-output velocity correspondence in the Zeeman-Sisyphus slower . . . 142
7.4 Background-free cycling detection for CaOH molecules . . . 145
7.5 Zeeman tuning of CaOH energy levels . . . 146
7.6 CaOH $\tilde{A}\,^2\Pi_{1/2}\,(000)$ Zeeman tuning . . . 147
7.7 Zeeman tuning of optical pumping feature in region D1 . . . 149
7.8 Resonance scan for magnetic guide state-preparation . . . 150
7.9 Optical pumping measurements and determination of g'_ℓ . . . 150
7.10 WFS manifold depletion by driving both excited-state features in D1 . . . 152
7.11 Optical pumping and repumping efficiency in Zeeman-Sisyphus decelerator . . . 152
7.12 State preparation in WFS by pumping region S1 . . . 154
7.13 Measuring change in $\tilde{X}\,^2\Sigma^+\,(100)$ population due to optical pumping . . . 155
7.14 Depletion of high velocities and accumulation at low velocities . . . 157
7.15 Zeeman-Sisyphus deceleration of CaOH without pumping in S1 . . . 158
7.16 Zeeman-Sisyphus deceleration of CaOH including pumping in S1 . . . 160
7.17 Time-of-arrival distribution for CaOH molecules at 15 m/s . . . 161
7.18 YbOH $\tilde{A}\,^2\Pi_{1/2}(000)$ Zeeman structure . . . 162
7.19 Spin-flip optical pumping transitions in YbOH . . . 163
7.20 Mechanical drawing and exploded view of a single coil unit . . . 164
7.21 Zeeman-Sisyphus magnets installed in 4 K shield . . . 166
7.22 Measured and simulated magnetic field profiles for a single Helmholtz unit . . . 166
7.23 Magnetic field magnitude along axis of the superconducting coils . . . 168
7.24 Contour plot of magnetic field in Zeeman-Sisyphus decelerator . . . 169
7.25 Cryogenic chamber housing Zeeman-Sisyphus magnets . . . 170
7.26 Heat sinking and electric connection of superconducting leads . . . 171
7.27 Construction of lugs for LTS leads. . . . 172
7.28 Magnetic guide installation . . . 173
7.29 Magnetic field distribution in permanent magnetic guide . . . 174

8.1 2D spectrum near $YbOCH_3$ bandhead . . . 179
8.2 2D spectrum exciting to vibrationally excited levels of the $YbOCH_3$ $\tilde{A}$ state . . . 182

8.3 DLIF spectra for $YbOCH_3$ and $YbOCD_3$ . . . 183
8.4 DLIF spectra for vibrationally excited levels in the $YbOCH_3$ $\tilde{A}$ state . . . 185
8.5 High-resolution spectrum near the $YbOCH_3$ $\tilde{A} \leftarrow \tilde{X}$ bandhead . . . 193
8.6 Chemical enhancement for $YbOCH_3$ spectral assignments . . . 194

9.1 Geometries of some laser-coolable asymmetric top molecules. . . . 199
9.2 Correlation diagram for laser-coolable linear and asymmetric top molecules. . . . 201
9.3 Visualization of *ab initio* molecular orbitals for laser coolable molecules. . . . 202
9.4 Visualization of CaSH normal modes. . . . 209
9.5 DLIF spectrum for $CaNH_2$ $\tilde{A}\ ^2B_2$ state . . . 213
9.6 DLIF spectrum for $CaNH_2$ $\tilde{B}\ ^2B_1$ state . . . 215
9.7 DLIF following excitation to $CaNH_2$ $\tilde{C}\ ^2A_1\ (v = 0)$ . . . 216
9.8 DLIF following excitation to CaSH $\tilde{B}\ ^2A''$ state . . . 218
9.9 DLIF following excitation to CaSH $\tilde{C}\ ^2A'$ state . . . 219
9.10 Rotationally-closed optical cycling schemes for asymmetric top molecules. . . . 222

10.1 Schematic layout of microwave-optical Stark-Sisyphus slower . . . 227
10.2 Energy levels relevant to Stark-Sisyphus deceleration . . . 228
10.3 Energy removal per stage of Stark-Sisyphus deceleration . . . 229
10.4 Comparison of DLIF spectra for CaOH, $CaOCH_3$, and $CaOC_{10}H_7$ . . . 231

A.1 Stark shifts and dipole moments for diatomic molecule without parity doublets . . . 234
A.2 Stark shift and lab-frame dipole moments in a two-level model . . . 235
A.3 Origin of ℓ-doubling . . . 237
A.4 Stark shifts and dipole moments for a linear molecule $\ell = 1$ bending mode . . . 239
A.5 $\langle\Sigma\rangle$ as a function of electric field . . . 241

C.1 Gas-handling system for ^{3}He fridge . . . 249

E.1 Transitions observed at high-resolution in YbOH . . . 260

F.1 Observed output powers from Coherent 699 dye laser . . . 264

Listing of tables

2.1 Angular momentum vectors and projections . . . 36
2.2 Molecular parameters for YbOH and CaOH $\tilde{X}\,^2\Sigma^+$ (000) states . . . 42
2.3 Molecular parameters for YbOH and CaOH $\tilde{A}\,^2\Pi(000)$ states . . . 43

4.1 Vibrational branching ratios for YbOH $\tilde{A}\,^2\Pi_{1/2}(000)$ . . . 80
4.2 Vibrational branching ratios for YbOH $\tilde{A}\,^2\Pi_{1/2}(100)$ . . . 82
4.3 YbOH photon budgets . . . 83
4.4 Vibrational branching ratios for CaOH $\tilde{A}\,^2\Pi_{1/2}(000)$ . . . 86
4.5 Vibrational branching ratios for CaOH $\tilde{B}\,^2\Sigma^+(000)$ . . . 88
4.6 CaOH photon budgets . . . 89
4.7 Vibrational branching ratios for $CaOCH_3$ $\tilde{A}\,^2E_{1/2}(v=0)$ . . . 94

5.1 Spin-rotation parameters for YbOH and related species . . . 110
5.2 YbOH pump-repump population measurements for VBR determination . . . 113

8.1 Normal mode labeling relevant to $YbOCH_3$ . . . 180
8.2 Vibrational splittings measured for $YbOCH_3$, $YbOCD_3$, and related species . . . 186
8.3 Branching ratios measured for low-lying $YbOCH_3$ excited states . . . 188

9.1 Comparison of calculated and measured VBRs for $SrNH_2$ . . . 205
9.2 Calculated FCFs for $CaNH_2$, CaSH, and SrSH . . . 206
9.3 Metal-ligand stretching mode FCFs computed for various asymmetric tops . . . 208
9.4 Normal modes and frequencies for $CaNH_2$ . . . 212
9.5 VBRs for the $CaNH_2$ $\tilde{A}\,^2B_2(v=0)$ state . . . 214
9.6 VBRs for the $CaNH_2$ $\tilde{B}\,^2B_1(v=0)$ state . . . 215
9.7 VBRs for the $CaNH_2$ $\tilde{C}\,^2A_1(v=0)$ state. . . . 217
9.8 Normal modes and frequencies for CaSH . . . 217
9.9 VBRs for the CaSH $\tilde{B}\,^2B_1(v=0)$ state . . . 218
9.10 VBRs for the CaSH $\tilde{C}\,^2A_1(v=0)$ state . . . 219
9.11 Rotational selection rules relevant for asymmetric top molecules . . . 220

B.1 Vibrational normal mode ordering for $MOCH_3$ symmetric top molecules. . . . 247

D.1 Computed 2D FCFs for YbOH $\tilde{A}\,^2\Pi_{1/2}(000)$ and $\tilde{A}\,^2\Pi_{1/2}(100)$ states . . . 258

E.1 YbOH lines measured at high resolution . . . 261

F.1 Mirror sets for Coherent 699 and 899 ring lasers . . . 263

Citations to Previous Work

Portions of this thesis or results described herein have previously been published in the references below. Where appropriate, citations and acknowledgments are also provided in the body of the thesis for derivative or collaborative work.

1. B. L. Augenbraun, A. Frenett, H. Sawaoka, C. Hallas, N. B. Vilas, A. Nasir, Z. D. Lasner, and J. M. Doyle, "Zeeman-Sisyphus Deceleration of Molecular Beams," Phys. Rev. Lett. **127**, 263002 (2021).

2. C. Zhang, B. L. Augenbraun, Z. D. Lasner, N. B. Vilas, J. M. Doyle, and L. Cheng, "Accurate prediction and measurement of vibronic branching ratios for laser cooling linear polyatomic molecules," J. Chem. Phys. **155**, 091101 (2021).

3. B. L. Augenbraun, Z. D. Lasner, A. Frenett, H. Sawaoka, A. T. Le, J. M. Doyle, and T. C. Steimle, "Observation and laser spectroscopy of ytterbium monomethoxide, $YbOCH_3$," Phys. Rev. A. **103**, 022814 (2021).

4. B. L. Augenbraun, J. M. Doyle, T. Zelevinsky, and I. Kozyryev, "Molecular Asymmetry and Optical Cycling: Laser Cooling Asymmetric Top Molecules," Phys. Rev. X **10**, 031022 (2020).

5. L. Baum, N. Vilas, C. Hallas, B. L. Augenbraun, S. Raval, D. Mitra, and J. M. Doyle, "Establishing a nearly closed cycling transition in a polyatomic molecule," Phys. Rev. A **103**, 043111 (2021).

6. E. T. Mengesha, A. T. Le, T. C. Steimle, L. Cheng, C. Zhang, B. L. Augenbraun, Z. Lasner, and J. Doyle, "Branching Ratios, Radiative Lifetimes and Transition Dipole Moments for YbOH," J. Phys. Chem. A **124**, 16, 3135-3148 (2020).

7. B. L. Augenbraun, Z. D. Lasner, A. Frenett, H. Sawaoka, C. Miller, T. C. Steimle, and J. M. Doyle, "Laser-Cooled Polyatomic Molecules for Improved Electron Electric Dipole Moment Searches," New J. Phys. **22** 022003 (2020).

Acknowledgments

First, I heartily thank my advisor, John Doyle. His fostering of a welcoming and supportive work environment has made my graduate years very happy. I am also extremely grateful that John not only tolerated, but even encouraged, my enthusiasm to work on many "side projects." These have turned into some of the most stimulating problems I got to tackle as a graduate student and are emblematic of John's scientific vision. It has been a pleasure learning from someone whose forward thinking always seems to keep him a few years ahead of his field.

In addition, I would like to thank Markus Greiner and Roxanne Guenette for serving on my committee. Meeting with them always provided stimulating and useful ideas, and had the added benefit of improving how I communicate with scientists outside of my niche.

To the PolyEDM team, I say thank you for your insight and guidance during our many meetings. Nick Hutzler has been an organized and visionary leader since the origin of the PolyEDM collaboration. Amar Vutha served as a role model for his clear and creative thinking. Tim Steimle has been a dear mentor, welcoming me into his lab and home on several visits to Arizona and instilling in me the excitement of spectroscopy. I appreciate his enthusiasm for science and for humoring my many questions.

Thanks to the entire Doyle group for their help and camaraderie. In particular, thank you to Zack Lasner, who not only started the YbOH experiment alongside me, but was always a willing participant in conversations that began with, "This might be a crazy idea, but...". Thanks to Alex Frenett, Hiro Sawaoka, Abdullah Nasir, and Cal Miller for helping to build up the YbOH lab, including constructing key parts of the cryogenic apparatus; the future of the experiment is in good hands. Thanks to Nathaniel Vilas and Christian Hallas for all of their help as we simultaneously

tackled the many problems that polyatomic molecules threw at us, and for their patience when I commandeered nearly all of their lasers for the Zeeman-Sisyphus slowing experiments. Yicheng Bao was an invaluable resource for solving all problems electronic and/or optical, and Loic Anderegg and Sean Burchesky provided useful insight gleaned from the CaF experiment. I want especially to thank two former Doyle group members, Louis Baum and Ivan Kozyryev, for serving as mentors when I was a young graduate student and becoming good friends in the years since.

The experiments I worked on would be little more than raw materials and open circuits without the excellent technical support I received from Stan Cotreau, Steve Sansone, Andy DiMambro, and Jim MacArthur. I learned a great deal under the patient tutelage of Stan, Steve, and Andy who (in their own unique ways) made the machine shop both productive and fun. Jim helped turn my many silly questions into reasonable answers and, eventually, useful devices.

I gratefully acknowledge the help of many people in the Harvard physics department who helped keep me on track and out of trouble for the past several years. Thanks to Adam Ackerman, Jacob Barandes, Lisa Cacciabaudo, Silke Exner, and Erica Mantone for all of their support.

I have been very fortunate to work closely with several others who became valued collaborators and teachers. Lan Cheng played a key role in our developing understanding of vibronic coupling in linear molecules and was very patient explaining the intricacies of his calculations. Wes Campbell collaborated on a few theory projects focusing on large molecules. I learned a great deal by watching his physical intuition and curiosity at work.

I would like to thank Tiku Majumder and Charlie Doret for acting as teachers and mentors long after they may have hoped to be rid of me. Their advice continues to be invaluable.

I thank my family for their endless love and support. Thanks to: my brother, JJ, for showing me to work hard and to always smile. To my sister, Sam, for reminding me to be adventurous and for keeping me humble. And to my parents, Chuck and Sara, for teaching me by example how to

live a life full of kindness, humor, and curiosity.

Lastly, and most importantly, I thank my wife, Melissa, for her encouragement and patience. Melissa: when we first met in 2016, I could not have predicted how much happiness you would bring into my life. Meeting you and marrying you bookended my time as a graduate student. I can confidently say that those two events were the best results of my time in graduate school.

You will reply that reality hasn't the slightest need to be of interest. And I'll answer you that reality may avoid the obligation to be interesting, but that hypotheses may not.

Jorge Luis Borges, "Death and the Compass"

1 Introduction

The development of new tools and the discovery of new phenomena enjoy a healthy feedback cycle. In the fields of atomic and molecular physics, tools providing exquisite control over internal and external quantum states have enabled groundbreaking studies of the fundamental symmetries of Nature [1–4]. Meanwhile, the quest to probe and control Nature with ever higher precision has motivated the development of new methods and instruments [5–7]. This thesis conveys one small facet of this interplay, where by aiming to study the apparent asymmetry between matter and antimatter we have developed methods to laser cool polyatomic molecules. In turn, these new tools have led us to discover that a much wider set of molecules is amenable to laser-based quantum

control than had previously been thought possible.

This story begins with efforts to laser cool the molecule ytterbium monohydroxide (YbOH) for use in electron electric dipole moment (EDM) measurements. In order to reach that experimental goal, we needed to develop better molecular beam sources, higher-sensitivity spectroscopic tools, and more efficient methods of manipulating molecules' motion. These experimental advances are described in Chapters 3–7. During this work, we realized that molecules with larger sizes and lower symmetries could likely be tamed using the tools we were developing. Our experimental and theoretical studies of complex polyatomic molecules, including asymmetric top molecules, are presented in Chapters 8 and 9.

Before presenting these technical results, we motivate the YbOH precision measurement experiment (Sec. 1.1) and explain the desire to work with cold molecules, especially polyatomic molecules (Sec. 1.2). Section 1.3 provides relevant background on methods to produce cold molecules. We conclude in Sec. 1.4 with a summary of the major results that appear in the body of this thesis.

1.1 Electron electric dipole moment measurements

Undiscovered physics manifests itself in astonishing ways, from the dark matter and energy that compose approximately 95% of the energy density of the known universe to the fact that the origin of the remaining 5% of "normal" matter cannot be explained. In particular, although one might naively expect matter and antimatter to be treated symmetrically by physical laws, we apparently live in a universe dominated (asymmetrically) by matter. This is evidenced by the fact that we do not live in fear of annihilation with stray pockets of antimatter,[1] as well as by astronomical observations demonstrating an extreme scarcity of antimatter [8]. This Baryon Asymmetry of the Universe (BAU) is one of the most significant challenges facing fundamental physics.

[1] Instead, we get to live fearing annihilation by problems of our own making.

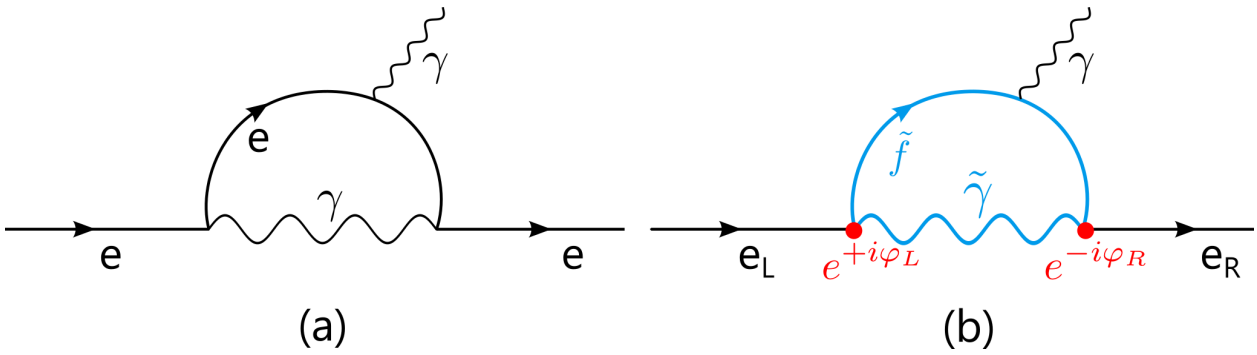

Figure 1.1: (a) Leading contribution to the electron's anomalous magnetic moment. (b) Feynman diagram arising in supersymmetric theories that can produce an electron EDM at 1-loop level. This example is modeled after Refs. [14, 15]. A left-handed electron emits a virtual photino and sfermion and picks up complex phase φ_L. The virtual sfermion interacts with an external electric field. At the recombination step, another complex phase φ_R is present, and due to T-violation it is possible that $\varphi_R \neq \varphi_L$. This asymmetry permits the development of an electric dipole moment (d_e).

Sakharov has observed that explaining the BAU requires certain symmetry violations [9]. In addition to some process that preferences matter over antimatter, violation of T-symmetry is required,[2] i.e. the physical laws must *not* be symmetric under time reversal [9, 10]. While there is T violation built into the Standard Model of particle physics, its effects are too small to explain the observed BAU. Extensions of the Standard Model, which are well motivated on other grounds as well [11], generically predict "new" particles and interactions— those that exist in Nature but have yet to be observed— that could constitute the requisite sources of T-violation [12, 13].

These high-energy particles (typically ∼TeV scale) can lead to low-energy effects. When "new" particles interact (perhaps virtually) with other fundamental particles, such as the electron, they could do so in a way that leads to T-violating electromagnetic moments. See Fig. 1.1 for an example that can arise via radiative corrections in simple supersymmetric theories [15]. It is important to note that the Feynman diagram shown in Fig. 1.1(b) is the simplest possible case, in which an EDM is generated at the 1-loop level. In reality, more complex Feynman diagrams must be considered and the associated EDMs could be correspondingly smaller [13, 16, 17]. The canonical example of these symmetry-violating electromagnetic moments is a permanent EDM, $\vec{d}$, which leads to an

[2] Technically the condition is related to CP-violation, where C is charge conjugation and P is parity reversal. However, CP is equivalent to T assuming that CPT is an exact symmetry.

additional term in an atomic/molecular Hamiltonian

$$H_d = -d_e \mathcal{E}_{\text{eff}} \, \vec{s} \cdot \hat{n}, \tag{1.1}$$

where $\mathcal{E}_{\text{eff}}$ is the effective electric field experienced by the probed electron and $\hat{n}$ is the direction of this field. For a fundamental particle with spin $\vec{s}$, it must be the case that $\vec{d}$ and $\vec{s}$ are aligned.[3] One can immediately see that H_d violates both P and T symmetries because $\vec{s}$ is P-even and T-odd while $\vec{\mathcal{E}}_{\text{eff}} = \mathcal{E}_{\text{eff}} \, \hat{n}$ is P-odd and T-even.

1.1.1 Atoms and molecules for EDM measurements

Conceptually, this discussion has translated the search for fundamental T-violation into a problem that can be solved by precision spectroscopy of electric or magnetic moments. A common tactic is to search for small energy shifts caused by these electromagnetic moments in the spectrum of an atom or molecule. Note that $\mathcal{E}_{\text{eff}}$ in H_d is *not* the field that an experimentalist would apply in the laboratory, but is instead a convenient shorthand for the scale of the EDM energy shifts including the effect of relativistic length contraction on the electron EDM averaged over its orbit; see Ref. [16]. Energy shifts caused by H_d are, of course, easier to measure as they become larger, motivating using the largest $\mathcal{E}_{\text{eff}}$ possible. Large internal electric fields and massive relativistic enhancements occur near the nuclei of heavy atoms, and for nuclei with $Z \sim 100$ it is possible to find species with $\mathcal{E}_{\text{eff}} \sim 100$ GV/cm [18–20]. This is about 6 orders of magnitude larger than could conceivably be constructed in the laboratory.

The form of H_d ($\propto \vec{s} \cdot \hat{n}$) indicates that the atomic/molecular species must be polarized in the laboratory frame in order to measure non-vanishing energy shifts. By polarizing the atomic/molecular

[3] This is intuitively consistent with observed atomic and nuclear structures that indicate spin is the only vector quantity associated with electrons and nucleons.

probe in the laboratory frame, $\langle \hat{n} \rangle$ is made nonzero and measurable energy shifts emerge. Atoms, due to their high symmetry and very widely spaced levels of opposite parity, can only attain laboratory frame alignment around 10^{-3}. For reasons described in the next section, molecules can often be (nearly) fully polarized in the laboratory frame. Thus, even though atoms and molecules may offer similar intrinsic $\mathcal{E}_{\text{eff}}$, only for molecules can most (or all) of $\mathcal{E}_{\text{eff}}$ actually be used.

1.1.2 Molecular polarization

A quantum mechanical treatment of Stark shifts and molecular polarization is presented in App. A. Here, we focus on simple quasi-classical pictures [21]. Classically, molecular polarization arises from the fact that an external electric field can exert a torque on a rotating molecular dipole moment[4] and cause it to precess about the applied field. In molecules for which the angular momentum, $\vec{N}$, is perpendicular to the molecule-frame dipole moment, $\vec{d}$, there is no component of the dipole moment along a laboratory-frame vector (see top left in Fig. 1.2). Stark shifts therefore arise only at second order, and are due to the nonuniform rotation caused by application of the electric field [21, 22]. The vast majority of diatomic molecules behave this way because their angular momentum comes purely from end-over-end rotation that is necessarily perpendicular to the molecule-frame dipole moment.

Contrast this with a situation in which a molecule *does* have a component of $\vec{N}$ directed along $\vec{d}$. In this case, shown in the bottom left of Fig. 1.2, there can be at least some amount of rotation about the dipole moment due to, e.g., vibration (ℓ), rigid body rotation (K), or electronic orbital angular momentum (Λ). Thus, the dipole moment has some projection along a laboratory-frame vector ($\vec{N}$) and can interact with electric fields at first order [21, 22]. Certain special diatomic molecules and *all*

[4]When we talk about a molecule's dipole moment, we mean the permanent dipole moment of the molecule in a reference frame rotating with the nuclear framework. Molecules are not fundamental particles, so there is no problem with them having molecule-frame permanent dipole moments.

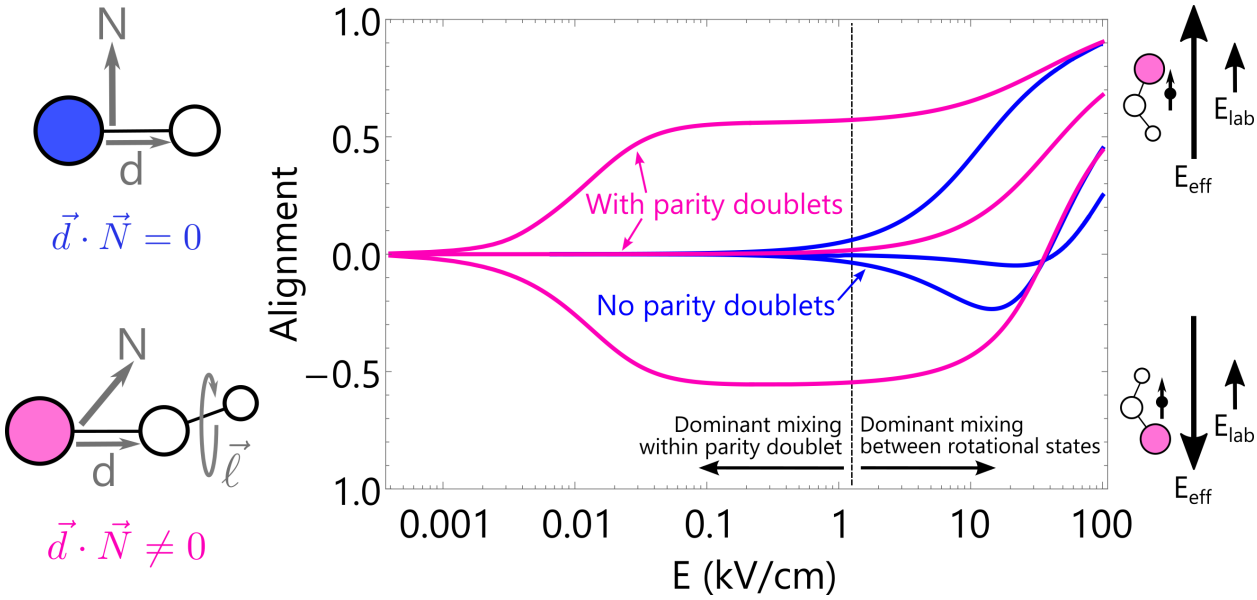

Figure 1.2: Molecular polarization as a function of applied laboratory electric field. Parameters are typical of YbOH molecules. Blue lines show alignment in a state without parity doubling ($N \leq 2, |M_N| \leq 1$ plotted). Pink lines show alignment of $N = 1$ sublevels in a vibrational level that has parity doubling, e.g. the fundamental bending vibrational state. We indicate two electric-field regimes: one where mixing occurs within a single rotational state and another where mixing occurs among many rotational states.

polyatomic molecules contain long-lived states for which $\vec{d} \cdot \vec{N} \neq 0$. In polyatomic molecules, this arises because rotation *about* the dipole moment can occur. In reality, the Stark shifts are not truly first order due to small "parity-doubling" effects that slightly split the states for which $\vec{d} \cdot \vec{N} \neq 0$ into opposite parity components ("parity doublets"), but these states are fully mixed and nearly-linear Stark shifts are realized at electric fields around 100 V/cm or smaller. See App. A for more details.

The degree of molecular alignment[5] relative to the laboratory-frame electric field is plotted for molecules with and without parity doublets in Fig. 1.2. (Parameters similar to those of YbOH are used for these calculations.) For molecules *without* parity doublets (shown in blue), fields $\mathcal{E}_{\text{lab}} \gtrsim 10$ kV/cm are required to achieve order-unity alignment because polarization occurs by mixing widely separated rotational levels. Moreover, at high fields *all* states approximately align with (but not against) the laboratory field. For molecules *with* parity doublets, significant align-

[5]The alignment is computed as the fraction of the molecule-frame dipole moment that is induced in the laboratory frame.

ment can be achieved at fields as small as $\mathcal{E}_{\text{lab}} \sim 10 - 100$ V/cm because mixing occurs within the parity doublet of a single rotational state.[6] Furthermore, the molecular levels can be aligned either parallel, antiparallel, or "neutral" relative to the laboratory axis. There exist states that are identical in all respects except for the orientation of $\hat{n}$, and therefore the direction of $\vec{\mathcal{E}}_{\text{eff}}$. At sufficiently high fields, adjacent rotational states become mixed and the Stark shifts closely resemble those of molecules lacking parity doublets— but there is a wide, experimentally useful range of electric field values (below about 5 kV/cm in Fig. 1.2) for which the isolated parity doublet picture holds.

Molecules with parity doublets offer many advantages in electron EDM measurements. First, full alignment is achieved at lower fields. This makes experimental design simpler and reduces any systematic effects proportional to the laboratory field. Perhaps more importantly, the parity-doubled level structure can be used to reduce *systematic* errors that could limit an experiment's precision. The oppositely aligned states have nearly identical level structures but opposite EDM shifts (see relative alignment between electron spin and $\mathcal{E}_{\text{eff}}$ in Fig. 1.2). This "internal co-magnetometer" allows one to reverse the electric field experienced by the electron without reversing any electric fields in the laboratory. Systematic effects related to field nonuniformity and imperfect field reversal can be strongly suppressed. Parity doublets and the associated internal co-magnetometers are a feature of the leading electron EDM measurements using ThO [23, 24] and HfF^+ [25] molecules.

ThO [23, 24] and HfF^+ [25] are two notable diatomic molecules that offer long-lived parity-doubled states; this is due to a special type of electronic structure (low-lying $^3\Delta_1$ states with electronic orbital angular momentum $\Lambda = 2$). These two molecules were used in recent limit-setting electron EDM measurements. However, the presence of parity doublets is a very special feature in diatomic molecules. In addition to being relatively uncommon, the diatomic molecules that *do*

[6] The zero-field splitting of the two parity-doubled levels is what prevents the alignment from being saturated even at zero field. See App. A.

contain parity doublets are certainly not amenable to direct laser cooling.[7] For diatomic molecules, one must choose between a species with parity doublets and a species that can be laser cooled.

1.1.3 The desire for laser cooling

The phase sensitivity of an electron EDM experiment scales as $\delta\phi \propto \tau$, where τ is the duration of coherent evolution. Laser cooling offers the ability to increase coherence times by orders of magnitude compared to the current best measurements conducted with molecular beams of neutral molecules.[8] To date, no limit-setting electron EDM experiment has taken advantage of the tools of laser cooling and trapping, primarily because the molecular structure of molecules used for EDM measurements has not been suited for laser cooling (to be described in Sec. 1.3 and 2.6).

As an example of what sort of gains are to be had, consider 10^6 trapped, EDM-sensitive molecules with 10 second coherence time — reasonable numbers given results from several related experiments (see Sec. 1.3). After one week of operation, such an experiment would have sensitivity to an electron EDM of $|d_e| < 10^{-32}\ e\,\text{cm}$, increasing sensitivity by three orders of magnitude compared to the current best limit and thus probing physics occurring at the PeV (1,000 TeV) scale [26].

1.1.4 The PolyEDM experiment

Because parity doubling can occur in all polyatomic molecules due to nuclear motions (not electronic structure), one can imagine *designing* molecules with an electronic structure that allows laser cooling without sacrificing parity doublets and the structural advantages they provide. This was the central idea that led to the PolyEDM experiment, which identified YbOH as a promising molecule for the task [26]. YbOH has a structure that permits laser cooling, a vibrational bending

[7] See Sec. 2.2 for a discussion of the sort of molecules that can be laser cooled. Suffice it to say, the structure described in that section cannot give rise to diatomic molecules with parity doublets.

[8] Ion trapping has also been used to achieve long coherence times [25].

mode that gives rise to parity doublets, and a heavy Yb nucleus with $\mathcal{E}_{\text{eff}} \sim 25$ GV/cm [19]. The PolyEDM experiment aims to laser cool YbOH molecules, trap them in an optical trap (e.g., focused optical dipole trap or lattice), and perform a spin-precision measurement in the lowest vibrational bending mode. In addition to the advantages of laser cooling (long coherence times) and parity doublets (systematic error rejection), performing an EDM experiment in a trap allows one to vary the spin precession time to combat systematic errors related to state preparation or readout. Furthermore, the trap volume is very small and only requires external fields to be controlled over a region a few mm on a side. All of these features promise a very precise electron EDM measurement, perhaps with sensitivity approaching the level of $|d_e| < 10^{-32}\ e\,$cm mentioned above.

1.2 Further applications of polyatomic molecules

Polyatomic molecules can advance numerous applications beyond the specific experiment that motivated our work with YbOH. By extending the achievable laser-molecule coherence time and allowing more precise quantum state control, laser cooling and trapping will enhance these applications. Here, we provide a brief sampler of exciting applications.

1.2.1 Probing variation of fundamental constants

Certain theories beyond the Standard Model predict variations of "fundamental" constants such as the proton-to-electron mass ratio, $\mu = m_p/m_e \sim 1836$ [4]. Variation of these constants would have observable effects on the energy level structure of atoms and molecules and could be detected through changes in the resonance frequencies of spectral features. Polyatomic molecules possess unique vibrational and rotational modes compared to diatomic molecules, and these features could make detecting variation of fundamental constants much easier. Sensitivity to μ varia-

tion will be enhanced whenever one considers a transition between nearly-degenerate energy levels where each level's energy depends differently on μ. Such an occurrence is common in polyatomic molecules. For example, it has recently been shown that in SrOH a combination of Sr-O stretching and Sr-O-H bending vibrations have nearly degenerate energies and μ-variation-sensitivity enhanced by $100\times$, if not more [27]. Moreover, large-amplitude motions in polyatomic species, such as inversion and hindered rotation, can also yield orders-of-magnitude enhanced sensitivity to μ variation [28–32]. These motions are present in any asymmetric top molecule containing an internal rotor (e.g., CH_3 group), but have *no* analog in linear or symmetric top molecules. Efficient state preparation, unit-efficiency readout, phase-space compression for enhanced counting statistics, and long interrogation times enabled by laser cooling may make these systems ideal testbeds for probing variation of fundamental constants in the laboratory.

1.2.2 Ultracold chiral species

In addition to its crucial role in fundamental physics and the global structure of the Universe, symmetry influences biology in unexpected ways. The single chirality of many biological molecules (left-handed amino acids but right-handed sugars) has fascinated physicists, chemists, and biologists for over 150 years. The origin of this biomolecular homochirality remains largely unsolved despite its importance for our understanding of the formation and evolution of life on Earth [33, 34]. Chiral molecules are necessarily polyatomic molecules, and more specifically they must be asymmetric top molecules. Photon cycling and laser cooling of chiral molecules provides fascinating opportunities for chiral separation [35] and for measurement of the slight energy difference between enantiomers (mirror image versions of a chiral species) [36]. Molecules such as, e.g., $CaOCHDCH_3$ or YbOCHDT are laser-coolable candidates. The long interrogation times enabled by traps will greatly enhance the precision of searches for fundamental parity violation, where precision $\ll 1$ Hz

on vibrational intervals are typically required [37].

Recently, it has also been shown theoretically that chiral molecules can offer enhanced sensitivity to parity-violating cosmic fields [38, 39]. Because such fields are present in models of cold dark matter and Lorentz-invariance violation, chiral molecules could represent important sensors of physics beyond the Standard Model. In particular, it was shown that chiral molecules acquire P-odd frequency shifts between enantiomers in the presence of pseudovector cosmic fields. It is possible that precision spectroscopy of laser-cooled chiral molecules could achieve the increased sensitivity required for such measurements to provide competitive limits on P-violating effects beyond the Standard Model, but input from electroweak chemistry will be required to determine suitable molecular candidates [39].

1.2.3 Collisions and cold chemistry

Both atom-molecule and molecule-molecule collisions are of fundamental and practical interest. Bringing atoms to quantum degeneracy has widely relied on elastic collisions[9] for thermalization. It is possible that creating Bose or Fermi degenerate gases of polyatomic molecules will also require knowledge of the underlying elastic and inelastic collision rates; atom-molecule collisions could be used for initial sympathetic cooling before molecule-molecule collisions are needed for final evaporation. This has been investigated even for complex molecules such as benzene and azulene [42]. Much theoretical effort has been devoted to the idea of *controlling* molecule-molecule collisions, where the numerous degrees of freedom features present in molecules tend to play an important role in achieving orientation/alignment that aid this control [43–47].

Ultracold temperatures would also provide a fruitful testing ground for control of chemical reactions. Because chemical reactions are "usually" activated by thermal effects, as $T \to 0$ one might

[9] There are some exceptional cases, e.g Refs. [40, 41].

expect reaction rates to approach zero [48]. In actuality, quantum effects take over in this temperature regime and tunneling and entanglement can cause observed rates to deviate significantly from zero. While such physics has been observed in bialkali species [49, 50], it would be very interesting to observe them in species containing the fundamental organic building blocks such as O, C, and H. Even at temperatures around 1 K, the combination of single-quantum-state control with the laser cooling of astrophysically relevant species (e.g., thiols, alcohols, and hydrocarbons) would provide stringent tests of calculated rate constants used in models to describe astrophysical evolution [51–53]. Furthermore, because laboratory fields can shift energy levels by up to a few Kelvin, external control of chemical reactions occurring below this energy scale may be possible [54–56].

1.2.4 Quantum computation and simulation

Ultracold dipolar molecules are an exciting new platform for quantum simulation [57–62] and quantum information processing [63–67]. While early studies tended to focus on diatomic species, interest has also widened to include symmetric top [60, 61, 68, 69] and asymmetric top molecules [70]. The complex internal structure of molecules allows robust encoding of quantum information, as recently proposed in Ref. [70]. Internal structure due to rotational, vibrational, and hyperfine interactions can allow the realization of qudits, higher dimensional analogs of two-level qubits [71]. This could enable improved error correction, larger Hilbert spaces with fewer physical particles, and faster computation times [72–75].

Additionally, ultracold molecules are a promising platform for quantum simulation or information processing due to their strong dipole-dipole interactions. For example, CaSH has a large molecule-frame dipole moment of $\sim$5.5 D along the a-axis and an additional dipole moment of $\sim$1.5 D along the b-axis [76].[10] Due to small parity doublets, DC fields $\lesssim 1$ kV/cm can be used to

[10]The bent structure is an important contributor to this larger a-axis dipole moment as can be seen by

access these large dipole moments in the laboratory frame. Thus, polyatomic molecules offer a viable route to achieving molecule-molecule couplings at least an order of magnitude stronger than can be achieved with the diatomic species laser cooled to date [78]. The presence of states with effectively zero dipole moment projection is also useful for "shelving" [67]. The parity-doublet structure giving rise to these states is generically present in polyatomic molecules, allowing one to choose experimentally convenient species without losing this feature.

1.3 Methods to produce cold molecules

In order to reap the benefits of polyatomic molecules, we must cool them to cold ($\lesssim 4\,\mathrm{K}$) or ultracold ($\lesssim 1$ mK) temperatures. This cooling is required to "compress" the molecular population into a small number of quantum states and to slow their thermal velocities to tens of meters per second; the former increases an experiment's signal-to-noise ratio and the latter enables long interrogation times to improve achievable precision and control. Because polyatomic molecules contain many internal degrees of freedom, achieving this cooling can be a very difficult task. Many research groups have tackled this problem, and we review some relevant methods here.

1.3.1 Association of ultracold atoms

A very successful method of producing ultracold diatomic molecules involves laser cooling atoms and then binding these pre-cooled atoms together (using photoassociation, magnetoassociation, etc.) [79–84]. While this has produced a number of ultracold diatomic molecules in single quantum states, including degenerate gases, it is not clear it can be generalized to produce *polyatomic* molecules. However, very recent work has shown some evidence for production of triatomic molecules in a mixture of ^{23}Na^{40}K and ^{40}K [85]. It is also unclear whether this exciting result

comparing the cases of CaSH ($d \approx 5.5$ D) and CaOH ($d \approx 1.4$ D) [76, 77].

can be extended to other species, especially large polyatomic molecules or molecules containing difficult-to-cool atomic species such as O, C, and/or H.

1.3.2 Optoelectrical Sisyphus cooling

Optoelectrical Sisyphus cooling, developed by Zeppenfeld and Rempe, uses state-dependent energy shifts and repeated microwave transitions/optical pumping steps to cool molecules as they move through an electric trap [86, 87]. Energy is removed by ensuring molecules move away from the trap's center along a "steep" potential and return to the center along a "shallow" potential. This technique relies on the linear Stark shifts that can be achieved in symmetric or asymmetric top molecules. It has been used to produce trapped samples of CH_3F and H_2CO at ∼mK temperatures and could potentially be used to observe molecule-molecule collisions in the trap. To date, the molecules that have been cooled using this method do not offer convenient optical transitions, so vibrational transitions with relatively long lifetimes have been used instead. The method could likely be adapted to make use of the optical transitions offered by the molecules discussed in this thesis, speeding up the cooling rates considerably.

1.3.3 Buffer-gas cooling

Buffer-gas cooling is a general technique that can cool atoms, diatomic, and even large polyatomic molecules by subjecting the species of interest to elastic collisions with a cold, inert gas. Several detailed reviews have described buffer-gas cooling, including Refs. [88–90]. Briefly, a hot sample of molecules is introduced into a cryogenic "cell" filled with an inert buffer gas (typically He or Ne). The buffer gas is cooled to $\sim 0.5 - 10$ K through collisions with the cell wall, and elastic collisions sympathetically cool the molecules of interest to nearly the same temperature. Because the molecules are isolated from the cell walls, this technique can be used even for unstable species

(like the radicals studied in this thesis). Inelastic collisions cool the internal degrees of freedom. Rotational cooling is quite efficient (occurring every 10-100 elastic collisions) because the timescale associated with typical molecular rotations roughly matches that for small-angle collisions with the buffer gas. Vibrational quenching is relatively inefficient (potentially taking $> 10^8$ elastic collisions) because the periods of oscillation in typical vibrational modes tend to be much more shorter than the timescale of a collision with buffer-gas atoms [88]. Buffer-gas cooling provides extreme phase-space compression: reducing translational temperatures to a few K, and leaving molecules in just a few tens of internal quantum states.

Buffer-gas cooling was pioneered by the atomic H community in the late 1970s/early 1980s. Early examples include the De Lucia group, which studied CO molecules, and later polyatomic molecules, in the presence of a ~ 4 K He buffer gas [91–93]. Important refinements in the Doyle group enabled buffer-gas loading of atoms and molecules into superconducting magnetic traps [94–97]. Further development by the Doyle and DeMille groups led to the demonstration of molecular beam sources generated from buffer-gas cells [98]. These cryogenic buffer-gas beams (CBGBs) can feature low forward velocities [89] and optimized cell designs were shown to benefit from hydrodynamic enhancement effects that led to beams several orders of magnitude brighter than previous technologies [99]. The primary benefit of a CBGB is that it allows the experiment to separate molecule *production* (occurring in a cryogenic region with poor optical access) from molecule *manipulation* (usually occurring in a room-temperature, ultra-high vacuum region). It is little exaggeration to say that CBGBs are one of the most important technological developments that enabled direct laser cooling of molecules.

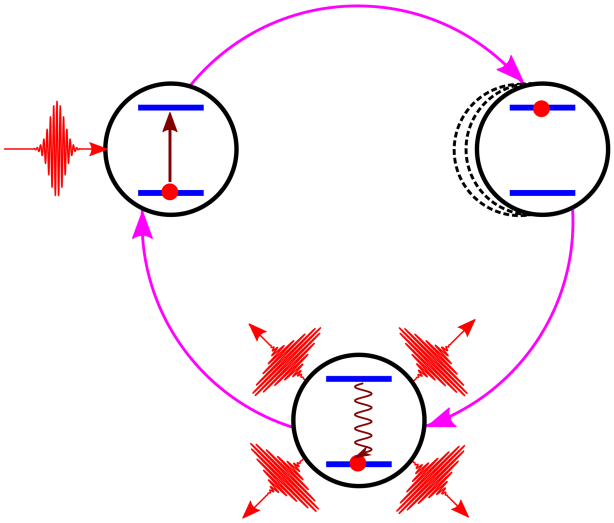

Figure 1.3: Schematic diagram of optical cycling in an ideal two-level system: directional photon absorption, momentum change due to photon absorption, and isotropic spontaneous emission leading to decay to the initial quantum level. Complex structures (of either atoms or molecules) can interrupt this cycle, e.g., by the addition of multiple decay pathways for spontaneous emission.

1.3.4 Direct laser cooling

The advent of laser cooling of neutral atoms revolutionized atomic physics in the 1980s and 1990s [5, 6]. In brief, laser cooling relies on the velocity-dependent forces that can be realized by rapidly and repeatedly scattering optical photons off of a gas of atoms [100]. Laser cooling typically relies on a cyclic process of laser photon absorption and spontaneous emission outlined in Fig. 1.3. Directed radiation pressure force from a laser beam and randomly oriented spontaneous emission can be used to slow and, with some modifications, trap atomic samples. In addition to the motional control that can be achieved, the tools of laser cooling (namely rapid photon cycling) also allow high-fidelity state preparation and readout. Cooling the atomic motion to have characteristic energy scale $\ll 1$ mK enabled groundbreaking studies of atomic interactions [101], simulation of condensed matter systems [7], construction of platforms for quantum information processing [102–104], studies of fundamental particle physics [105], and practical applications in sensing and navigation [106].

Because molecules— especially polyatomic molecules— offer much richer internal structures than atoms, it stands to reason that laser cooling of molecules would have similar revolutionary effects. However, the rich internal structure also makes the task of laser cooling molecules appear quite challenging. In particular, the many vibrational and rotational states present in molecules constitute a vast reservoir of "loss channels" that could interrupt the optical cycle [mainly in the spontaneous decay process of Fig. 1.3]. In a typical molecule, electron excitation followed by spontaneous photon emission might cause dozens (or more) of vibrational and rotational states to become populated— too many to feasibly control with lasers in the laboratory.

In 2004, Di Rosa published a seminal paper that identified a large class of diatomic molecules (including CaH, SrH, and a number of other hydrides and fluorides) with electronic and vibrational structure that made them amenable to direct laser cooling [107]. The molecules identified had structures in which electronic excitation and decay were very *unlikely* to cause a change in vibrational state. The "decoupling" between electronic and vibrational excitations comes from the fact that molecules like CaH and SrH feature a single valence electron with transitions between orbitals that are shifted away from the molecular bond (see further discussion in Ch. 2). In essence, Di Rosa made the problem of loss to vibrational dark states experimentally manageable. It was then pointed out that losses to the many rotational states could be eliminated with the proper choice of which optical transition was used for cooling [108]. Soon thereafter, radiation-pressure force deflection [109] and laser cooling [110] was demonstrated for the diatomic molecule SrF. Laser slowing and a magneto-optical trap (MOT) of SrF followed quickly [111–113], as did the realization of MOTs for CaF [114, 115] and YO [116].

The SrF, CaF, and YO experiments all followed a similar set of steps (Fig. 1.4) for cooling molecules to temperatures sufficiently low for conservative trap loading. First, molecules were produced by a CBGB (described above) and extracted into a beam with typical forward velocity

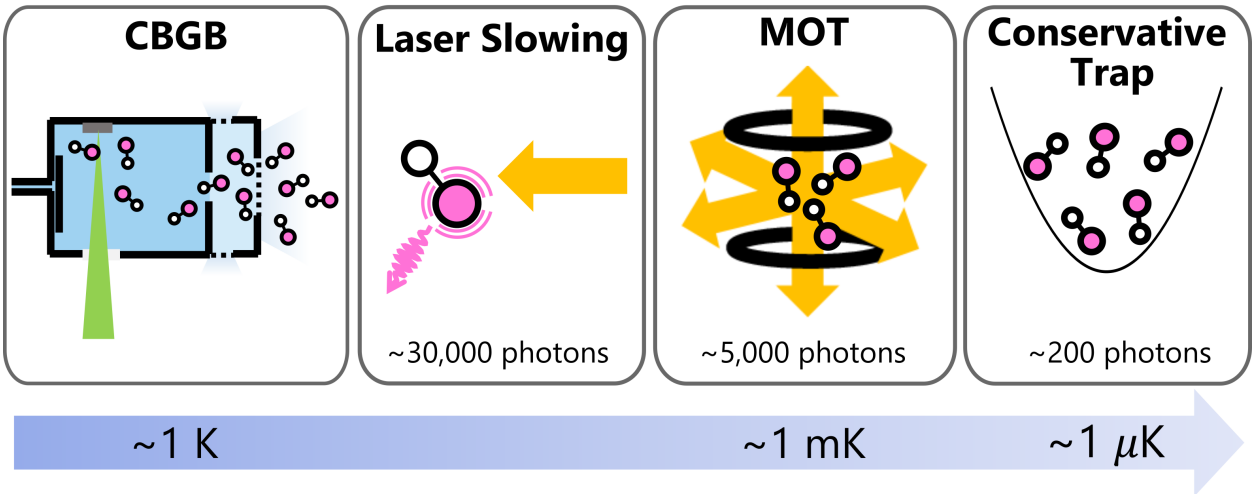

Figure 1.4: Overview of typical molecular laser cooling sequence.

~ 100 m/s. This is a relatively low velocity, but much larger than the MOT capture velocity of ~ 10 m/s. Molecules were next slowed down by subjecting them to the radiation pressure force of counter-propagating laser beams [117, 118]. This slowing step was universally found to be the most difficult part of the sequence to optimize. The slowed molecules were then loaded into a MOT and quickly cooled to the Doppler limit and, using gray molasses techniques in the same region [119, 120], below the Doppler limit. Finally, molecules could be loaded into a conservative trap of choice, either optical [121, 122] or magnetic [123, 124]. In Fig. 1.4 we give a sense of the temperature scales and number of photons required for each step.

In the midst of the exciting progress with diatomic molecules, Isaev and Berger pointed out that substitution of the halogen atom (e.g., F) with a pseudohalogen group (e.g., OH, CN, or NC) could produce polyatomic molecules with optical cycling properties similar to those of successfully cooled diatomic species [36]. Concurrent theoretical work in the Doyle group used simple theoretical methods to propose laser cooling schemes for molecules of the motif MOR, where M is an alkaline-earth atom, O is oxygen, and R is a ligand such as H, CH_3, or CH_2CH_3 [125]. Work in the Doyle group began on laser cooling SrOH before these theory proposals, and transverse laser

cooling of a molecular beam of SrOH was demonstrated soon thereafter [126]. This laser cooling demonstration proved that despite the complex vibrational structure of polyatomic molecules, well-chosen species could be controlled using the same techniques as had been used for simpler molecules and for atoms. Following the groundbreaking results laser cooling SrOH, many more theoretical proposals examined the prospects of laser cooling polyatomic molecules [127, 128]. One such proposal was the identification by Kozyryev and Hutzler of YbOH as a promising laser cooling candidate [26]; that work set the stage for this thesis.

1.4 Thesis overview

In the remainder of this thesis, we describe results extending optical cycling and laser cooling to increasingly complex polyatomic molecules. Here, we provide an overview of the major results of these efforts, emphasizing the essential relationships among them.

1.4.1 Laser cooling polyatomic molecules for EDM measurements

The thesis originated with the PolyEDM experiment, which aims to use polyatomic molecules at ultracold temperatures to search for the electron EDM. Ytterbium monohydroxide (YbOH) was identified as a promising candidate for this in 2017 [26], although at that time only a single spectroscopic study of this molecule had been reported [129]. Over the course of this thesis, we have demonstrated robust production of YbOH molecules through a variety of mechanisms, performed detailed spectroscopy at both low and high resolution, and demonstrated mechanical control over the motion of YbOH molecular beams by applying optical forces. In addition, we have laser cooled molecular beams of YbOH using both Doppler and Sisyphus cooling forces, demonstrating reduction in transverse temperatures from 20 mK to below 0.5 mK. By repumping molecules lost to

excited Yb-O stretching and Yb-O-H bending vibrational modes, we are able to scatter around 500 photons per molecule.

1.4.2 Spectroscopy and theory to identify new laser-coolable species

To laser cool YbOH, we needed to know the vibrational branching ratios (in order to know which vibrational states to repump) and the rotational assignments of transitions within each vibrational band (in order to drive the rotationally closed transitions described above [108]).[11] Determining the vibrational branching ratios led us to construct an apparatus that was optimized for highly sensitive fluorescence measurements. The techniques needed for these measurements could easily be applied to many polyatomic molecules, and during the course of this thesis we have experimentally observed such diverse species as $CaOCH_3$, $YbOCH_3$, CaSH, and $CaNH_2$ using similar techniques. At the same time, the precise measurements of YbOH indicated that many "unexpected" decays can occur with probability that, although small in an absolute sense, become important for a laser cooling experiment that requires scattering upwards of 10,000 photons. In Ch. 4 we discuss these measurements, and theoretical ideas that sprang from them inform many of the discussions in Ch. 8 and 9. The synergy between theory and experiment, and between understanding of YbOH and other polyatomic molecules, was an important aspect of this thesis.

1.4.3 Tools for cooling complex molecules

Because YbOH has a large mass and properties slightly less favorable for optical cycling, we expected from the outset that it would be difficult to slow molecular beams of YbOH using exactly the same techniques as had been demonstrated for simple molecules like CaF and SrF [111, 117].

[11] It is important to mention that Tim Steimle (Arizona State University) was an indispensable leader in performing both of these tasks.

Rather, we planned to develop new tools that made especially efficient use of optical cycling to control the motion and internal state of YbOH molecules. The most important result of this thesis toward such ends is the development of a Zeeman-Sisyphus slower (Ch. 7). This deceleration method leverages the large energy shifts experienced by magnetic molecules in Tesla-level magnetic fields to slow molecules to the capture velocity of typical traps. In order to "actuate" the energy removal, the molecules need to scatter just a handful optical photons (fewer than 10). Molecules slowed to around 10 m/s experience a deceleration per photon that is over 100× larger than can be achieved with the radiation pressure force, showing that this is a highly efficient method. The Zeeman-Sisyphus decelerator is applicable to a much wider ranger of molecules, and tools such as this will hopefully play a significant role in bring increasingly complex molecules to the ultracold regime. As will be discussed in Ch. 10, our thinking about complex polyatomic molecules has been strongly influenced by how "photon efficient" methods to manipulate molecular motion can modify the steps laid out in Fig. 1.4.

Bohr protested: 'Nobody will trust me unless I can explain every atom and molecule.' Rutherford immediately replied: 'Bohr, explain the hydrogen atom, explain helium, and everyone will believe the rest.'

Mario Bertolotti, in "The History of the Laser"

2

Molecular Structure

Many of the recent advances pushing the boundaries of which molecules are considered "laser-coolable" arose simply from identification of species with certain favorable structures [107, 125, 130]. In order to appreciate the results presented throughout the rest of this thesis, it is necessary to have an understanding of these structural characteristics. This chapter provides a description of molecular structure relevant to this thesis, building up to an explanation of how optical cycling can be achieved in polyatomic molecules. Our discussion is just a sliver of the vast subject of molecular structure, and the interested reader is referred to one of the excellent texts on the subject, including Refs. [131–137].

2.1 Born-Oppenheimer approximation

The level structure of a molecule is determined by the complete molecular Hamiltonian, $\mathscr{H}$, which generically contains terms depending on the electronic, nuclear, and spin coordinates [131, 135, 138]. Assuming that we can neglect the spin portion of the Hamiltonian for the time being, we are left with electronic and nuclear contributions: $\mathscr{H} = \mathscr{H}_e + \mathscr{H}_n$. The total wavefunction satisfies the Schrodinger equation $\mathscr{H}\psi = E\psi$, which cannot be solved exactly.

We can simplify the situation by noting that the nuclei and electrons feel similar electrostatic forces, but electrons move much more rapidly due to their smaller mass. Qualitatively, we can imagine that the electrons move so quickly that they can follow any change in nuclear configuration more or less instantly. This is the essence of the Born-Oppenheimer (BO) approximation, which is treated more rigorously in many textbooks on molecular physics [131, 135, 136, 139, 140].[1] Mathematically, the BO approximation motivates us to factorize the total wavefunction as

$$\psi(\mathbf{r}, \mathbf{R}) = \psi_e(\mathbf{r}; \mathbf{R})\psi_n(\mathbf{R}). \tag{2.1}$$

The nuclear wavefunction, $\psi_n(\mathbf{R})$, is a function of the nuclear coordinates only. The electronic wavefunction, $\psi_e(\mathbf{r}; \mathbf{R})$, is a function of the electronic coordinates but depends parametrically on the nuclear coordinates for any given arrangement of nuclei.

Given that $\mathscr{H}_e\psi_e = E_e\psi_e$, and that $\psi(\mathbf{r}, \mathbf{R}) = \psi_e(\mathbf{r}; \mathbf{R})\psi_n(\mathbf{R})$, we obtain

$$\left[\mathscr{H}_n + E_e(\mathbf{R})\right]\psi_n = E\psi_n(\mathbf{R}). \tag{2.2}$$

In this Schrödinger equation, the electronic energy E_e appears as a portion of the potential energy

[1] We are using somewhat sloppy language here, not distinguishing between things like the crude adiabatic approximation, the Born-Oppenheimer approximation, the Born-Huang approximation, etc. Any reader who is interested in these subtleties, or agitated by the loose treatment, should consult Refs. [140, 141].

that can vary as the nuclei move. The electrons influence the motion of the nuclei by setting up a potential in which the nuclei themselves evolve.

To a good approximation, we can separate the nuclear vibrational and rotational wavefunctions by working in a coordinate system that rotates with the molecule [138]. In this system, when vibration-rotation coupling can be neglected, we can write $\psi_n = \psi_v \psi_r$. This means the total wavefunction can be expressed as

$$\psi = \psi_e \psi_v \psi_r, \tag{2.3}$$

i.e., we have fully separated the electronic, vibrational, and rotational motions. This factorization mirrors the way we think about the molecules we aim to laser cool: whenever possible, we consider the electronic, vibrational, and rotational motions as separate parts of the laser cooling problem. Breakdown of the BO approximation will be discussed in Sec. 2.5.

2.1.1 Transition strengths

Transition intensities can be calculated from the square of the transition moment integral [135]

$$\mathbf{M} = \int \psi'(\mathbf{r}, \mathbf{R})^* \, \boldsymbol{\mu} \, \psi''(\mathbf{r}, \mathbf{R}) \, d\tau, \tag{2.4}$$

where integration with respect to τ implies integrating over all electronic and nuclear coordinates, single primes denote excited states, and double primes denote ground states. Invoking the BO approximation, we can write $\psi(\mathbf{r}, \mathbf{R}) = \psi_n(\mathbf{R}) \psi_e(\mathbf{r}; \mathbf{R})$. Then the transition moment integral becomes

$$\mathbf{M} = \int \psi_{n'}(\mathbf{R})^* \left(\int \psi^*_{e'}(\mathbf{r}; \mathbf{R}) \, \boldsymbol{\mu} \, \psi_{e''}(\mathbf{r}; \mathbf{R}) \, d\tau_e \right) \psi_{n''}(\mathbf{R}) \, d\tau_n. \tag{2.5}$$

We have separated integration over all nuclear coordinates ($d\tau_n$) and electronic coordinates ($d\tau_e$). Let us now define an electronic transition dipole moment as $\boldsymbol{\mathcal{R}}_{e''}^{e'}(\mathbf{R}) = \langle\psi_{e'}|\boldsymbol{\mu}|\psi_{e''}\rangle$, and we explicitly denote its dependence on the nuclear coordinates. We can imagine expanding $\boldsymbol{\mathcal{R}}_{e''}^{e'}(\mathbf{R})$ in a Taylor series about some value of $\mathbf{R}$ and retaining only the first (constant) term, which we will denote by $\boldsymbol{\mathcal{R}}_{e''}^{e'}$.[2] This simplifies Eq. 2.5 and allows us to write

$$\mathbf{M} = \boldsymbol{\mathcal{R}}_{e''}^{e'} \int \psi_{n'}(\mathbf{R})^* \psi_{n''}(\mathbf{R})\, d\tau_n. \tag{2.6}$$

The transition moment has factored into an electronic and nuclear portion, as would be expected from the BO approximation treatment. If we explicitly include both vibrational and rotational nuclear motions, we can write the intensities of rovibronic transitions as [135]

$$I_{(e'v'J')\rightarrow(e''v''J'')} = \left|\boldsymbol{\mathcal{R}}_{e''}^{e'}\right|^2 q_{v'\rightarrow v''} S_{J''}^{J'}, \tag{2.7}$$

where $\boldsymbol{\mathcal{R}}_{e''}^{e'}$ is the electronic transition dipole moment between electronic states e' and e'', $q_{v'\rightarrow v''}$ is a Franck-Condon factor (FCF) between vibrational states v' and v'', and $S_{J''}^{J'}$ is a Hönl-London factor between states J' and J''. We can interpret this factorization as stating that the intrinsic strength of some transition is set by $\left|\boldsymbol{\mathcal{R}}_{e''}^{e'}\right|^2$ while the distribution of that intensity among vibrational and rotational lines are set by $q_{v'\rightarrow v''}$ and $S_{J''}^{J'}$. We will have more to say about $q_{v'\rightarrow v''}$ and $S_{J''}^{J'}$ in Secs. 2.3.1 and 2.4.2, respectively.

[2] More details about the choice of point on which to center the expansion can be found in Ref. [135]. Often, the value of $\boldsymbol{\mathcal{R}}_{e''}^{e'}$ is inferred from measurements or $\boldsymbol{\mathcal{R}}_{e''}^{e'}(\mathbf{R})$ can be found via *ab initio* calculations and used in conjunction with numerical vibrational wavefunctions to compute the necessary integral.

2.2 Electronic structure

The molecules discussed in this thesis are complex, many-body systems containing at least three nuclei and several dozen electrons. Electronic wavefunctions arise from a Hamiltonian that describes electronic kinetic energy as well as electron-electron and electron-nuclear interactions. The formation of a bound molecule is the result of energy minimization— trading off between kinetic and potential energies. The formed molecules can "solve" this problem effortlessly, but how shall we understand such a system?

We will focus on molecules in which an alkaline-earth atom, M, bonds to some electronegative ligand, L (e.g., F, OH, OCH_3, SH, etc.), because these molecules are expected to have the structure desired for laser cooling [36, 125, 128, 130, 142]. As explained in Ref. [143], the alkaline-earth atoms tend to form ionically-bonded molecules due to their low ionization energies.[3] Whether M transfers one or both of its valence electrons to the bonding partner depends on whether L can form singly or doubly charged anions. For the examples of L listed above, singly-charged anions form, so M retains one electron even after forming a bond.

The relevant structural details can largely be extracted from a simple picture involving just three ingredients: a positively charged metal ion, M^{2+}, an optically active "valence" electron near the metal, and a negatively charged ligand, L^-. The presence of an unpaired electron leads to low-lying, metal-centered electronic excitations that can be used for optical cycling and laser cooling. One would naively expect the unpaired electron to have dominant s orbital character in the electronic ground state. More detailed ligand-field theory calculations [144, 145] show that this is largely true, but also that the interaction with the negatively charged ligand deforms the valence electron to minimize electron-electron repulsion [143]. For example, in the ground state this deformation is realized via mixing of $s\sigma$ and $p\sigma$ orbitals on M, a process shown schematically in Fig. 2.1.

[3] Alkaline-earth atom ionization energies fall in the range 5 eV (for Ba) to 9 eV (for Be).

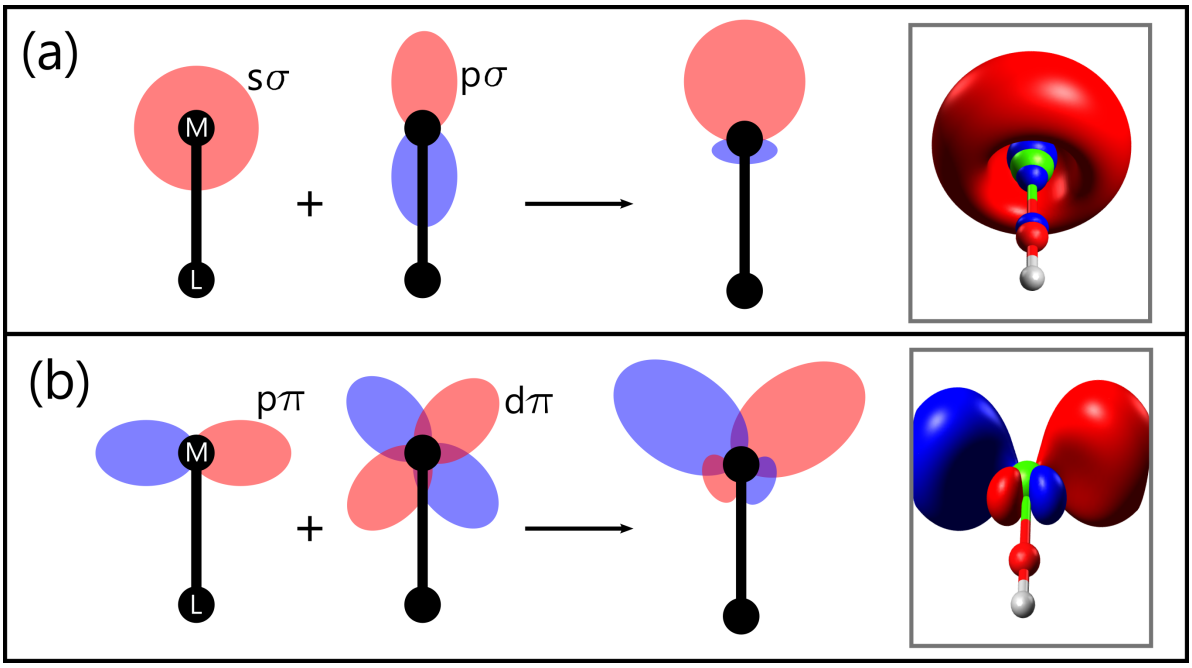

Figure 2.1: Illustration of orbital mixing reducing the interaction between valence electron and negatively charged ligand. (a) Mixing of $s\sigma$ and $p\sigma$ orbitals to generate the $\tilde{X}\,^2\Sigma^+$ state. (b) Mixing of $p\pi$ and $d\pi$ orbitals to generate the $\tilde{A}\,^2\Pi$ state. In both cases, the rightmost image shows quantum chemical calculations of the electronic distribution confirming this simple orbital mixing picture.

The orbital notation will be described more in the next paragraph. It has been found that in CaF, the ground electronic state ($\tilde{X}\,^2\Sigma^+$) arises from a mixture of approximately 80% of the $4s\sigma$ orbital and about 20% of the $4p\sigma$ orbital, while the lowest electronic state $\tilde{A}\,^2\Pi$ is made up of about 70% $4p\pi$ and 25% $3d\pi$ character [144]. Similar values are found for Ba-containing monohalides [145] and larger monomethoxide species [146].

An energy level diagram of the low-lying electronic states can be constructed from these ideas [143, 147]. The basic idea is to consider the Hamiltonian $\mathbf{H} = \mathbf{H}_{M^+} + \mathbf{H}_{L^-} + \mathbf{H}'$, where $\mathbf{H}_{M^+}$ and $\mathbf{H}_{L^-}$ describe the energy levels of the free ions and $\mathbf{H}'$ describes the interaction between the optically active valence electron and the ligand [144, 145]. When the ligand is treated as a point charge perturbation, it has three qualitative effects on the spectrum [147]:

1. It can shift the atomic ion's energy levels.
2. It can split the m_l components of each atomic nl state. We can think of this as arising from strong electrostatic forces along the bond, producing a Stark effect that resolves m_l compo-

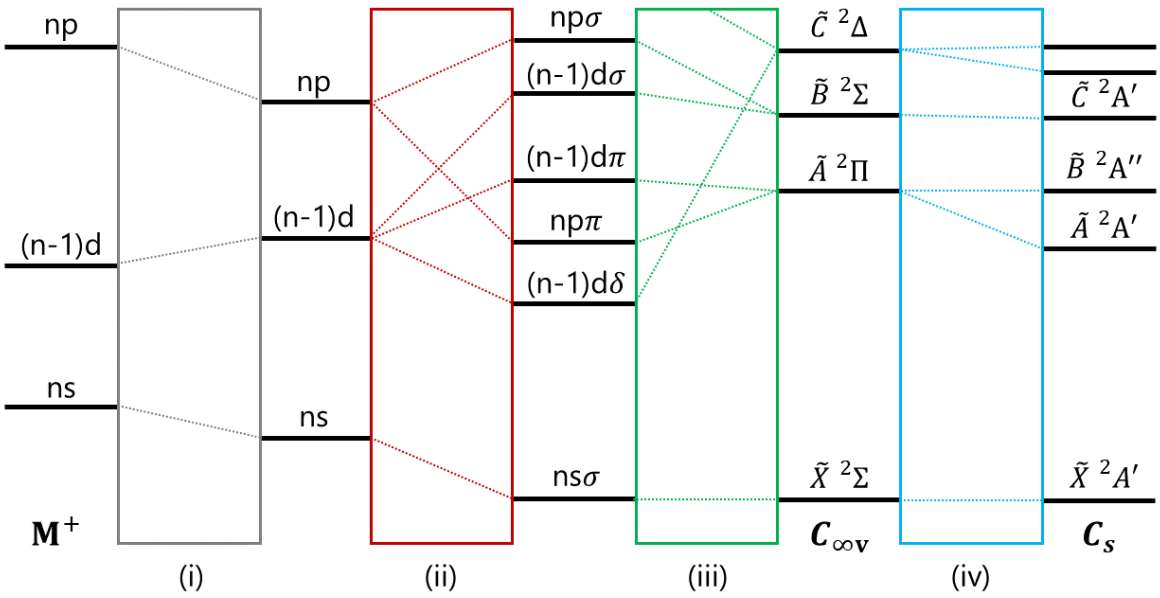

Figure 2.2: Correlation of low-lying electronic states from atomic ion (M^+) to linear ($C_{\infty v}$) and nonlinear (C_s) molecules. The labeled regions correspond to the following qualitative processes: (i) Shifting of atomic ion levels, (ii) Splitting of atomic m_l components, (iii) Mixing of energy levels with the same m_l, (iv) Cylindrical symmetry breaking due to a nonaxial ligand. Modeled after diagrams in Refs. [143, 147, 148].

nents along the bond axis. As is typical for the Stark effect, we do not resolve $+m_l$ and $-m_l$ components, and therefore label states as $\lambda = |m_l| = 0, 1, 2, \ldots$. States with $\lambda = 0, 1, 2, \ldots$ are denoted by $\sigma, \pi, \delta, \ldots$, respectively.[4]

3. It can mix orbitals obeying the selection rule $\Delta m_l = 0$. This may seem innocuous at first, but is actually quite important because this effect means each molecular orbital is a linear combination of atomic ion orbitals. Not only does this greatly affect the ordering of molecular states, it also means the molecular parameters of a given state will appear as an "average" of the atomic states that it comprises.

Figure 2.2(i-iii) shows the development of the energy levels as these effects are sequentially added. This diagram also shows how we name electronic states. For a linear molecule ($C_{\infty v}$ point group symmetry), we label electronic states by letters: $\tilde{X}$ for the ground state, $\tilde{A}, \tilde{B}, \ldots$ for the first, second, ..., electronically excited states, respectively.[5] In addition, because in most cases the

[4]We are using lower-case letters here because we are describing the single valence electron. Below, we will use capital letters to describe the total electronic state.

[5]If there are any electronic states with different multiplicity than the ground state, these will be labeled by lower case letters $\tilde{a}, \tilde{b}, \ldots$ in order of increasing energy.

electronic states can be identified by their electronic orbital angular momentum (Λ) and spin multiplicity ($2S+1$), we use the labeling scheme ${}^{2S+1}\Lambda$. For states with definite projection of spin onto the molecular axis, we can also add a subscript (Ω) to specify the *total* angular momentum projection on the internuclear axis (see also discussion of angular momentum coupling below).

This description has so far assumed the ligand can be treated as a point charge, meaning the M^+L^- system has cylindrical symmetry about the $M-L$ axis. Such symmetry is exact only for linear molecules (diatomic or polyatomic). If ML is a nonlinear molecule but still retains some axial symmetry (e.g., $MOCH_3$ as discussed in Ch. 8) then the picture is largely unchanged except that there will be no formal distinction between the symmetries of degenerate electronic states (e.g., for C_{3v} symmetry, $\Pi, \Delta, \ldots$ states are all classified as having E symmetry). If the ligand breaks the axial symmetry (e.g., MSH as discussed in Ch. 9), then the orbital degeneracy described in steps (2) and (3) just above is no longer guaranteed, and degenerate electronic states can split. For example, a Π electronic state of CaOH will correlate to states of A' and A'' symmetry for CaSH, as shown in Fig. 2.2(iv) and described in Ch. 9. Interested readers should consult Ref. [139] to learn about the symmetry groups and species discussed here.

2.3 Vibrational structure

Within each electronic state resides a ladder of vibrational states. The typical vibrational energies are in the range $100-3000$ cm^{-1}. As discussed, the vibrational wavefunctions are best expressed in terms of a coordinate system that rotates with the molecule [136, 138, 149]. The most convenient choice of coordinates is the normal coordinate system, since this eliminates cross terms between kinetic energy and potential energy. In this way, the vibrational Hamiltonian in the harmonic approximation can be written

$$\mathscr{H}_v = \sum_{i=1}^{3N-6} \mathscr{H}_i = \sum_{i=1}^{3N-6} \left(-\frac{\hbar^2}{2}\frac{\partial^2}{\partial Q_i} + \frac{1}{2}\lambda_i Q_i^2 \right), \tag{2.8}$$

where the Q_i are the $3N-6$ normal coordinates.[6] Note that the Hamiltonian has separated into a sum of Hamiltonians describing each normal coordinate. The total vibrational wavefunction can be written as the product of wavefunctions for each normal coordinate, i.e.

$$\psi_v(Q_1, Q_2, \ldots, Q_{3N-6}) = \prod_{i=1}^{3N-6} \psi_i(Q_i) = \psi_1(Q_1)\psi_2(Q_2)\cdots\psi_{3N-6}(Q_{3N-6}), \tag{2.9}$$

and the total vibrational energy can be written as

$$E_v = E_1 + E_2 + \cdots + E_{3N-6}. \tag{2.10}$$

See App. B for information on the conventions used to label the vibrational modes in polyatomic molecules.

Applying the Hamiltonian 2.8 to the wavefunction 2.9 generates $3N-6$ independent single-variable equations

$$-\frac{\hbar^2}{2}\frac{\partial^2\psi_i}{\partial Q_i^2} + \frac{\lambda_i}{2}Q_i^2\psi_i = E_i\psi_i. \tag{2.11}$$

The solutions of these equations are the well-known simple harmonic oscillator wavefunctions [135]. Some vibrational modes will be doubly (or more) degenerate, a notable example being the bending vibrations of linear triatomic molecules. In this case, we must instead solve a two (or more) dimensional Schrödinger equation in order to find the eigenvalues and eigenfunctions. Standard

[6] There are $3N-6$ vibrational modes for a general nonlinear molecule: the N-body system has $3N$ degrees of freedom, but 3 are associated with translations and 3 with rotations, leaving $3N-6$ for vibrations. Linear molecules have $3N-5$ degrees of freedom because they may not rotate about the internuclear axis. We choose to write $3N-6$ for full generality, but care must be taken to use the correct the formulas for linear molecules.

results from the theory of multidimensional quantum harmonic oscillators apply [150]. This is treated in detail in, e.g., Ref. [138], and the important point is that these degenerate modes can carry vibrational angular momentum. The degenerate eigenstates can either be described in terms of real degenerate normal coordinates Q_{t1} and Q_{t2} or in a "polar" representation that makes this angular momentum more transparent via the presence of vibrational quantum numbers v_t and l_t associated with total vibrational energy and orbital vibrational energy, respectively.

The vibrational energies within the harmonic approximation are given by

$$G(v_1, v_2, \ldots, v_{3N-6}) = \sum_i \omega_i \left(v_i + \frac{d_i}{2} \right), \tag{2.12}$$

where ω_i is the vibrational frequency and d_i the degeneracy of the i^{th} normal mode. To a higher approximation, we must include anharmonic terms in the molecular potential that can both shift and couple the different modes [135]. The wavefunctions are then linear combinations of the harmonic oscillator functions and the vibrational term value becomes

$$G(v_1, v_2, \ldots, v_{3N-6}) = \sum_i \omega_i \left(v_i + \frac{d_i}{2} \right) + \sum_{j \leq i} x_{ij} \left(v_i + \frac{d_i}{2} \right) \left(v_j + \frac{d_j}{2} \right) + \sum_{t \leq t'} g_{tt'} l_t l_{t'}, \tag{2.13}$$

where x_{ij} and $g_{tt'}$ are anharmonicity constants, t runs over degenerate vibrational modes, and l_t is the vibrational angular momentum of the t^{th} mode. The anharmonicity constants x_{ii} are similar to the constant $\omega_e x_e$ in diatomic molecules and arise from higher-order terms in the expansion of the potential energy surface along the stretching vibrational coordinates. The constants x_{ij} describe level shifts due to coupling between vibrational modes [135, 151]. The $g_{tt'}$ constants lift the ℓ-degeneracy, e.g. between the $(02^0 0)$ and $(02^2 0)$ states. In a linear triatomic molecule, g_{22} could arise from either quartic terms in the bending potential or from stretch-bend interaction terms [152].

2.3.1 Franck-Condon factors

The vibrational portion of the line intensity, Eq. 2.7, is the Franck-Condon factor (FCF) and this quantity is determined by the wavefunction overlap between ground and excited states:

$$q_{v'\to v''} = \left| \int \psi^*_{v'} \psi_{v''} d\tau_n \right|^2 . \tag{2.14}$$

Note that the FCFs obey a sum rule, $\sum_{v'} q_{v'\to v''} = \sum_{v''} q_{v'\to v''} = 1$.[7]

FCFs play a fundamental role in laser cooling molecules because they determine the distribution of intensity among possible vibrational transitions. From the point of view of laser cooling, we seek molecules in which a single transition has $q_{v'\to v''} \approx 1$ to ensure that many photon scattering events can be realized without population decaying into a large number of vibrational states. When a transition has the property that $q_{v'\to v''}$ is ≈ 1 for $v' = v''$ and ≈ 0 for $v' \neq v''$, we call that transition "diagonal" because the FCFs arranged into a matrix would approximate a diagonal matrix (ideally the identity matrix).

FCFs are determined by the degree of vibrational wavefunction overlap between initial and final state, as stated in Eq. 2.14. This overlap will be maximized when the two states have similar geometries (so there is no offset between the vibrational wavefunctions) and when the potentials have similar curvatures (so there is no width mismatch between the vibrational wavefunctions). That is, transitions that involve small change in molecular geometry *and* small change in vibrational frequency will tend to have nearly diagonal FCFs; transitions in which either the geometry or vibrational frequency changes significantly will have non-diagonal FCFs.[8] The latter condition is

[7] Technically the sum must extend over discrete and continuum states.

[8] The condition on molecular geometry is generally considered much more important. For example, starting from a bond length of 2 Å and frequency of 500 cm^{-1} (representative of molecules similar to YbOH), a 3% change in bond length reduces $q_{0\to 0}$ from 1.0 to 0.5 (assuming equal vibrational frequencies). On the other hand, the vibrational frequencies must change by over an order of magnitude (assuming equal bond lengths) to produce a similarly poor FCF.

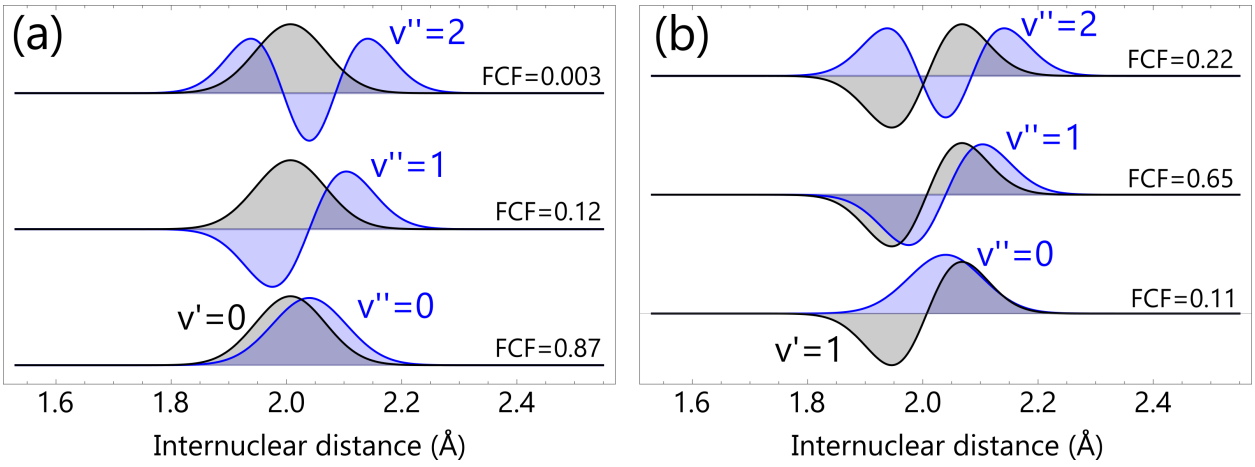

Figure 2.3: Franck-Condon factors derived from vibrational wavefunction overlap in a one-dimensional harmonic oscillator model. (a) Lowest vibrational wavefunction ($v' = 0$) for the $\tilde{A}\,^2\Pi_{1/2}$ electronic state of YbOH in black, and a selection of vibrational wavefunctions ($v'' = 0, 1, 2$) for the $\tilde{X}\,^2\Sigma^+$ state in blue. FCFs computed from the overlap integrals are also indicated. (b) Similar, but for the $v' = 1$ level of $\tilde{A}\,^2\Pi_{1/2}$. To generate these data, we have used $r_e(\tilde{X}) = 2.0397$ Å, $r_e(\tilde{A}) = 2.0070$ Å, $\omega_{\tilde{X}} = 529$ cm^{-1}, and $\omega_{\tilde{A}} = 585$ cm^{-1}, see Ref. [153].

especially important for, e.g., the bending modes of linear polyatomic molecules where the ground and excited state equilibrium geometries are equal, but the vibrational frequencies are not.

A graphical depiction of one-dimensional wavefunction overlap is shown in Fig. 2.3, where the parameters are chosen to match those of relevant YbOH $\tilde{A}\,^2\Pi_{1/2} \rightarrow \tilde{X}\,^2\Sigma^+$ transitions. The computed FCFs originating from $v' = 0$ are $q_{0\rightarrow0} \approx 0.87$ and $q_{0\rightarrow1} \approx 0.12$. These calculations are relatively close to the measured values of approximately 0.9 and 0.1, respectively (see Ch. 4). Similarly, the FCFs originating from $v' = 1$ are calculated to be $q_{1\rightarrow0} \approx 0.11$ and $q_{1\rightarrow1} \approx 0.64$, and $q_{1\rightarrow2} \approx 0.22$, in reasonable agreement with the measured values of 0.06, 0.65, and 0.15, respectively. It is remarkable that such a simple model— a one-dimensional, harmonic approximation— captures the FCFs with some degree of accuracy. Nonetheless, the disagreement is significant and more accurate FCF calculations must take into account the full multidimensional wavefunctions, anharmonicity, and coupling between vibrational modes (see Ch. 4 and Refs. [154–156]).

While computing $q_{v'\rightarrow v''}$ from Eq. 2.14 is computationally challenging, there are sometimes selection rules that guarantee cases in which $q_{v'\rightarrow v''} = 0$. In order for the integral $\int \psi^*_{v'}\psi_{v''}d\tau_n$ to be

nonvanishing, the integrand must contain at least one term that is totally symmetric with respect to the symmetry operations of the point group to which the molecule belongs [135]:

$$\Gamma^{(v')} \otimes \Gamma^{(v'')} \supseteq \Gamma_{\text{sym}}. \tag{2.15}$$

Here, $\Gamma^{(v)}$ specifies the symmetry species of ψ_v and Γ_{sym} is the totally symmetric representation of the relevant point group (i.e., Σ^+ for linear molecules, etc.). For linear triatomic molecules, Eq. 2.15 means that $\Delta\ell_2 = 0$ and therefore $\Delta v_2 = 0, \pm 2, \pm 4, \ldots$. Similar selection rules can be derived for symmetric top molecules [139]. Violation of this vibrational selection rule does occur and will be discussed in Sec. 2.5 and Ch. 4. In such cases, it is the *vibronic* symmetry (rather than the vibrational or electronic symmetries alone) that determines which transitions are allowed (see Refs. [135, 139]).

2.3.2 Vibrational branching ratios

The FCFs characterize the degree of vibrational wavefunction overlap. They differ slightly from the vibrational branching ratios (VBRs) due to the ω^3 dependence of the transition dipole. Including that factor, the VBRs are given by

$$b_{v' \to v''} = \frac{q_{v' \to v''} \omega^3_{v',v''}}{\sum_{v''} q_{v' \to v''} \omega^3_{v',v''}}. \tag{2.16}$$

The distinction can be important, especially when considering decays to high-frequency vibrational modes such as those involving stretching of hydrogen bonds.

2.4 Rotational Structure

Within a given vibronic (electronic-vibrational) state, there is a ladder of rotational states. Molecular end-over-end rotations have typical energy scales on the order of $0.1 - 1$ cm^{-1}. To lowest order, molecular rotation can be described as a rigid rotor. The rigid rotor Hamiltonian has well-known solutions [137]. The rotational eigenstates of a symmetric top molecule are described by the spherical harmonics and the energy eigenvalues are $E = AR_z + BR(R+1)$, where A and B are the rotational constants about and perpendicular to the molecule's figure axis[9], R is the angular momentum quantum number, and R_z its projection on the molecule axis.[10] Linear molecules can be treated as special cases of symmetric tops for which only the B rotational constant is defined. Rotational states of *asymmetric* top molecules will be treated in Ch. 9 as linear combinations of symmetric top basis states, so a good understanding of symmetric species is needed first.

2.4.1 Angular momentum and coupling

Molecules contain many sources of angular momentum and these can couple together in various ways. Table 2.1 lists the angular momenta that are relevant to this thesis. Even within the same molecule, these angular momenta may couple in different ways depending on the electronic state. In general, certain quantities will be conserved exactly and represent good quantum numbers. Many more quantities are *approximately* conserved because the interactions that cause them to evolve in time are relatively weak. When describing molecular states, it is profitable to choose a basis that most closely aligns with these conserved (or nearly-conserved) quantities.

Hund has identified five limiting cases of angular momentum coupling that are useful to de-

[9] $A = h/8\pi^2 cI_{aa}$ and $B = h/8\pi^2 cI_{bb}$, where I_{aa} (I_{bb}) is the principle moment of inertia about (perpendicular to) the symmetry axis.

[10] We will see below that depending on the other angular momenta present in the molecule, the "pattern-forming" angular momentum could be J, N, etc.

Table 2.1: Angular momentum vectors, decompositions, and projections on the internuclear axis ($\hat{n}$). Note that Σ is not a good quantum number in Hund's case (b); in that case, we instead decompose $\boldsymbol{J} = \boldsymbol{N} + \boldsymbol{S}$.

Quantity	Decomposition	Projection on $\hat{n}$	Physical Description
$\boldsymbol{L}$		Λ	Electron orbit[a]
$\boldsymbol{R}$		K_R	Rigid-body rotation
$\boldsymbol{S}$		Σ	Electron spin
$\boldsymbol{G}$		ℓ	Vibration
$\boldsymbol{N}$	$\boldsymbol{R} + \Lambda\hat{n} + \boldsymbol{G}$	$K\,(= K_R + \Lambda + \ell)$	Total orbit
$\boldsymbol{J}$	$\boldsymbol{N} + \Sigma\hat{n}$	$P\,(= K + \Sigma)$	Total excluding nuclear spin
Ω	$\Lambda + \Sigma$	$\Lambda + \Sigma$	Electron total projection
$\boldsymbol{I}$			Nuclear spin
$\boldsymbol{F}$	$\boldsymbol{J} + \boldsymbol{I}$		Grand total[b]

[a] Electron orbit may be "quenched" in nonlinear molecules. Then Λ is replaced by ζ_e (maybe non-integral).
[b] While the relation $\boldsymbol{F} = \boldsymbol{I} + \boldsymbol{J}$ holds for the molecules discussed in this thesis, it is not universally true. The ^{171,173}YbOH isotopologues are important examples in which $\boldsymbol{I}$ and $\boldsymbol{S}$ couple more strongly to each other than either one couples to $\boldsymbol{J}$.

scribe the molecular states often observed in Nature; Hund's cases are a collection of basis sets that describe these limiting cases [131, 135]. For our purposes, familiarity with two Hund's cases [called (a) and (b)] is sufficient. Also, we can focus on molecules with $S = 1/2$ (doublet species). Figure 2.4 shows how the various angular momenta couple under Hund's cases (a) and (b) basis sets for both linear and nonlinear (symmetric top) molecules.[11] The primary difference between linear and nonlinear molecules is that in linear molecules the rigid body rotation is necessary perpendicular to the internuclear axis ($\boldsymbol{R} \perp \hat{n}$) while nonlinear molecules can have rigid body rotation both perpendicular to and about the symmetry axis ($\boldsymbol{R}$ can have a projection along $\hat{n}$).

Hund's case (a) basis sets [see Fig. 2.4(i) and (iii)] best describe states in which the electron spin is strongly coupled to the electronic orbital angular momentum [131]. $\boldsymbol{L}$ is strongly coupled to the internuclear axis by electrostatic interactions and spin-orbit coupling causes the electron, too, to precess rapidly about the internuclear axis. Both $\boldsymbol{L}$ and $\boldsymbol{S}$ are therefore resolved along

[11] In Fig. 2.4, we neglect both nuclear spin and vibrational angular momenta. These can couple to the $\boldsymbol{J}$ shown in the figures to produce $\boldsymbol{F}$. For the molecules discussed in this thesis, it is generally the case that $\boldsymbol{G}$ will be resolved along the internuclear axis while $\boldsymbol{I}$ instead precesses about $\boldsymbol{J}$.

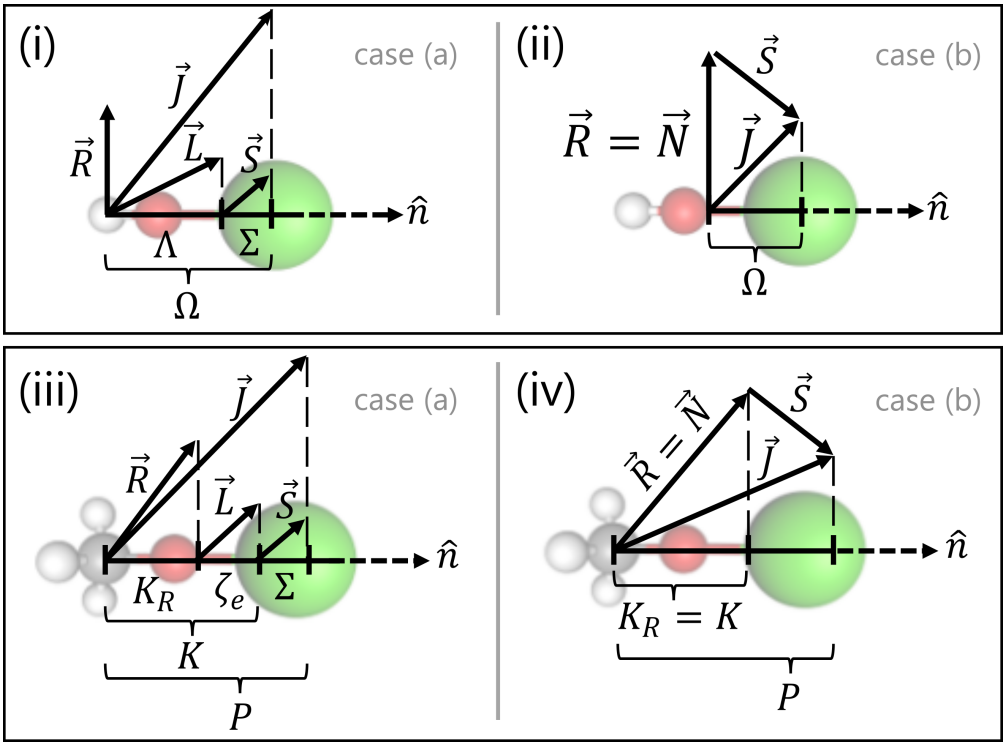

Figure 2.4: Angular momentum coupling in Hund's case (a) and (b) basis sets for linear and symmetric top molecules. (i) Linear Hund's case (a), (ii) Linear Hund's case (b), (iii) Symmetric top Hund's case (a), (iv) Symmetric top Hund's case (b). We neglect nuclear spin and vibrational angular momenta, but they could be added in the natural way.

the internuclear axis with projections Λ and Σ, respectively.[12] In addition to Λ and Σ, their sum ($\Omega = \Lambda + \Sigma$) is also a good quantum number.

Hund's case (b) basis sets [see Fig. 2.4(ii) and (iv)] are most appropriate for molecules with weak or nonexistent spin-orbit coupling (e.g., $^2\Sigma$ states in which there is no orbital angular momentum) [131]. In this case, the electron spin does not have a well-defined projection along the internuclear axis and Σ is not specified. Instead, $\boldsymbol{L}$ couples with $\boldsymbol{R}$ to form $\boldsymbol{N}$. Then, $\boldsymbol{S}$ couples with $\boldsymbol{N}$ to produce the total angular momentum $\boldsymbol{J}$. For the case of $^2\Sigma$ electronic states for linear molecules, $\boldsymbol{L} = 0$ so $\boldsymbol{R} = \boldsymbol{N}$. Spin-rotation interaction splits the $\boldsymbol{J} = \boldsymbol{N} \pm \boldsymbol{S}$ states.

[12] In nonlinear molecules, the electronic orbital angular momentum can be impeded or "quenched" by the presence of off-axis nuclei and the projection is not necessarily integral [157]. We denote the projection of $\boldsymbol{L}$ in this case by ζ_e.

2.4.2 Hönl-London factors

The Hönl-London factors, $S_{J''}^{J'}$, describe the distribution of intensity among different rotational components of a given vibronic transition. Hönl-London factors for transitions between various Hund's cases can be found in the literature for linear molecules [158–161] and for symmetric tops [162].

The energy eigenstates of a real molecule will, in general, be linear combinations of the Hund's case basis functions. Rotational line strengths can be calculated as follows [135]: first, choose a basis in which to express each state involved in the transition (for us, typically a Hund's case (a) or (b) basis is chosen); second, compute the Hönl-London factors for transitions between the basis sets describing these two states; third, express each eigenstate as a linear combination of the basis states (that is, diagonalize the two Hamiltonians); finally, use these linear combinations and the precomputed Hönl-London factors to calculate the strength of any rotational lines of interest. If the Hönl-London factors are arranged in a matrix ordered like the basis set elements, then cross-multiplication of this matrix by the eigenstates involved in a transition provides the desired line strength.

2.5 Born-Oppenheimer approximation breakdown and perturbations

In Eq. 2.3, we invoked the BO approximation in order to write the molecular wavefunction as $\psi = \psi_e\psi_v\psi_r$, a product of electronic, vibrational, and rotational parts. This factorization breaks down when parts of the molecule interact in a way that cannot be separated. In those cases, the actual wavefunction can still be written as a linear combination of factorized wavefunctions. For example, if vibronic interactions (between vibrational and electronic motions) cause a breakdown of the

factorization between electronic and nuclear wavefunctions, then we must write

$$\psi = \psi_r \sum_i c_i \psi_e^{(i)} \psi_v^{(i)}. \tag{2.17}$$

Examples of this vibronically-induced BO approximation breakdown are the Renner-Teller [163] and Jahn-Teller [164] effects. By causing mixing between different electronic and vibrational wavefunctions, these effects can lend intensity to nominally forbidden (or weak) decays and complicate the task of laser cooling polyatomic molecules.

By contrast, if vibration-rotation interactions cause BO-approximation breakdown, such as in the Coriolis interaction, we would instead have to write

$$\psi = \psi_e \sum_i \psi_v^{(i)} \psi_r^{(i)}. \tag{2.18}$$

This can have dramatic effects on the rotational structure as well as on the strength of vibrational transitions that may become mixed in through the BO approximation breakdown. Again, this could lead to intensity borrowing effects that affect which transitions must be repumped in order to achieve photon cycling and laser cooling.

2.5.1 Renner-Teller coupling

When no bending vibrations are excited, the electronic states of a linear polyatomic molecule with nonzero electronic orbital angular momentum ($\Lambda > 0$) are doubly-degenerate due to the cylindrical symmetry of the molecule. When bending vibrations are excited, nuclei move off axis and generate a non-cylindrical electrostatic interaction. The multipole moments generated by this off-axis charge distribution can interact with the electron's orbit, leading to a coupling between the electron orbital and vibrational angular momenta. The *total* angular momentum projection K, rather than

Λ or ℓ individually, is the conserved angular momentum projection on the molecule axis. This is the essence of the Renner-Teller effect, a manifestation of BO approximation breakdown that has been covered in more depth by a number of authors [132, 140, 163, 165–169]. As will be seen in Ch. 4, we have made direct measurements of vibrational branching ratios that violate the nominal selection rule $\Delta\ell = 0$ and are attributed to the Renner-Teller effect.

Motivated by the picture presented above, the Hamiltonian is often expanded in a multipole expansion, such as [132]

$$H_{RT} = V_{11}\left(Q_+ e^{-i\theta} + Q_- e^{+i\theta}\right) + V_{22}\left(Q_+^2 e^{-2i\theta} + Q_-^2 e^{+2i\theta}\right) + \cdots \tag{2.19}$$

where $Q_\pm$ are raising and lowering operators on the vibrational angular momentum ℓ, θ is the azimuthal angle of the electron's orbit, $e^{\pm i\theta}$ act as ladder operators on the electronic angular momentum Λ, and the coefficients V_{ii} quantify the strength of the interaction. Matrix elements of the $Q_\pm$ operators are typical of a two-dimensional harmonic oscillator, see Ref. [132].

The V_{11} ("dipolar") term mixes states with $\Delta v_2 = \pm 1$, $\Delta\ell = \pm 1$, $\Delta\Lambda = \mp 1$, and $\Delta K = 0$, while the V_{22} ("quadrupolar") term mixes states with $\Delta v_2 = \pm 2$, $\Delta\ell = \pm 2$, $\Delta\Lambda = \mp 2$, and $\Delta K = 0$. While *shifts* of energy levels are not of direct concern to laser cooling experiments, *mixings* between different (unperturbed) states are important because they may lead to unexpected loss channels. The dipolar (leading order expansion) term mixes states within the $\widetilde{A}$ manifold at *second* order in perturbation theory, e.g. when combined with a spin-orbit interaction between the $\widetilde{A}$ and $\widetilde{B}$ states. Meanwhile, the quadrupolar (second order expansion) term can mix states within $\widetilde{A}$ at *first* order [170, 171]. Decays induced by either of these terms could therefore be expected to contribute at similar levels. As we will see in Ch. 4 this is indeed observed for CaOH and numerical estimates of Renner-Teller-induced decays will be discussed in Sec. 4.3 and 4.2.

2.6 Forming a closed optical cycle: linear molecules

In this section, we summarize the level structure of transitions selected for laser cooling of linear (triatomic) molecules such as YbOH and CaOH. These transitions are used for laser cooling YbOH (see Ch. 6) and Zeeman-Sisyphus slowing of CaOH (see Ch. 7). We defer discussion of cycling transitions in symmetric top molecules to Ch. 8 and in asymmetric top molecules to Ch. 9.

The ground states of CaOH and YbOH ($\tilde{X}\,^2\Sigma^+$) have no electronic orbital angular momentum and are therefore best described by a Hund's case (b) basis set. By contrast, the lowest excited states of both molecules have one unit of electronic orbital angular momentum ($\tilde{A}\,^2\Pi_{1/2}$) and a large spin-orbit interaction, so they are best described by a Hund's case (a) basis set.

2.6.1 $\tilde{X}\,^2\Sigma^+$ structure

The low-J rotational levels[13] of the YbOH and CaOH $\tilde{X}\,^2\Sigma^+$ states can be accurately described by the effective Hamiltonian [131, 172, 173]

$$H_{\text{eff}}(\tilde{X}\,^2\Sigma^+) = B\boldsymbol{N}^2 + \gamma \boldsymbol{N}\cdot\boldsymbol{S} + b_F \boldsymbol{I}\cdot\boldsymbol{S} + \frac{c}{3}\left(3I_zS_z - \boldsymbol{I}\cdot\boldsymbol{S}\right), \tag{2.20}$$

where B is the rotational parameter, γ is the spin-rotation parameter, b_F is the Fermi contact parameter, and c is the dipolar hyperfine parameter. Measured values of these parameters are presented in Tab. 2.2. Roughly speaking, the structure expected will be a ladder of rotational levels with energies $\approx BN(N+1)$. Within each N level, the spin-rotation term can generate two substates $J = N \pm S$, and hyperfine can further split these states.

Using matrix elements from the literature [131], Hamiltonian 2.20 can be diagonalized to yield the energies $E_{N,J,F}$ in an $|N, J, F\rangle$ basis.[14] Exact expressions for the energies can be found in

[13] We will neglect vibrational angular momentum here, but see App. A for some details.

[14] Note that J is not really a good quantum number due to hyperfine-induced mixing terms, but we retain

Table 2.2: Molecular parameters for YbOH and CaOH $\tilde{X}\,^2\Sigma^+$ (000) states. All values in MHz.

Parameter	YbOH [172]	CaOH [174]
B	7 348.40053(29)	10 023.0841(7)
γ	−81.150(57)	34.7593(10)
b_F	4.80(18)	2.602(3)
c	2.46(48)	2.053(10)

Ref. [176]. To the extent that the hyperfine splittings can be neglected (they are unresolved in optical transitions for both CaOH and YbOH), the energy levels in non-bending ($\ell = 0$) modes are [177]

$$F_1(N) = BN(N+1) + \frac{\gamma}{2}N \tag{2.21}$$

$$F_2(N) = BN(N+1) - \frac{\gamma}{2}(N+1), \tag{2.22}$$

where the subscripts 1 and 2 label the two different combinations of $J = N \pm S$. Hyperfine interactions cause a small splitting of each F_1 or F_2 term, typically $\lesssim 5$ MHz for CaOH or YbOH. This energy level progression is shown in Fig. 2.5(a). A ladder of rotational states (labeled by N) is split into spin-rotation components labeled by J. Hyperfine splitting further splits the J states. The parity of each level is simply $p = (-1)^N$ [131].

2.6.2 $\tilde{A}\,^2\Pi_{1/2}$ structure

The low-J rotational levels of YbOH and CaOH $\tilde{A}\,^2\Pi$ states can be modeled by the effective Hamiltonian [131, 178]

$$H_{\text{eff}}(\tilde{A}\,^2\Pi) = T_0 + AL_zS_z + B\boldsymbol{N}^2 + \frac{1}{2}(p+2q)\left(e^{-2i\phi}J_+S_+ + e^{+2i\phi}J_-S_-\right), \tag{2.23}$$

it as a label. For small hyperfine interaction, it is approximately conserved. See Sec. 2.5 in Ref. [175].

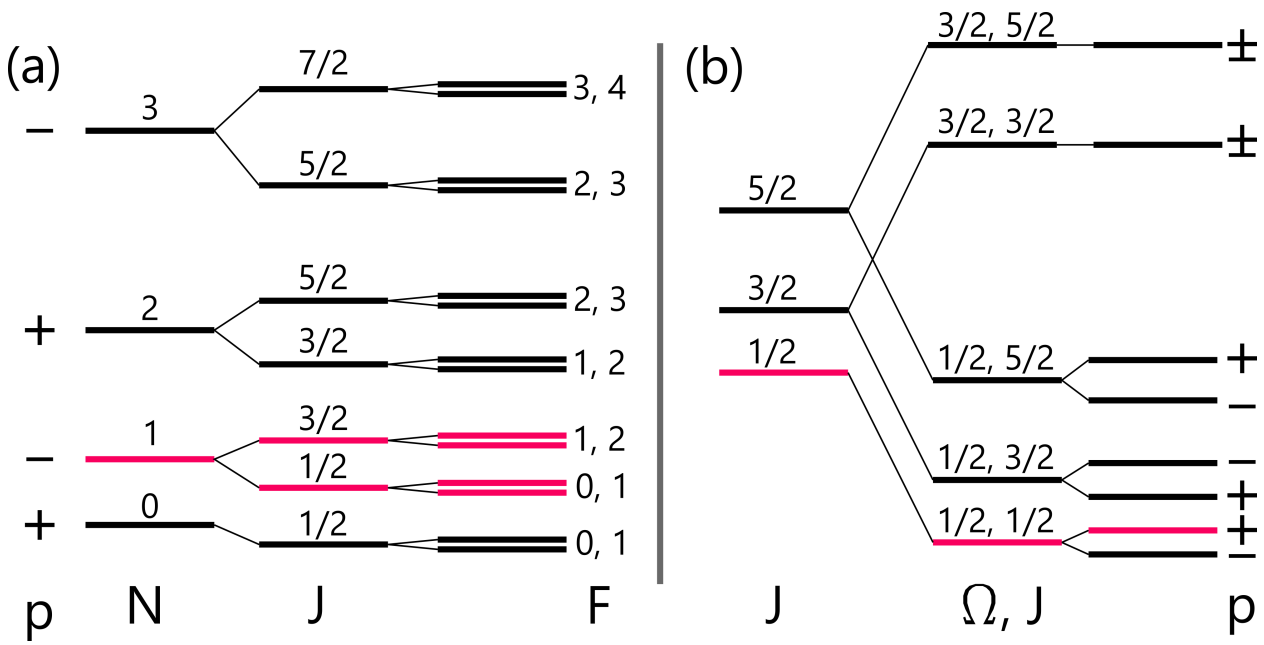

Figure 2.5: Level diagrams of CaOH/YbOH $\tilde{X}\,^2\Sigma^+\ (000)$ and $\tilde{A}\,^2\Pi(000)$ states (not to scale). Very similar diagrams apply for any vibrationally excited states that do not carry nuclear orbital angular momentum ($\ell = 0$ states). (a) Low-N levels of $\tilde{X}\,^2\Sigma^+(000)$ state, including sequential addition of spin-rotation and hyperfine couplings. This is drawn assuming positive γ, which is the case for CaOH but not YbOH. (b) Low-J levels of $\tilde{A}\,^2\Pi(000)$ state, including sequential addition of spin-orbit, Λ-doubling, and hyperfine interactions. Levels involved in laser cooling scheme are highlighted in red.

Table 2.3: Molecular parameters for YbOH and CaOH $\tilde{A}\,^2\Pi(000)$ states. All values in MHz.

Parameter	YbOH [173]	CaOH [180]
A	$40\,471\,981^a$	$2\,003\,156(35)$
B	$7\,586.30(9)$	$10\,229.51(7)$
$p+2q$	$-13\,133.0(9)$	$-1\,304(2)$

[a] Fixed during analysis.

where ϕ is the electronic angular coordinate.[15] Here, T_0 is the excitation energy, A is the spin-orbit coupling parameter, B is the rotational parameter, and $\frac{1}{2}(p+2q)$ is the Λ-type doubling parameter. Measured values of these parameters are presented in Tab. 2.3. Hyperfine structure here is even smaller than in the ground state and can be neglected [179].

Matrix elements from the literature [131] can be used to diagonalize Hamiltonian 2.23. The level structure found is shown schematically in Fig. 2.5(b). Widely-separated spin-orbit compo-

[15] The factors $e^{\pm 2i\phi}$ essentially ensure the matrix elements obey $\Delta\Lambda = \pm 1$ selection rules. See Ref. [131].

nents $\Pi_{1/2}$ and $\Pi_{3/2}$ each contain a ladder of rotational levels. Each J level is split by the Λ-doubling into two parity components. The Λ-type doubling is significant in the $\Pi_{1/2}$ state but negligible in the $\Pi_{3/2}$ state. This difference can be seen from the form of the Λ-doubling term in Eq. 2.23, which can directly couple $\Omega = \pm 1/2$ basis states but not $\Omega = \pm 3/2$ ones. The energy levels of the $|\Omega| = 1/2$ component can be approximately described as [177]

$$F_{1,\pm}(J) = T_0 - A/2 + BJ(J+1) \mp (-1)^{J-\frac{1}{2}} \frac{(p+2q)}{2}(J+1/2), \tag{2.24}$$

and those of the $|\Omega| = 3/2$ component as [177]

$$F_2(J) = T_0 + A/2 + BJ(J+1) \tag{2.25}$$

because the Λ-doubling is negligible. We have neglected hyperfine in this description. For molecules like YbOH and CaOH the excited state hyperfine interaction is generally smaller than in the ground state (which was already negligible) [179].

2.6.3 Cycling transitions

To achieve optical cycling, we seek an excited state that can rapidly scatter photons (short natural lifetime) while introducing minimal loss to other electronic, vibrational, and rotational levels. When there *is* loss, it generally involves population flowing into "dark" states; this population could be recovered by applying either laser or microwave fields to "repump" it back into the optical cycle. The fewer loss channels that are present, the easier it is to scatter many photons while using a small number of lasers.

Electronic closure

Electronic losses are mitigated by driving to one of the lowest excited electronic states, minimizing the number of levels between the excited state used for optical cycling and the ground state. Intermediate electronic states *are* present in some molecules, e.g. the $A'^{2}\Delta_{3/2}$ state in YO, but do not significantly inhibit laser cooling [116, 181, 182]. In YbOH, there are concerns about intermediate electronic states arising from Yb $4f^{13}$ orbitals, but at present we do not have enough data to comment on how they will affect YbOH cooling.

Vibrational closure

Vibrational losses are mitigated by choosing molecules with favorable VBRs and applying laser repumpers to all ground states that accumulate significant population. This is essentially dependent on the molecule chosen and the number of lasers tolerated by the experimentalist. The determination of which vibrational states must be repumped, and how many photons can be scattered as each additional repumper is applied, is discussed in Ch. 4 using YbOH, CaOH, and $CaOCH_3$ as examples.

The photon scattering process is one in which molecules go through a series of photon absorption and spontaneous emission cycles that can be described as a Bernoulli sequence. Supposed we have applied laser repumpers such that a molecule has a probability p to decay to a state that is *not* addressed by laser light. The probability P_n for a molecule to experience n absorption-emission cycles is given by $P_n = (1-p)^n$. The average number of photons scattered by molecules is $\bar{n} = \frac{1}{1-p}$. We often refer to this as the "photon budget," and it sets the (exponential) scale for how many photons can be scattered before significant fractions of the population are lost. For example, if laser slowing requires 10,000 photon scatters and we would like 90% of the initial population to remain after slowing, we require $p \approx 10^{-5}$. Clearly, understanding vibrational branching ratios as small

as 1 part in 10^5 can be crucial to achieve efficient laser cooling.

Rotational closure

For each vibrational repumping transition that is driven, we can eliminate *rotational losses* by driving a cleverly chosen transition and relying on angular momentum and parity selection rules [108]. Examining Fig. 2.5 and invoking the selection rules $|\Delta J| \leq 1$ and $\Delta p = \pm 1$, we see that $J' = 1/2(p = +)$ can decay only to $N'' = 1(p = -)$. This means that driving $N'' = 1 \rightarrow J' = 1/2(p = +)$ forms a rotationally closed cycle, so long as we address both the $N'' = 1, J'' = 1/2$ and $N'' = 1, J'' = 3/2$ sublevels; this is easily done by adding "spin-rotation" sidebands to the laser beam by passing it through an acouto-optical modulator (AOM).[16] In spectroscopic notation, the driven rotational transitions are referred to as ${}^pQ_{12}(N'' = 1)$ and $P_1(N'' = 1)$ [22].

There is one complication of this choice of closed rotational transition: it involves driving transitions for which $F'' > F'$, so that for a given laser polarization there will be dark magnetic sublevels that do not couple to the laser light. There are many strategies to destabilize these dark states [184], including switching of the polarization between two orthogonal directions and application of a small magnetic field to cause Zeeman precession between bright and dark states. Polarization switching at ~ 1 MHz rates can be achieved by passing a laser beam through a Pockels cell. Zeeman precession can be realized by applying a few Gauss magnetic field, leading to precession rates of a few MHz. We have used both of these methods in the work described in this thesis. In some cases, the dark states can even be used as a resource to achieve deep laser cooling [119, 183, 185].

[16] Hyperfine structure of the molecules discussed in this thesis is unresolved in optical transitions, so we do not need to add extra sidebands to address these states. This contrasts with experiments using diatomic fluorides [183].

For a moment, nothing happened. Then, after a second or so, nothing continued to happen.

Douglas Adams, "The Hitchhiker's Guide to the Galaxy"

3

Molecule Production, Slow Beams, and ^{3}He Pot

Decelerating molecular beams to velocities at which they may be trapped is generally recognized as the most difficult step of any laser cooling experiment. (See Fig. 1.4 for typical steps used for trap loading.) YbOH molecules, with their high mass, are especially problematic to slow to trappable velocities. To reduce the amount of laser slowing that would be required, we devoted significant effort toward producing molecular beam sources optimized for low forward velocities. Cell optimization can be a tedious, but crucially important, undertaking. Much previous effort has been

devoted to this task [89, 99, 186]. Beams with near-effusive velocity distributions have been observed, and for particles with mass similar to that of YbOH, this means peak forward velocities below 30 m/s [99].

In this chapter, we summarize our cell optimization efforts. We begin in Sec. 3.1 by discussing our systematic studies of two-stage buffer-gas cell design. We were able to demonstrate production of Yb atomic beams with forward velocity as low as 20 m/s. The desire to produce even slower beams motivated us to cool the second-stage cell below below 1 K in order to remove additional kinetic energy from atoms/molecules as they are extracted into a beam. Section 3.2 describes a pumped ^{3}He fridge that was constructed to accomplish this cooling. Finally, in Sec. 3.3 we discuss the performance of these ^{3}He-cooled CBGBs. We conclude in Sec. 3.4 by pointing out some technical improvements that could be made in future versions of this system.

3.1 Initial buffer-gas cell characterizations

Our attempts to optimize the forward velocities of YbOH molecular beams began from a cell very similar to the one described in Refs. [186, 187]. Excellent background details can be found in those sources as well as the detailed review in Ref. [89]. The general layout of the buffer-gas cells that we tested is shown in Fig. 3.1. The cell consists of two primary components, a "first stage" and a "second stage." A gap between the first and second cells allows venting of some buffer-gas, and we typically tune the gap so that the buffer-gas density in the second cell is about $10\times$ lower than in the first cell. The second cell ends with an aperture, typically about 9 mm in diameter, and often covered by a piece of copper mesh. The mesh provides some fine-tuning over the He buffer-gas density inside the second-stage cell and can also cause some He buffer-gas atoms to experience nearly "backwards" head-on collisions with exiting atoms or molecules; this provides a slowing effect that can reduce the boosting of beams as they exit the cell.

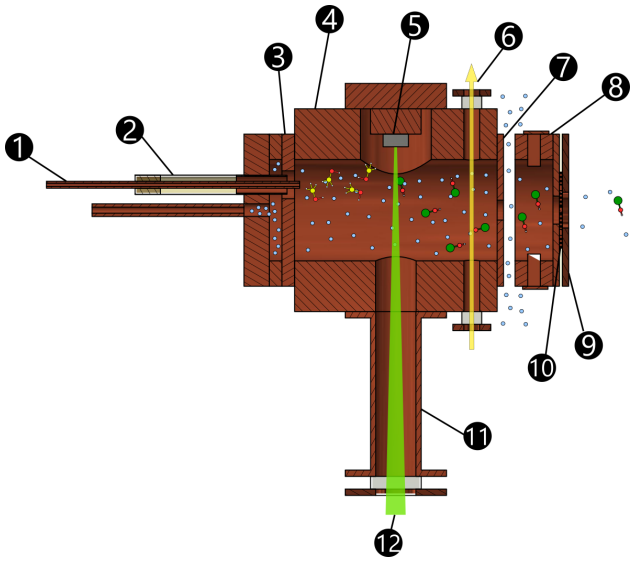

Figure 3.1: Overview of typical buffer-gas cell used for atomic and molecular beam production. Helium gas is represented as small blue dots, and molecules are drawn as structural cartoons. Some relevant parts of the cell assembly are (clockwise from the top left): ❶ Heated fill line, ❷ Thermal standoff, ❸ Diffuser, ❹ First-stage cell main body, ❺ Ablation target, ❻ Absorption probe, ❼ First-stage cell aperture, ❽ Second-stage cell body, ❾ Second-stage cell aperture, ❿ Second-stage cell mesh, ⓫ Ablation snorkel, ⓬ Ablation laser. Figure is adapted from Ref. [187] with permission.

We began our own optimization efforts by studying the velocities of Yb atomic beams, primarily because it is significantly easier to detect Yb atoms than it is to detect YbOH molecules. Velocities are measured outside the cell using laser-induced fluorescence (LIF) from a Doppler-sensitive probe beam. We direct a low power (~ 100 μW, ~ 1 cm diameter) laser beam onto the front of the cell and through the cell apertures. The laser power is kept sufficiently low to prevent any accidental radiation-pressure force slowing. For Yb atoms, we use the intercombination line ($^1S_0 \rightarrow ^3P_1$ at 556 nm) for detection. The fluorescence is imaged from the side of the apparatus on an sCMOS camera through the same window used for laser ablation. The imaging setup allows us to record the LIF as a function of velocity and distance from the cell exit. Integration over slices of the image provides the velocity distribution at each position, and by comparing the mean velocities as a function of position we can study the effect of boosting collisions outside of the cell. We also measure atomic velocities about 40 cm downstream in a room-temperature UHV region. These measurements are conducted using LIF from a probe beam directed at 45° relative to the atomic

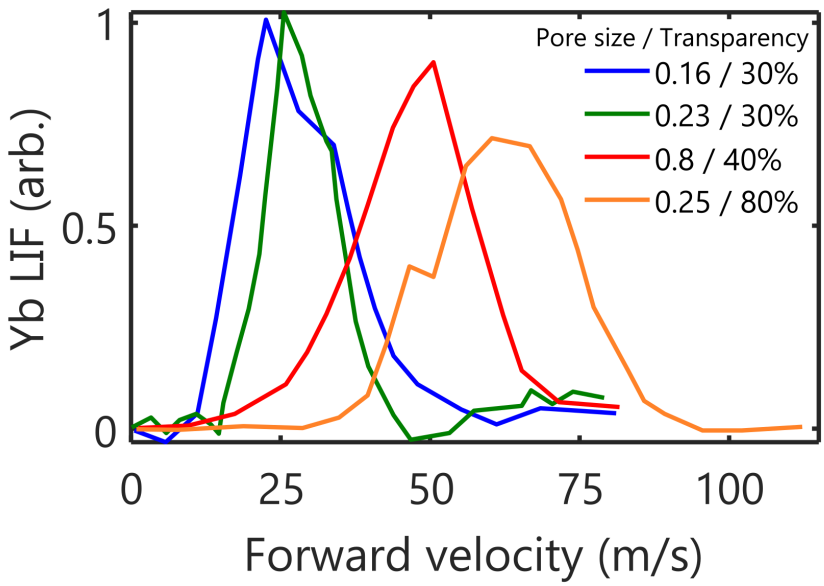

Figure 3.2: Effect of second-stage cell mesh on Yb beam velocities. Lines are color coded according to the mesh's pore size (in mm) and transparency (in %). In all case we used a first-stage cell with 25 mm bore, 7 mm first aperture, 2.6 mm gap first-to-second stage cell gap, 9.5 mm long second-stage cell, and a 9 mm aperture on the second-stage cell. The traces are normalized.

beam. The LIF is captured onto either a PMT or an EMCCD.

3.1.1 Varying mesh parameters

Figure 3.2 shows our measurements of Yb atomic beams for different meshes used on the second-stage cell exit. This data shows that both pore size and mesh transparency can have important effects on the forward velocity distribution measured outside the cell. The slowest beams were observed with meshes that had pore size around 0.2 mm and transparency around 30%. Increasing either the pore size or the transparency led to faster beams. For example, increasing the pore size while holding the transparency nearly constant[1] leads to a speedup of nearly 25 m/s. This is similar to previous reports of the effect of mesh size on K atomic beams, where a difference of about 15 m/s was observed for beams produced with meshes containing 0.2 mm as compared to 0.8 mm pore

[1]Unfortunately we were limited by the availability of certain copper woven meshes and could not hold the transparency exactly constant for these tests.

sizes [186]. At the same time, the transparency of the mesh apparently plays an important role, and increasing the transparency from around 30% to 80% (for a fixed pore size of about 0.25 mm) led to a speedup of around 40 m/s. This could be due to decreased density inside the second-stage cell, leading to insufficient collisions to reduce the boosting associated with extraction from the first-stage cell. For the remainder of the data presented in this chapter, we used the 30% transparency mesh with pore size 0.23 mm.

3.1.2 Varying second-stage cell length

The second-stage cell's length could affect forward velocities produced by the cell in several ways. At constant density, a longer second-stage cell would provide more collisions as particles leave the cell which could do a better job "scrambling" the forward velocity boosting cause by the first stage cell. At the same time, for a longer second-stage cell, one could imaging using a lower density inside the second-stage cell while maintaining the same total number of collisions for particles exiting; the smaller density gradient from inside to outside the second stage cell would then provide less boosting as particles expand into vacuum. These are two quite different physical effects and it is hard to know *a priori* which may be dominant (or if both will be equally important). We studied the effect of second-stage cell length by constructing two cells, one with a 20 mm long second-stage and another with a 40 mm long second stage.

Velocity distributions measured 40 cm downstream (long after any boosting effects have saturated) are shown in Fig. 3.3. The ^{4}He buffer-gas flow has, as expected, a dramatic effect on the total number of atoms extracted from the cell and on their velocity distribution. The shorter second-stage cell [20 mm long; see Fig. 3.3(a)] is optimized in terms of atomic yield at flows around $2-4$ sccm, at which point the peak forward velocity is around 40 m/s. The longer second-stage cell [40 mm long; see Fig. 3.3(b)] produces between 5 and 10 times fewer atoms, although the peak

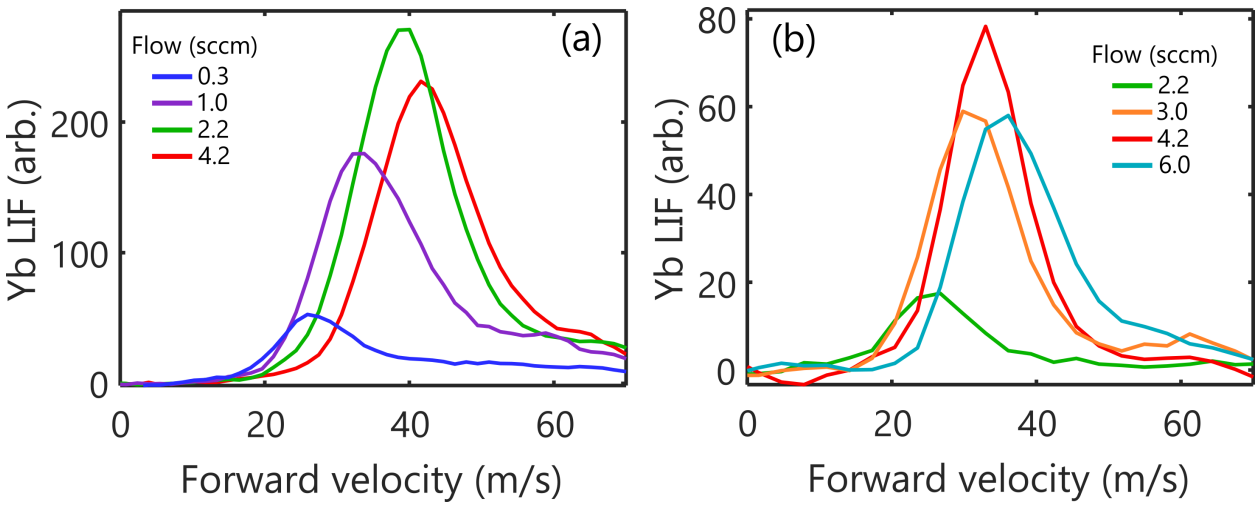

Figure 3.3: Effect of second-stage cell length on Yb atomic beam velocities measured about 40 cm downstream. (a) 20 mm long second-stage cell. (b) 40 mm long second-stage cell.

forward velocities are observed to be around $5-10$ m/s slower than the shorter cell's outputs. The low velocity tails for the two sources are similar in terms of lowest velocities achieved and number of atoms at those velocities. In either case, we can find parameters that allow the source to run with peak forward velocity around 25 m/s.

For the 40 mm long second-stage cell, we have also measured velocity distributions inside the beambox in order to understand the effect of boosting collisions that occur as atoms exit the cell. These data are collected by imaging LIF just in front of the second-stage cell and computing the mean velocity measured in each 2.5 mm long interval. Results are shown in Fig. 3.4 for a variety of buffer-gas flow rates. We can achieve Yb atomic beams with mean forward velocity below 30 m/s after all boosting effects have saturated. For especially low ^{4}He buffer-gas flows, we have even observed beams with mean forward velocity slightly below 20 m/s, albeit at significantly reduced flux.

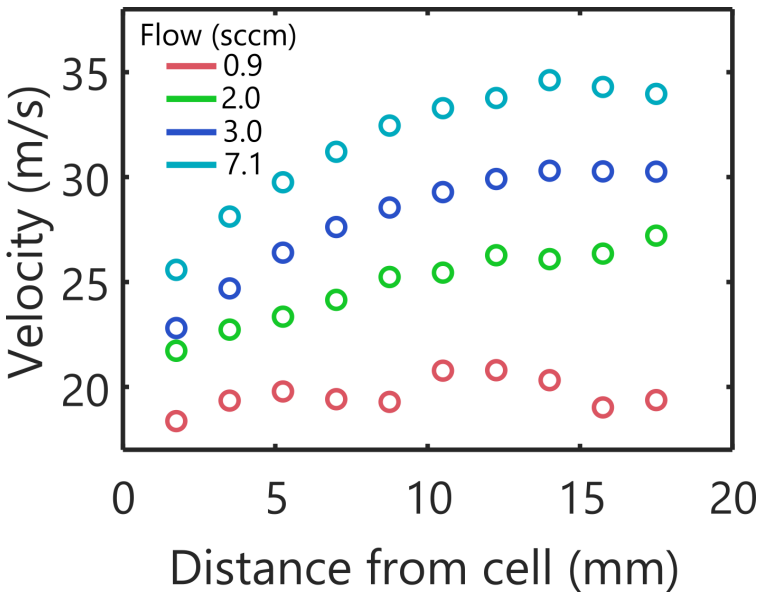

Figure 3.4: Boosting of Yb atomic beams measured just outside a 40 mm long second-stage cell. The mean forward velocity as a function of distance from the second-cell aperture is plotted for various ^{4}He buffer-gas flows.

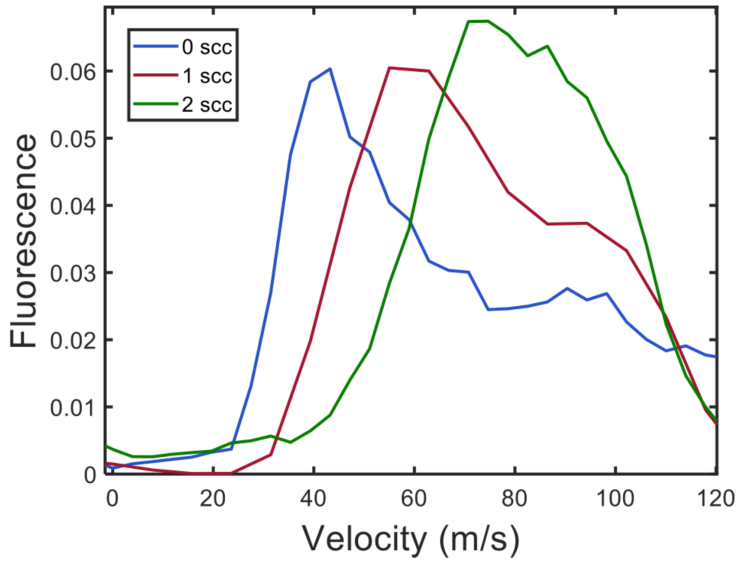

Figure 3.5: Velocity distributions of Yb atomic beams measured 40 cm downstream from the source after different amounts of methanol have been introduced into the cell. Speedup of Yb atomic beams due to methanol "icing" is clearly observed.

3.1.3 Varying first cell volume: combating "icing" speedup

A reliable way to generate high yields of YbOH (and similar molecules) involves ablating atomic Yb (or other metal) in the presence of water or methanol vapor. While a full characterization of this molecule production method will be presented in Sec. 5.1, here we describe how improved cell designs were used to partially mitigate an unfortunate side effect that it caused. The problem is illustrated in Fig. 3.5, where we show the velocity distributions of Yb atomic beams 40 cm downstream as a function of how much methanol had been introduced into the cell.[2] This cell, with relevant parameters listed in the footnote[3], produced beams with peak forward velocities around 30-35 m/s when "clean." Methanol was flowed into the cell at a typical rate of about 0.1 sccm (see Sec. 5.1). Over the first twenty minutes of running, we observed a dramatic change as the entire velocity distribution shifted toward higher velocity. Based on separate characterizations of the YbOH yield, it would not be feasible to run at lower methanol flow and still produce sufficient YbOH for eventual experiments. Similar effects were observed when ablating Ca, as well. Furthermore, the same effect was observed when water (instead of methanol) flowed into the cell.

We developed a simple physical model for this phenomenon based on the idea that the methanol flowed into the cell freezes on the cell walls and impedes thermalization between the ^{4}He buffer gas and the cell. Firing the ablation laser causes a rapid heating of the buffer gas inside the cell and the ice-coated walls are unable to extract this heat efficiently. Note that in this scenario, the problem appears to be localized to inside the first-stage cell. A very simple mechanism to combat this problem is to expand the cell's bore so that more ^{4}He is present inside the cell, essentially a larger energy reservoir. We machined a new cell with 1.7" diameter bore, roughly tripling the interior volume; keeping the cell aperture fixed, the buffer-gas density will remain the same so the

[2] Methanol was flowed into the cell in order to produce YbOH molecules, but note that we are tracking Yb atom velocities in this data.

[3] First-stage cell: 1" inner bore, 2" length, 7 mm aperture. Second-stage cell: 2.5 mm gap, 10 mm long, 9 mm aperture, 0.23 mm pore-size mesh at 30% transparency. ^{4}He buffer-gas flow set to 6 sccm.

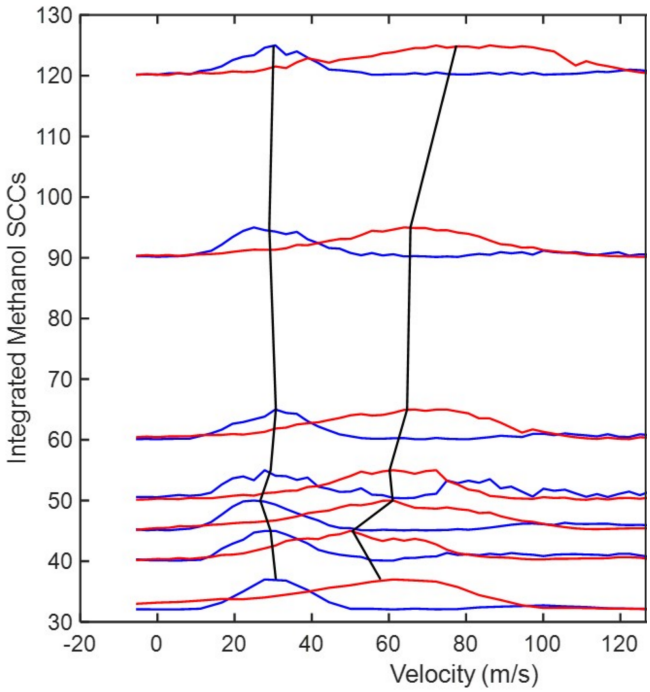

Figure 3.6: Velocity distributions between cells and after second cell vs. methanol flow. Blue (red) traces show the velocity measured after the 2nd cell (1st cell) aperture. Curves are offset by the amount of methanol that has been allowed to flow into the cell. Black lines indicate the peak velocity of each distribution.

number of ^{4}He atoms in the cell should also triple [89].

Figure 3.6 shows velocity distributions measured as methanol was introduced into the "large bore" cell. The detection camera was positioned so that we could simultaneously monitor velocities between the first- and second-stage cells as well as downstream from the second-stage cell. These data indicate that the larger cell bore effectively eliminates the speedup due to methanol flow, even over a range of methanol flows approximately $60\times$ larger than was shown in Fig. 3.5. While the velocity between the cells may show a small amount based on the distributions coming out of the first-stage cell, the second-stage cell appears to be capable of removing that extra velocity increase. It is important to note that the same method has *not* fixed the speedup due to H_2O ice; evidently the water ice forms a more pernicious insulating layer on the inside of the copper cells. We are investigating ways to combat the speedup due to water ice, but have not solve the problem at this

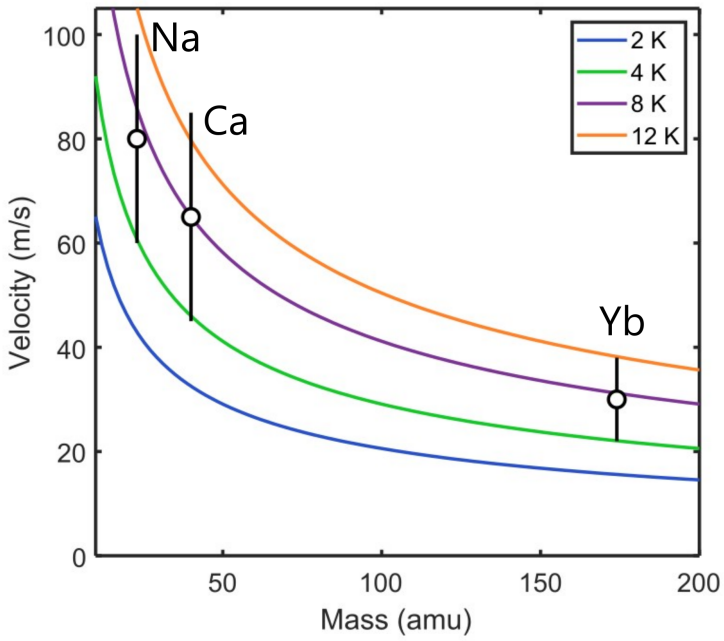

Figure 3.7: Comparison between forward velocities of Na, Ca, and Yb atomic beams produced under nominally identical conditions. The vertical bars represent the full-width-at-half-maximum spread of the velocity distributions. Colored lines indicate the thermal velocity expected at some relevant temperatures.

point in time.

3.1.4 Comparison between species of varying mass

The results above are described for Yb atomic beams, but we have also taken data for other atomic species to check that our cell optimizations are more broadly applicable. In addition to Yb, we have studied the forward velocities of beams of Na and Ca atoms. We can think of these measurements as representing a systematic variation of the mass of particles produced by the CBGB. In Fig. 3.7 we plot the velocities measured downstream for these particles using the 40 mm long second-stage cell described above and recorded at the same flow (4 sccm) and ablation energy (18 mJ). In all cases, the first and second-stage cells were both held at 2 K. We see that the peak forward velocity of each species approximately follows a curve that results from considering the expected thermal velocity at around 8 K. The vertical bars in Fig. 3.7 represent the full-width-at-half-maximum of the atomic

beam brightness, indicating that for each species there was a substantial tail down to velocities equivalent to the thermal velocity expected for 4 K. The fact that the measured distributions do not follow exactly the thermal prediction for a 2 K source is due to boosting effects as the beam is formed and indicates that our sources do not behave effusively.

3.2 Pumped He-3 refrigerator

The cells described above demonstrate that we can produce beams of Yb with velocities around 25 m/s, but it was very difficult to produce sources with lower peak forward velocity. Perhaps the most obvious way to reduce the kinetic energy of particles produced in a CBGB is simply to lower the temperature of the buffer-gas itself. Not only should this reduce the mean thermal velocity of the species of interest, but it should also reduce the momentum imparted by any boosting collisions with the buffer-gas atoms near the cell aperture.

We designed a ^{3}He fridge with the goal of cooling the second-stage cell to around 0.7 K. By cooling just the second-stage cell, we avoid the large heat loads incident on the first-stage cell due to the ablation laser and the heated fill line. The remaining heat loads on the second-stage cell come from blackbody radiation, He buffer-gas flow, and conduction through mechanical supports. The front of the second-stage cell has direct line-of-sight to the room temperature vacuum chamber; blackbody radiation leaking through the radiation shields contributes about 1 mW of heat load. This is expected to be the dominant heat load on the second-stage cell. Both conduction along the Vespel standoffs between the first- and second-stage cells and the cooling power required to bring $\sim$5 sccm (a typical value) of buffer-gas from $\sim$2 K to $\sim$0.7 K are expected to contribute $<$0.1 mW.

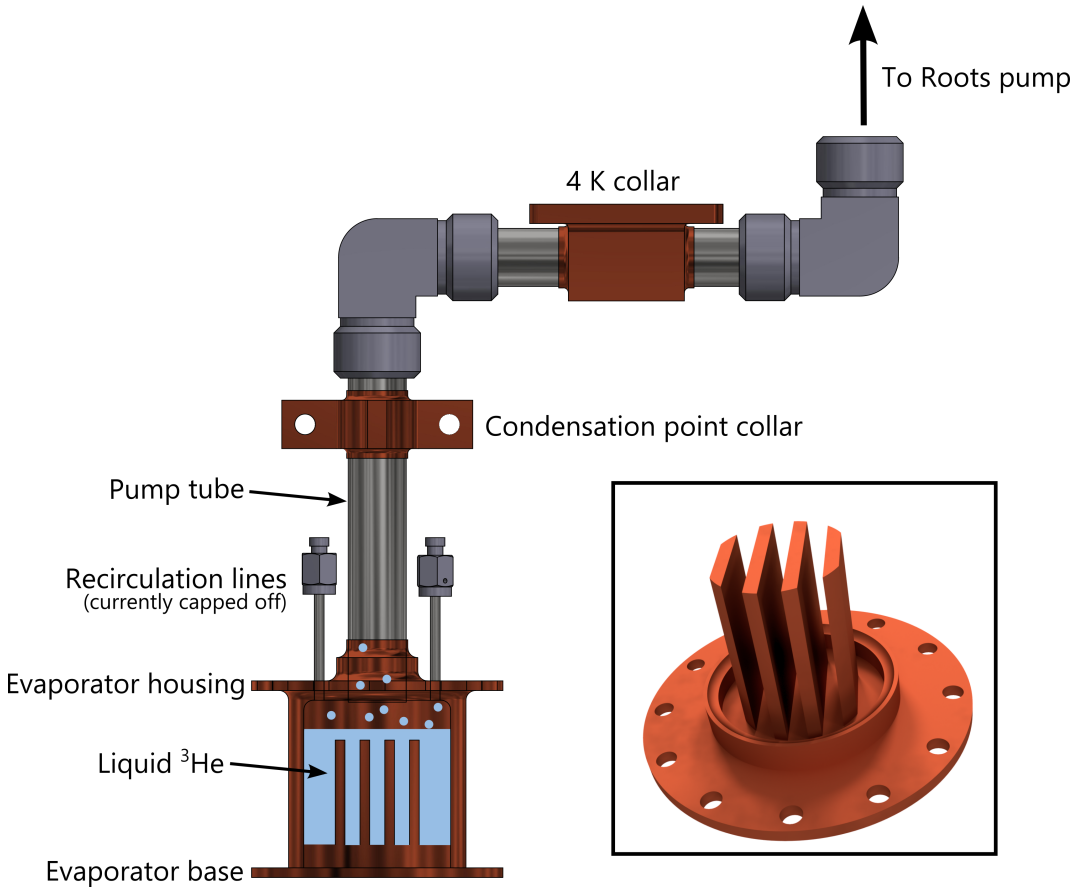

Figure 3.8: Schematic diagram of ^{3}He fridge. Liquid in the evaporator is pumped through the pump tube by a multi-stage Roots pump. Inset: rendering of the evaporator base, showing the fin structure for increased thermal copper-liquid contact.

3.2.1 Design

A schematic of our home-built ^{3}He fridge is presented in Fig. 3.8. In this "single-shot" design, ^{3}He is introduced into a reservoir and pumped out of it using the same set of tubes; there are distinct loading and pumping phases. While liquid, the ^{3}He is held in an evaporator constructed of high thermal conductivity copper. The evaporator base and housing are each machined from Cu10100 and brazed together to form a reservoir. Photographs of these parts prior to brazing are shown in Fig. 3.9. Fins are machined into the evaporator base in order to improve the liquid-to-metal contact (see inset of Fig. 3.8). Thermal contact to the pot can be made using a set of 1/4"-20 holes around the top and bottom of the evaporator assembly. The evaporator is suspended from a pump tube

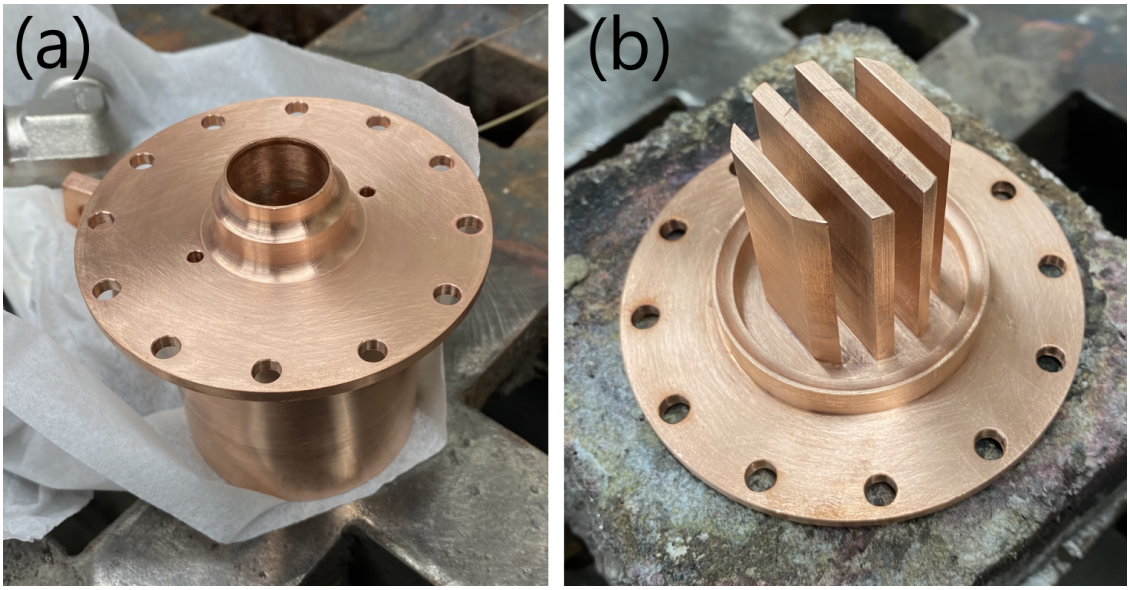

Figure 3.9: Photographs of evaporator parts before brazing. (a) Evaporator housing. (b) Evaporator base.

made from thin-walled SS316 tube in order to minimize conductive heat loads.

The pumping line (SS316, 0.75" OD, 0.035" wall thickness) is brazed to the top of the evaporator housing. The housing is machined with fillets to reduce thermal stresses at the braze joint. The pumping lines include several right angles to prevent line-of-sight between room temperature and the liquid interface. In addition, the tube interior was blackened[4], although this appeared to have only order-of-unity effects on the reflectivity, especially at glancing angles.[5] The pump tube is thermally anchored at several points. The 2 K thermal anchor is attached to the "1 K" stage of our pulse tube[6] and ensures that the ^{3}He liquefies just before it reaches the evaporator housing. The 4 K thermal anchor allows pre-cooling of the ^{3}He gas in order to reduce the heat load on all colder stages. We included a set of 1/16" SS316 tubes that could be used to convert this design to a continuously operating, recirculating refrigerator. For all of the work described in this thesis, those lines were capped off and the fridge was run in single-shot mode.

[4]We used InstaBlak SS-370 GEL.

[5]It's really the reflectivity around ~ 10 μm wavelengths that matters for 300 K blackbody radiation; we did not make any measurements of the reflectivity at this wavelength.

[6]We use a PT415 with integrated ^{4}He pot to reach about 2 K. The system is essentially identical to that described in Ref. [187].

The dimensions of the fridge assembly are chosen to achieve a reasonable hold time based on the estimated cooling power required. We choose pump tube dimensions to ensure that conduction between the 2 K thermal anchor and the evaporator housing is smaller than the blackbody heat load on the second-stage cell. At the same time, we want a pump tube with sufficiently large diameter to allow high conductance pumping. A good compromise is found with 0.75" OD, 0.035" wall thickness tubing. For a distance of 3" between the top of the evaporator and the 2 K thermal anchor, the conductive heat load through this pumping tube is estimated to be 0.5 mW, about half of the blackbody heat load on the second-stage cell. The total design heat load of 1.5 mW corresponds to approximately 9 cc/hr of liquid ^{3}He boil-off. Thus, an evaporator volume of around 75 cc should enable around 8 hours of run time. We designed the evaporator housing to have an interior volume around 95 cc, with 75 cc of available volume once the fins are taken into account.

In fact, the expected run time will be reduced because a substantial fraction of the ^{3}He must be evaporated in order to cool the remaining liquid to 0.7 K. Figure 3.10 shows the fraction of liquid ^{3}He remaining after cooling to some base temperature.[7] If we cool the liquid by pumping on it at an initial temperature of 3.2 K, then nearly half of the liquid will boil off in order to cool the remainder to 0.7 K. If the initial temperature of the liquid is lower before pumping begins, less liquid is lost during the cooldown phase. For example, if the liquid is cooled all the way to the 2 K thermal anchor's temperature, about 85% of the initial liquid will remain after cooling to 0.7 K. Ultimately, the ^{3}He consumption required to cool the remaining liquid reduces the maximum expected hold time to $4-7$ hours, strongly dependent on the initial temperature before cooldown.

In order to reach the target base temperature of ~ 0.5 K, the pressure above the liquid ^{3}He must be reduced to around 1 torr. The liquid ^{3}He is pumped by a multistage Roots pump (Adixen ACP40) with pumping speed around 8 L/s at pressures ~ 0.1 torr. Given the impedance of our

[7] Values for the ^{3}He specific heat and latent heat of vaporization underlying these calculations were taken from Refs. [188] and [189], respectively.

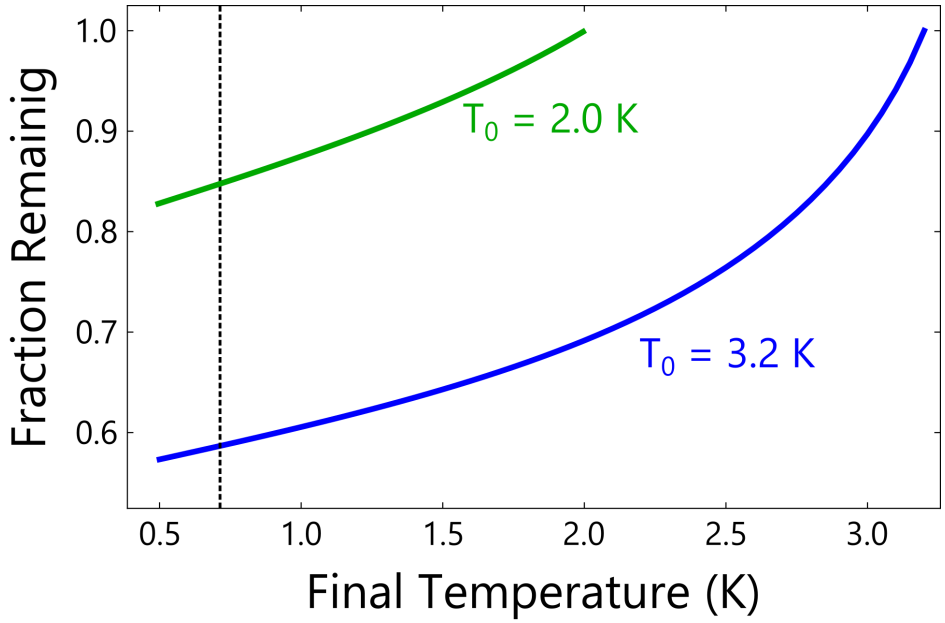

Figure 3.10: The fraction of liquid ^{3}He remaining after cooling down to a given base temperature by evaporation. The blue curve assumes an initial temperature of 3.2 K, near the ^{3}He critical point. The green curve assumes an initial temperature matching the 2 K thermal anchor. The dashed vertical line indicates our target base temperature, 0.7 K.

pumping lines, we expect a pressure differential of a few tenths of a torr between the evaporator and the pump inlet, indicating that our desired base temperature is achievable. Due to the high price of ^{3}He, the gas-handling system (see App. C) is designed to ensure no gas is lost.

3.2.2 Performance

After installing the fridge into the beam box (including all pumping lines), but before introducing ^{3}He into the pot, we carefully leak tested it at cryogenic temperatures using ^{4}He. These tests were meant to ensure that no leaks opened up upon cooling the apparatus, e.g. due to uncompensated thermal stresses near the braze joints. These tests essentially consisted of cooling the beambox down to base temperature, filling the pot with ^{4}He, and measuring how much (if any) of the loaded ^{4}He ended up being captured in the charcoal sorbs after some wait time. We repeated this process two more times under slightly different conditions: (1) a baseline test involving a full cooldown-warmup cycle, but without introducing any ^{4}He into the pot, and (2) a calibration test in which

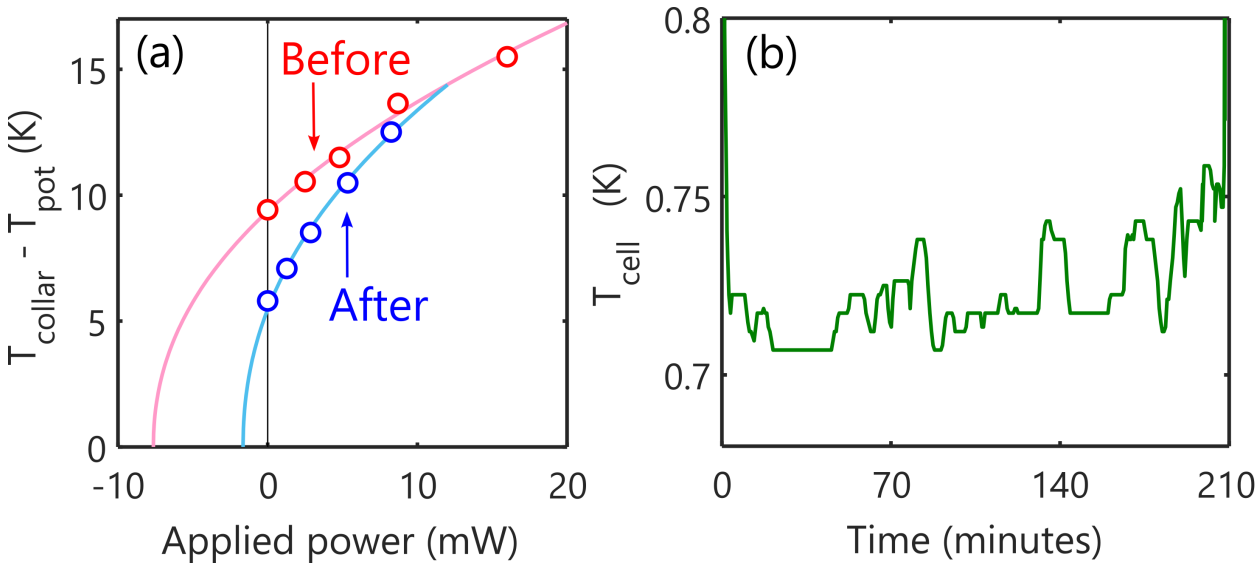

Figure 3.11: (a) Determination of heat loads on ^{3}He pot before and after efforts were taken to minimize blackbody radiation inside the 4 K shield. Points are recorded temperature difference between condensation point collar and evaporator housing.Lines are fit to account for the temperature-dependent thermal conductivity of SS316. Before optimization, the horizontal intercept of the fitted line indicated about 8 mW of ambient heat load. After improvements this was reduced to 1.6 mW. (b) Temperature of 2nd stage cell as a function of time during operation of the ^{3}He pot. Approximately 3.5 hours of operation at around 0.7 K is possible. Temperature excursions are due to additional heat loads imposed while running molecular beams.

introduced ~ 0.75 cc of ^{4}He into the sorbs through the buffer-gas fill line, leaving the pot empty the entire time. During each warmup, we monitored the amount of ^{4}He released from the charcoal sorbs by pumping on the chamber with a standard leak-checker. These tests were consistent with no observable leak from the ^{3}He pot.

Following these leak tests, we connected the ^{3}He gas-handling system (Fig. C.1). During the initial cooldown, several problems were identified. First, the loading rate was very slow, requiring over 5 hours to load an estimated 60 cc of liquid ^{3}He into the pot. Furthermore, after we began pumping on the pot, a base temperature around 0.82 K was only able to be maintained for less than 30 minutes. The ^{3}He boil-off rate implied a heat load of ~ 8.5 mW, which was consistent with measurements performed by measuring the temperature rise caused by applying heat loads through a resistive heater [see Fig. 3.11(a)]. The short hold time was found to be due to an unexpectedly large blackbody heat loads inside the 4 K radiation shields.

We identified several sources of unwanted blackbody radiation, including unused screw holes in the shields, insufficient baffling around where the heated fill line enters the chamber, and radiation from the heated fill line used to introduce water/methanol into the cell. After improving the radiation shielding and anchoring the heated fill line to 90 K, the heat loads on the cell and ^{3}He pot were reduced to around 1.5 mW, just above the design goal.[8] Measured cooling curves before and after these improvements are shown in Fig. 3.11(a). Because about 1 mW of heat load appears unavoidable due to blackbody through the 4 K/40 K beamline apertures, this was deemed good enough. After reducing the blackbody heat loads, we were able to achieve a base temperature around 0.7 K with roughly 3.5 hour hold time [Fig. 3.11(b)]. We also outfitted the gas-handling system with over-pressure rings to allow loading at elevated pressure, up to 990 torr. This reduced the loading time to about $3-4$ hours.

3.3 ^{3}He-pot-cooled buffer-gas beams

With the ^{3}He pot operational, we measured molecular beam velocities both inside the cryogenic source (between the cell exit and the 4 K shield) and in a room-temperature beamline extension that was added to the vacuum chamber. To ensure that sufficient buffer-gas density was present even in the 0.7 K 2nd stage cell, we used ^{3}He as a buffer gas. We focused primarily on atomic beams, simply due to the much higher signal-to-noise ratios attainable that led to faster data collection rates. Data were collected with the 2nd cell anchored at both 3.2 K (while the ^{3}He pot was loading) and 0.7 K (while the ^{3}He pot was being pumped). Atomic beam velocities were measured by shining a low power laser beam (typically about 50 μW) through the cell apertures, counter-propagating against the atomic beam. The power was kept low to avoid power broadening was

[8] Future improvements must add radiation shielding around any heated fill lines used for molecule production to prevent undue heating of the second-stage cell and fridge.

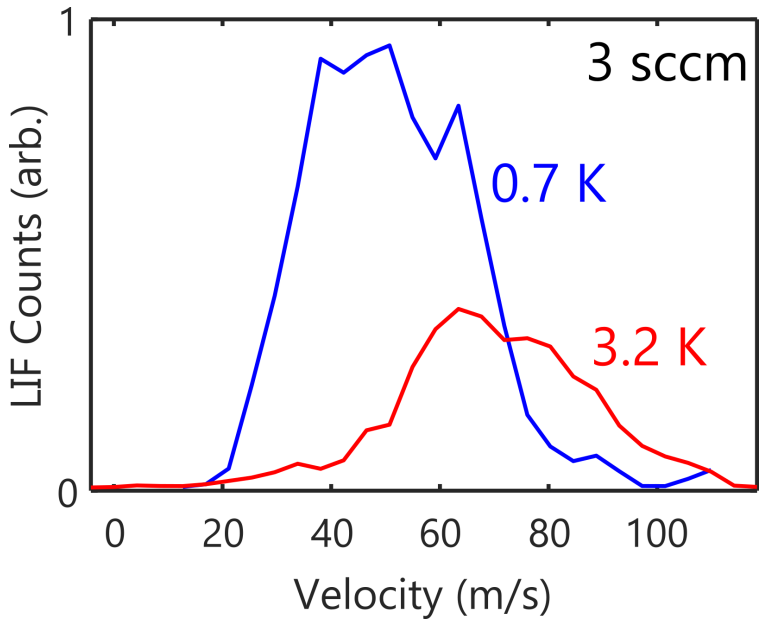

Figure 3.12: Comparison of Ca atomic beam velocity distributions with ^{3}He pot held at 3.2 K (red) and 0.7 K (blue). Buffer-gas flow in both cases is 3 sccm and ablation energy is 15 mJ.

to eliminate any "accidental" radiative pressure force that could bias our measurements toward lower velocity. An sCMOS camera imaged the fluorescence produced by the atomic beam through the same window that is used for the ablation laser beam and in-cell absorption monitor.

Ca atoms

Our first tests were conducted with Ca atomic beams using a 2nd stage cell that was 40 mm long with 25 mm inner bore, spaced by 2.3 mm from the 1st stage cell, and with a 40% transparency mesh covering the 9 mm diameter exit aperture. Figure 3.12 shows a comparison of Ca velocity distributions measured inside the 4 K shield, integrated up to 20 mm after the 2nd cell exit aperture. Upon cooling the ^{3}He pot to 0.7 K, the velocity distributions shifts toward lower velocities (by about 20 m/s at the peak) and the detected atom flux is increased by a factor of about 3. The increase in signal at lower 2nd stage cell temperature was unexpected, but highly reproducible; in fact, signal increases of up to an order of magnitude were observed during continued operation of the source. Aside from some vague hypotheses related to beam "collimation" due to reduced

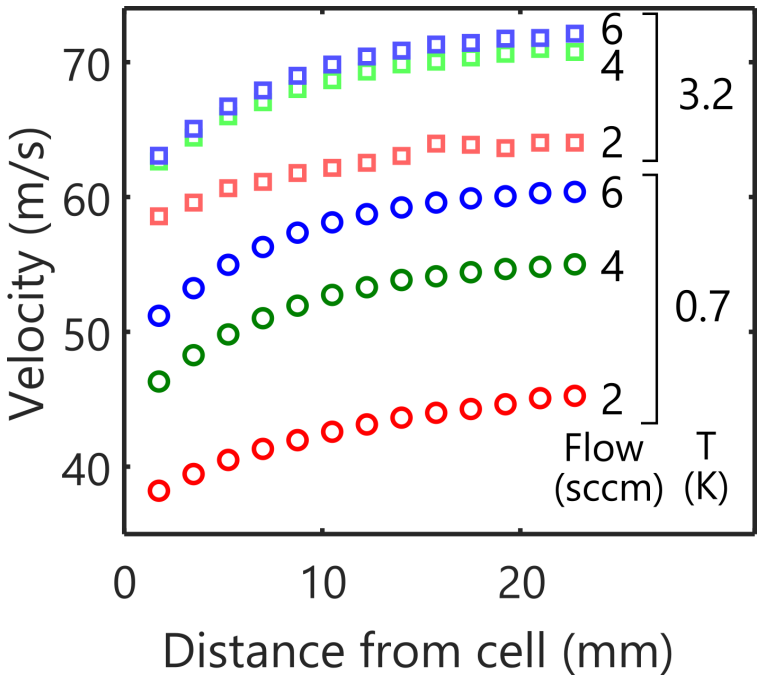

Figure 3.13: Comparison of mean forward velocities of Ca atomic beams as a function of distance from 2nd cell aperture and ^{3}He buffer-gas flow. Circles (squares) show data collected with 2nd cell at 0.7 K (3.2 K) for three different buffer-gas flow rates: 2 sccm (red), 4 sccm (green), and 6 sccm (blue).

transverse velocities, we do not currently have a good physical model for what causes the signal increase. Under the conditions shown in Fig. 3.12, the cold 2nd stage cell produces a beam with peak forward velocity around 45 m/s, and a significant low-velocity tail down to about $30-35$ m/s.

We varied the ^{3}He buffer gas flow to study how the forward velocity and boosting depended on this parameter. Repeating this flow scan at both 0.7 K and 3.2 K provides another measure of the velocity reduction caused by cooling the 2nd stage cell. The results are displayed in Fig. 3.13. Boosting effects appear to saturate at distances around 15 mm from the cell exit, consistent with expectations for the size of the zone of freezing. Comparing the observed amount of boosting (typically between 5 and 10 m/s) with that expected for elastic ^{40}Ca$-^3$He collisions at 0.7 K or 3.2 K, it appears that Ca atoms experience an average of between 1 and 2 collisions after exiting the cell. After the boosting, the beams produced with a 2nd cell at 0.7 K have typical forward velocities about 15-20 m/s lower than those produced at 3.2 K. Consider the data collected at 4 sccm. The

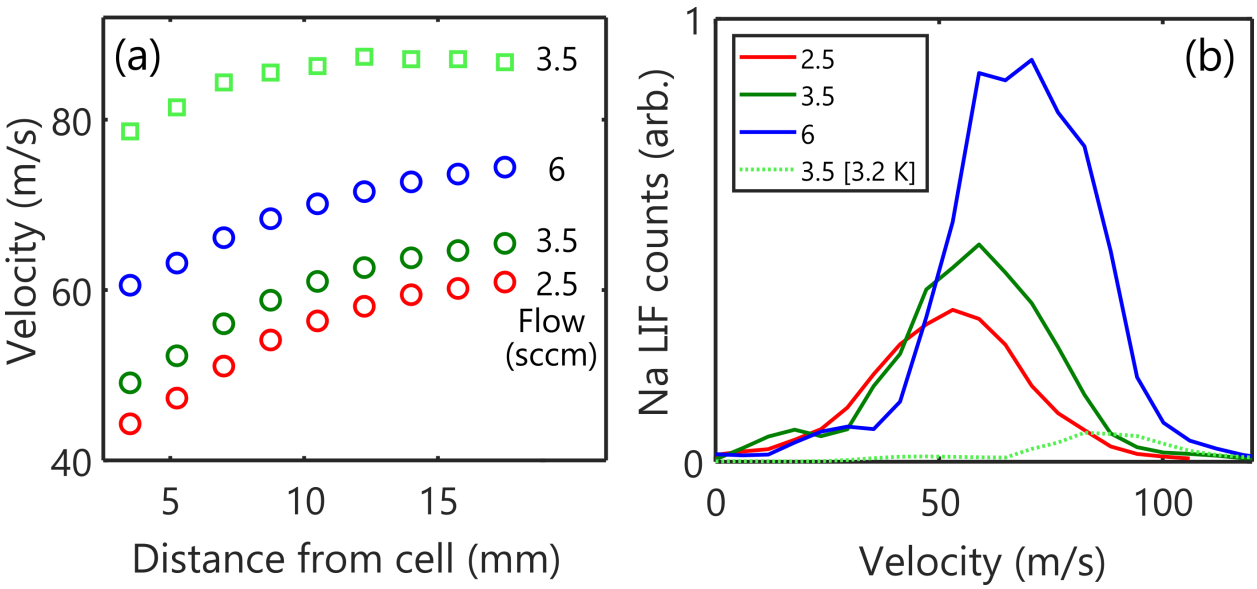

Figure 3.14: (a) Comparison of mean forward velocities of Na atomic beams as a function of distance from 2nd cell aperture and ^{3}He buffer-gas flow. Circles (squares) show data collected with 2nd cell at 0.7 K (3.2 K) with the buffer-gas flow rates as labeled. (b) Velocity distributions averaged over a distance up to 20 mm beyond the 2nd cell exit taken for the same set of parameters.

mean boosted velocities (55 m/s and 70 m/s for data at 0.7 K and 3.2 K, respectively) correspond to kinetic energies that differ by a factor of 1.7. A very naive estimate would have expected the kinetic energy to be reduced by a factor of 2 based on the extra cooling provided by the 2nd stage cell at 0.7 K as compared to 3.2 K, so the velocity reduction appears reasonable.

Na atoms

Using the same cell geometry, we collected similar datasets using ^{23}Na atoms by monitoring their velocities inside the 4 K shield. Measured velocity distributions and boosting curves are shown in Fig. 3.14. In this case, when the ^{3}He pot is at 3 K we observed peak forward velocities around 90 m/s, and these are reduced to about 55 m/s once the pot is cooled down to 0.7 K [see Fig. 3.14(a)]. The magnitude of velocity boosting is typically around 15-20 m/s. This is larger than was observed for Ca, which is expected based on the mass difference. Furthermore, it appears that the boosting occurs out to larger distances, beyond the 20 mm field of view that we imaged. Extrapolating to

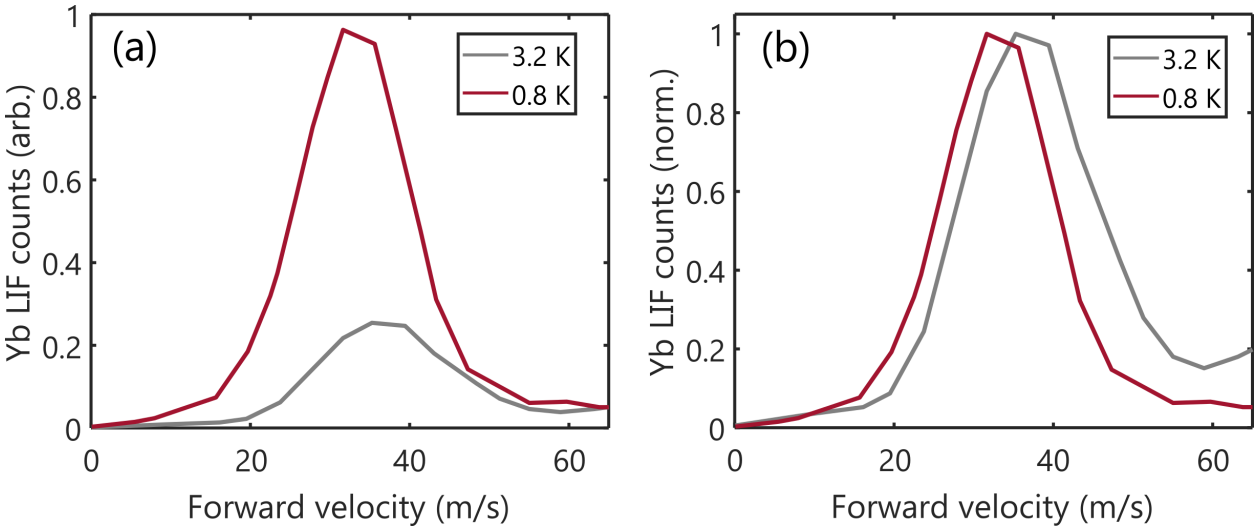

Figure 3.15: Yb atomic beam velocities with ^{3}He pot at 3.2 K and 0.7 K, detected 40 cm downstream from the cell. (a) Raw counts. (b) Normalized by peak height.

the asymptotically boosted velocity, cooling from 3.2 K to 0.7 K reduces the forward velocity of Na atomic beams by about $20 - 25$ m/s, i.e. by a factor of 1.8 reduction in equivalent kinetic energy. Again, this is close to the factor expected due to reducing the cell temperature by a factor of just over 4. After cooling down the pot, we again observe a large increase in atomic flux detected outside the cell, by a factor of about 5 in this case [see Fig. 3.14(b)].

Yb atoms

Finally, we studied the effect of ^{3}He pot-cooled on Yb beams. The results in this case were a bit surprising: while we did observe large increases in molecule flux upon cooling down the ^{3}He pot, the associated velocity reduction was significantly less than expected. Data collected at 5 sccm ^{3}He buffer-gas flow are shown in Fig. 3.15. This data was collected with a 20 mm long second-stage cell installed. The peak velocity is reduced from 35 m/s at 3.2 K to around 30 m/s at 0.8 K. Based on the scaling from Ca and Na data described above, we would have expected the temperature change to contribute a velocity reduction of $\Delta v \approx 18$ m/s, much larger than observed. In terms of absolute numbers, this data is consistent with an increase in flux of about a factor of $5\times$ for the

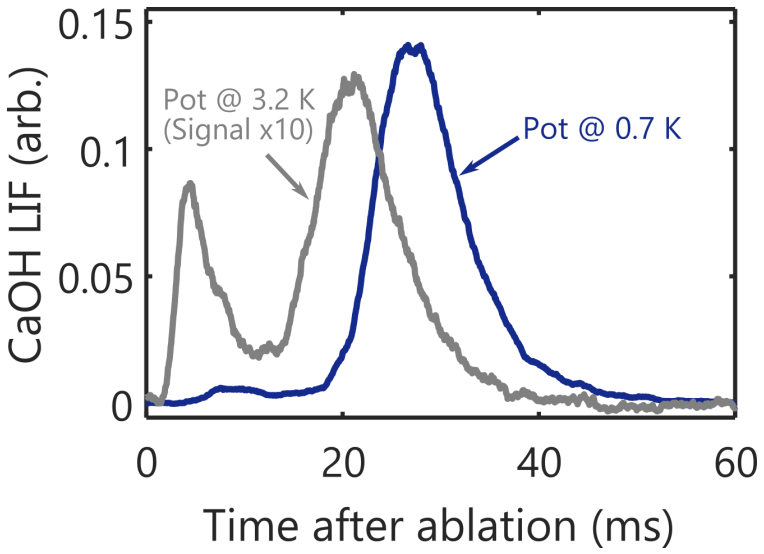

Figure 3.16: CaOH molecular beam time-of-arrival with ^{3}He pot at 3.2 K and 0.7 K. The signal recorded with the pot at 3.2 K has been scaled up by $10\times$ for ease of comparison.

30 m/s velocity class and nearly $10\times$ for the velocity range below 20 m/s, so the ^{3}He pot appears to provide some useful increase in slow molecules. However, we do not have a model for how to improve the velocity reduction achievable, and this is a matter of ongoing work.

CaOH molecules

So far, our studies of the ^{3}He-pot-cooled second-stage cells have focused on atomic species. We did not expect any significantly different behavior for molecular species, and we used molecular beams of CaOH to test this expectation. Figure 3.16 shows the behavior of CaOH molecular beams produced with the ^{3}He pot at both 3.2 K and at 0.7 K. These data were collected on a PMT 110 cm downstream from the cell during preparations for our Zeeman-Sisyphus deceleration experiments (see Ch. 7). Looking at the time-of-arrival distribution of the molecular beams shown, it is clear that the flux is increased by over an order of magnitude. For molecules, as compared to atoms, some of this signal increase can come from the fact that the thermal population of the detected $N'' = 1$ state is about $1.5\times$ higher at 0.7 K as compared to 3.2 K. In addition, the mean forward velocity is reduced when the pot is cooled down. The time of peak fluorescence corresponds to

about 60 m/s for the 3.2 K condition and 45 m/s for the 0.7 K condition. Velocity distributions collected under these conditions can be found in Ch. 7 and are consistent with the observed time-of-arrival distributions presented here. The key feature of these data is that they agree with the general trends observed for the atomic beams that were studied in detail above.

3.4 Potential improvements

In summary, we have presented studies aimed at optimizing the forward velocities of atomic and molecular beams produced by a cryogenic buffer-gas source. First, we studied the effect of cell geometry in order to produce beams of Yb atoms with forward velocities below 25 m/s. Second, we constructed a pumped ^{3}He pot that can cool the 2nd stage cell of our CBGB source to 0.7 K. Using this cold 2nd stage, we have demonstrated a reduction in forward velocity for beams of Ca, Na, and CaOH. Oddly, we did not observe a significant velocity reduction in the case of Yb beams, and the causes of this are not well understood at present. The ^{3}He-pot-cooled cells can be applied widely to CBGBs that must operate at the lowest possible output velocities. Such a source represents an excellent starting point for molecular laser cooling experiments with complex polyatomic molecules, first because the lower temperatures provide phase-space compression beyond that achieved with previous CBGBs and second because the reduced forward velocity eases the task of molecular beam slowing (see Ch. 7).

While our ^{3}He fridge was relatively simple to construct, there are several areas that could be improved in future iterations. Most importantly, the current duty cycle (equal time required to load the pot as it can be held at base temperature) is clearly not ideal. Reducing the loading time could be achieved in several ways, such as decreasing the temperature at the condensation point collar or increasing the pressure at the top of the pump tube during loading. The former option is difficult due to the base temperature of the "1 K" stage of our main pulse tube being limited to

about 2 K. Currently, our system can load at absolute pressures of about 990 torr (as measured at the room temperature side of the pump tube). If KF joints along the loading pathway are replaced with joints rated for higher pressure, this could be increased. (See App. C for a schematic drawing of the gas handling system.) Increasing the hold time could be achieved by further reducing heat loads, e.g. improved thermal shielding, gold-plating of all sub-Kelvin surfaces, and using a thinner pump tube. A dedicated 40 K radiation shield around the heated fill line is also necessary in order to allow simultaneous operation of the ^{3}He fridge with flowing precursor gases for molecule production. Converting the system to a fully recirculating design is perhaps the best, though most difficult, option. We designed our ^{3}He fridge to be compatible with recirculation by including thin SS316 tubes on the evaporator housing. A similar system has been described in the literature [190] and such a design could be adapted for our purposes.

'Explain all that,' said the Mock Turtle.
'No, no! the adventures first,' said the Gryphon in an impatient tone: 'explanations take such a dreadful time.'

Lewis Carroll, "Alice's Adventures in Wonderland"

4

High-Sensitivity Branching Ratio Measurements

Whether for laser cooling, state manipulation, or high-fidelity detection, optical cycling depends on the availability of spectroscopic data. Without accurate information about vibrational branching ratios, one cannot know which lasers must be applied (and in what order) to achieve some desired degree of photon cycling. Because diatomic molecules have only a single vibrational degree of freedom, it is generally obvious which laser must be added to increase the number of photon scatters. To wit, if repumpers up to the v^{th} level are present, one must simply add the $(v+1)^{\text{th}}$

repumper.[1] Polyatomic molecules, on the other hand, contain at least three vibrational manifolds. The relative intensities *within* each manifold only sometimes follow simple patterns (e.g., due to possible vibrational selection rules), and the relative intensities *between* manifolds often do not follow intuitive patterns (e.g., due to perturbations and higher-order terms in the Hamiltonian). For polyatomic molecules, therefore, measurements of vibrational branching ratios are extremely important to guide progress toward optical cycling and laser cooling.

In this chapter, we describe an apparatus that was constructed to measure vibrational branching ratios with decay strengths as small as 1 part in 10^5. In Sec. 4.1, we describe the apparatus used and its calibration. The primary innovation that enabled this level of sensitivity is the use of optical cycling in the detection region, which allowed us boost the fluorescence signal by "probing" each molecule many times. We have used this system to study YbOH (Sec. 4.2), CaOH (Sec. 4.3), and $CaOCH_3$ (Sec. 4.5) molecules. To the best of our knowledge, our data provide the most sensitive determination of VBRs reported for each of these species. For YbOH and CaOH, this system allowed us to identify all vibrational loss channels from a given excited state that must be repumped in order to scatter, on average, nearly 100,000 photons per molecule.[2] For $CaOCH_3$, the sensitivity was somewhat lower, enabling determination of losses that must be repumped to achieve nearly 10,000 photon scatters per molecule. Additionally, the $CaOCH_3$ measurements enabled us to extract quantitative information about vibronic coupling in the electronically excited states. Finally, in Sec. 4.6 we discuss some possible limitations of the DLIF measurements.

[1] This statement is a *slight* simplification. For example, the pattern could break down if there are near-degeneracies among the electronically excited manifolds.

[2] A few caveats apply to this statement: because the spectrometer measures relative fluorescence intensities, it is insensitive to both nonradiative losses and radiative losses that fall outside the system's detection bandwidth. We will discuss these possibilities in Sec. 4.6.

4.1 Dispersed fluorescence spectroscopy

In a typical molecular laser cooling experiment, the vast majority of photons are emitted following excitation to the lowest vibrational level of a low-lying electronically excited state, e.g., $\tilde{A}\,^2\Pi_{1/2}(v = 0)$. The branching ratios from this "main" excited state play the primary role in determining which repumping lasers are required, and in what order they must be added, to maximize the achievable photon budget. Dispersed laser-induced-fluorescence (DLIF) spectroscopy is a standard technique to measure the emission wavelengths and intensities associated with spontaneous emission from electronically excited states. A sample of molecules is excited to some electronically excited state and the molecules spontaneously emit photons as they decay back to the ground electronic state. On each cycle, the wavelength of an emitted photon corresponds to the energy difference between initial excited state and the particular vibrational ground state the decay populates. The probability to emit one wavelength as compared to any other is set by the branching ratios for decay to each vibrational ground state. This fluorescence is collected, dispersed by a diffraction grating, and imaged onto an EMCCD; this detection process builds up an image comprising a set of peaks, with the height of each peak indicating the relative probability that photons of that wavelength are emitted. After calibration, the peak heights can be analyzed to provide the vibrational branching ratios.

While dispersed fluorescence measurements are a classic tool in spectroscopy, the use of DLIF to determine VBRs for laser-coolable molecules was pioneered by the group of Tim Steimle [191–193]. In order for DLIF spectroscopy to provide useful information for molecular laser cooling, care must be taken to control several factors in the experimental setup. Continuous-wave (as opposed to pulsed) excitation is desirable to make sure that a single rovibronic excited state is populated and to avoid any possible signal contamination due to the broad wings of typical pulsed laser intensity spectra. Additionally, is desirable to use a rotationally cold sample of molecules, both to boost the

signal and to ensure that high-lying states which could be prone to perturbations are not probed. It is also important to ensure that the molecular beam does not suffer collision-induced population transfer which could lead to fluorescence artifacts not attributable to the electronic state targeted by laser excitation in the detection region.

Previous molecular beam DLIF studies of laser-coolable molecules have been limited to relative intensity sensitivities above about 0.1%. Roughly speaking, this can provide sufficient information to achieve about 1,000 photon scatters per molecule in an optical cycling experiment. Because 3D laser cooling and trapping can require at least an order of magnitude more photon scatters, such sensitivity is not quite sufficient to determine feasible cooling schemes. In a "traditional" DLIF spectroscopy experiment, a single laser beam is used to drive some rotationally lossy transition, resulting in approximately 1 photon scatter per molecule. By applying a small amount of photon cycling in the detection region, it is possible to increase the number of photons scattered per molecule and therefore increase the signal-to-noise ratio considerably. As described now, this is the route we follow to achieve higher levels of relative intensity sensitivity, improving upon the previous state-of-the-art by about 1 to 2 orders of magnitude.

4.1.1 Spectrometer apparatus

Our DLIF measurements are conducted using a relatively simple beam line (see Fig. 4.1). Molecular beams were produced in a setup similar to that described in Ch. 3. The primary difference is that the beams used for spectroscopy were optimized for highest flux, not for lowest velocity. In particular, we used a single-stage cell and ablated a solid metal target (either Yb or Ca) in the presence of ^{4}He buffer-gas. We simultaneously flowed water vapor into the cell through a hot capillary held near 275 K.[3] The molecular production was further enhanced by driving the $^1S_0 \rightarrow {}^3P_1$ inter-

[3]For the $CaOCH_3$ measurements, the water vapor was replaced with methanol vapor.

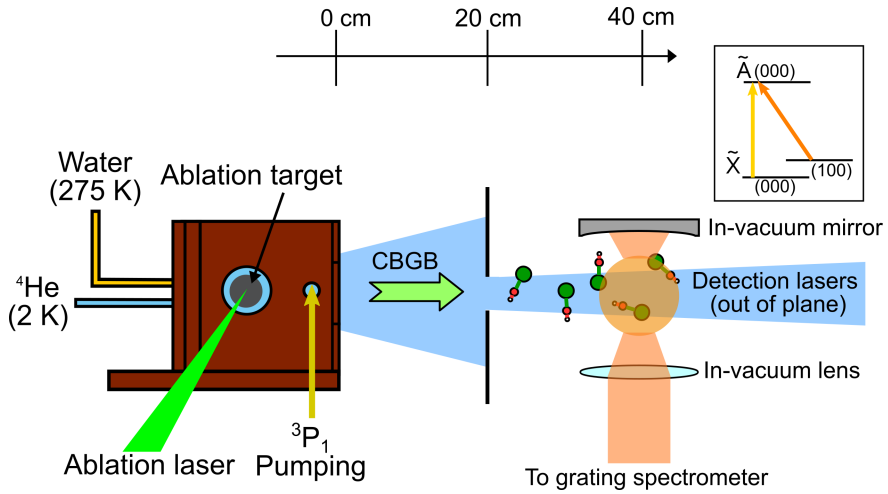

Figure 4.1: Schematic diagram (not to scale) showing the experimental setup for DLIF branching ratio measurements. Depending on the molecular species being probed, either Yb or Ca ablation targets are used. The collected LIF is sent to a Czerny-Turner spectrometer (not shown) and imaged onto an EMCCD. Inset: the vibrational levels addressed to achieve optical cycling in the detection region.

combination line at 555 nm (657 nm) for Yb (Ca). The details of this enhancement are discussed in Sec. 5.1.2 and Ref. [194]. Approximately 1 W of enhancement laser power was used for the YbOH measurements and about 300 mW were used for the CaOH measurements (both limited by the power output by either our SFG or cw dye laser sources). The molecules were extracted from the cell through a 7 mm aperture and propagated 40 cm to a room-temperature detection region.

In the detection region, the molecules interact with laser beams tuned to drive population to a targeted excited state. For measurements of the $\tilde{A}\,^2\Pi_{1/2}(000)$ VBRs, the $\tilde{A}\,^2\Pi_{1/2}(000) \leftarrow \tilde{X}\,^2\Sigma^+(000)$ and $\tilde{A}\,^2\Pi_{1/2}(000) \leftarrow \tilde{X}\,^2\Sigma^+(100)$ transitions are driven simultaneously in the detection region. Each laser beam carries two frequencies to drive the rotationally-closed ${}^pQ_{12}(0.5)$ and $P_1(1.5)$ lines. For YbOH (CaOH), this allows scattering an average of approximately 70 (150) photons per molecule. Much of our improved relative intensity sensitivity originates from populating the excited state many times. Note that in order to use optical cycling in this way, it is important to drive all laser transitions through the *same* excited state so that the fluorescence photons always provide information about a single rovibronic level's intrinsic VBRs.

A portion of the molecular fluorescence is collimated by a 35 mm diameter lens placed inside the room-temperature detection chamber. A spherical mirror of 25 mm diameter opposite the collection lens increases the collection efficiency by about 30%. Overall, we estimate that approximately 2% of the emitted fluorescence is collected.[4] The (approximately collimated) collected fluorescence is then delivered to a 0.67 m Czerny-Turner style spectrometer (McPherson model 207A) through a series of 2″ diameter mirrors. A lens system just before the entrance slit is used to focus the light into the spectrometer. The lens is used to approximately match to the spectrometer's specified f-number ($f = 4.7$) in order to fill the grating.

We use a 300 grooves/mm Al-coated diffraction grating, blazed at 500 nm and measuring 120 mm $\times$ 140 mm. The grating dispersion is 4.96 nm/mm. This grating provides a good compromise between achievable resolution and the spectral width that will be observed in a single spectrum. Our EMCCD has a pixel size of 16 μm and assuming it takes around 2.5 pixels to resolve a line, the approximate FWHM system resolution is around 0.2 nm. For the molecules of interest, the most closely-spaced features tend to be separated by at least 0.5-1 nm, indicating that this resolution is sufficient for our purposes. In fact, we often run with a somewhat wider entrance slit which reduces the resolution further.

Each collected DLIF spectrum covers approximately 50 nm of spectral range, limited by a combination of the grating's dispersion and the size of the EMCCD's sensor. Multiple images must be recorded and stitched together to produce a spectrum that covers the full wavelength range of interest (typically $\sim 100 - 150$ nm). We often accomplished this by taking a relatively small dataset ($\sim 1,000$ ablation shots) at a particular grating position before tuning the grating by an equivalent of about 6 nm in the center position and recording another dataset. This was useful because it allowed us to exclude any artifacts that appeared in individual datasets due to, e.g., small amounts

[4] Note that future experiments could significantly improve their signal-to-noise ratio by improving the fluorescence collection system.

of stray light incident on the grating that do not tune in the correct way as the grating angle is changed. A handful of artifacts like this were observed with apparent relative intensity below the 10^{-4} level. By improving the alignment of the light onto the grating we were able to suppress such artifacts by a factor of around 5-10; scanning the grating in small steps allowed us to exclude them from our analysis more completely.

4.1.2 Calibration

We carefully calibrated both the wavelength and relative intensity response of the spectrometer. The wavelength axis calibration was confirmed by allowing a small amount of laser scatter to pass through the spectrometer while simultaneously reading the laser's frequency to MHz-level precision on a wavemeter. For each grating position, this provides a mapping from EMCCD pixel to wavelength. After collecting molecular DLIF traces, we tested the wavelength calibration by measuring vibrational intervals and comparing against independent high-resolution measurements. We found that the measured intervals agreed with previously reported values to within ± 5 cm^{-1}, quite satisfactory given the resolution of the system.

The relative intensity response of the imaging system (including spectrometer mirrors, grating, and EMCCD spectral response) was calibrated by coupling a few hundred nW of laser power into the spectrometer and recording the number of counts measured by the EMCCD. This was repeated for a range of wavelengths covering the spectral region probed in our measurements. A plot of the relative intensity response of the system is shown in Fig. 4.2. When applied to the collected data, we make sure to normalize for constant photon flux (rather than constant power). Unfortunately, due to the laser sources available in the lab, the range of wavelengths between about 685 nm and 750 nm could not be accessed; we assume a linear interpolation between these limits. The laser power itself was calibrated using a commercial power meter with NIST-traceable calibrated sensor.

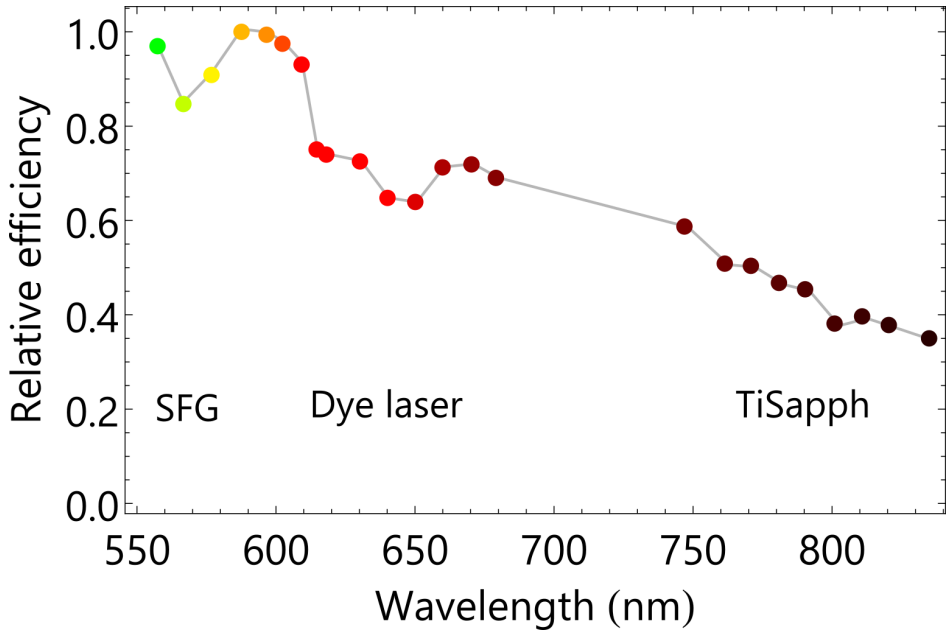

Figure 4.2: Relative intensity response of the combined spectrometer/EMCCD system. Points show the relative number of counts measured on the EMCCD, normalized by the intensity measurement on a commercial power meter. The gray line indicates an interpolating function used for normalization between the measured points. Also indicated is the type of laser source used for calibration within different spectral ranges.

Intensity calibrations are notoriously difficult, and normalizing against the laser power measured in this way is the dominant error in most of our branching ratio measurements. Testing the calibration for five sensors available in the lab, we estimate that this contributes $\sim 5\%$ calibration and readout uncertainty. For the smallest observed spectral features, the determined branching ratios are limited by the noise floor at the level of $\sim 1 \times 10^{-5}$ for CaOH and YbOH measurements and $\sim 5 \times 10^{-4}$ for $CaOCH_3$.

4.2 YbOH measurements

For YbOH molecules, we measured the vibrational branching ratios from $\tilde{A}\,^2\Pi_{1/2}(000)$ and from $\tilde{A}\,^2\Pi_{1/2}(100)$ using the spectrometer setup. The $\tilde{A}\,^2\Pi_{1/2}(000)$ DLIF measurements were recorded by simultaneously driving the $\tilde{A}\,^2\Pi_{1/2}(000) \leftarrow \tilde{X}\,^2\Sigma^+(000)$ (577 nm) and $\tilde{A}\,^2\Pi_{1/2}(000) \leftarrow \tilde{X}\,^2\Sigma^+(100)$ (595 nm) transitions. In both cases, the rotationally closed ${}^pQ_{12}(N'' = 1)$ and $P_1(N'' = 1)$ transi-

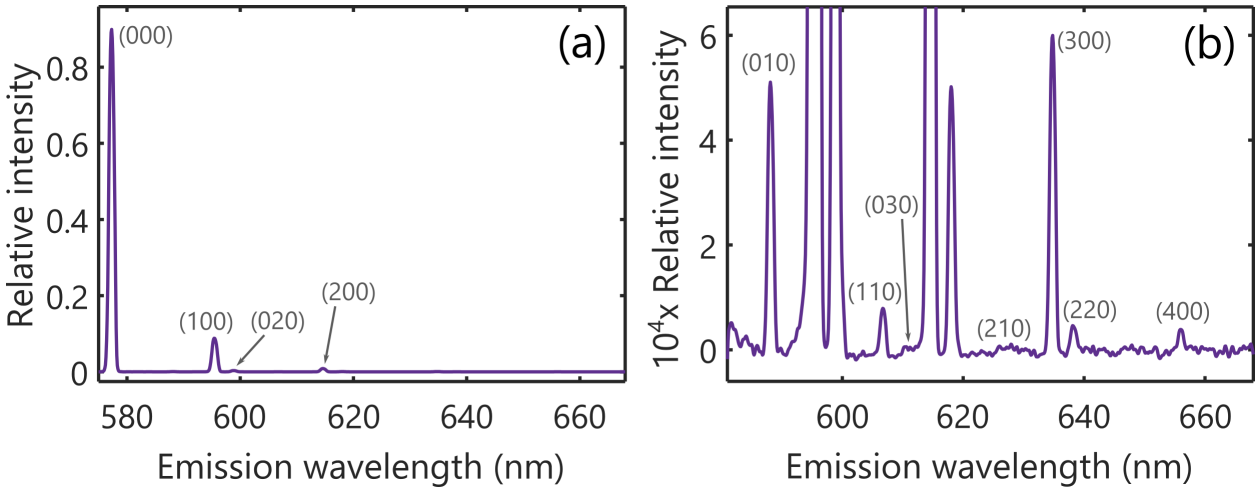

Figure 4.3: DLIF measurement following excitation of YbOH to the $\tilde{A}\,^2\Pi_{1/2}(000)(J' = 1/2, p = +)$ state. Gray labels above each peak identify the ground vibrational level (v_1, v_2, v_3) populated by the associated decay. (a) Full range of observed intensities. (b) Detail near the noise floor, demonstrating that spectral features with relative intensities as low as about 2×10^{-5} can be identified.

tions were driven and rf sidebands generated by an AOM were used to address both spin-rotation components. Around 200 mW at each wavelength was used in order to strongly saturate the transitions in the detection region. The $\tilde{A}\,^2\Pi_{1/2}(100)$ DLIF measurements were recorded by simultaneously driving the $\tilde{A}\,^2\Pi_{1/2}(100) \leftarrow \tilde{X}\,^2\Sigma^+(000)$ (558 nm) and $\tilde{A}\,^2\Pi_{1/2}(100) \leftarrow \tilde{X}\,^2\Sigma^+(100)$ (575 nm) transitions. Again, the rotationally-closed transitions were addressed and appropriate sidebands were added to each laser beam to address both spin-rotation states. About 300 mW of laser power was available at each wavelength.

4.2.1 $\tilde{A}\,^2\Pi_{1/2}\,(000)$ measurements

Results of the $\tilde{A}\,^2\Pi_{1/2}(000)$ DLIF measurements in the range between 570 nm and 670 nm are shown in Fig. 4.3. Numerical values for the measured vibrational energies (relative to the ground vibrational state) and extracted VBRs are presented in Tab. 4.1. The most prominent features in the spectrum arise from fluorescence to the (000), (100), (200), and (020) levels.[5] Transitions involving

[5]We are unable to resolve the (02^00) and (02^20) levels in our setup.

Table 4.1: Energies (in cm^{-1}) of the $X^2\Sigma$ state of YbOH and VBRs (in %) of the transitions from $A^2\Pi_{1/2}(000)$ to these states. The energies have an estimated uncertainty of ± 5 cm^{-1} and the noise level of the smallest VBRs is at the level of 9×10^{-6}. Columns in italics compare our measurements ("Meas.") against theoretical predictions ("Calc."; see Ref. [195]) and previous measurements conducted by the group of Tim Steimle ("[153]").

	Levels			VBRs		
State	Meas.	*Calc.*	*[153]*	Meas.	*Calc.*	*[153]*
(000)	0	*0*	*0*	89.44(61)	*87.691*	*89.73*
(010)	319	*322*	*328*	0.054(4)	*0.053*	–
(100)	528	*532*	*529*	9.11(55)	*10.774*	*9.74*
(02^00)	627	*631*	*625*	0.335(20)	*0.457*	*0.27*
(02^20)	–	*654*	–	–	*0.022*	–
(110)	840	*846*	*851*	0.0100(13)	*0.007*	–
(03^10)	947	*952*	–	0.0020(9)	*<0.001*	–
(200)	1052	*1062*	*1053*	0.914(62)	*0.863*	*0.26*
(12^00)	1144	*1154*	–	0.055(4)	*0.063*	–
(12^20)	–	*1173*	–	–	*0.004*	–
(210)	1369	*1369*	–	0.0019(12)	*<0.001*	–
(300)	1572	*1600*	*1576*	0.067(4)	*0.054*	*<0.05*
(22^00)	1651	*1680*	–	0.0050(9)	*0.007*	–
(400)	2079	*2160*	–	0.0045(9)	*0.002*	–

these four levels have been observed at high resolution, as well. The DLIF spectrum also reveals a number of vibrational states that have not been previously observed.

As shown in Tab. 4.1, there is reasonable agreement between our measurements and those of Ref. [153]. The primary disagreement is in the relative strengths of the (200) and (020) features, which are found to differ by a factor of ~ 3 in our measurements but had previously been reported as being approximately equal. As will be described in Sec. 5.2, our pump-probe measurements seem to confirm that the (200) decay is somewhat stronger than the (020) feature. Comparing against high-level *ab initio* theory calculations conducted by the group of Lan Cheng, we observed excellent quantitative agreement for the stronger transitions and promising qualitative agreement for the weaker transitions (with intensity below about 0.1%). Note that the theory calculations also support the observation that the VBR to $\tilde{X}\,^2\Sigma^+(200)$ is a few times stronger than that to $\tilde{X}\,^2\Sigma^+(020)$.

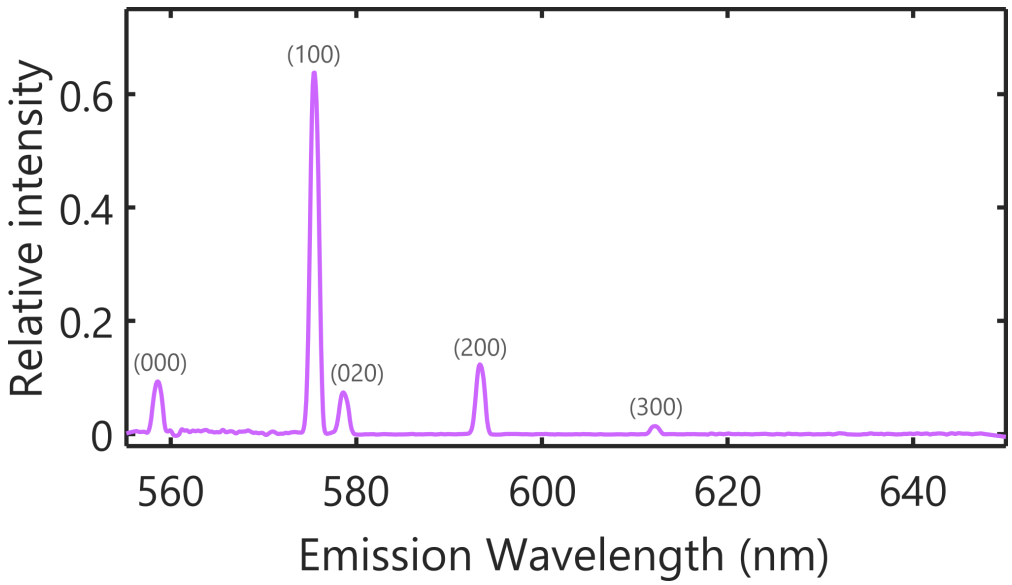

Figure 4.4: DLIF measurement following excitation of YbOH to the $\tilde{A}\,^2\Pi_{1/2}(100)(J' = 1/2, p = +)$ state. Gray labels above each peak identify the ground vibrational level (v_1, v_2, v_3) populated by the associated decay.

4.2.2 $\tilde{A}\,^2\Pi_{1/2}\,(100)$ measurements

Results of the $\tilde{A}\,^2\Pi_{1/2}(100)$ DLIF measurements in the range between 555 nm and 650 nm are shown in Fig. 4.4. Our noise level for these measurements was on the order of a few parts in 10^3, about 100 times worse than was achieved for the $\tilde{A}\,^2\Pi_{1/2}(000)$ state. Because the $\tilde{A}\,^2\Pi_{1/2}(100)$ state has very strong off-diagonal decays, we were not able to photon cycle efficiently in order to boost this signal significantly. Even with two lasers applied, we only scattered a few photons per molecule in the detection region and this causes the reduced sensitivity. From a practical standpoint, this level of sensitivity is sufficient because in the planned YbOH laser cooling scheme only 1 in every 70 photons should be scattered from the $\tilde{A}\,^2\Pi_{1/2}(100)$ state.

Numerical values for the measured branching ratios are presented in Tab. 4.2. The spectrum is significantly less diagonal than was observed for the $\tilde{A}\,^2\Pi_{1/2}(000)$ state. Decays to $\tilde{X}\,^2\Sigma^+(000)$ and $\tilde{X}\,^2\Sigma^+(200)$ have roughly equivalent strengths, both at the 10% level. In addition, a strong decay to $\tilde{X}\,^2\Sigma^+(020)$ is observed, as is a reasonably strong decay to $\tilde{X}\,^2\Sigma^+(300)$. A very weak feature attributed to decays to the $\tilde{X}\,^2\Sigma^+(400)$ feature is also apparent, but is barely observable above the

Table 4.2: VBRs (in %) of the transitions from YbOH $\tilde{A}\,^2\Pi_{1/2}(100)$ to various ground states. Columns in italics compare our measurements ("Meas.") against previous measurements conducted by the groups of Tim Steimle ("[153]") and with calculations following the method of App. D ("Calc.").

State	Meas.	*[153]*	*Calc.*
(000)	9.7	*6.19*	*14.49*
(100)	67.9	*64.90*	*64.5*
(020)	7.7	*11.61*	—
(200)	12.9	*14.98*	*17.7*
(300)	1.5	*2.32*	*3.2*
(400)	0.2	—	*0.5*

noise level. The strong activity in the Yb-O stretching mode suggests that the poor VBRs are primarily determined by a large change in molecular geometry between $\tilde{X}\,^2\Sigma^+(000)$ and $\tilde{A}\,^2\Pi_{1/2}(100)$. Indeed, numerical calculations of the FCFs as described in App. D achieve reasonable agreement with the measured branching ratios.

4.2.3 Discussion of YbOH results

The YbOH measurements extended our knowledge of VBRs from the YbOH $\tilde{A}\,^2\Pi_{1/2}(000)$ significantly: the previous weakest observed feature was at the 0.26% while we observed features with relative intensities as small as 0.002%. Many of the newly observed vibrational branching features violate the nominal $\Delta\ell = 0$ selection rule and likely arise due to perturbations or vibronic coupling effects. Because YbOH has a very large spin-orbit interaction compared to CaOH, it is interesting that these perturbations are not *more* widespread in YbOH— we will discuss this below, after presenting the CaOH measurements. The excellent agreement achieved between experiment and theory gives confidence in our understanding of YbOH branching ratios.

We can use the measured branching ratios to infer an expected number of photon scatters per molecule as additional vibrational repumping lasers are added to the experiment. Assuming both the $\tilde{X}\,^2\Sigma^+(000)$ and $\tilde{X}\,^2\Sigma^+(100)$ states are driven through the $\tilde{A}\,^2\Pi_{1/2}(000)$ level, these

Table 4.3: Photon budgets achievable for YbOH as a function of vibrational states repumped. "Photons if closed" indicates the average number of photons scattered before only $1/e$ of the population remains in a bright state. For bending modes with $\ell = 1$, both $N'' = 1$ and $N'' = 2$ states can be populated due to parity doubling. We assume the relative branching ratios to these two states follow the values predicted by the Hönl-London factors. In addition, we neglect the possibility of branching to electronic levels between the $\tilde{A}$ and $\tilde{X}$ states.

State	VBR (%)	Photons if closed
(000)	89.44	9
(100)	9.11	70
(200)	0.914	170
(02^00)	0.335	400
(300)	0.067	550
(12^00)	0.055	775
$(010), N = 1$	0.054	1 335
(02^20)	0.050	4 000
$(110), N = 1$	0.01	6 800
(22^00)	0.005	10 360
(400)	0.0045	19 500
(03^10)	0.002	31 000
(210)	0.0019	

values are shown in Tab. 4.3. These numbers should be taken with a good deal of caution, especially for expected photon budgets above a few thousand. The primary reason for this is that it is currently unknown whether any electronic states arising from $Yb^+(4f^{13})$ configurations may disrupt the optical cycle, e.g. by acting as loss channels between the $\tilde{A}\,^2\Pi_{1/2}$ and $\tilde{X}\,^2\Sigma^+$ electronic manifolds [196–198]. If metastable states arising from these excitations have transition dipole moments at the $\sim 10^{-4}$ level, then decays to these metastable levels will begin to dominate the VBRs observed in our optical spectra after a few thousand photon scatters. This is an open area of inquiry being investigated both theoretically and experimentally. We attempted to search for fluorescence that could arise from the $\tilde{A}\,^2\Pi_{1/2}(000)$ level decaying to these metastable states, but did not observe any within the detection bandwidth of our EMCCD-based system. This is not particularly meaningful, because the fluorescence is likely to occur at wavelengths near $1\ \mu m$ that we were not able to detect [196]. These metastable states are expected to have significantly different bond lengths and vibrational frequencies, so decays that do occur to them are likely to spread over a number

of vibrational modes; this makes the prospects for repumping losses to such states relatively unpromising.

4.3 CaOH measurements

For CaOH molecules, we measured vibrational branching ratios from the $\tilde{A}\,^2\Pi_{1/2}(000)$ and $\tilde{B}\,^2\Sigma^+(000)$ levels. The $\tilde{A}\,^2\Pi_{1/2}(000)$ DLIF measurements were recorded by driving the $\tilde{A}\,^2\Pi_{1/2}(000) \leftarrow \tilde{X}\,^2\Sigma^+(000)$ (626 nm) and $\tilde{A}\,^2\Pi_{1/2}(000) \leftarrow \tilde{X}\,^2\Sigma^+(100)$ (651 nm) transitions. Around 200 mW at each wavelength was used in order to strongly saturate the transitions in the detection region. The $\tilde{B}\,^2\Sigma^+(000)$ DLIF measurements were recorded by simultaneously driving the $\tilde{B}\,^2\Sigma^+(000) \leftarrow \tilde{X}\,^2\Sigma^+(000)$ (554 nm) and $\tilde{B}\,^2\Sigma^+(000) \leftarrow \tilde{X}\,^2\Sigma^+(100)$ (574 nm) transitions. About 350 mW (200 mW) of main-line (first repumper) power was used.

4.3.1 $\tilde{A}\,^2\Pi_{1/2}\,(000)$ measurements

Results of the $\tilde{A}\,^2\Pi_{1/2}(000)$ DLIF measurements in the range between 620 nm and 720 nm are shown in Fig. 4.5. Numerical values for the measured vibrational energies (relative to the ground vibrational state) and extracted VBRs are presented in Tab. 4.4. Again, we find that the dominant decay pathways are to the (000), (100), (02^00), and (200) levels. Note that while Tab. 4.4 includes a measurement for decay to (02^20), this value comes from a combination of direct DLIF data and the numbers presented in Ref. [199]. We could only partially resolve the (02^20) feature in our DLIF traces, but the small shoulder on the (020) peak of Fig. 4.5(b) is consistent with the assigned value. Unlike in YbOH, the VBR to the (02^00) level is *larger* than that to (200). This is primarily because in CaOH, the ground and excited-state geometries more nearly resemble on another, leading to better wavefunction overlap and therefore more diagonal branching ratios in the Ca-O stretching (ν_1)

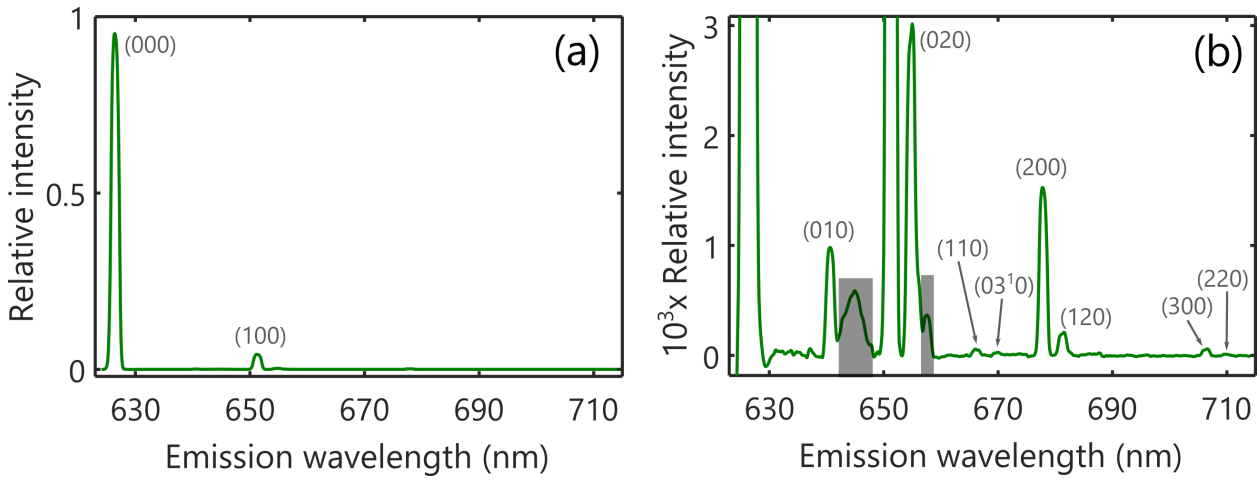

Figure 4.5: DLIF measurement following excitation of CaOH to the $\tilde{A}\,^2\Pi_{1/2}(000)(J' = 1/2, p = +)$ state. Gray labels above each peak identify the ground vibrational level (v_1, v_2, v_3) populated by the associated decay. (a) Full range of observed intensities. (b) Detail near the noise floor. Gray boxes cover features that are due to atomic Ca emission, present in the spectrum as an impurity.

mode. Also shown in Tab. 4.4 are *ab initio* predictions performed by the group of Lan Cheng; these show excellent agreement with the measurements. The primary disagreement between theory and experiment is in the values of the VBRs to relatively high-lying bending modes, (03^10) and (04^00), which could indicate that details of the bending potential are not fully captured by the *ab initio* calculations.

4.3.2 $\tilde{B}\,^2\Sigma^+\,(000)$ measurements

We have also measured VBRs from the CaOH $\tilde{B}\,^2\Sigma^+(000)$ level. To record this data, we simultaneously drove the $\tilde{B}\,^2\Sigma^+(000, N' = 0) \leftarrow \tilde{X}\,^2\Sigma^+(000, N = 1)$ and $\tilde{B}\,^2\Sigma^+(000, N' = 0) \leftarrow \tilde{X}\,^2\Sigma^+(100, N = 1)$ cycling transitions. We achieved relative intensity sensitivity around the level of 1 part in 10^4, where the lower sensitivity primarily arises due to less averaging. The CaOH optical cycling scheme proposed by Ref. [199] envisions using the $\tilde{B}\,^2\Sigma^+(000)$ level as a repumping pathway, so approximately 20× fewer photons would be scattered from this excited state as compared to the "main" $\tilde{A}\,^2\Pi_{1/2}(000)$ level. The extent of loss incurred by vibrational branches out of

Table 4.4: Energies (in cm^{-1}) of the $X^2\Sigma$ state of CaOH and VBRs (in %) of the transitions from $A^2\Pi_{1/2}(000)$ to these states. The energies have an estimated uncertainty of ± 5 cm^{-1} and the noise level of the smallest VBRs is at the level of 7×10^{-6}. Columns in italics compare our measurements ("Meas.") against theoretical predictions ("Calc."; see Ref. [195]) and previous measurements conducted by other groups ("[200]" and "[193]").

	Levels			VBRs		
State	Meas.	*Calc.*	*[200]*	Meas.	*Calc.*	*[193]*
(000)	0	*0*	*0*	94.59(29)	*95.429*	*95.7(2)*
(010)	354	*355*	*354*	0.099(6)	*0.063*	—
(100)	611	*611*	*606*	4.75(27)	*3.934*	*4.3(2)*
(02^00)	693	*695*	*686*	0.270(17)	*0.298*	0.3^{+1}_{-2}
(02^20)	—	*718*	—	0.067(12)	*0.079*	—
(110)	953	*954*	*952*	0.0064(7)	*0.003*	—
(03^10)	1035	—	—	0.0034(8)	*<0.001*	—
(200)	1211	*1214*	*1207*	0.174(16)	*0.157*	—
(12^00)	1288	—	*1286*	0.021(3)	*0.022*	—
(12^20)	—	—	—	0.005(1)	*0.005*	—
(040)	1400	—	*1389*	0.0021(7)	*<0.001*	—
(300)	1804	—	*1800*	0.0068(8)	*0.006*	—
(22^00)	1874	—	*1872*	0.0020(7)	*0.002*	—

this level is correspondingly smaller.

Results of the $\tilde{B}\,^2\Sigma^+(000)$ DLIF measurements in the range between 550 nm and 630 nm are shown in Fig. 4.6. Numerical values for the measured vibrational energies and extracted VBRs are presented in Tab. 4.5. The dominant VBRs correspond to decays to the (000), (100), and (010) levels of the $\tilde{X}\,^2\Sigma^+$ state. The diagonal $\tilde{B}\,^2\Sigma^+(000) \rightarrow \tilde{X}\,^2\Sigma^+(000)$ decay has a slightly larger VBR than the corresponding diagonal feature from the $\tilde{A}\,^2\Pi_{1/2}(000)$ level. While the strongest off-diagonal feature is the Ca-O stretching mode, as expected, the relatively large branching ratio to $\tilde{X}\,^2\Sigma^+(010)$ is notable because it violates the nominal $\Delta\ell = 0$ selection rule. Nonetheless, this is in line with previous measurements conducted by the Steimle group [193]. It was proposed that this feature gains intensity through a spin-orbit-vibronic coupling mechanism [140]. Very near the noise floor of the measurements (below the $\sim 10^{-4}$ level) we observe weak features that may be assigned to decays to the (210), (300), and (140) levels of $\tilde{X}\,^2\Sigma^+$ on the basis of their energies. However, these

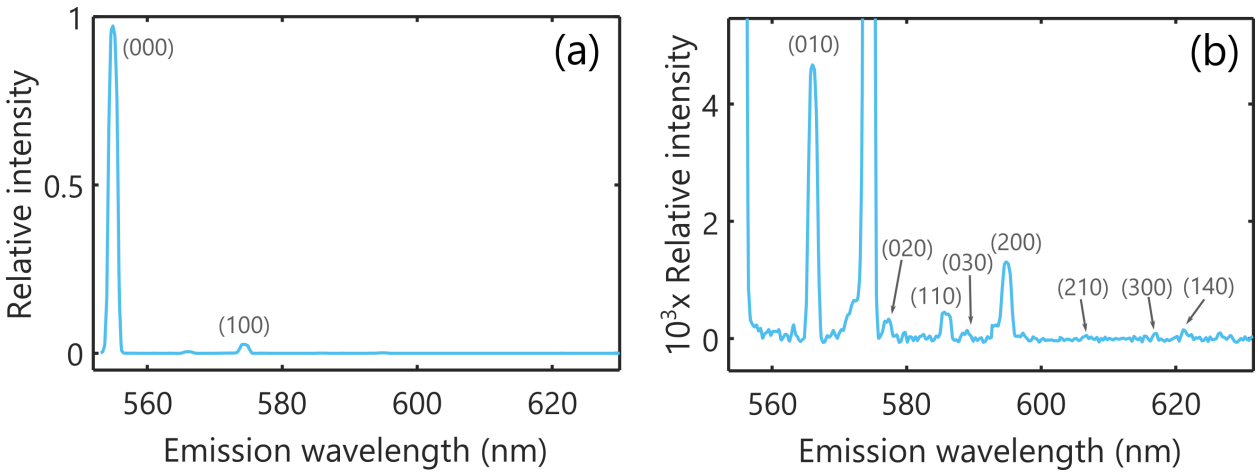

Figure 4.6: DLIF measurement following excitation of CaOH to the $\tilde{B}\,^2\Sigma^+(000)(N'=0, p=+)$ state. Gray labels above each peak identify the ground vibrational level (v_1, v_2, v_3) populated by the associated decay. (a) Full range of observed intensities. (b) Detail near the noise floor.

features have similar intensities to unassigned and/or spurious features; higher signal-to-noise ratio measurements must be conducted to gain confidence in these assignments.

4.3.3 Discussion of CaOH results

For CaOH, we have seen direct evidence of many decays that gain intensity due to perturbations and vibronic coupling effects. As is discussed in more detail in Ref. [199], decays to $\tilde{X}\,^2\Sigma^+(12^00)$ and (02^20) arise due to Fermi resonance in the ground state and vibronic coupling in the excited state, respectively. Both of these decays occur at the $\sim 0.02-0.06\%$ level, indicating that they could limit photon cycling to $\lesssim 5,000$ photon scatters without repumping. The relative strength of such decays was not fully anticipated and was one of the major developments that forced us to take into account the importance of perturbations to developing laser cooling schemes.

Especially when compared with the YbOH measurements, the CaOH measurements helped to sure up our understanding of how vibronic coupling mechanisms affect laser cooling schemes. The measured VBR for decay from $\tilde{A}\,^2\Pi_{1/2}(000)$ to $\tilde{X}\,^2\Sigma^+(010)$ in CaOH is about 0.1%, which is slightly

Table 4.5: Energies (in cm^{-1}) of the $X^2\Sigma$ state of CaOH and VBRs (in %) of the transitions from $\tilde{B}\,^2\Sigma^+(000)(N'=0)$ to these states. The energies have an estimated uncertainty of ± 5 cm^{-1} and the noise level of the smallest VBRs is at the level of 2×10^{-5}. Columns in italics compare our measurements ("Meas.") against previous measurements conducted by the group of Tim Steimle ("[193]").

	Levels		VBRs	
State	Meas.	*[193]*	Meas.	*[193]*
(000)	0	*0*	96.7	*97.5(1)*
(010)	357	*353*	0.46	*0.3(1)*
(100)	609	*609*	2.7	*2.2(1)*
(020)	696	–	0.031	–
(110)	948	–	0.042	–
(030)	1038	–	0.010	–
(200)	1209	–	0.129	–
(210)	1545	–	0.003	–
(300)	1806	–	0.004	–
(140)	1932	–	0.008	–

stronger than the same vibrational branch in YbOH.[6] This may appear surprising because the spin-orbit interaction is significantly larger in YbOH than it is in CaOH, while the direct vibronic coupling parameter is very similar in these two species [195]. Previous expectations [148, 201] had been that the strength of decay to $\tilde{X}\,^2\Sigma^+(010)$ would grow with spin-orbit parameter. In fact, we observed similar intensities for decay to (010) in both CaOH and YbOH, and this is consistent with the *ab initio* predictions of Ref. [195]. Lan Cheng has helped us explain this by noting that the spin-orbit vibronic coupling only pulls intensity into $\tilde{A}\,^2\Pi_{1/2}$ through the (distant) $\tilde{A}\,^2\Pi_{3/2}(010)$ level, which suppresses the strength of this effect relative to the direct vibronic coupling mechanism.

In Ref. [199], a laser cooling scheme for CaOH is proposed in which the "main" cycling transition is $\tilde{A}\,^2\Pi_{1/2}(000) \leftarrow \tilde{X}\,^2\Sigma^+(000)$ and the first repumping transition is $\tilde{B}\,^2\Sigma^+(000) \leftarrow \tilde{X}\,^2\Sigma^+(100)$. This means that about 95% of photons will be scattered from the $\tilde{A}\,^2\Pi_{1/2}(000)$ excited state and about 5% of the photons will be scattered from the $\tilde{B}\,^2\Sigma^+(000)$ state. Weighting the VBRs measured for these states appropriately, we can estimate the average number of photon scatters achievable

[6] Recall that the VBR for YbOH $\tilde{A}\,^2\Pi_{1/2}(000) \rightarrow \tilde{X}\,^2\Sigma^+(010)$ was about 0.05%.

Table 4.6: Photon budgets achievable for CaOH as a function of vibrational states repumped. "Photons if closed" indicates the average number of photons scattered before only $1/e$ of the population remains in a bright state. For bending modes with $\ell = 1$, both $N'' = 1$ and $N'' = 2$ states can be populated due to parity doubling. We assume the relative branching ratios to these two states follow the values predicted by the Hönl-London factors.

State	Weighted VBR (%)	Photons if closed
(000)	94.70	18
(100)	4.65	150
(02^00)	0.259	250
(200)	0.171	440
$(010), N = 1$	0.082	680
(02^20)	0.064	1 200
$(010), N = 2$	0.036	2 100
(12^00)	0.020	3 500
(300)	0.0065	4 500
$(110), N = 1$	0.0060	6 200
(12^20)	0.0049	9 000
(03^10)	0.0028	12 000
$(110), N = 2$	0.0024	17 500
(04^00)	0.0020	28 000
(22^00)	0.0019	56 000

as increasingly more states are closed. These values are shown in Tab. 4.6. As for YbOH, these values should be treated with some skepticism because small sources of noise or very weak lines that were not observed could contribute loss channels that are comparable to the ones that were used to infer the photon budgets. Unlike YbOH, there should not be any accessible excitations to metastable orbitals between the $\tilde{X}$ and $\tilde{A}$ states, so loss to intermediate metastable states is probably not relevant for CaOH.

4.4 Vibronic coupling effects in linear polyatomic molecules

In Ch. 2, we explained that within the BO approximation, vibrational selection rules forbid decays with $\Delta\ell \neq 0$, e.g. decays from $\tilde{A}\,^2\Pi_{1/2}(000)$ to $\tilde{X}\,^2\Sigma^+(010)$ and (02^20). In the DLIF spectra presented above, decays to both of these states were observed with branching ratio $b_{i\to f} \approx 0.05\%$. In

reality, BO approximation breakdown at the parts per thousand level is not unexpected, and transitions with $\Delta\ell = \pm 1$ have been previously observed in alkaline-earth monohydroxides [201–204]. We have shown [199] that one can apply perturbation theory to the Renner-Teller Hamiltonian 2.19 to make accurate estimates of these branching ratios. We will focus on CaOH, because the available spectroscopic data makes perturbative estimates possible in this case.

Decays to $\tilde{X}\,^2\Sigma^+(010)$ can be explained by either direct vibronic coupling between $\tilde{A}\,^2\Pi_{1/2}(000)$ and $\tilde{B}\,^2\Sigma^+(010)$ or by second-order vibronic coupling between $\tilde{A}\,^2\Pi_{1/2}(000)$ and $\tilde{A}\,^2\Pi_{1/2}(010)$. The direct coupling [148] can occur due to the V_{11} term in Eq. 2.19 and is related to matrix elements such as $\langle\tilde{B}|V_{11}e^{i\theta}|\tilde{A}\rangle$. To first order, the fraction of (01^10) character mixed into $\tilde{A}\,^2\Pi_{1/2}(000)$ can be expressed as

$$f^{(1)}_{(010)} \equiv |\langle\tilde{B}(01^10)\,^2\Pi|\tilde{A}(000)\,^2\Pi_{1/2}|^2 \approx \left|\frac{\langle\tilde{B}|V_{11}e^{i\theta}|\tilde{A}\rangle/2}{(E_B+\omega_2)-E_A}\right|^2, \tag{4.1}$$

where we have labeled the kets by the vibronic symmetry of each state, ω_2 is the bending frequency, and E_B and E_A are the unperturbed origins of the $\tilde{A}(000)$ and $\tilde{B}(000)$ states. To relate the matrix element to measurable parameters, we note that a spectroscopic constant, g_K, is also determined by the same interaction[7] [169],

$$g_K \approx \frac{\omega_2|\langle\tilde{B}|V_{11}e^{i\theta}|\tilde{A}\rangle|^2}{4\Delta E^2_{BA}}. \tag{4.2}$$

Combining Eqs. 4.1 and 4.2 yields

$$f^{(1)}_{(010)} \approx \frac{g_K}{\omega_2(1-\omega_2/\Delta E_{BA})^2}. \tag{4.3}$$

Previously reported CaOH spectroscopy has found $g_K = 0.5937\,\mathrm{cm}^{-1}$ [170], $\omega_2 = 366.435\,\mathrm{cm}^{-1}$ [205], and $\Delta E_{BA} = -2024.14\,\mathrm{cm}^{-1}$ [170]. Substituting these values into Eq. 4.3 gives the direct vibronic

[7] The constant g_K characterizes an energy offset in certain $K = \Lambda + \ell$ components of the vibronic levels of a $^2\Pi$ electronic state.

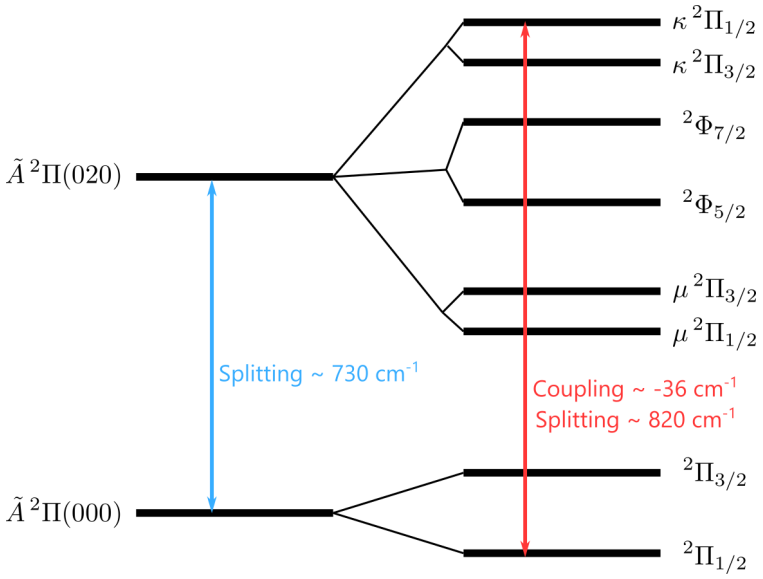

Figure 4.7: Vibronic components involved in quadrupolar Renner-Teller perturbation that lends intensity to $\tilde{A}\,^2\Pi_{1/2}(000) \rightarrow \tilde{X}\,^2\Sigma^+(02^20)$ decays. Vibronic components of the $\tilde{A}\,^2\Pi(020)$ state that have the same symmetry label are distinguished using conventional κ and μ labels [132].

mixing fraction $f^{(1)}_{(010)} \approx 1.2 \times 10^{-3}$. There are also second order contributions due to cross-terms between the Renner-Teller Hamiltonian and the spin-orbit interaction. These contributions are smaller than the direct vibronic coupling for CaOH [199], at least partially because they require the coupling to occur between $\Pi_{1/2}$ and $\Pi_{3/2}$ components and the spin-orbit splitting between these unperturbed states suppressed the presence of the spin-orbit parameter in the perturbation theory expansion's numerator [195].[8]

Loosely, the nominal $\tilde{A}\,^2\Pi_{1/2}(000)$ state contains about 0.12% (01^10) character. Assuming the "diagonal" VBR between $\tilde{B}(010)$ and $\tilde{X}(010)$ is about 95% (similar to the other diagonal transitions), we estimate that the Renner-Teller perturbation leads to an effective VBR between $\tilde{A}\,^2\Pi_{1/2}(000)$ and $\tilde{X}\,^2\Sigma^+(010)$ of $\approx 1.1 \times 10^{-3}$. This is in excellent agreement with the measured value of $0.99(6) \times 10^{-3}$ reported in Tab. 4.4.

The Renner-Teller perturbation can also cause mixing with states that differ by $\Delta\ell = \pm 2$, lend-

[8] Lan Cheng originally pointed this out to us. See the Supplemental Information to Ref. [195] for an understanding of why the spin-orbit-vibronic coupling effects have similar magnitude in CaOH and YbOH, despite the much larger spin-orbit interaction in YbOH.

ing intensity to decays from $\tilde{A}\,^2\Pi_{1/2}(000)$ to $\tilde{X}\,^2\Sigma^+(02^20)$. In this case, the intensity borrowing is due to the "quadrupolar" (second-order) term in Hamiltonian 2.19 which can mix $\tilde{A}\,^2\Pi(000)$ and $\tilde{A}\,^2\Pi(02^20)$ at first order in perturbation theory.[9] Using the matrix elements of Ref. [170] and the basis set of Ref. [205], we find that the perturbation matrix element between $\tilde{A}\,^2\Pi(000)$ and $\tilde{A}\,^2\Pi(02^20)$ can be written as $\langle H_{\mathrm{RT}}\rangle = \epsilon\omega_2/\sqrt{2}$, where $\epsilon\omega_2 \approx -36$ cm^{-1} has been measured previously [205]. The vibronic components that are coupled are indicated in Fig. 4.7, and it is the $\kappa\,^2\Pi_{1/2}(K=1)$ component that perturbs $\tilde{A}\,^2\Pi_{1/2}(000)$ because that vibronic component has dominant $\ell = 2$ character (see Ref. [205]). The splitting of the relevant unperturbed states is around 830 cm^{-1}. Thus, we estimate a mixing fraction

$$f^{(1)}_{(02^20)} \equiv |\langle \tilde{A}(02^20)\,\kappa^2\Pi|\tilde{A}(000)\,^2\Pi_{1/2}\rangle|^2 \approx \left(\frac{(-36\ \mathrm{cm}^{-1})/\sqrt{2}}{830\ \mathrm{cm}^{-1}}\right) \approx 9\times10^{-4}. \tag{4.4}$$

Including the ν^3 factor for spontaneous decay, this leads to a VBR estimate between $\tilde{A}\,^2\Pi_{1/2}(000)$ and $\tilde{X}\,^2\Sigma^+(02^20)$ of $\approx 7.5\times10^{-4}$. This is in good agreement with the measured value of $6.7(1.2)\times10^{-4}$ reported in Tab. 4.4.

4.5 $CaOCH_3$ measurements

By flowing methanol, rather than water, vapor into the cell we were able to produce $CaOCH_3$ molecules. We recorded a set of DLIF spectra to determine the VBRs from the $\tilde{A}\,^2E_{1/2}$ state. While VBRs for this level have been reported previously in Ref. [193], it appeared we would be able to achieve improved relative intensity sensitivity. We were particularly interested in making a direct observation of decay to the fundamental Ca-O-C bending mode, as this could gain intensity via the pseudo-Jahn-Teller interaction and provide a method to study vibronic coupling in nonlinear

[9] A similar interaction has previously been observed between the $\tilde{A}\,^2\Pi(010)$ and $\tilde{A}\,^2\Pi(03^30)$ states [170].

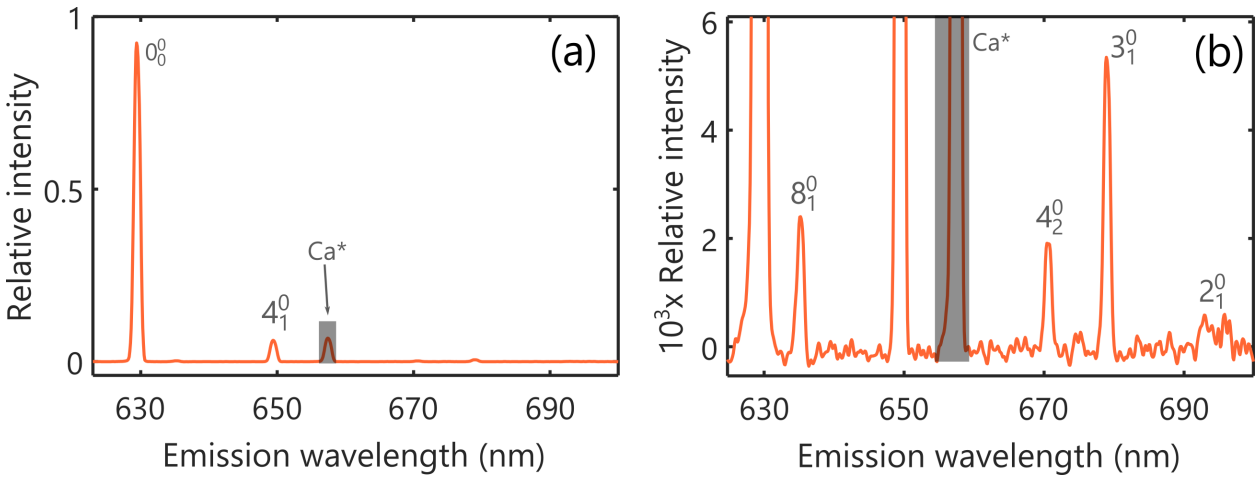

Figure 4.8: DLIF measurement following excitation of $CaOCH_3$ to the $\tilde{A}\,^2E_{1/2}(v=0, J'=1/2, p=+)$ state. Gray labels above each peak identify the vibrational transition using the nomenclature set out in App. B. (a) Full range of observed intensities. (b) Detail near the noise floor.

molecules.

In order to excite $CaOCH_3$ to the $\tilde{A}\,^2E_{1/2}$ state, we drove the $0_0^0\ \tilde{A}\,^2E_{1/2}(K'=1, J'=1/2^+) \leftarrow \tilde{X}\,^2A_1(K=0, N=1)$ transition in the detection region.[10] Due to the larger off-diagonal VBRs, the number of photons scattered per molecule in the detection region was only about 10. For this reason, the relative intensity sensitivity achieved in our $CaOCH_3$ measurements was approximately 0.1%, a slight improvement over the previous measurements [193, 206] that was nonetheless sufficient to reveal weak features that had been previously unobserved.

4.5.1 $\tilde{A}\,^2E_{1/2}(v=0)$ Measurements

The DLIF spectrum resulting from excitation of the $CaOCH_3$ $\tilde{A}\,^2E_{1/2}(v=0)$ level is shown in Fig. 4.8. The extracted vibrational energies and branching ratios are presented in Tab. 4.7. The dominant features observed in this spectrum arise from decays to the Ca-O stretching mode, ν_4, the fundamental O-C stretching mode, ν_3, and the fundamental Ca-O-C bending mode, ν_8. We also observe a relatively strong feature due to decay of metastable $^3P_1$ Ca atoms (labeled Ca*).

[10] For symmetric top molecules, we use the vibrational transition nomenclature described in App. B.

Table 4.7: Energies (in cm^{-1}) of the $X^2\Sigma$ state of $CaOCH_3$ and VBRs (in %) of the transitions from $\tilde{A}\,^2E_{1/2}(v=0)$ to these states. The energies have an estimated uncertainty of ± 5 cm^{-1} and the noise level of the smallest VBRs is at the level of 3×10^{-4}. Columns in italics compare our measurements ("Meas.") against previous measurements conducted by the groups of Tim Steimle ("[193]") and Jinjun Liu ("[206]").

	Levels			VBRs		
State	Meas.	*[193]*	*[206]*	Meas.	*[193]*	*[206]*
0_0	0	*0*	*0*	92.9	*93.1(3)*	*90.4(5.5)*
8_1	143	*145*	*149*	0.24	–	–
4_1	489	*502*	*490*	6.14	*6.3(3)*	*5.9(5)*
4_2	974	–	*973*	0.19	–	*0.9(2)*
3_1	1156	*1140*	*1157*	0.54	*0.6(3)*	*2.5(2)*
2_1	1460	–	*1450*	0.046	–	–
$3_1 4_2$	–	–	*1647*	–	–	*0.3(2)*

The atomic feature appears more prominently in this spectrum (as compared to in the CaOH data) primarily due to lower production of $CaOCH_3$. Our scan did not extend far enough to the red to observe a feature arising from decay to the $\nu_3 + \nu_4$ combination mode, but such a decay was observed in Ref. [206]. Near the expected location of the CH_3 symmetric bending mode (ν_2), we observed a very weak fluorescence feature. We tentatively assign this feature to the 2_1^0 band, but future measurements are necessary to confirm this assignment and refine the measured value. Note that this feature appears at nearly the same intensity as other features that could not be readily assigned.

Decays to the Ca-O and O-C stretching modes are expected to be strong on the basis of geometry changes in the molecule. Decay to the Ca-O-C bending mode (ν_8) is indicative of interactions among the electronically excited states. It is also interesting to note that the symmetry *allowed* decay to 2 quanta of the Ca-O-C bending mode (8_2^0) was not observed above our noise level. A few very weak features are observed just above the noise floor but do not correspond to any obvious vibrational splitting in $CaOCH_3$; for now, we leave these peaks unassigned, and future investigations will be necessary to definitively determine if they originate from $CaOCH_3$ fluorescence.

4.5.2 Pseudo-Jahn-Teller effect

In a previous study of the $CaOCH_3$ molecule, a relatively strong 8_1^0 feature (decay to the Ca-O-C bending mode) was predicted via *ab initio* methods and it was hypothesized that this nominally forbidden decay could gain intensity via a pseudo-Jahn-Teller mechanism [206]. Now that we have directly observed the fluorescence due to this 8_1^0 vibronic transition, we can use the observed VBR to infer mixing parameters and compare to the *ab initio* calculations. A very simple estimate proceeds as follows. Start with the measured 8_1^0 VBR (0.24%) and ν_8 frequency (143 cm^{-1}). Using a perturbative analysis, we can assume that the admixture of $v_8 = 1$ character in the electronically excited state probed by our DLIF is related to the mixing between $\tilde{A}(v_8 = 0, 1)$ via:

$$\text{Admixture} = \sqrt{2.4 \times 10^{-3}} = \frac{\langle \tilde{A}, v_8 = 1 | H' | \tilde{A}, v_8 = 0 \rangle}{\nu_8}, \tag{4.5}$$

which can be inverted to give

$$\langle \tilde{A}, v_8 = 1 | H' | \tilde{A}, v_8 = 0 \rangle \approx 7 \text{ cm}^{-1} \tag{4.6}$$

as the effective coupling between the $\tilde{A}(v_8 = 0, 1)$ states. This matrix element can in turn be written as $k_8 + 2C_{AB}\lambda_8$, where k_8 describes direct coupling between $\tilde{A}(v_8 = 0, 1)$ and λ_8 characterizes the pseudo-Jahn-Teller coupling between $\tilde{A}\,^2E$ and $\tilde{B}\,^2A_1$. C_{AB} gives the mixing between $\tilde{A}\,^2E$ and $\tilde{B}\,^2A_1$ due to spin-orbit coupling. As shown in Ref. [206], the k_8 term is negligible and we can therefore write

$$\langle \tilde{A}, v_8 = 1 | H' | \tilde{A}, v_8 = 0 \rangle \approx 2C_{AB}\lambda_8 \tag{4.7}$$

$$= 2\frac{a\zeta_e d}{\sqrt{2}\Delta E_{AB}}\lambda_8, \tag{4.8}$$

where $a\zeta_e d$ is the spin-orbit coupling parameter for the $\tilde{A}$ state. Combining Eqs. 4.5 and 4.8, we infer a value $\lambda_8 \approx 135$ cm^{-1}. This is in reasonably good agreement with the *ab initio* value of $\lambda_8^{\text{theory}} = 150$ cm^{-1} computed by Ref. [206], especially considering the approximations made. It is worth emphasizing that these results show the power of our high-sensitivity DLIF apparatus for studies of fundamental physical chemistry: accurate intensity measurements can give access to detailed information about excited-state potential energy surfaces.

4.6 Limitations of DLIF spectra

While the DLIF spectra described above provide much detailed information about the vibrational states populated following spontaneous emission from some excited electronic state, they do not necessarily provide a complete picture of the possible loss channels. This is because the VBRs inferred from a DLIF measurement are really just ratios of emission intensities. Any loss process that does not lead to emission of a photon within our detection bandwidth will not be accounted for in our assigned branching ratios. There are, in principle, a number of possible processes like this. Some salient examples include (1) spontaneous emission of photons to states that are not in our detection bandwidth, (2) dissociation of the electronically excited molecule, and (3) intramolecular vibrational relaxation.

To address concern (1), for CaOH and YbOH we recorded additional DLIF spectra farther to the red than was shown in the DLIF traces above. We focused particularly on the region around the wavelength expected for decays to $\tilde{X}\,^2\Sigma^+(001)$. No fluorescence features were observed for either species above the level of about 0.01%. It is of course possible that there *are* emission features that we simply missed, but the probability of this is relatively low for CaOH, especially given the excellent agreement with *ab initio* branching ratio predictions. For YbOH, there is great concern that decays from $\tilde{A}\,^2\Pi_{1/2}\,(000)$ could populate metastable states arising from excitations of the Yb

$4f^{13}$ electrons. These would be expected to wavelengths much redder than 800 nm, meaning our spectrometer as currently built would not be sensitive to the fluorescence. Theoretical work to understand these metastable states is currently being pursued by the group of Lan Cheng, and future experimental work informed by such theory may be necessary. Concern (2) appears unlikely to cause systematic errors in our VBR measurements because the dissociation energies for CaOH and YbOH are both relatively high compared to the $\tilde{A}\,^2\Pi_{1/2}$ and $\tilde{B}\,^2\Sigma^+$ states that we probed. For example, predictions of the YbF dissociation energy place it around 40,000 cm^{-1} [207], and YbOH is likely to be similar. Similarly, concern (3) appears unlikely for the small molecules probed here because the density of states is not particularly high in the vicinity of the $\tilde{A}\,^2\Pi_{1/2}$ or $\tilde{B}\,^2\Sigma^+$ levels probed by our measurements.

Ultimately, the most reliable way to establish (or rule out) loss channels beyond those observed in the DLIF spectra is to optically cycle many photons and look for unexpected loss of population. This technique is very similar to the steps taken to establish laser cooling. Focusing on the case of YbOH, we will describe such measurements in Ch. 5.

It makes me so happy. To be at the beginning again, knowing almost nothing...

Tom Stoppard, "Arcadia"

5

YbOH Spectroscopy and Photon Cycling

In this chapter, we describe spectroscopy undertaken to achieve photon cycling with YbOH molecules. Prior to the PolyEDM experiment, there had been a single spectroscopic study of YbOH molecules [129]. The Steimle group at Arizona State University was instrumental in extending the spectroscopic knowledge of YbOH to a level at which laser cooling could be possible. One of the most important contributions to this effort was a detailed study of the low-lying excited states of YbOH, collected using pulsed laser excitation spectroscopy at mid-to-low resolution. The results are presented in Ref. [153]. Armed with low-resolution information about the $\tilde{X}$ state vibrational levels and the low-lying electronically excited states, we conducted high-resolution YbOH spectroscopy aimed at achieving photon cycling. Data was collected both at Arizona State University (described in

Refs. [172, 173]) and at Harvard (described in this chapter). We begin this chapter (Sec. 5.1) by providing an overview of the methods we have used to produce YbOH molecules, including "enhancing" chemical reactions by using excited-state chemistry. Using the YbOH sources described, high-resolution spectroscopy, described in Sec. 5.2, was conducted using a number of pump-probe style measurements that uniquely identified the rotationally-closed transitions for the main cycling. The four dominant cycling and repumping transitions in YbOH are identified. In Sec. 5.3 we show how the completed spectroscopy enables photon cycling for YbOH molecules, including a demonstration of optical forces exerted on a molecular beam. The spectroscopy and optical cycling demonstrations presented in this chapter set the stage for the laser cooling discussed in Ch. 6.

5.1 Production of YbOH

We have used a number of methods to produce YbOH molecules. All of them rely on buffer-gas cooling following laser ablation of a suitable target. The simplest is via ablation of pressed pellets of $Yb(OH)_3$ powder. Our first YbOH signals were observed using such a source, but the long-term stability and overall yield were both quite poor. Some attempts were made to produce better pressed targets, for example by mixing in various binders and metal powders to improve the target integrity. A separate tact is to ablate metallic Yb in the presence of a gas that contains an OH group available for chemical reaction. Because ablation of metallic targets can be quite robust, this has been a reliable method for other experiments to produce molecules like CaF (e.g., by ablating atomic Ca in the presence of SF_6 vapor) [117]. To produce YbOH, we have used both methanol (CH_3OH) and water (H_2O) vapor to react with ablated Yb metal. It is relatively well established that the reaction of such gases with Yb to produce YbOH proceeds through the excited electronic states, especially the atomic ^3P manifold [194, 208, 209]. Because the excited state is relatively short-lived and not necessarily populated by the ablation process, it is possible to *enhance*

the amount of YbOH produced by optically pumping population into the ^3P manifold inside the buffer-gas cell. This has previously been demonstrated following ablation of pressed $Yb(OH)_3$ targets [194], and we have shown that it can be extended to reactions with both gas-phase water and methanol flowed into the cell through a hot capillary. In this section, we provide an overview of these production mechanisms.

5.1.1 Yb metal reactions

Water and methanol are both liquids at room temperature, but have reasonable vapor pressures (about 25 and 90 torr, respectively). The vapors were introduced into the buffer-gas cell through a capillary held between 275 and 285 K. The design of this capillary (or "hot fill line") followed that of Ref. [187] except that in later iterations we constructed the entire line from copper in order to improve the temperature uniformity. The other major difference is that our fill line enters the cell from the rear, next to the He buffer-gas inlet (see Fig. 3.1).

5.1.2 Enhanced production via excited-state chemistry

In recent work by the Hutzler group, it was shown that laser excitation of Yb atoms to the $^3P_1$ state at approximately 556 nm could be used to enhance the production of YbOH molecules following laser ablation of a pressed $Yb(OH)_3$ target [194]. Due to the nature of their ablation target, it is not immediately clear what the reaction pathway is, but theoretical studies presented in the same work suggested that either Yb + H_2O or Yb + H_2O_2 would be reasonable. We sought to study the same enhancement mechanism using ablation of a metallic Yb target in the presence of water or methanol vapor.

We generated up to 1 W of 556 nm light using a commercial SFG system (TiSapph + 1550 nm fiber laser). The enhancement laser beam is directed into the cell through one of the windows also

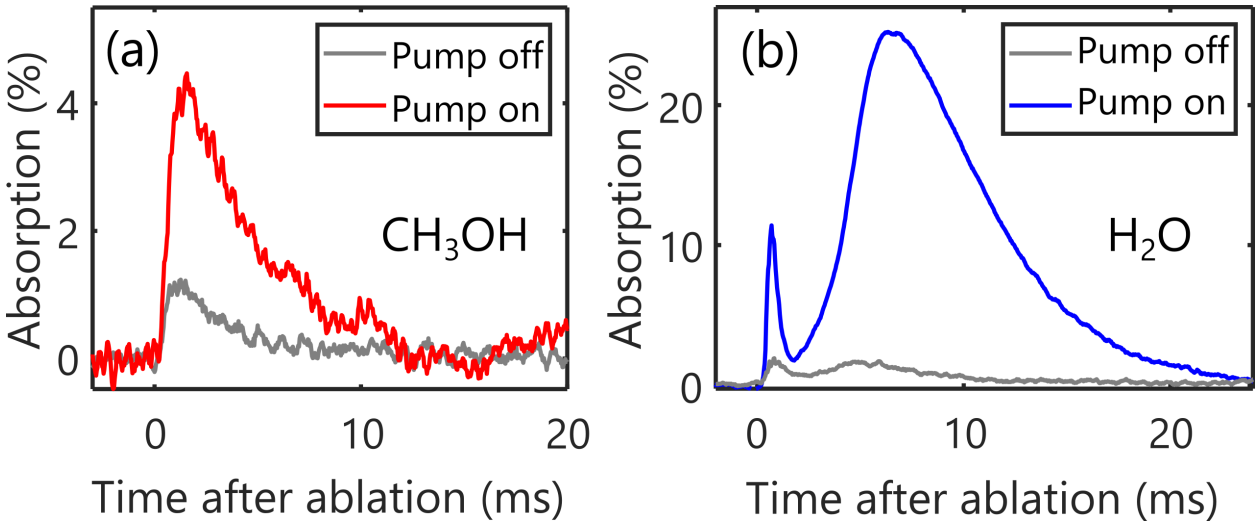

Figure 5.1: Enhancement of YbOH production by pumping the Yb $^1S_0 \rightarrow ^3 P_1$ transition inside the buffer-gas cell when (a) methanol and (b) water is flowed into the cell.

used for probing in-cell absorption. In order to reduce the heat load on the cell, the laser is turned on for a variable time (usually about 15 ms) and given our typical 2 Hz duty cycle causes a steady-state heat load of about 20 mW. We found that YbOH production was maximized when the light was directed at a relatively steep angle such that it scattered off the inside of the 1st cell's exit aperture. Sending light perfectly transverse to the cell or directly down the bore (counterpropagating against the molecular beam) produced little or no enhancement of the reaction.

Figure 5.1 shows the effect of driving the Yb $^1S_0 \rightarrow ^3 P_1$ transition with about 500 mW of laser power when Yb atoms are ablated in the presence of either methanol or water vapor. In both cases, the buffer-gas flow into the cell was 4 sccm and the ablation energy was set to 18 mJ. Roughly similar production is observed is the absence of enhancement light. Approximately 1% absorption of the probe is observed in these cases, which corresponds to about 5×10^7 molecules per cm^3. When the enhancement pump is turned on, the methanol reaction yield is increased by a factor of about 3.5 [Fig. 5.1(a)] while the water reaction yield is increased by a factor of about 25 [Fig. 5.1(b)]. The corresponding densities are approximately 2×10^8 cm^{-3} and 1×10^9 cm^{-3} for methanol and water reactions, respectively. The enhanced water reaction produces YbOH densities about a fac-

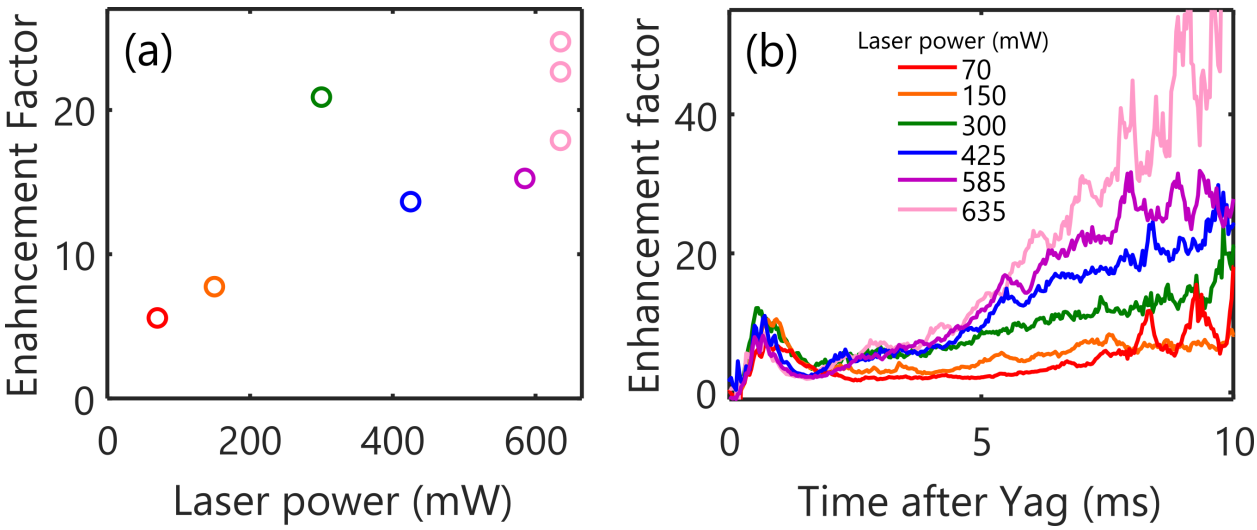

Figure 5.2: (a) Enhancement of total YbOH production in Yb+H_2O reaction as a function of laser power used to drive the $^1S_0 \rightarrow ^3P_1$ transition. (b) For each laser power, enhancement as a function of time after ablation. Preferential enhancement of molecules produced at later times is observed.

tor of two lower than the CaOH production reported in Ref. [187]. Given our cell volume, this corresponds to about 10^{11} molecules per ablation pulse.

It is notable that the timescale over which molecules are produced is quite different for methanol and water reactions (see Fig. 5.1). In the reaction with methanol, the molecules are produced in a span of about 5-10 ms immediately following the ablation pulse. On the other hand, the reaction with water shows a clear "two-peaked" structure, where there is a very rapid burst of production within the first 1-2 ms after ablation, followed by a second— substantially stronger— period of YbOH production that occurs out to around 10 ms. We do not have a complete model for what causes this difference, but it is possible that the timing indicates that the methanol reaction occurs very close to the ablation plume while the water reaction occurs throughout the bulk of the cell.

Focusing on the Yb-water reaction, we have performed detailed studies of the enhancement as a function of laser power. The results are shown in Fig. 5.2(a), where we plot the enhancement of integrated in-cell absorption as a function of laser power. It appears that even at the highest laser powers we could supply to the cell (~ 650 mW), the enhancement was still in the linear regime,

with overall production enhancement factors around 20-25. The scatter among repeated traces gives an idea of the relative fluctuations over a few hours of running. In addition, we can plot the enhancement as a function of time, as shown in Fig. 5.2(b). The observed enhancement is $> 10\times$ for times between 5 and 10 ms after ablation. In the molecular beams measured outside the cell, there is some correlation between molecules that exit the cell later and molecules that have lower forward velocities. The fact that the enhancement is larger at later times is promising because it indicates that even production of molecules with lower forward velocity are likely to be enhanced.

5.2 High-resolution YbOH spectroscopy

The vibrational branching ratio measurements presented in Ch. 4 dictate which vibrational states must be repumped to achieve some level of photon cycling. Actually *achieving* photon cycling requires selecting particular, rotationally-resolved transitions within each vibronic transition. In this section we describe the high-resolution spectroscopy carried out to find the rotationally-closed cycling transitions for the main cycling and first three repumping transitions.[1]

5.2.1 Vibrational repumper searches

Prior to the start of the PolyEDM experiment, for ^{174}YbOH, only the $\tilde{A}\,^2\Pi_{1/2}(000) \leftarrow \tilde{X}\,^2\Sigma^+(000, 100)$ bands had been assigned at high resolution [129]. These measurements were conducted in a Broida oven at relatively high temperature and low resolution ($\lesssim 1$ GHz). As was later described in Ref. [173] and [210], a reassignment of the spectrum taking into account low-J lines with resolved spin-rotation structure produced an improved fit and revised molecular constants.

A typical experimental setup used for vibrational repumper spectroscopy is shown in Fig. 5.3.

[1]This section focuses on spectroscopy conducted at Harvard, but we worked closely with Tim Steimle as his group obtained increasingly detailed spectroscopic data at Arizona State University.

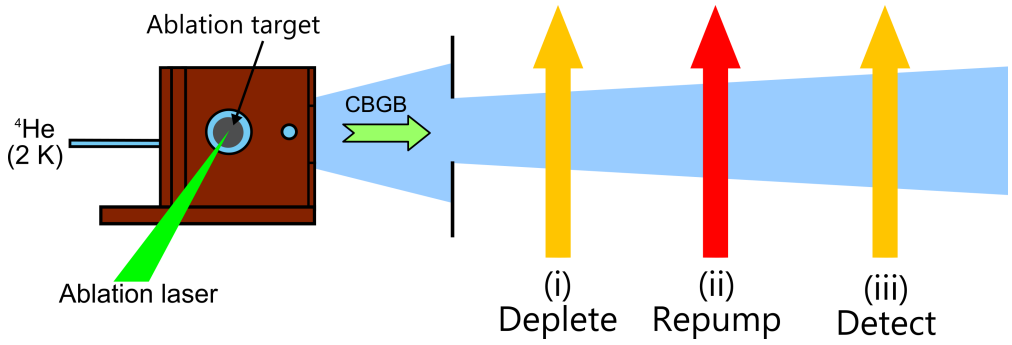

Figure 5.3: Schematic of a typical beamline used for repumper spectroscopy (not to scale). Molecules exiting in a CBGB pass through three interaction regions. In the depletion region (i) they are pumped out of the state whose populate is monitored downstream in the detection region (iii). In the intermediate repumping region (ii) the frequency of a laser is scanned over a resonance that is expected to return population to the detectable state.

In brief, molecules in a CBGB are sent through three consecutive interaction regions. In the furthest downstream [region (iii)], the lasers are probed using laser-induced fluorescence (LIF) by driving some convenient detection transition. The light in this region is collected onto a detector. Before reaching the detection region, the molecules can be pumped [region (i)] into some other state that is not detected. With just regions (i) and (iii) active, the LIF signal is ideally fully extinguished. A repumping laser can then be applied in region (ii) which is nearly resonant with some transition that return population to the detectable state. A frequency scan in this region (ii) can thus be used to find the transitions that repump lost population.

Often, more than one transition is driven in region (i) in order to deplete population from multiple ground states at once. We will see examples of this in searches for repumping transitions beyond the $\tilde{X}\,^2\Sigma^+(100)$ repumper. Moreover, we often drive multiple transitions in the detection region in order to perform photon-cycling detection for improved signal-to-noise ratio. Generally, both $\tilde{X}\,^2\Sigma^+(000)$ and $\tilde{X}\,^2\Sigma^+(100)$ states are driven in the detection region in order to boost the LIF signal; there is insufficient interaction time with the laser beams for higher-order repumpers to improve the signal noticeably.

It is worth remarking upon one major advantage of this pump-probe method of searching for

repumping transitions. As long as we drive transitions on the rotationally-closed $N'' = 1 \rightarrow J' = 1/2$ transitions, population will always remain in $N'' = 1$ of whichever vibrational levels become populated.[2] This saves us the hassle of performing rotational assignments, because the "spectra" that we obtain contain just the $N'' = 1$ features.

Using versions of the setup shown in Fig. 5.3, we have found the rotationally-resolved repumping transitions associated with the $\tilde{X}\,^2\Sigma^+(000)$, (100), (200), and (02^00) levels. The frequencies of all determined transitions are listed in App. E. We now provide an overview of the data underlying these numbers.

X(100) repumper

Initial searches for the $\tilde{X}\,^2\Sigma^+(100)$ repumper were conducted by driving $\tilde{A}\,^2\Pi_{1/2}(000) \leftarrow \tilde{X}\,^2\Sigma^+(000)$ in the depletion region, scanning a laser near the expected $\tilde{A}\,^2\Pi_{1/2}(000) \leftarrow \tilde{X}\,^2\Sigma^+(100)$ resonance in the repumping region, and monitoring $\tilde{A}\,^2\Pi_{1/2}(000) \leftarrow \tilde{X}\,^2\Sigma^+(000)$ fluorescence downstream. Using the previously available spectroscopic constants, it was relatively straightforward to locate the $\tilde{X}\,^2\Sigma^+(100)$ repumping transition, although a bit of effort was required because the scans were taken before the revised molecular constants had been fully determined. The detected LIF signal is shown in Fig. 5.4(a). This scan determined the spin-rotation splitting in $N'' = 1$ to be around 160 MHz, implying a spin-rotation parameter $|\gamma_{100}| \approx 107$ MHz. This is quite inconsistent with the value of $\gamma_{100} \approx -5$ MHz determined by Ref. [129], but is in good agreement with the updated value of $\gamma_{100} \approx -110$ MHz found in Ref. [173].

Having determined the $\tilde{X}\,^2\Sigma^+(100)$ spin-rotation splitting, we added rf sidebands to the repumping laser at 160 MHz and drove $\tilde{A}\,^2\Pi_{1/2}(000) \leftarrow \tilde{X}\,^2\Sigma^+(000)$ in the depletion region and

[2] A small caveat here: for bending modes with vibrational angular momentum, there will be $J'' = 3/2, N'' = 2$ ground states that become populated. So far we have not worked with such states in YbOH, so that subtlety has not arisen. For CaOH molecules, it has [195, 199].

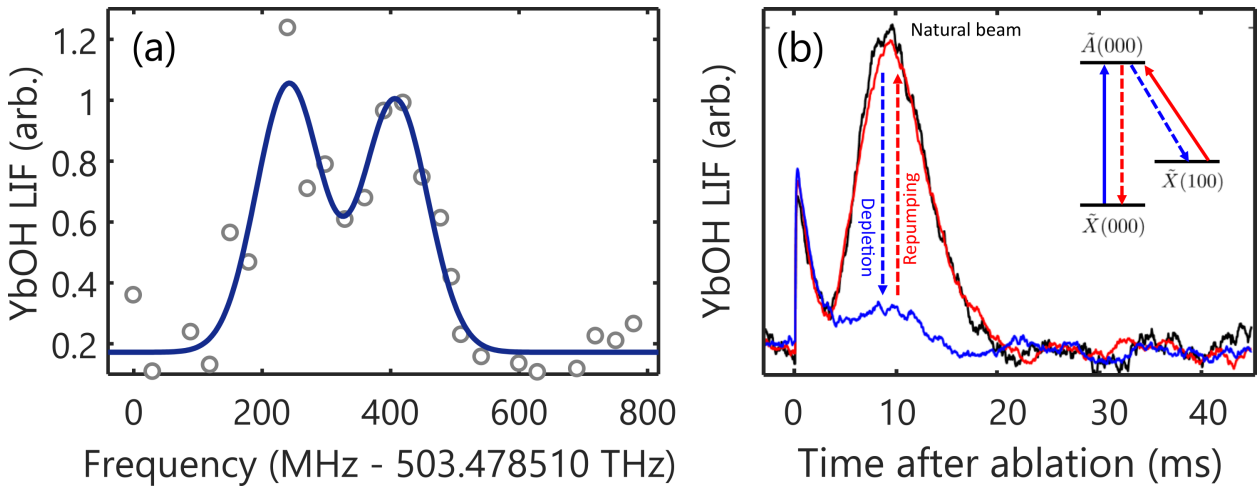

Figure 5.4: Spectroscopy of the $\tilde{A}\,^2\Pi_{1/2}(000) \leftarrow \tilde{X}\,^2\Sigma^+(100)$ repumping transition. (a) Scan of the over the $\tilde{X}\,^2\Sigma^+(100)$ repumping resonance. The observed doublet, with a splitting measured as 166(10) MHz, is due to ground-state spin-rotation structure. (b) Pump-repump efficiency for $\tilde{X}\,^2\Sigma^+(100)$ state. Black trace shows unperturbed beam, blue trace shows detected signal when $\tilde{X}\,^2\Sigma^+(000)$ state is addressed in the pumping region, and red trace shows detected signal when $\tilde{X}\,^2\Sigma^+(000)$ state is addressed in the depletion region and $\tilde{X}\,^2\Sigma^+(100)$ is addressed in the repumping region.

$\tilde{A}\,^2\Pi_{1/2}(000) \leftarrow \tilde{X}\,^2\Sigma^+(100)$ in the repumping region. We see that we can deplete about 90% of the initial $\tilde{X}\,^2\Sigma^+(000)$ population when no light is applied in the repumping region, and most of this population is expected to have accumulated in $\tilde{X}\,^2\Sigma^+(100)$. Applying light to repump the $\tilde{X}\,^2\Sigma^+(100)$ population in the repumping region confirms this, because nearly all of the initial signal is recovered when this is done. This demonstrates that we can efficiently "juggle" population between vibrational states and is consistent with the fact that the dominant off-diagonal decay from $\tilde{A}\,^2\Pi_{1/2}(000)$ is to $\tilde{X}\,^2\Sigma^+(100)$.

X(200) repumper

The $\tilde{X}\,^2\Sigma^+(200)$ repumper was found by driving $\tilde{A}\,^2\Pi_{1/2}(000) \leftarrow \tilde{X}\,^2\Sigma^+(000)$ and $\tilde{A}\,^2\Pi_{1/2}(000) \leftarrow \tilde{X}\,^2\Sigma^+(100)$ in both the depletion region and detection region. It was separately verified that we achieved $> 90\%$ depletion of the $\tilde{X}\,^2\Sigma^+(000, 100)$ levels. The YbOH VBRs indicate that under these conditions, a majority of the population should be pumped into $\tilde{X}\,^2\Sigma^+(200)$. At the time, the location of the $\tilde{X}\,^2\Sigma^+(200)$ level was known only to an accuracy of about ± 3 cm^{-1} from the

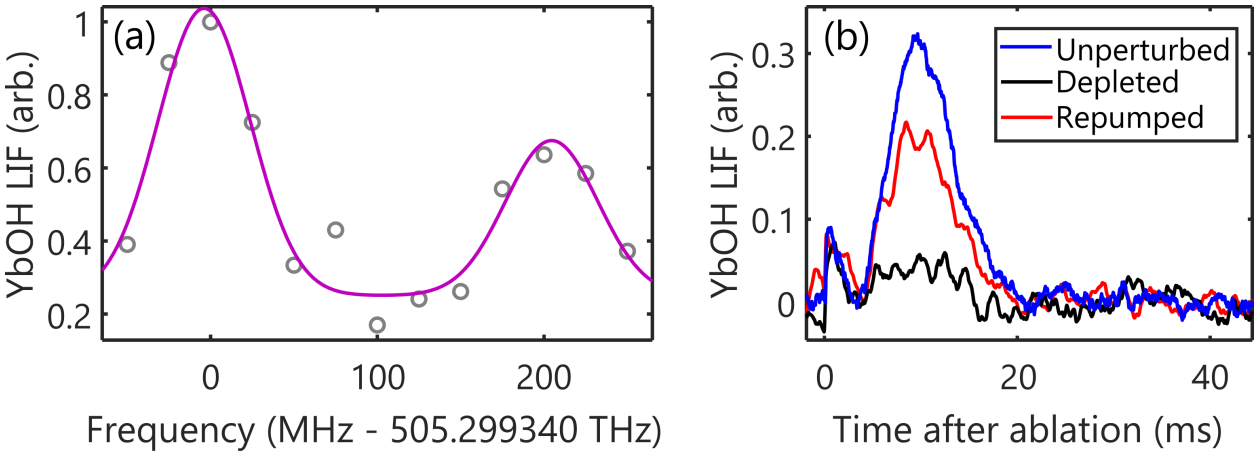

Figure 5.5: Spectroscopy of the $\tilde{A}\,^2\Pi_{1/2}(100) \leftarrow \tilde{X}\,^2\Sigma^+(200)$ repumping transition. (a) Scan over the $\tilde{X}\,^2\Sigma^+(200)$ repumping resonance. The observed doublet, with a splitting measured as 210(15) MHz, is due to ground-state spin-rotation structure. (b) Molecular beam LIF traces without depletion, with depletion, and with depletion and repumping. When both of the features observed in (a) are addressed simultaneously in the repumping region, nearly 60% of the population is returned to the detectable states.

Steimle group's DLIF spectra. We chose to conduct searches by scanning around the expected $\tilde{A}\,^2\Pi_{1/2}(100) \leftarrow \tilde{X}\,^2\Sigma^+(200)$ resonance near 593 nm. A repumping effect was observed after scanning the $\tilde{X}\,^2\Sigma^+(200)$ repumper about 0.5 cm^{-1}. Finer scans at reduced power revealed two subfeatures separated by around 220 MHz, as shown in Fig. 5.5(a). By addressing both of these features simultaneously with AOM sidebands, we recovered about 60% of the population into the detected states ($\tilde{X}\,^2\Sigma^+(000)$ and $\tilde{X}\,^2\Sigma^+(100)$), see Fig. 5.5(b). This is consistent with the VBRs of Sec. 4.2, which would predict about 55% revival in this condition.[3]

X(020) repumper

To search for the $\tilde{X}\,^2\Sigma^+(02^00)$ repumper, we used depletion lasers driving $\tilde{X}\,^2\Sigma^+(000)$, (100), and (200) and monitored the $\tilde{X}\,^2\Sigma^+(000)$ and (100) populations in the detection region. Greater than 80% depletion was generally achieved, and the majority of the population was expected to be pumped into the $\tilde{X}\,^2\Sigma^+(02^00)$ level. Initial scans were conducted on the $\tilde{A}\,^2\Pi_{1/2}(100) \leftarrow$

[3]This number may seem low given that the $\tilde{A}\,^2\Pi_{1/2}(000)$ state decays to $\tilde{X}\,^2\Sigma^+(200)$ with about 3× the intensity as compared to $\tilde{X}\,^2\Sigma^+(02^00)$, but the value is largely limited by the fact that the $\tilde{A}\,^2\Pi_{1/2}(100)$ state used for repumping is not very diagonal.

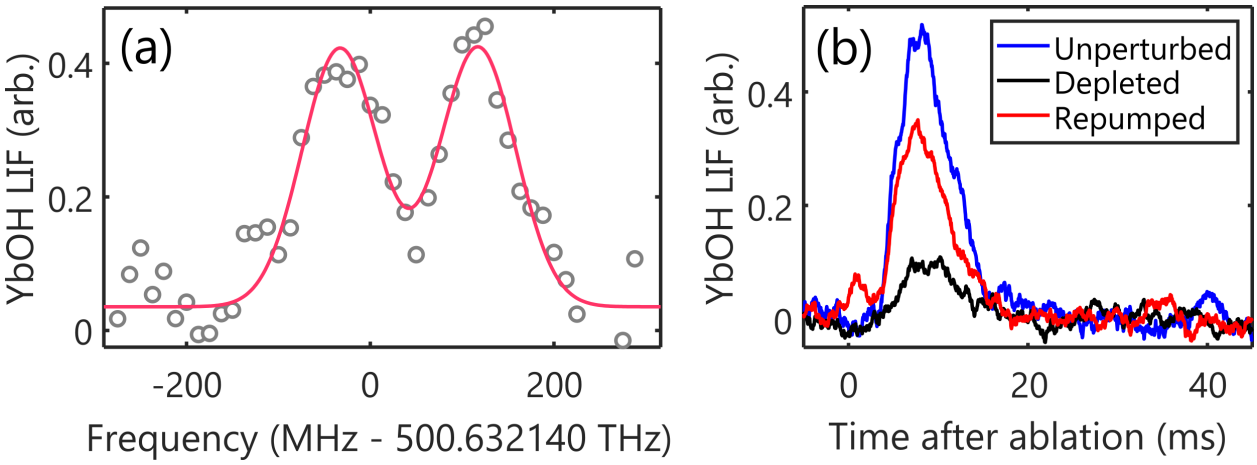

Figure 5.6: Spectroscopy of the $\tilde{A}\,^2\Pi_{1/2}(000) \leftarrow \tilde{X}\,^2\Sigma^+(02^00)$ repumping transition. (a) Scan over the $\tilde{X}\,^2\Sigma^+(02^00)$ repumping resonance. The observed doublet, with a splitting measured as 155(10) MHz, is due to the ground-state spin-rotation structure. (b) Molecular beam LIF traces without depletion, with depletion, and with depletion and repumping. When both of the features observed in (a) are addressed simultaneously in the repumping region, about 60% of the depleted population is returned to the detectable states.

$\tilde{X}\,^2\Sigma^+(02^00)$ transition (near 578 nm) informed by low-resolution data provided by the Steimle group with uncertainty around 1-2 cm^{-1}. A repumping feature was observed within 1 cm^{-1} of the central expected frequency. Because the $\tilde{A}\,^2\Pi_{1/2}(100)$ state was not well understood at the time, we conducted more detailed spectroscopy by driving the weak $\tilde{A}\,^2\Pi_{1/2}(000) \leftarrow \tilde{X}\,^2\Sigma^+(02^00)$ transition near 599 nm. As shown in Fig. 5.6, we are able to resolve the ground-state spin-rotation splitting, which is measured to be 155(10) MHz. If we address both spin-rotation components simultaneously in the repumping region, we can return about 60% of the pumped population to the detectable states. This is in reasonable agreement with the VBRs described in Sec. 4.2, which would predict 70% revival.

X(300) repumper

After finding the $\tilde{X}\,^2\Sigma^+(000)$, (100), (200), and (02^00) states, we began searching for the $\tilde{X}\,^2\Sigma^+(300)$ repumper. Chronologically, this search began before we had conducted the high-sensitivity branching ratio measurements outlined, so we suspected that by depleting on the transitions $\tilde{A}\,^2\Pi_{1/2}(000) \leftarrow$

$\tilde{X}\,^2\Sigma^+(000,100)$ and $\tilde{A}\,^2\Pi_{1/2}(100) \leftarrow \tilde{X}\,^2\Sigma^+(200,02^00)$, nearly all of the molecular population would end up in the (300) level. We spent a great deal of effort scanning over a region ~ 8 cm^{-1} wide in the expected vicinity of the $\tilde{A}\,^2\Pi_{1/2}(100) \leftarrow \tilde{X}\,^2\Sigma^+(300)$ transition (near 612 nm). We did not locate any repumping features.

Now that the $\tilde{A}\,^2\Pi_{1/2}(000)$ and $\tilde{A}\,^2\Pi_{1/2}(100)$ branching ratios are known more accurately, the measured values indicate that between 50 and 60% of the population would be pumped into $\tilde{X}\,^2\Sigma^+(300)$, with the remainder being split mainly between (010) and (12^00). Driving $\tilde{A}\,^2\Pi_{1/2}(100) \leftarrow \tilde{X}\,^2\Sigma^+(300)$ in the repumping region would return about 40% of the population to the detectable $\tilde{X}\,^2\Sigma^+(000,100)$ states. Finally, assuming the spin-rotation structure spans ~ 200 MHz or more, at any given laser frequency we would only repump roughly 20% of the initial beam signal. All of this is to say that locating the $\tilde{X}\,^2\Sigma^+(300)$ transition is more difficult than originally anticipated. Finding the transition frequency to repump this state is the highest priority for increasing the photon budget for YbOH.

5.2.2 Ground-state spin-rotation parameters

We have observed resolved spin-rotation structure within the $\tilde{X}\,^2\Sigma^+(000)$, (100), (200), and (02^00) states. The measured spin-rotation parameters $\gamma_{[v]}$ are presented in Tab. 5.1. Two notable features of the YbOH measurements are that (1) $|\gamma_{[v]}|$ increases by about 30% for each excitation of the Yb-O stretching mode and (2) the $\gamma_{[v]}$ values for YbOH are negative.[4] Both of these features are similar to findings for the YbF molecule. YbOH and YbF together behave quite differently from the alkaline-earth monohydroxides (and derivatives), for which the spin-rotation parameters are found to be positive and nearly constant as a function of vibrational level. Both the large vibrational-

[4]The pump-probe measurements conducted at Harvard were intended to determine the magnitude, but not sign, of $\gamma_{[v]}$. The Steimle group's measurements determined the negative values for (000) and (100), and we are assuming the sign remains the same for the (200) and (02^00) states.

Table 5.1: Spin-rotation parameters, $\gamma_{[v]}$, for YbOH measured in this work. Relevant comparisons from other authors are also listed. All values are listed in MHz units.

Level	YbOH	YbOH[a]	YbF[b]	CaOH[c]	SrOH[c]
(000)	−80	−81.15	−13.41679	34.765(19)	72.774(16)
(100)	−110	−110(2)	−33.81036	34.549(29)	72.210(32)
(200)	−145	–	−53.89(73)	–	–
(02^00)	−100	–	N/A	35.045(29)	71.736(32)

[a]Values from Ref. [173].
[b]Values from Ref. [211].
[c]Values from Ref. [212].

state dependence and the negative sign of the spin-rotation parameters have been explained as being due to second-order spin-orbit interactions with the complicated excited state structure of YbOH [173, 211].

From a practical standpoint, this unusual behavior means that each vibrational repumper will require a unique sideband frequency to achieve closure of the spin-rotation structure. Readily attainable AOMs can be used to generate sidebands at frequencies up to 800 MHz (and even significantly higher with minimal effort), so this should not significantly complicate any laser cooling experiments. The change in spin-rotation splitting will also affect the field at which the electron spin decouples from molecular rotation, but in all relevant cases the decoupling field will likely remain below a few hundred Gauss.

5.2.3 Excited state spectroscopy

A(100) state

We studied the use of $\tilde{A}\,^2\Pi_{1/2}(100)$ for vibrational repumping by placing laser beams driving $\tilde{X}\,^2\Sigma^+(000)$, (100), and (02^00) in the depletion region and a laser beam tuned near the expected $\tilde{A}\,^2\Pi_{1/2}(100) \leftarrow \tilde{X}\,^2\Sigma^+(200)$ transition in the repumping region (carrying about 400 mW). We the monitored the YbOH LIF following excitation on $\tilde{A}\,^2\Pi_{1/2}(100) \leftarrow \tilde{X}\,^2\Sigma^+(000, 100)$ in the de-

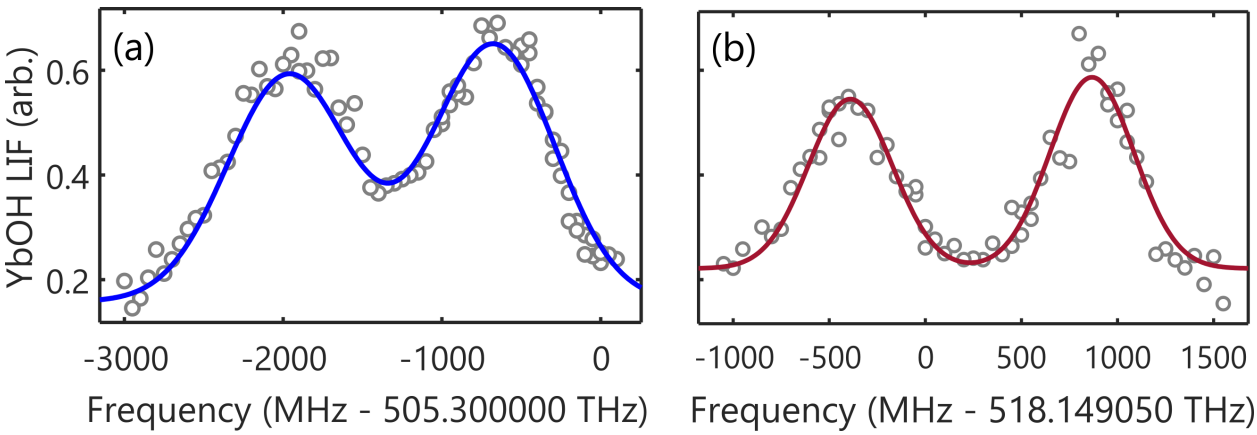

Figure 5.7: Double resonance spectroscopy of the $\tilde{A}\,^2\Pi_{1/2}(100)$ state following depletion of population transfer into (a) $\tilde{X}\,^2\Sigma^+(200)$ and (b) $\tilde{X}\,^2\Sigma^+(02^00)$. The LIF due to excitation on $\tilde{A}\,^2\Pi_{1/2}(000) \leftarrow \tilde{X}\,^2\Sigma^+(000, 100)$ is monitored in the detection region. The splittings are measured to be 1290(50) MHz and 1260(50) MHz for subfigures (a) and (b), respectively.

tection region. We also took data while reversing the roles of the laser driving $\tilde{X}\,^2\Sigma^+(200)$ and $\tilde{X}\,^2\Sigma^+(02^00)$. Spectra recorded under these conditions are shown in Fig. 5.7. Two features are apparent in the spectra, with a mean measured splitting of 1275(70) MHz. This substructure arises from the fact that the large Λ-type doubling in $\tilde{A}\,^2\Pi_{1/2}(100)$ pushes the $p = +$ components of $J' = 1/2$ and $J' = 3/2$ very close together. (See Fig. 2.5.) In fact, the $J' = 1/2$ state is at *higher* energy than the $J' = 3/2$ state. Our measurements of this splitting are consistent with the rotationally-assigned spectra of Ref. [173] which predicts the unusual state ordering and a splitting around 1.27 GHz.

[17.73] state

The pulsed-laser spectroscopy conducted by the Steimle group located a number of electronically excited states that could provide useful repumping pathways [153]. Among these, a state approximately 17731 cm^{-1} above $\tilde{X}\,^2\Sigma^+(000)$ (named the [17.73] state on the basis of its energy) was found to have a relatively large branching ratio to $\tilde{X}\,^2\Sigma^+(000)$. The remaining decays are distributed mainly among the Yb-O stretching modes, but with FCFs $\gtrsim 1\%$ for all Yb-O stretching

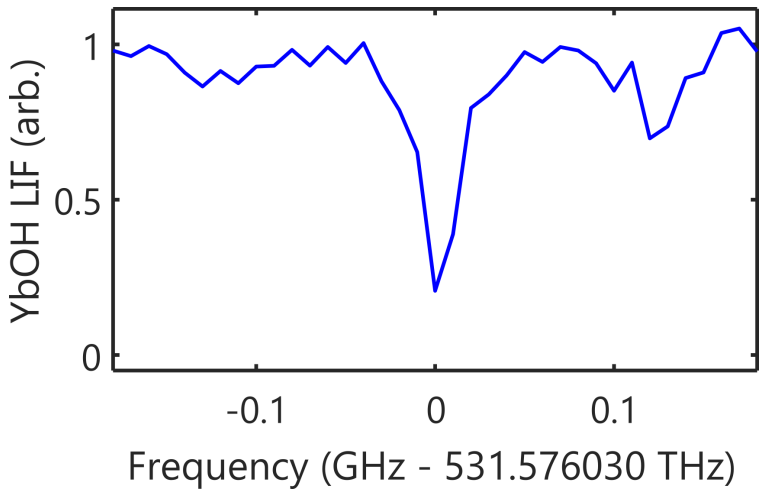

Figure 5.8: Depletion spectroscopy while driving the $[17.73] \leftarrow \tilde{X}\,^2\Sigma^+(000)$ transition on a P-branch line originating from $N'' = 1$. The central depletion fraction is limited by decay of the $[17.73]$ state to $\tilde{X}\,^2\Sigma^+(100)$ which is detectable.

modes up through (400).

We located the $[17.73]$ state using a variety of methods, including driving $[17.73] \leftarrow \tilde{X}\,^2\Sigma^+(000)$ in the depletion region and looking for reduction of the $\tilde{X}\,^2\Sigma^+(000)$ population in the detection region. Results from such a scan are shown in Fig. 5.8. Sideband structure is clearly evident, as well as a central feature that is strongly depleted due to the off-diagonal decays from $[17.73]$. Because we detect both the $\tilde{X}\,^2\Sigma^+(000)$ and (100) states, the depletion is not complete; approximately 75% depletion would be expected, reasonably consistent with our observation of about 80% reduction in YbOH LIF. In addition, we have found the lines required to repump excited vibrational levels through the $[17.73]$ state. The $[17.73]$ has strong coupling to $\tilde{X}\,^2\Sigma^+(000)$ as well as a number of excited Yb-O stretching and Yb-O-H bending modes [153], making it a useful resource for repumping lines that would have been expected to couple very weakly to the $\tilde{A}\,^2\Pi_{1/2}(000, 100)$ levels.

5.2.4 Vibrational branching ratios from pump-repump measurements

With the repumping frequencies established, we can measure the flow of population under different pumping and/or repumping configurations in order to determine the excited state branching

Table 5.2: YbOH pump-repump population measurements for VBR determination. Only the $\tilde{X}\,^2\Sigma^+(000)$ state is detected, and the detected fraction is controlled for natural population and imperfect depletion.

Depletion $[\tilde{X}\,^2\Sigma^+(000) \rightarrow \ldots]$	Repumping $[\tilde{X}\,^2\Sigma^+(100) \rightarrow \ldots]$	Detected fraction
$\tilde{A}\,^2\Pi_{1/2}(000)$	$\tilde{A}\,^2\Pi_{1/2}(000)$	90.0(9)%
$\tilde{A}\,^2\Pi_{1/2}(000)$	$\tilde{A}\,^2\Pi_{1/2}(100)$	17.5(9)%
$\tilde{A}\,^2\Pi_{1/2}(100)$	$\tilde{A}\,^2\Pi_{1/2}(000)$	68.8(6)%
$\tilde{A}\,^2\Pi_{1/2}(100)$	$\tilde{A}\,^2\Pi_{1/2}(100)$	14.7(4)%

ratios. For example, if we pump population out of $\tilde{X}\,^2\Sigma^+(000, 100)$ by driving to $\tilde{A}\,^2\Pi_{1/2}(000)$ and then measure how much population returns by individually repumping either $\tilde{X}\,^2\Sigma^+(200)$ or $\tilde{X}\,^2\Sigma^+(02^00)$, we can infer relative branching ratios to these two levels. We optionally drove $\tilde{X}\,^2\Sigma^+(200)$ or $\tilde{X}\,^2\Sigma^+(02^00)$ in depletion in order to further boost the population in the other state. This is very similar to the method described in Refs. [187, 199] and we used the same Markov chain analysis method.

We first focused on just the $\tilde{X}\,^2\Sigma^+(000, 100)$ and $\tilde{A}\,^2\Pi_{1/2}(000, 100)$ states. Examples of the amount of $\tilde{X}\,^2\Sigma^+(000)$ population detected after depleting on $\tilde{X}\,^2\Sigma^+(000) \rightarrow \tilde{A}\,^2\Pi_{1/2}(v_100)$ and repumping on $\tilde{X}\,^2\Sigma^+(100) \rightarrow \tilde{A}\,^2\Pi_{1/2}(v_1'00)$ are reported in Tab. 5.2. Fitting these data to a Markov chain model [187] yielded the following VBRs: $b_{(000)\rightarrow(000)} = 87(2)\%$, $b_{(000)\rightarrow(100)} = 11(2)\%$, $b_{(100)\rightarrow(000)} = 7(2)\%$, and $b_{(100)\rightarrow(100)} = 65(3)\%$.

We next included lasers to address the $\tilde{X}\,^2\Sigma^+(200, 02^00)$ states in the depletion and/or repumping regions. Using a similar analysis, we found the following VBRs: $b_{(000)\rightarrow(200)} = 0.58(8)\%$ and $b_{(000)\rightarrow(020)} = 0.38(7)\%$. These values should be compared with the branching ratios measured in the YbOH DLIF experiments (Sec. 4.2), which gave VBRs of $b_{(000)\rightarrow(200)} = 0.914(62)\%$ and $b_{(000)\rightarrow(020)} = 0.335(20)\%$. Both methods agree that the branching to $\tilde{X}\,^2\Sigma^+(200)$ is around $2-3\times$ stronger than the branching to $\tilde{X}\,^2\Sigma^+(02^00)$. This ratio is significantly different than the result of Ref. [153], which reports the branching ratios as nearly identical. The fact that we have used two completely different methods that both indicate the decay of $\tilde{A}\,^2\Pi_{1/2}(000)$ to $\tilde{X}\,^2\Sigma^+(200)$ is

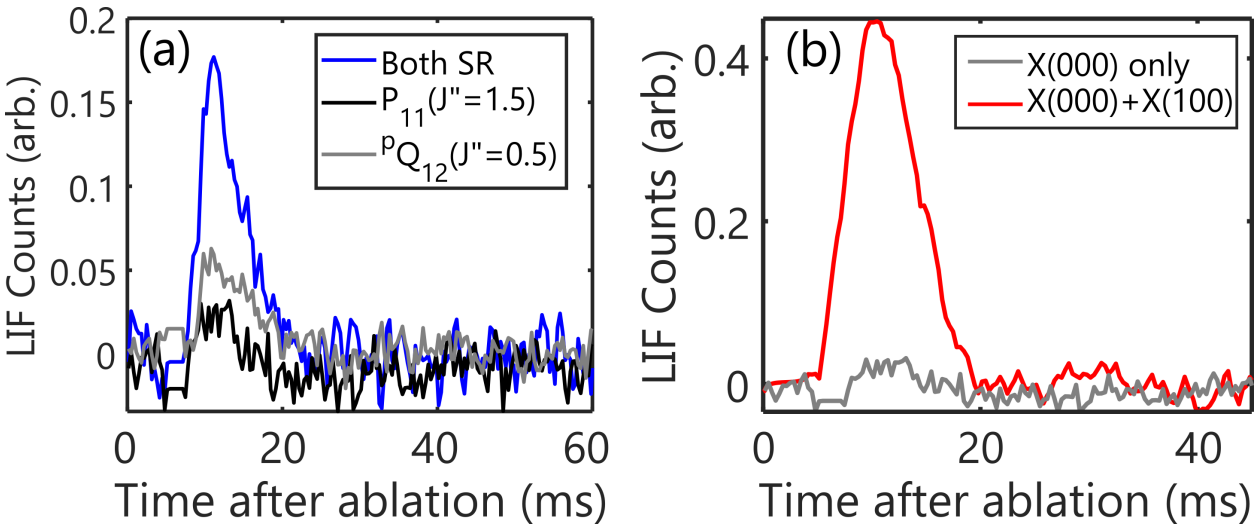

Figure 5.9: Demonstration of optical cycling via LIF enhancement. (a) Optical cycling due to closing the spin-rotation structure in the $\tilde{X}\,^2\Sigma^+(000)$ state. (b) Optical cycling due to closing spin-rotation structure and adding a repumping laser to the $\tilde{X}\,^2\Sigma^+(100)$ level.

stronger than that to $\tilde{X}\,^2\Sigma^+(02^00)$ should give confidence in this claim. The pump-repump data is more likely to suffer from systematic errors, e.g. not correctly accounting for natural populations in the various states, so for quantitative purposes the DLIF data of Tabs. 4.1 and 4.2 should be trusted more.

5.3 YbOH optical cycling

We plan to use the $\tilde{A} \leftarrow \tilde{X}$ electronic transition for optical cycling. As described in Sec. 2.6, we address molecules in the $\tilde{X}(N'' = 1)$ state and drive a P-branch transition. Angular momentum and parity selection rules prevent population excited to the $J' = 1/2, p = +$ state from decaying to any level except for $N'' = 1$ [108]. While spin-rotation substructure within the $N'' = 1$ manifold is well resolved (typical splittings $\sim 100 - 200$ MHz for YbOH), hyperfine structure is smaller than the transition's natural linewidth [172].

Optical cycling is demonstrated in Fig. 5.9. In Fig. 5.9(a) we show the effect of "closing" the spin-rotation structure. In the gray trace, only the ${}^pQ_{12}(J'' = 0.5)$ line is addressed. On aver-

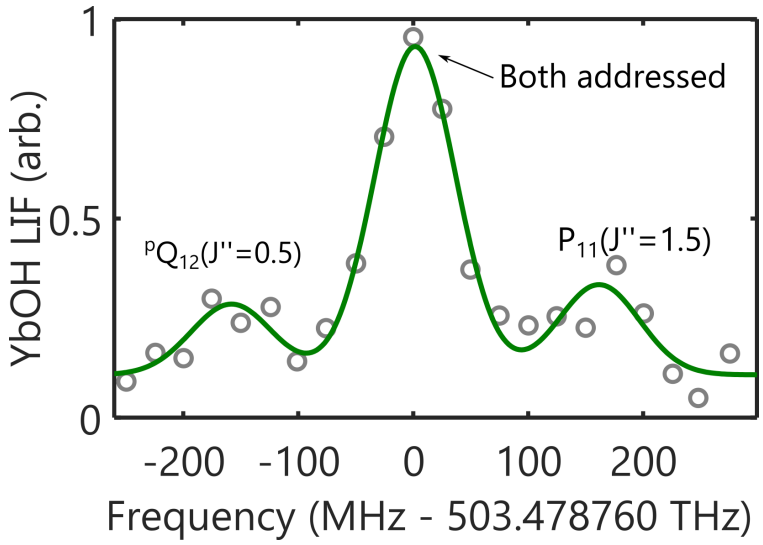

Figure 5.10: LIF spectrum showing photon cycling with the $\tilde{X}\,^2\Sigma^+(100)$ repumper. The observed spectrum consists of three peaks due to scanning two laser frequencies split by 165 MHz over the spin-rotation components of the $N'' = 1$ state. The central peak is larger than the sum of the two individual spin-rotation features, demonstrating photon cycling.

age, molecules in this condition scatter about 2 photons before decaying to the dark $J'' = 1.5$ spin-rotation component. Adding a second laser frequency (generated by an AOM) to excite the $P_1(J'' = 1.5)$ transition simultaneously with the ${}^pQ_{12}(J'' = 0.5)$ line, we see a factor of four increase in detected fluorescence (blue trace). Note that when both sidebands are applied, the signal is larger than the sum of signals recorded while driving individual sidebands. The increase in fluorescence implies that molecules scattered 8 photons on average. The theoretically expected number of photons comes from the probability for a molecule excited to $\tilde{A}\,^2\Pi_{1/2}(000)$ *not* to return to the $\tilde{X}\,^2\Sigma^+(000)$ level, which from the measurements in Sec. 4.2 is $\bar{n} \approx 1/0.11 \approx 9$, consistent with our observations.

In Fig. 5.9(b) we show the fluorescence enhancement caused by a vibrational repumping laser driving $\tilde{A}\,^2\Pi_{1/2}(000) \leftarrow \tilde{X}\,^2\Sigma^+(100)$. In gray we plot the fluorescence detected when just a single spin-rotation component of $\tilde{X}\,^2\Sigma^+(000)$ is driven and in red we plot the fluorescence when both spin-rotation components of $\tilde{X}\,^2\Sigma^+(000)$ and $\tilde{X}\,^2\Sigma^+(100)$ are addressed. The fluorescence is increased by a factor of about 20, indicating that approximately 40 photons are scattered on av-

erage per molecule in the detection region. Theoretically, we would have expected to observed $\bar{n} \approx 1/(1 - q_{(000)\to(000)} - q_{(000)\to(100)}) \approx 68$ photons. The number of photons detected was likely limited by the laser-molecule interaction time, which was only about 100 μs for the data presented. Figure 5.10 shows the LIF measured as the $\tilde{A}\,^2\Pi_{1/2}(000) \leftarrow \tilde{X}\,^2\Sigma^+(100)$ repumping laser (with AOM sidebands applied) is scanned over resonance. We see two spin-rotation features when a single AOM sideband addresses a single transition. The central feature occurs when all spin-rotation components are driven simultaneously. The fact that the central feature is larger than the sum of the individually addressed lines is once again a clear demonstration of photon cycling.

The struggle itself toward the heights is enough to fill one's heart. One must imagine Sisyphus happy.

Albert Camus, in "The Myth of Sisyphus"

6

Laser Cooling of YbOH Molecules

Having demonstrated efficient photon cycling, we aimed to laser cool YbOH molecules.[1] Our goal was to perform both Doppler and Sisyphus laser cooling of the transverse motion of YbOH molecules in a molecular beam. These experiments serve several important purposes. First, they are an excellent test of optical cycling and demonstrate that a closed cycle has been established without unanticipated loss channels. Interaction time limitations make it difficult to directly detect scattering of $\sim$100s of photons, but laser cooling can be used to confirm this number of photons has been scattered. Second, they allow us to gauge the achievable cooling rates and estimate quantities

[1] Some of the results described in this chapter were published in Ref. [213].

such as capture velocity and scattering rate expected in a three-dimensional cooling scheme. Third, transverse cooling can be used in later experiments to enhance on-axis molecular beam flux. In a trapping experiment, transverse cooling would boost the number of capturable molecules, while in a beam-based experiment the cooling would increase both the molecule number and the feasible coherence time.

At the time this work was conducted, direct laser cooling had been demonstrated for a number of diatomic molecules, namely alkaline-earth monofluorides (SrF [78, 109–113, 214, 215], CaF [114, 115, 117, 119, 120, 216], YbF [217]) and an oxide (YO [116, 181, 218]). Only a single polyatomic molecules had been directly laser cooled (SrOH [126, 219]). YbOH has a much more complex molecular structure, so it was unclear to what extent its laser cooling would behave similarly to that of simpler species.

In this chapter, we report on the direct laser cooling of YbOH molecules under both Doppler and Sisyphus cooling conditions. Sisyphus cooling is found to be more efficient and reduces the temperature of a YbOH beam from 20 mK to below 0.5 mK in one dimension. We begin with a brief overview of the laser cooling theory (Sec. 6.1). Next, in Sec. 6.2, we provide some technical details related to the molecular beam source and apparatus used for these laser cooling experiments. We then describe our Doppler and Sisyphus cooling of YbOH molecular beams (Sec. 6.3) and also discuss numerical simulations of the YbOH laser cooling process using the optical Bloch equations (OBEs).[2]

6.1 Laser cooling theory

The physical mechanisms responsible for Doppler and Sisyphus cooling are well understood from many decades of research with atoms [100]. More recently, the Tarbutt group has conducted im-

[2]Cal Miller deserves credit as the major contributor to these OBE simulations.

pressive theoretical studies to understand laser cooling processes for multilevel molecules [185, 220]. Here, we provide a short overview of the Doppler and Sisyphus cooling, relying on simple models.

6.1.1 Doppler cooling theory

The force on a stationary molecule due to repeated absorption and spontaneous emission of photons is given by

$$F_{\text{sp}} = \hbar k \Gamma \rho_{ee}, \tag{6.1}$$

where $k = 2\pi/\lambda$ is the photon wavenumber (for wavelength λ), $\Gamma = 1/\tau_{\text{sp}}$ is the spontaneous decay rate (τ_{sp} is the excited state's radiative lifetime), and ρ_{ee} is the excited state population. Here, F_{sp} has a neat interpretation as the product of momentum change ($\hbar k$) times the photon scattering rate $R_{\text{sc}} \equiv \Gamma \rho_{ee}$. The scattering rate is clearly of central importance. For a multilevel molecule with n_e excited state and n_g ground states, we can write [113]

$$R_{\text{sc}} = \frac{\Gamma_{\text{eff}}}{2} \frac{s_{\text{eff}}}{1 + s_{\text{eff}} + (2\Delta/\Gamma)^2}, \tag{6.2}$$

where

$$\Gamma_{\text{eff}} = \frac{2n_e}{n_g + n_e}\Gamma, \tag{6.3}$$

$$I_{\text{sat,eff}} = \frac{2n_g^2}{n_g + n_e} I_{\text{sat}}, \tag{6.4}$$

and

$$s_{\text{eff}} = I_{\text{tot}}/I_{\text{sat,eff}}. \tag{6.5}$$

For a two-level atom $n_g = n_e = 1$ and we retain the standard two-level definitions that can be found in, e.g., Ref. [100]. These "effective" parameters tell us that, due to the large number of states involved, molecular laser cooling requires higher laser powers and results in weaker optical forces as compared to atoms. For example, the YbOH $\tilde{A}\,^2\Pi_{1/2}(000) \leftarrow \tilde{X}\,^2\Sigma^+(000)$ cycling transition (driven from $N'' = 1$ to $J' = 1/2$) involves $n_g = 12$ and $n_e = 4$, so that $I_{\text{sat,eff}} = 18 I_{\text{sat}} \approx 100$ mW/cm^2. At the same time, the maximum scattering rate is reduced to $R_{\text{sc}}^{(max)} = \Gamma/4$, half the value achievable in a two-level system.[3]

If we consider a molecule moving with velocity $\vec{v}$, both R_{sc} and F_{sp} acquire velocity dependence through the Doppler shift [100]

$$F_{\text{sp}} = \hbar k \frac{\Gamma_{\text{eff}}}{2} \frac{s_{\text{eff}}}{1 + s_{\text{eff}} + 4(\Delta - \vec{k}\cdot\vec{v})^2/\Gamma^2}, \tag{6.6}$$

where Δ is the laser detuning from resonance.

Doppler forces arise from the fact that a laser detuned below resonance ($\Delta < 0$) will provide a stronger force for molecules moving opposite the direction of $\vec{k}$ as compared to molecules moving in the same direction as $\vec{k}$. Doppler cooling makes use of this fact to produce a force cooling toward $v = 0$. When exposed to counterpropagating to laser beams detuned below resonance, molecules tend to scatter more photons from the laser beam opposing their motion. The molecular velocity is thereby damped toward zero. Exact expressions for the Doppler cooling force can be found in Ref. [100], but the salient feature is that in the limit $s_0 \ll 1$, the force has the form

$$F_D \approx 4\hbar k^2 s_0 \frac{2\Delta/\Gamma}{\left(1 + (2\delta/\Gamma)^2\right)^2} v. \tag{6.7}$$

This force damps toward $v = 0$ when $\Delta < 0$: cooling occurs at red detuning, while heating occurs

[3] When the $\tilde{X}\,^2\Sigma^+(100)$ level is also repumped through $\tilde{A}\,^2\Pi_{1/2}(000)$, these values will become even less favorable.

at blue detunings. The force is only significant over a finite range of velocities and the "capture velocity" is $v_c \sim \Gamma/k$. For YbOH, this works out to $v_c \approx 4$ m/s.

While the force 6.7 suggests the ability to cool to $v = 0$, in reality fluctuations in the photon absorption and emission lead to a finite temperature known as the Doppler cooling limit [100]. At low intensity and at $\Delta = -\Gamma/2$, $T_D = \hbar\Gamma/2k_B$. At high laser intensity this temperature grows $\propto \sqrt{s_{\text{eff}}}$, and the limiting temperature also increases as Δ varies away from $-\Gamma/2$. For YbOH, $T_D \approx 200\ \mu$K.

6.1.2 Sisyphus cooling theory

It is possible to cool below the Doppler limit using well-known "Sisyphus" techniques [100]. The cooling phenomena we have observed are well described as a magnetically-assisted Sisyphus effect, which has been described previously in, e.g., Refs. [148, 185, 220, 221]. The same basic physics occurs in any level structure with dark sublevels that is driven by an intense standing wave and exposed to a remixing magnetic field [175, 221–223]. Consider an $F'' = 1 \rightarrow F' = 0$ transition driven by an intense, linearly polarized laser beam with wavelength λ (see Fig. 6.1). In this case, the $F'' = 1, M_F'' = \pm 1$ states do not couple directly to the laser light and experience no AC Stark shifts. The $F'' = 1, M_F'' = 0$ state does interact with the laser light and at blue (red) detuning, the $F'' = 1, M_F'' = 0$ state experience a positive (negative) AC Stark shift due to coupling with the $F' = 0, M_F' = 0$ state. When the laser light forms a standing wave, the AC Stark shifts have a spatial period of $\lambda/2$.

To see how cooling arises, focus on the blue-detuned case illustrated in Fig. 6.1. A molecule initially in the $F'' = 1, M_F'' = 0$ state rides up a potential hill and loses kinetic energy until it is optically pumped to a dark $F'' = 1, M_F'' = \pm 1$ state. The optical pumping is most likely to occur near an antinode, so ideally an energy nearly equal to the maximum AC Stark shift can be

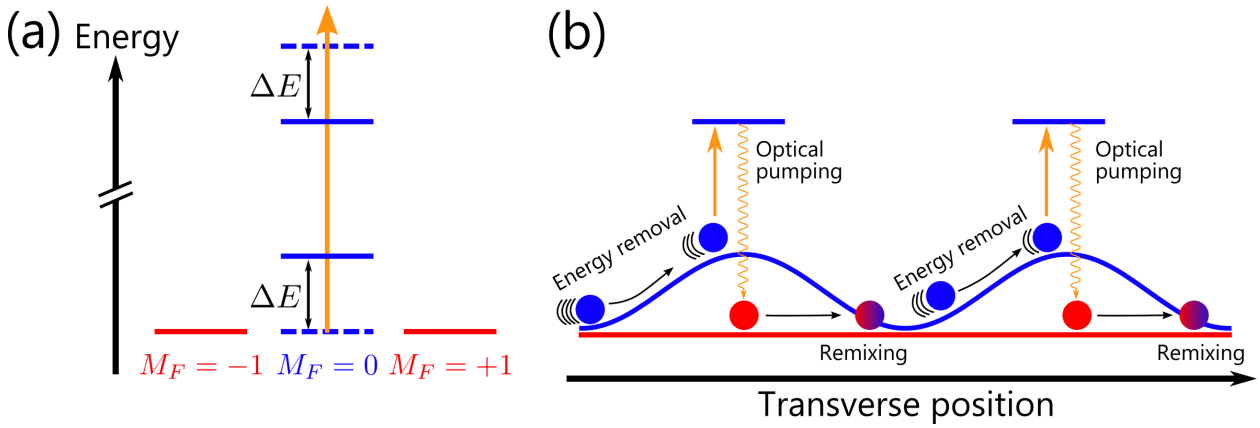

Figure 6.1: Illustration of Sisyphus cooling mechanism for an $F'' = 1 \rightarrow F' = 0$ transition. (a) Energy level diagram in the presence of a blue-detuned laser beam. Dashed lines indicate field-free levels while solid lines indicate levels in the presence of an intense standing wave. (b) Overview of cooling mechanism. As explained in the main text, molecules ride up the AC-Stark-shifted potential before being optically pumped to a dark state and remixed into a bright state, repeating the process. For red-detuned light, the bright state's AC Stark shift is negative and molecules continually ride *down* potential slopes, gaining energy. Figure modeled after Refs. [148, 175].

removed. Once pumped into a dark state, the molecule is uncoupled from the laser light. If a $\mathcal{B}$-field is applied at some angle to the laser polarization, molecules in the $F'' = 1, M_F'' = \pm 1$ states are remixed back into $F'' = 1, M_F'' = 0$ due to Larmor precession at rate $\omega_{\mathcal{B}}$. The magnitude of $\mathcal{B}$ must be chosen carefully. If it is too small, the remixing will be slow and limit how many pumping cycles the molecule experiences inside the standing wave. If $\mathcal{B}$ is too large, the precession will be too rapid and the molecules will vary between bright at dark states at random positions throughout the standing wave, removing less than the maximum possible energy on each cycle. Under ideal conditions, the optical scattering rate is $R_{\text{op}} \sim 4v_\perp/\lambda$ and $\omega_{\mathcal{B}} \sim R_{\text{op}}$, where R_{op} is the optical pumping rate and $v_\perp$ is the molecular velocity along the standing wave [175]. Because the energy removal at each step is set by the energy shifts caused by the standing wave, the effective friction force which can be much larger than Doppler cooling forces.

The level structure of YbOH is not as simple as the $F'' = 1 \rightarrow F' = 0$ case considered above. We drive a ground state with $N'' = 1$ to an excited state with $J' = 1/2$. As shown in Fig. 2.5, the ground state contains $F'' = 0, 1, 1, 2$ levels while the excited state contains $F' = 0, 1$ levels. Among

the many possible transitions are a number with dark states, and a simple modification of the above arguments shows that the same qualitative force should arise in these case. A full treatment of the motion of multilevel molecules through intense standing waves can be found in Refs. [185, 220].

6.2 Laser cooling apparatus

Figure 6.2 shows a schematic diagram of the experimental apparatus and Fig. 6.3 shows photographs of the setup. YbOH molecules are produced in a cryogenic buffer-gas beam (CBGB) [89, 90]. Unlike the beams described in Ch. 3, this cell is not optimized for low forward velocity, but instead for large and reliable molecule yield. In this configuration, a cryogenic cell is held at ~ 2 K and filled with ^{4}He buffer-gas. Hot methanol gas (~ 250 K) is flowed into the cell through a thermally isolated capillary. Laser ablation of Yb metal, followed by a chemical reaction between the Yb atoms and methanol, produces YbOH molecules that are cooled by the He buffer gas. YbOH molecules entrained in the He buffer gas are then extracted into a beam. A typical He flow of 3 sccm is used and the molecules are extracted from the cell through a 16 mm $\times$ 2.4 mm slit (vertical $\times$ horizontal). A typical YbOH CBGB contains $\sim 10^9$ YbOH molecules in the $N'' = 1$ rotational level, as measured via absorption spectroscopy. The mean forward velocity is $v_f \sim 90$ m/s and the transverse velocity spread is $v_\perp \sim 15$ m/s. A 2.7 mm $\times$ 3 mm aperture placed 20 cm downstream from the cell collimates the molecular beam to an effective transverse temperature of $T_\perp \sim 20$ mK.

Just after the aperture, the molecules enter a cooling region of variable length up to $\ell_{\text{int}} \sim 50$ mm (interaction time $t_{\text{int}} \sim 500\,\mu$s). The cooling region contains light at four different wavelengths (see Fig. 6.2, bottom panel). The main photon cycling transition is $\tilde{A}\,^2\Pi(000) \leftarrow \tilde{X}\,^2\Sigma^+(000)$ (577 nm) [129, 173]. Significant optical pumping into higher lying vibrational states occurs. Dominant decays are to the $\tilde{X}\,^2\Sigma^+(100), (200)$, and (02^00) levels, and vibrational repumping is required to return this population to the main cooling cycle. Thus, the cooling region also includes light

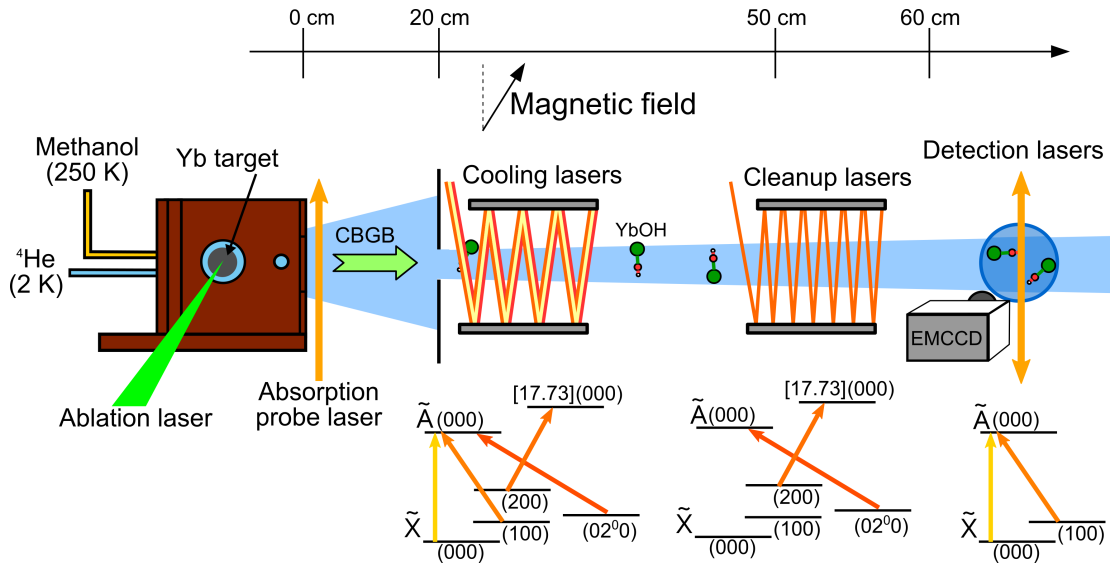

Figure 6.2: Schematic of the experimental apparatus (not to scale). A cryogenic beam of YbOH is produced by ablating a Yb metal target into methanol followed by buffer-gas cooling with ∼2 K He. The beam is extracted toward a cooling region. A magnetic field is applied at an angle to the laser polarization in order to remix dark states and aid in the Sisyphus cooling. Vibrational repumping in a clean-up region enhances the LIF detection downstream. Level diagrams below the beamline show the transitions driven in each region.

to drive $\tilde{A}\,^2\Pi(000) \leftarrow \tilde{X}\,^2\Sigma^+(100)$ (595 nm, "first repump"), $\tilde{A}\,^2\Pi(000) \leftarrow \tilde{X}\,^2\Sigma^+(02^00)$ (599 nm, "second repump"), and $[17.73](000) \leftarrow \tilde{X}\,^2\Sigma^+(200)$ (600 nm, "third repump"). The main cooling light at 577 nm is generated by the second harmonic of a Raman fiber amplifier, while all repumping and imaging wavelengths are generated by cw dye lasers. Up to 150 mW of main cooling light, 100 mW of (100) repumping light, and 50 mW of (200) and (02^00) repumping light are incident on the molecules from each direction.

To produce the cooling force, the main and first repump laser beams propagate perpendicular to the molecular beam making 12 round-trip passes between mirrors to create a standing wave. Each beam has diameter ∼4 mm. In the case of Doppler cooling (as opposed to the Sisyphus configuration) the standing wave is purposely destroyed by misaligning the retro-reflected beams. The second and third repump laser beams, of diameter 6 mm, enter the cooling region through separate fibers, cover the cooling region, and do not form standing waves. A variable magnetic field is present in the cooling region to provide the remixing between dark and bright states necessary

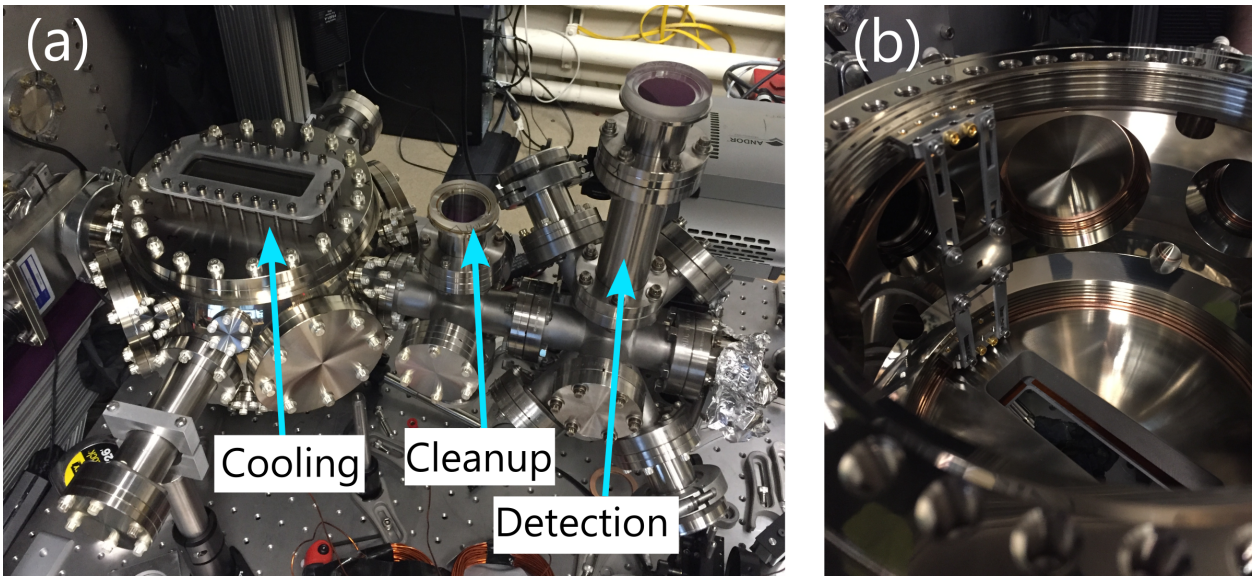

Figure 6.3: Photograph of UHV chamber used for laser cooling experiments. (a) Beam line. Molecules propagate from left to right. The cooling region includes custom-machined flanges for long interaction times during transverse laser cooling. (b) Interior of the cooling region showing the collimating aperture used to set the transverse temperature of the molecular beam to approximately 20 mK.

for the magnetically-assisted Sisyphus effect [184, 221]. The field is oriented at 45 degrees to the cooling light's polarization axis to ensure near-optimal remixing. The magnetic field is typically ~ 1.5 Gauss, as this leads to a Larmor precession time roughly matching the molecular transit time between a node and antinode of the standing wave [217]. For both Doppler and Sisyphus cooling, the light from each laser is split into two frequency components separated by the spin-rotation (SR) splitting of the $N'' = 1$ state; these address the $P_1(N'' = 1)$ and ${}^pQ_{12}(N'' = 1)$ lines [22] (see Fig. 2.5).

The SR structure in the $\tilde{X}\,{}^2\Sigma^+$ state, which arises from interaction with $\Omega = 1/2$ excited electronic states [131], is unusual because the splitting scales quickly with vibrational level (see Tab. 5.1). The same effect has been observed in YbF and is attributed to competing contributions from the $\tilde{A}\,{}^2\Pi_{1/2}$ vibrational states and vibrational levels of $\Omega = 1/2$ excited electronic states arising from an $Yb^+(f^{13})$ configuration [172, 196–198, 211]. To address both SR components, we pass each laser beam through an acousto-optic modulator (AOM) which adds a frequency sideband at the appro-

priate rf interval. The proton hyperfine splittings in ^{174}YbOH are unresolved in optical excitation (< 3 MHz) due to the large distance between the hydrogen nucleus and the predominantly metal-centered valence electron [172].

After the cooling region, the molecules travel 40 cm in free flight and then encounter clean-up and imaging regions. In the "clean-up" region, only the (200) and (02^00) repumping light is present in order to return any population in excited vibrational states back to the lowest vibrational levels in preparation for imaging via laser-induced fluorescence (LIF). In the imaging region, the molecular beam is imaged with an EMCCD by driving the $\tilde{A}(000) \leftarrow \tilde{X}(000)$ and $\tilde{A}(000) \leftarrow \tilde{X}(100)$ transitions and collecting LIF at 577 nm. The imaging light contains 10 mW of main line and 40 mW of (100) repumping light. The detection light is always resonant and retroreflected in order to avoid systematic effects due to Doppler shifts in the imaging light. The imaging system is calibrated to ensure that the magnification and collection efficiency are roughly uniform over the entire field of view of 22 mm.

6.3 Laser cooling results

6.3.1 Sisyphus cooling results

Molecular beam images recorded by the EMCCD are shown in Fig. 6.4. In these images, the molecules propagate from left to right while the detection lasers propagate in the vertical direction. Therefore, the vertical extent of the signal is indicative of the transverse velocities in the molecular beam while the horizontal extent of the signal simply reflects the width of imaging laser beams used. Figure 6.4(a) shows a molecular beam that was exposed to resonant light (neither heating nor cooling) in the "cooling" region. When the light in the "cooling" region is detuned below resonance ($\Delta = -1.8\Gamma$), the molecules accumulate in two lobes at positions displaced from the center

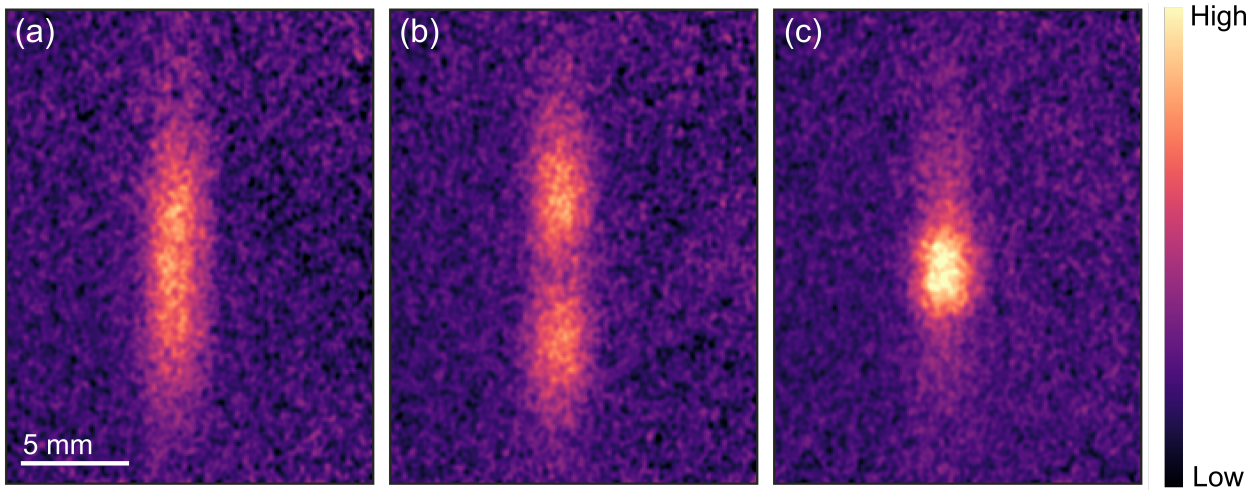

Figure 6.4: Images of the YbOH molecular beam under Sisyphus conditions at various detunings. The images represent the average over 20 experimental cycles and are plotted on the same color scale. The molecular beam travels from left to right while the detection laser beams are in the vertical direction. (a) On-resonance light ($\Delta = 0$) in the cooling region. (b) Red-detuned light at $\Delta = -1.8\Gamma$, heating the molecules away from low velocities. (c) Blue-detuned light at $\Delta = +1.8\Gamma$, leading to substantial cooling and enhancing the on-axis density relative to the on-resonance case.

of the unperturbed beam [see Fig. 6.4(b)]. This is a signature of heating because the molecules acquire, on average, a larger transverse velocity. By contrast, when the cooling light is detuned above resonance ($\Delta = +1.8\Gamma$), we observe a large enhancement of molecules concentrated near the center of the unperturbed beam [see Fig. 6.4(c)]. This indicates cooling, as the transverse velocities of molecules were reduced and the beam expanded less while propagating from the cooling to the detection region.

We note that Sisyphus heating concentrates population at specific non-zero velocities. This is because Sisyphus heating is operative at red detuning, but only over a small range of velocities. The Doppler forces become dominant beyond the capture velocity of the Sisyphus force, and population accumulates at the velocity for which these forces balance. This allows us to estimate a value for the capture velocity of the Sisyphus effect of approximately 1 m/s at $I/I_{\mathrm{sat}} \sim 65$. As discussed below, this is in good agreement with our theoretical model.

Integrating across the central region of the EMCCD images results in Fig. 6.5(a). At the highest intensities ($I/I_{\mathrm{sat}} \sim 70$) and $\Delta = 0$, roughly 40% of the molecules remain for detection. Using the

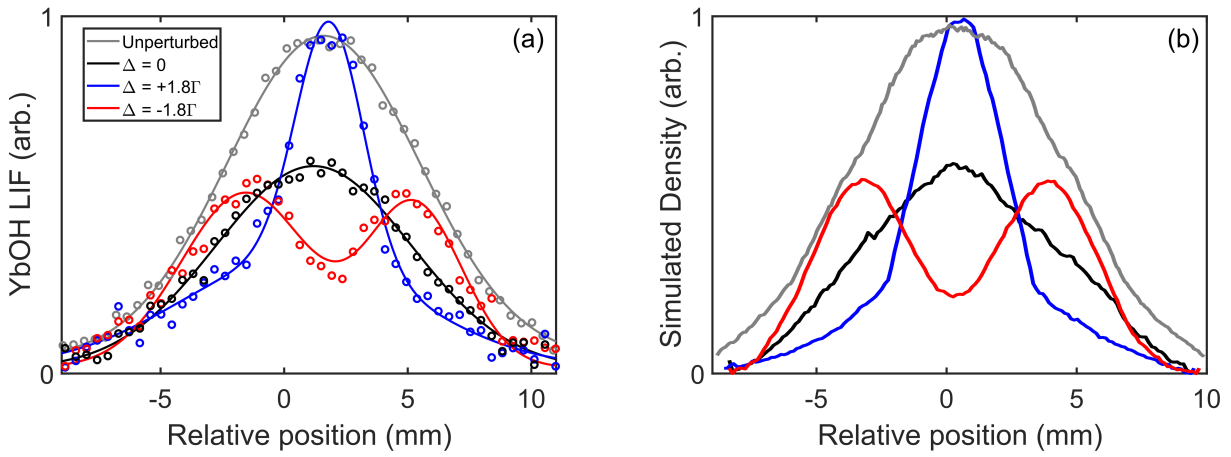

Figure 6.5: (a) Integrated images under Sisyphus cooling conditions. We integrate over the central portion of each EMCCD image and plot the resulting density distribution in the direction of the cooling light. The relatively flat top of the cooled beam is indicative of cooling to the collimating aperture's width. Lines represent Gaussian fits as described in the text. (b) Simulated spatial distribution in the imaging region for the same experimental parameters.

measured branching ratios (Ch. 4), our cycling scheme is closed to about 99.82(7)%. Combining this with the observed loss, we determine that the molecules scatter an average of 500^{+100}_{-50} photons in the cooling region. The scattering rate is measured independently to be $\Gamma_{sc} \approx 1.5 \times 10^6$ s^{-1}. The combination of this scattering rate and the molecule-laser interaction time is consistent with the estimated number of photons scattered as determined by loss to dark states. By varying the laser detuning, we can map out the molecular density distributions as the Sisyphus effect changes from heating to cooling. The integrated beam traces for such a scan are shown in Fig. 6.6 and the extracted widths are compared against Doppler cooling data (described below) in Fig. 6.9.

In order to interpret the integrated images we fit the transverse beam profiles to a set of Gaussians. The resonance condition molecular beam profile [Fig 6.5(a)] is first fit to a single Gaussian. In all experimental conditions it is found that the width of the beam is unchanged if light is present in the cooling region but tuned to resonance; only the overall amplitude of the beam signal changes in this case. Next, the cooled beam profile [Fig. 6.5(b)] is fit to the sum of two Gaussians: one whose width is constrained to match the uncooled signal and another whose width is allowed to vary. In this way we capture the fact that not all molecules in the experiment are below the transverse cap-

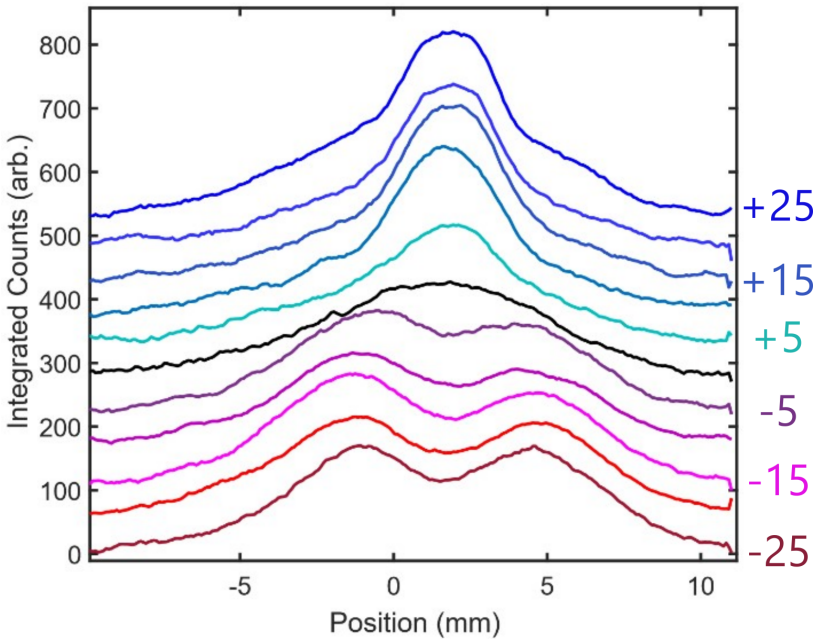

Figure 6.6: Transverse density of molecular beams under Sisyphus cooling/heating conditions. Traces are shown collected with "cooling" region detuning ranging from -25 to $+25$ MHz in 5 MHz steps (as labeled on righthand side). Signal baselines are offset for clarity. The emergence of cooled and heated features is clearly evident.

ture velocity of the Sisyphus force. The relative areas under the "cooled" and "uncooled" portions give a measure of the fraction of molecules within the Sisyphus capture range. In our data the cooled portion of the beam typically contains up to 60% of the molecules. This is consistent with the capture velocity estimated above and the expected transverse velocity distribution produced by the collimating aperture. At maximum intensity, the Sisyphus cooling configuration reduces the FWHM of the cooled molecular beam from $8.5(5)$ mm to $3.0(4)$ mm.

In the Sisyphus configuration, we expect the transverse temperature to decrease as the standing wave intensity is increased, as shown in Fig. $6.7(a)$. The data shows a clear saturation of the minimum beam width at a size set by the collimating aperture, i.e. the molecules expand negligibly during the 40 cm of free flight following this aperture. In order to fit the images to a transverse temperature, we follow Ref. [126] in comparing the beam width after the cooling region to a Monte Carlo model of ballistic expansion. This yields a minimum temperature of 500^{+100}_{-450} μK. The temper-

ature has large and asymmetric error bars because the cooled beam is close to the size of the 3 mm collimating aperture, so fitting the cooled cloud size yields very limited temperature resolution. At this temperature, the uncertainty of the fit is comparable to the central value, such that we can only place an upper limit on the temperature. We therefore interpret the extracted temperature as a bound, $T_\perp < 600\ \mu$K. Because there is no fundamental temperature limit to the Sisyphus cooling near this scale, the actual temperature is likely much lower; this is discussed in more detail below, where we present the results of calculations using the optical Bloch equations.

Figure 6.7(b) shows the fraction of the molecular beam that has been cooled. The value increases with intensity to approximately 60% at $I/I_{\text{sat}} \sim 65$, and is not yet saturated at the intensities explored in this work. Given the spread of velocities in the unperturbed molecular beam, this value of the cooled fraction is consistent with the estimated capture velocity of $\sim$1 m/s. From this cooled fraction, we estimate that around 5×10^4 molecules are in the ultracold part of the distribution. Accounting for the loss to dark states and reduction in transverse temperature, this corresponds to an increase in phase-space density[4] (PSD) in one dimension of a factor of 6.

Based on the physical mechanism underlying the magnetically-assisted Sisyphus effect, we expect the cooling efficiency to show a dependence on the externally applied magnetic field. This effect is shown in Fig. 6.8, where we plot the measured molecular beam width as a function of current through the remixing coils. For the coils used to generate these magnetic fields, weak minima in the beam width appear around $\mathcal{B} = 3$ G. In general, the cooling appears to be relatively efficient for any value of $\mathcal{B} \lesssim 5$ G. This is roughly consistent with the sizes of fields that were found to enable Sisyphus cooling of YbF molecules [217]. We can estimate the expected optimal $\mathcal{B}_c$ field by arguing that the remixing rate should be roughly matched to the rate at which molecules

[4]Here, the phase-space density is given by $n\lambda_{dB,x}\lambda_{dB,y}\lambda_{dB,z}$ where n is the number density and $\lambda_{dB,i} = h/\sqrt{2\pi m k_B T_i}$ is the de Broglie wavelength for molecules with mass m and temperature T. Because the cooling is only in one dimension, PSD scales with the square root of the temperature rather than as $T^{3/2}$.

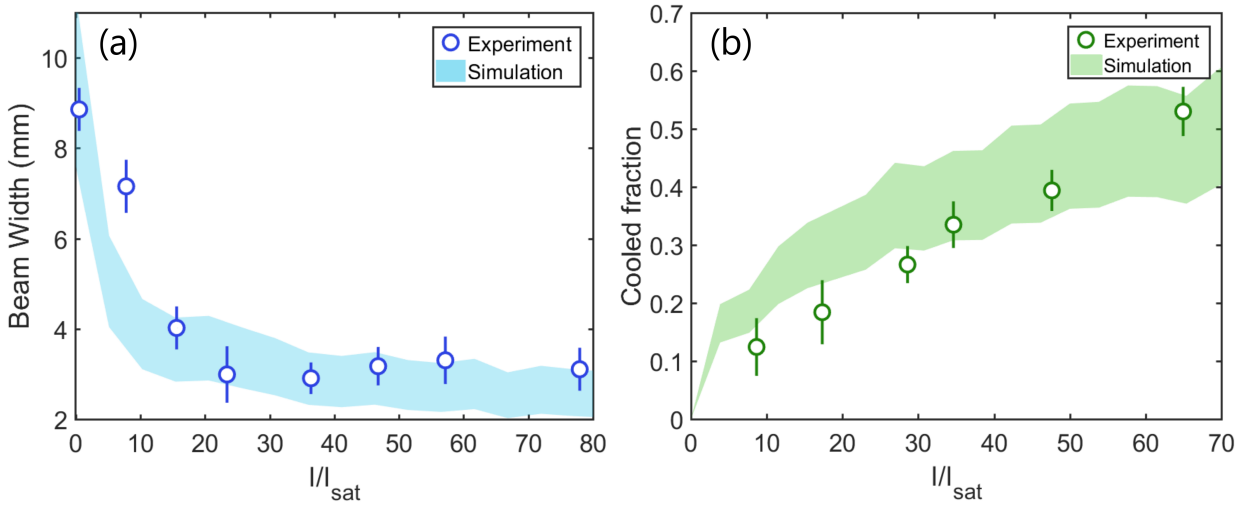

Figure 6.7: (a) Dependence of the molecular beam width on Sisyphus cooling light intensity, at detuning $\Delta = +1.5\Gamma$. The beam width initially decreases as the cooling intensity is increased, before saturating to a width set by the collimating aperture. Temperature resolution is limited to ∼600 μK in direct fits of the width. (b) Fraction of the beam within the "cold" portion of the beam, as determined by our two-Gaussian fit. Data taken at $\Delta = +1.5\Gamma$. Error bars on experimental points come from the spread in repeated measurements. Shaded regions represent the spread in simulation outputs when the simulated laser beam overlap in the cooling region is varied, as described in the main text.

move between standing-wave nodes/antinodes: $\bar{g}\mu_B\mathcal{B}_c \approx \bar{v}/(\lambda/2)$, where $\bar{v}$ is a typical speed of a cooled molecule and $\bar{g}$ is the average g-factor in the ground-sate manifold. Taking $\bar{v} \sim v_c$ we find $\mathcal{B}_c \approx 1.5$ G, close to the range over which we observe cooling to be efficient.

6.3.2 Doppler cooling results

By misaligning the retro-reflected laser beams by ~ 2 beam waists to remove the standing wave condition in the cooling region, we are also able to study pure Doppler cooling of the molecular beam. The fitted beam widths as a function of laser detuning are shown in Fig. 6.9, which are collected at the same magnetic field ($B \sim 1.5$ G) and with the same number of photons scattered (~ 500) as for Sisyphus cooling. In contrast to Sisyphus cooling, the Doppler scan shows cooling at red detuning and heating at blue detuning. The Doppler cooling and heating are efficient over a large range of frequencies due to the power broadening at the high intensities used in this study.

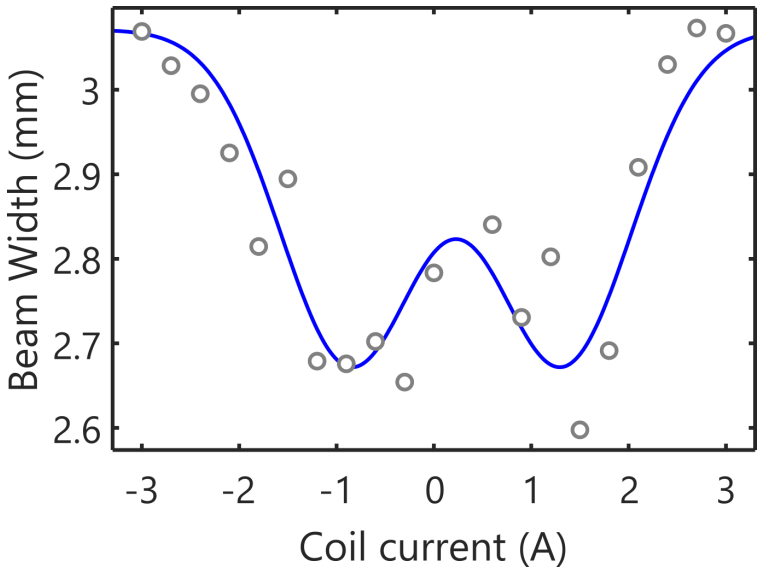

Figure 6.8: Magnetic field dependence of the Sisyphus cooling. Beam (half-)width is plotted against the magnetic field applied in the cooling region. Coils were measured to produce approximately 2.7 G/A.

The overall magnitude of the cooling and heating forces are significantly smaller in the Doppler configuration than in the Sisyphus configuration.

6.3.3 Comparison to theory

We have constructed a detailed model of the laser cooling forces based on Refs. [185, 220, 221]. Because the spin-rotation splitting is large compared to the detunings in the experiment, we model the force on a molecule as the average of the forces on isolated $J' = 1/2 \leftrightarrow J'' = 3/2$ and $J' = 1/2 \leftrightarrow J'' = 1/2$ subsystems ($\vec{J} = \vec{N} + \vec{S}$), weighted by the number of states. We account for the presence of excited vibrational levels in the $\tilde{X}$ manifold, following Ref. [113], by scaling the saturation intensity to account for the multi-level systems. For each subsystem we solve generalized optical Bloch equations to compute the time evolution of the density matrix as the molecule is dragged at constant velocity through a standing wave. Once the density matrix has reached a periodic steady state, we compute the average force and scattering rate as a function of velocity. We repeat this simulation at a range of magnetic fields, detunings, intensities, and polarizations.

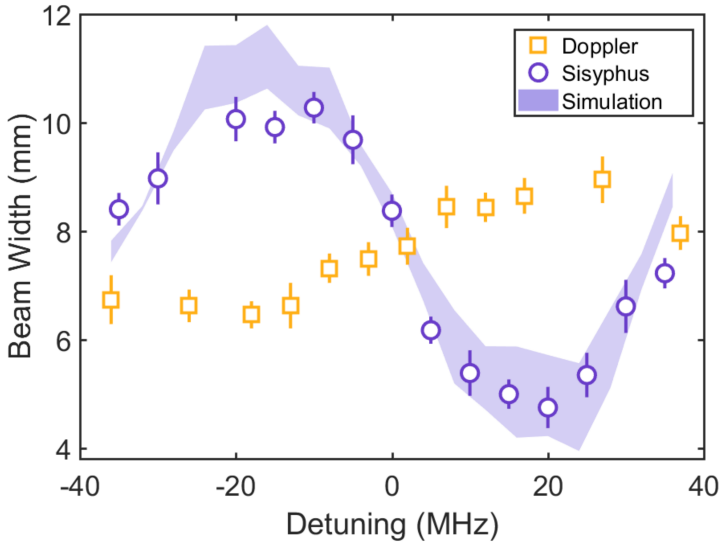

Figure 6.9: Comparison of Doppler and Sisyphus cooling as a function of detuning. Data taken at an intensity of $I/I_{\text{sat}} \sim 15$. The magnetically-assisted Sisyphus effect has the opposite detuning dependence and higher cooling efficiency when compared to Doppler cooling. Error bars on experimental points come from the spread in repeated measurements. Shaded regions represent the spread in simulation outputs when the simulated laser beam overlap in the cooling region is varied, as described in the main text.

Using the theoretically generated force profiles, we simulate the propagation of molecules through the experimental setup including the full three-dimensional structure of the molecular beam and the transverse profiles of each laser beam, accounting for imperfect laser beam overlap in the cooling region. We incorporate random decays into dark vibrational states and momentum diffusion from spontaneous emission. The intensity, magnetic field, number of photons scattered, polarization, and detuning are all set to the experimentally measured parameters. A representative set of simulated beam profiles is shown in Fig. 6.5(b) in comparison to the experimental data. In order to assess the uncertainty in the simulation, we leave all parameters fixed to the measured values but vary the assumed laser beam overlap in the cooling region (the most poorly determined parameter), effectively scaling the cooling force up or down by a factor of $\sim$2. Error bars associated with theory curves show the spread of predicted values under this variation (see Figs. 6.7 and 6.9).

Though the temperature sensitivity of our direct measurements is limited by the collimation aperture width as described above, we extrapolate to lower temperatures using this theoretical sim-

ulation. First, we validate the model at higher temperatures, where excellent agreement is seen between the measured and predicted beam widths and cooled fractions (see Fig. 6.7). At saturation parameters > 20 where the experimental temperature sensitivity has fallen off, our simulation predicts the temperature continues to drop as would be expected intuitively. At the highest intensity realized in the experiment, the model predicts temperatures as low as 10^{+20}_{-5} μK, which is below the Doppler limit (200 μK) and approximately 60 times the recoil limit (150 nK) for YbOH. This temperature is comparable to those achieved in the recent work on transverse Sisyphus cooling of YbF molecules [217], where a similar extrapolation was required in order to assign the very low transverse temperatures observed. Our model also allows us to compute a capture velocity for the Sisyphus cooling of $v_c = 0.8(2)$ m/s. This is in good agreement with the value determined from the data above and also consistent with the observed fraction in the "cooled" part of the distributions. Using the minimum predicted temperature would yield a PSD increase of a factor of 40, as compared to the more conservative estimate based on the temperature limit included above.

6.4 Conclusion

In summary, we demonstrated Sisyphus and Doppler laser cooling of the polyatomic radical ^{174}YbOH. Under Sisyphus conditions, the transverse temperature of the YbOH beam is reduced from $\sim$20 mK to $< 600\,\mu$K with $\sim$500 photons scattered per molecule. Sisyphus cooling is found to be significantly more efficient (per photon scattered) than Doppler cooling, as expected due to the large light shifts induced by the near-resonant standing waves [126, 221]. We compared our results to simulations based on the optical Bloch equations and find agreement over a range of parameters. Validating this model is important as it can be used to guide future experiments to cool and trap YbOH and other molecules sensitive to BSM physics. Due to the expected optical pumping to unaddressed vibrational states, the on-axis density of the cooled molecular beam is approximately equal

to the unperturbed beam. The decrease in temperature leads to an increase in the PSD around a factor of 6 under the very conservative assumption of 600 μK for the transverse temperature of the cooled beam.

Our results are a proof-of-principle demonstration toward further laser cooling of YbOH to temperatures low enough for optical trapping. The transverse cooling demonstrated here could be extended to two dimensions, increasing the number of molecules that can ultimately be captured in an optical trap. The temperature limits determined here are set by the number of photons scattered per molecule, which in turn is set by the number of vibrational repump lasers used in the experiment. The branching ratio measurements reported in Ch. 4 indicate how we could bring this figure to $> 10,000$ photons, sufficient to produce a magneto-optical trap of YbOH. Transverse Sisyphus cooling could also contribute directly to improvements in beam-based precision measurements by increasing the number of molecules probed while also allowing longer beam lines, and thus longer coherence times. Straightforward extension of the technique to ^{173}YbOH would be useful for proposed nuclear magnetic quadrupole moment measurements [26, 224]. A more complex repumping scheme will be required in this case because each $\tilde{X}(N'' = 1)$ level will split into two closely spaced sets of three levels that are separated by approximately 6 GHz due to large ^{173}Yb (I=5/2) magnetic and nuclear electric quadrupole hyperfine interactions, similar to ^{173}YbF [225].

Science is magic that works.

Kurt Vonnegut, in "Cat's Cradle"

7

Zeeman-Sisyphus Deceleration

Even with the slowest cryogenic beams we can achieve, the molecules produced by our beam source have velocities at least several times faster than can be captured into typical traps. For example, the capture velocity of a CaOH MOT is expected to be around $v_{\text{trap}} \approx 10 - 15$ m/s [216] while the peak velocities of our optimized CaOH sources are around 40 m/s. The larger mass of YbOH may reduce the MOT capture velocity to around $v_{\text{trap}} \approx 5 - 10$ m/s, while our slowest YbOH beams have peak forward velocities around $20 - 25$ m/s. Some form of slowing is required to bridge this gap.

To date, the slowing required to load (diatomic) molecular MOTs has been achieved using the

radiation pressure force exerted by high-power lasers [117, 118, 181]. Laser-coolable molecules are generally not amenable to Zeeman slowing [100], though recent work has proposed similar alternatives [226–228]. Instead, both frequency-broadened (white-light) and frequency-chirped slowing schemes have been used for molecular beam deceleration [117, 118, 181]. Because of the small momentum change caused by each photon absorption-emission cycle, radiative slowing from typical CBGB velocities requires scattering $n_\gamma \sim 10^4$ photons to reach v_{trap}. This n_γ is at least an order of magnitude larger than the number of scattered photons that has so far been demonstrated for any polyatomic molecule [229].[1] Radiative forces are especially inefficient for decelerating significant numbers of large polyatomic species that are both massive and are limited (either technically or intrinsically) to optically cycle only $\sim$100s of photons [230, 231]. To circumvent this, a number of non-radiative slowing methods have been developed [232–237], but these are inherently pulsed, slowing "packets" of molecules $\lesssim 100$ μs in duration. Slowing of continuous molecular beams was achieved with a "cryofuge" decelerator in work complementary to that presented here [238, 239].

In this chapter, we describe a superconducting magnetic/optical decelerator that slows molecular beams to trappable velocities while using fewer than 10 spontaneous photon scatters.[2] In Sec. 7.1, we describe the basic idea of this scheme: deceleration is achieved by a combination of two large, static magnetic field regions and three electron-spin-flip optical transitions. Next, Sec. 7.2 describes optical pumping spectroscopy conducted to find and optimize the transitions used by the Zeeman-Sisyphus scheme. These optical pumping spin-flip transitions lead to efficient deceleration of CaOH molecular beams that is described in Sec. 7.3. The ultimate goal of this work was to develop a slowing method for YbOH molecules, and Sec. 7.4 describes ongoing work to decelerate YbOH molecules and complications that may arise. Finally, Sec. 7.5 presents technical details of the apparatus constructed for Zeeman-Sisyphus deceleration, including the superconducting

[1] Even the "simple" polyatomic species CaOH appears to require at least 10 lasers for such a task [199].
[2] Portions of this chapter have been presented in Ref. [240].

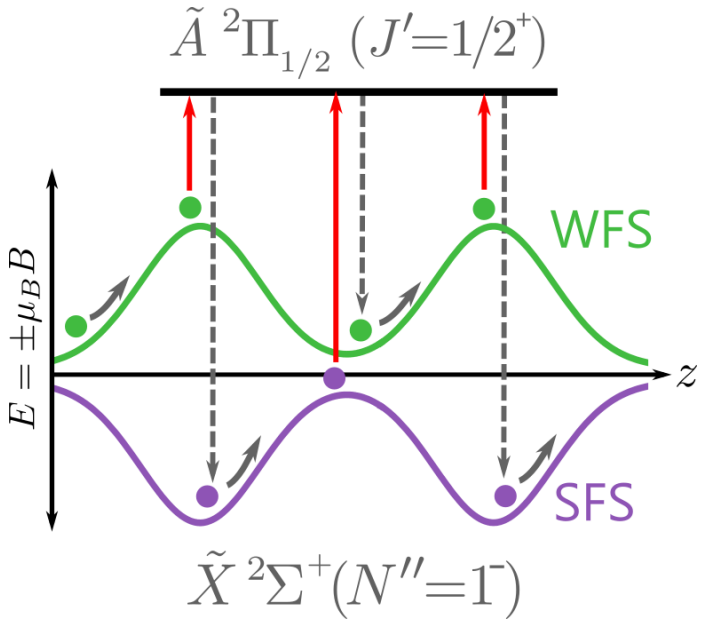

Figure 7.1: Overview of the Zeeman-Sisyphus deceleration scheme. Molecules enter the magnetic field region in a weak-field-seeking state and decelerate as they travel toward the peak magnetic field. At the peak magnetic field, molecules are optically pumped to a strong-field-seeking (SFS) state and continue to decelerate. Near the field minimum, molecules are pumped back to the weak-field-seeking (WFS) state and the process can be repeated for additional deceleration.

magnets, the cryogenic chamber that supports them, and a magnetic guide used to transport population from the decelerator's output to the detection region.

7.1 Overview of Zeeman-Sisyphus deceleration

To produce this decelerator, we leverage the large energy shifts induced by Tesla-scale magnetic fields. The principle of our decelerator is depicted in Fig. 7.1. In brief, molecules in a weak-field-seeking (WFS) state are incident on a region of increasing magnetic field magnitude and decelerate as they climb the potential. Near the magnetic field maximum, the molecules are optically pumped through an electronically excited state to a strong-field-seeking (SFS) state and continue to decelerate as they exit the high-field region. In this way, an energy $\Delta E_{\text{stage}} \approx 2\mu_B \mathcal{B}_{\text{max}}$ can be removed from molecules passing through each deceleration stage, where μ_B is the Bohr magneton and $\mathcal{B}_{\text{max}}$ is the maximum magnetic field in the high-field region. This so-called "Zeeman-Sisyphus" pro-

cess [241, 242] can be repeated to remove additional energy. Furthermore, the deceleration applies to all molecules regardless of their arrival time, and thus is effective for continuous (or long-pulsed) molecular beams. Because a fixed *energy* is removed in each stage, the decelerator will slow to rest $1\mu_B$ molecules of any mass produced at or below the same threshold temperature.

Note that in Fig. 7.1 we have implied a particular choice of electronic transition ($\tilde{A}\,^2\Pi_{1/2} \leftarrow \tilde{X}\,^2\Sigma^+$). This is an important feature of the deceleration scheme. In the $\tilde{X}\,^2\Sigma^+$ state, the electron spin is uncoupled from all other angular momenta. Thus, at magnetic fields sufficiently large to decouple any hyperfine/spin-rotation structure, the projection of the electron spin on the laboratory field axis (M_S) will be a good quantum number. Driving between WFS and SFS states involves reversing the value of M_S. An electric dipole transition cannot directly change the value of M_S, seeming to make this task difficult. However, in the $\tilde{A}\,^2\Pi_{1/2}$ state, the spin-orbit interaction is orders of magnitude larger than the Zeeman shift at any reasonable value of magnetic field. The Zeeman sublevels of he $\tilde{A}\,^2\Pi_{1/2}$ state are therefore best characterized by the quantum number M_J and are generally linear combinations of $M_S = \pm 1/2$. In this sense, the spin-orbit coupling is a crucial ingredient that enables the spin-flip transitions required to pump between WFS to SFS manifolds in the ground state.

7.1.1 Previous work

This scheme is motivated by previous experimental [243] and theoretical results [241, 242]. In Ref. [243], CaF molecules were loaded into a 4 T deep superconducting trap using a version of this magnetic slowing scheme. By performing the slowing essentially inside the trap region, issues related to divergence losses during molecular beam propagation were largely mitigated. This experiment successfully slowed and loaded CaF molecules into the trap, establishing a strong proof of principle for magnetic slowing and direct trap loading methods. However, the environment

of a superconducting trap is not ideal for further cooling and it is difficult to extract the trapped molecules to a shallower trap for subsequent experimentation. These challenges motivate schemes with a clearer distinction between the slowing and trapping, decoupling the two steps.

One such proposal was developed in Ref. [241], which considered a decelerator composed of about 60 stages of permanent magnets. The magnets were to be arranged in a Halbach configuration, alternately producing high- and low-field regions, with molecules propagating through a central bore. This theoretical investigation found that very high slowing efficiencies could be achieved for slowing to the capture velocity of a MOT, even for molecular beams with peak forward velocities around 150 m/s. Furthermore, the design allowed alternation of guiding and slowing stages which strongly reduced divergence losses within the decelerator.

Unfortunately, the design of Ref. [241] required a very long decelerator (around 1.3 m in length) and small bore (approximately 6 mm diameter) in order to achieve peak fields around 1.4 T for deceleration. These two design constraints lead to significant concerns about molecular beam attenuation due to gas buildup within the decelerator. Finally, this design required the optical pumping lasers to propagate down the decelerator's bore. Because the laser light is thus present at all locations along the decelerator, it was found that the maximum field in the decelerator had to be maintained below a threshold value at which lossy rotational transitions could be driven. This artificially limits the amount of deceleration that can be achieved in each stage. In addition, all SFS→WFS transitions are driven on the slope of a rapidly changing magnetic field, requiring high laser intensities due to the associated Zeeman broadening.

7.1.2 A superconducting Zeeman-Sisyphus decelerator

We have constructed a Zeeman-Sisyphus decelerator based on a set of superconducting coils, as shown in Fig. 7.2. Our particular decelerator comprises two magnets with $\mathcal{B}_{\max} \approx 2.8$ T, leading

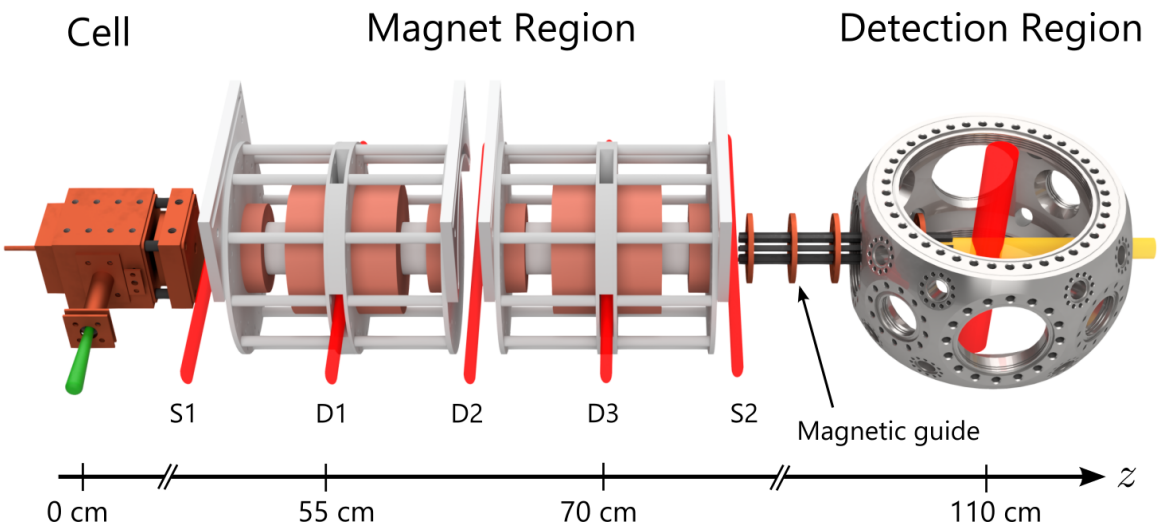

Figure 7.2: Schematic of the experimental setup (not to scale). Molecules are produced in a two-stage cryogenic buffer-gas beam. They travel through two superconducting magnets in Helmholtz configuration and are optically pumped in three deceleration pumping regions (D1, D2, D3) by transverse laser beams at 626 nm. State-preparation regions (S1 and S2) pump molecules into WFS states in order to populate magnetically guidable states. Molecules are detected via laser-induced fluorescence by simultaneous excitation at 626 nm and 574 nm.

to $\Delta E_{\text{stage}} \approx 3.8$ K. The total energy removal for two stages ($\sim$7.6 K) is therefore well matched to CBGBs, which can have typical kinetic energies $E_{\text{kin}} \lesssim 8$ K (see Sec. 3.1 and 3.3). The slowing process starts as molecules in a cryogenic buffer-gas beam (CBGB) [89] are incident on the fringing magnetic field of a compensated solenoid. WFS molecules in the beam decelerate as they enter the field produced by a solenoid. In region D1, at the peak magnetic field $\mathcal{B}_{\text{max}} \sim 2.8$ T, molecules are pumped into the SFS manifold and therefore continue to decelerate as they exit the high-field region of the magnet. Eventually the molecules reach region D2, where they are pumped from SFS states back into WFS states in order to restart the deceleration process in the second magnet. Molecules are pumped back into the SFS manifold in region D3 in order to continue decelerating even as they exit the final magnet. Velocity-sensitive detection occurs via laser-induced fluorescence in a room-temperature ultra-high vacuum chamber.

There are two other optical pumping regions shown in Fig. 7.2 which, while not strictly necessary to achieve slowing, are useful to maximize the amount of population that is decelerated and detected. First, in region S1, located at $\mathcal{B} \sim 0.06$ T on the fringing field of the first magnet, state-

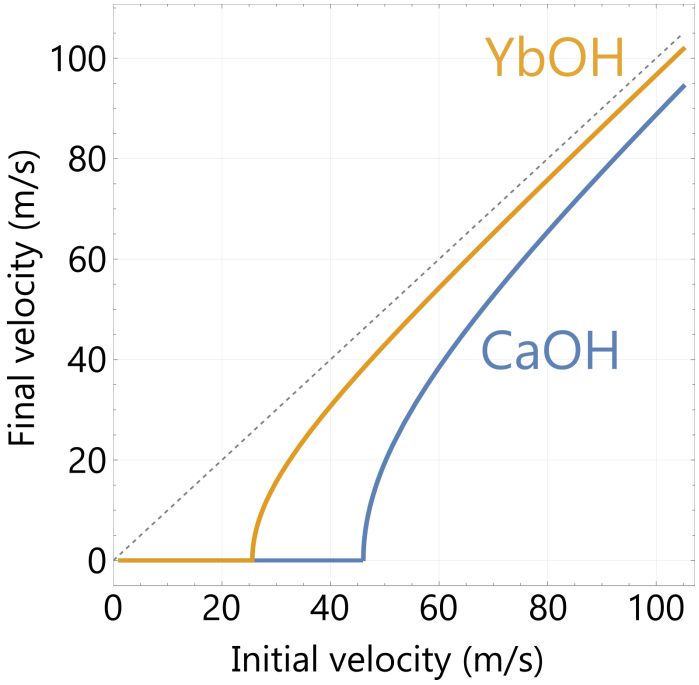

Figure 7.3: Correspondence between initial and final velocities in a two-stage Zeeman-Sisyphus slower with $\mathcal{B}_{\text{max}} = 2.8$ T for both CaOH and YbOH. The line for which initial and final velocities are equal is shown as the gray dashed line.

preparation is performed by pumping all molecules in SFS states to the (slowable) WFS manifold. Because the CBGB equally populates WFS and SFS states, this state preparation roughly doubles the amount of population available for slowing. Second, in region S2, located at $\mathcal{B} \sim 0.06$ T on the fringing field of the final magnet, molecules exiting the decelerator are pumped back into the WFS manifold. Pumping in S2 is useful because it allows a magnetic guide to be used after the decelerator to help preserve molecular flux as the molecules travel from the cryogenic magnet region to the room-temperature detection chamber.

The deceleration capability of our two-stage Zeeman-Sisyphus decelerator is shown in "velocity space" in Fig. 7.3. Because each decelerator stage removes almost exactly ΔE_{stage}, there is a nearly one-to-one correspondence between input and output velocities based on kinetic energy removal. We plot this for both CaOH and YbOH molecules. This calculation only considers the energy removal, not losses that may occur at low velocity (see below for full trajectory simulations). For

the parameters of our slower, CaOH (YbOH) molecules produced near 45 m/s (25 m/s) can be slowed to rest.

7.1.3 Advantages of superconducting design

There is some overhead associated with superconducting coils (principally the use of a cryocooler). Nonetheless, the use of superconducting coils leads to a number of technical advantages in decelerator performance as compared to permanent magnet designs. First and foremost, stronger magnetic fields can be achieved over a larger bore. While Halbach arrays can be designed to reach $\mathcal{B}_{\text{max}} \lesssim 1.4$ T over bores a few mm in diameter, it is straightforward to design superconducting solenoids with $\mathcal{B}_{\text{max}} \lesssim 4$ T and with bores a few cm in diameter. That is, a superconducting coil can simultaneously enable greater deceleration per stage and larger spatial acceptances. Second, the cryogenic apparatus required to support the superconducting coils naturally leads to excellent vacuum due to high-speed cryopumping. Third, superconducting coils can easily be designed with transverse optical access in order to drive laser transitions only at particular positions along the solenoids, eliminating concerns about "accidental" resonances along the slowing path that lead to population loss. This has the added advantage that we drive all transitions at points where the magnetic field is approximately flat, minimizing Zeeman broadening and reducing the laser power requirements.

Transverse optical access is especially important when the decelerator is operated at high $\mathcal{B}_{\text{max}}$. This is because at certain critical fields, undesirable transitions from the $N'' = 1$ level may come into resonance that can remove molecules from the optical cycle [241, 243]. For example, at zero field the $Q(1)$ transition is approximately $3B'$ ($\sim$30 GHz for CaOH, but only $\sim$3 GHz for YbOH) above the rotationally closed $P(1)$ line. If these Q-branch transitions are driven at any point throughout the decelerator, they can cause significant population loss to other rotational levels, e.g. $N'' = 3$.

One option to avoid such losses is to limit $\mathcal{B}_{\text{max}}$ so that these resonances never occur. This undesirably limits ΔE_{stage}; for YbOH and related species, the restriction can be quite severe. Alternatively, transverse optical access ensures that laser-molecule interaction occurs only at the desired locations, eliminating concerns about transitions driven at other positions throughout the decelerator.

7.2 CaOH optical pumping spectroscopy

While our Zeeman-Sisyphus slower was designed with YbOH in mind, we performed initial tests of the deceleration performance using CaOH molecules. As a test species, CaOH offered a number of advantages: more mature spectroscopy, slightly more diagonal FCFs, and simpler Zeeman structure in the excited $\tilde{A}\,^2\Pi_{1/2}$ state. The excited-state Zeeman structure is described in more detail in App. G. To drive the necessary transitions, we were very fortunate to temporarily "adopt" a number of lasers from the Doyle group's CaOH experiment. In what is described below, we used three lasers at 626 nm for deceleration: an SFG source to drive the optical pumping transitions in D1 and D3, a cw dye laser to address region D2, and a separate dye laser to address regions S1 and S2. For detection, we used a combination of a cw dye laser at 626 nm and a doubled Raman fiber amplifier at 574 nm.

7.2.1 Detection scheme

Initial tests of the Zeeman-Sisyphus apparatus were conducted by measuring the optical pumping performance in each pumping region. State-selective detection of molecules in the downstream detection region was used to read out the effects of these optical pumping steps. We detected CaOH molecules using the optical cycling scheme shown in Fig. 7.4. This involves driving the $\tilde{A}\,^2\Pi_{1/2}(000, J' = 1/2^+) \leftarrow \tilde{X}\,^2\Sigma^+(000, N'' = 1^-)$ (626 nm) and $\tilde{B}\,^2\Sigma^+(000, N' = 0^+) \leftarrow$

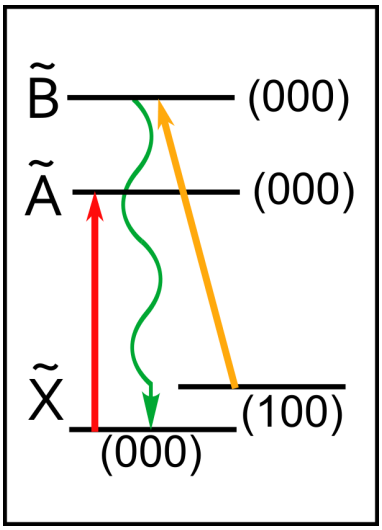

Figure 7.4: Detection scheme used for CaOH molecules. Excitation at 626 nm (red arrow) and 574 nm (yellow arrow) results in fluorescence at 555 nm (green arrow).

$\tilde{X}\,^2\Sigma^+(100, N'' = 1^-)$ (574 nm) transitions simultaneously. Both excitation lasers carry rf sidebands at 52 MHz in order to address the rotationally-closed ${}^pQ_{12}(1)$ and $P_1(1)$ lines. The resulting $\tilde{B}\,^2\Sigma^+(000, N' = 0^+) \rightarrow \tilde{X}\,^2\Sigma^+(000, N'' = 1^-)$ fluorescence at 555 nm allows nearly background-free detection. On average, molecules emit approximately 7 photons at 555 nm under these conditions. While this is many fewer than the ~ 150 photons scattered on the 626 nm diagonal line, the signal-to-noise ratio is significantly higher due to the background-free conditions. For optical pumping measurements, both detection lasers were directed transverse to the molecular beam in order to be velocity-insensitive. For velocity-*sensitive* detection, as will be discussed below, we counterpropagated the 574 nm laser beam against the molecular beam and used the Doppler shift to assign velocities.

7.2.2 CaOH Zeeman level structure

Figure 7.5 shows the magnetic field dependence of CaOH $\tilde{X}\,^2\Sigma^+(000)$ energy levels. While we focus on CaOH specifically in these plots, the same qualitative structure occurs for other $^2\Sigma^+$ poly-

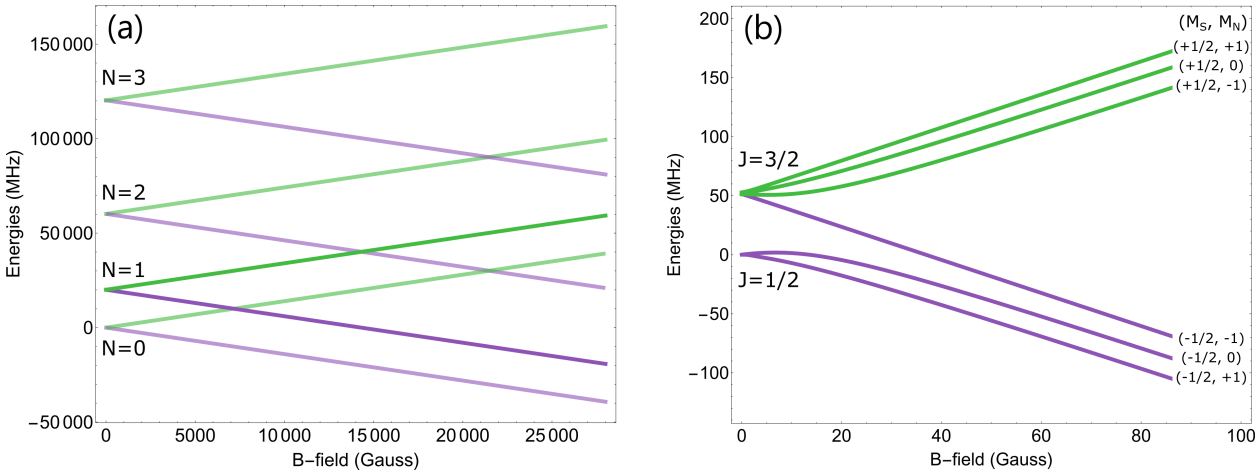

Figure 7.5: Zeeman tuning of the $\tilde{X}\,^2\Sigma^+(000)$ levels. Weak-field-seeking states are shown in green and strong-field-seeking states in purple. (a) Tuning of the $\tilde{X}\,^2\Sigma^+$ levels with $N'' \leq 3$ over the full range accessible in our decelerator. (b) Tuning of the $N'' = 1$ states at low fields ($\mathcal{B} \lesssim 100$ Gauss). Quantum numbers relevant for low and high fields are also shown. Levels not used in our experiment are shown as faded lines.

atomic molecules.[3] Near zero field, the energy levels are grouped in widely-spaced sets specified by N'', each set containing two spin-rotation components $J'' = N'' \pm 1/2$. For the alkaline-earth monohydroxides, this spin-rotation splitting is on the order of $50 - 150$ MHz in the $N'' = 1$ levels [172, 212]. Proton hyperfine structure is unresolved in optical transitions for these molecules, with typical scale around $1 - 5$ MHz [172, 174]. Applying a magnetic field can shift and split the zero-field spin-rotation states, and for fields at which the Zeeman energy is much greater than the spin-rotation splitting, the levels reorganize according to their projection of electron spin angular momentum onto the lab frame, labeled by M_S; the electron spin is fully decoupled from the other angular momenta. This occurs for fields in the range $50 - 150$ Gauss. All optical pumping steps in the Zeeman-Sisyphus decelerator occur in this "high-field" (decoupled) regime where the energy levels tune approximately linearly with slope $\pm\mu_B$. The fields in our decelerator are everywhere low enough that no level crossings occur between states of equal parity, eliminating concerns about loss of population to other rotational states due to adiabatic crossings [186, 243].

[3]We are focusing here specifically on alkaline-earth monohydroxides for which the metal atom has no nuclear spin; large hyperfine splittings may be present in other isotopologues.

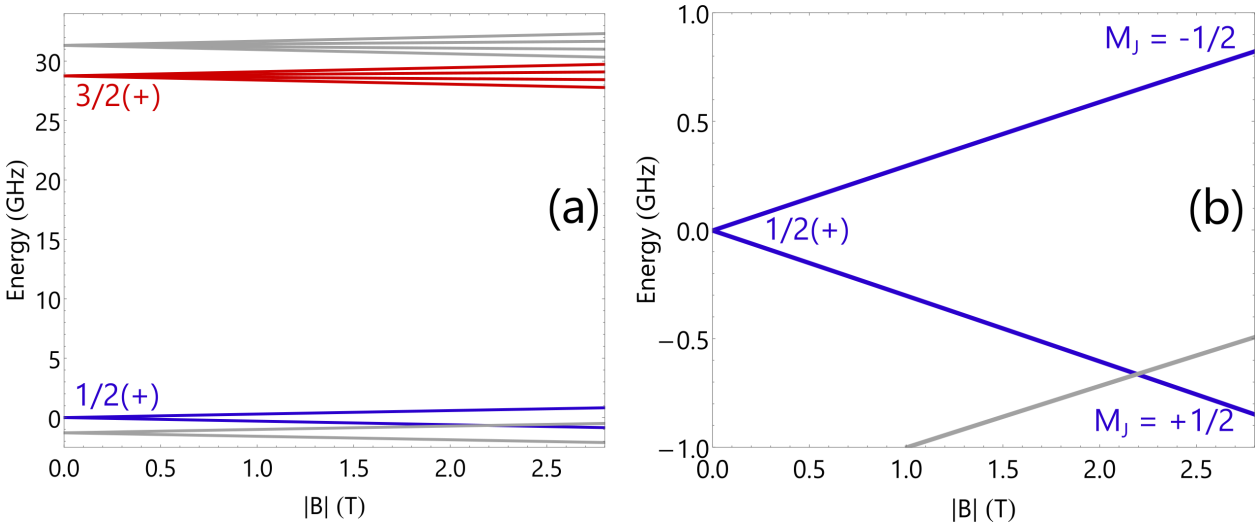

Figure 7.6: Zeeman structure of the CaOH $\tilde{A}\,^2\Pi_{1/2}(000)$ levels with $J' \leq 3/2$. States are labeled according to their zero-field quantum numbers $J(p)$, where p is the parity. States with the same parity as $N'' = 1$ are shown in gray. Levels that correlate with $J' = 1/2$ at $\mathcal{B} = 0$ are shown in blue and those that correlated with $J' = 3/2$ are shown in red. (a) All $J' = 1/2$ and $3/2$ levels. (b) The $J' = 1/2$ levels used in this experiment.

The excited-state Zeeman structure is also relatively simple, as shown in Fig. 7.6. In this figure, the large splitting between $J' = 1/2$ and $J' = 3/2$ levels is evident, as is the smaller Λ-doubling that separates opposite-parity levels with the same J' quantum number.[4] We use the $J' = 1/2, p = +$ level of $\tilde{A}\,^2\Pi_{1/2}(000)$ in order to drive rotationally-closed cycling transitions. One would nominally expect a $^2\Pi_{1/2}$ level to show negligible Zeeman tuning because the electron spin and orbital angular momenta approximately cancel. For reasons discussed in App. G, a small amount of Zeeman tuning is expected to occur, and at the highest fields in our decelerator the $M_J = \pm 1/2$ levels are separated by nearly 2 GHz.[5] Because these M_J levels are of mixed M_S character, the spin-flip optical pumping transitions can be driven rather efficiently.

[4]This structure can be contrasted to that found in YbOH, where the rotational constant and Λ-doubling parameter are nearly equal, pushing equal-parity $J' = 1/2$ and $3/2$ levels very close together. See Fig. 7.18.

[5]Luckily, the measured splitting is nearly equal to that of the ground-state hyperfine splitting in Na atoms and we could borrow a resonant EOM from the Ni group to address both excited-state features using a single laser beam (see Sec. 7.2).

7.2.3 Optical pumping without magnetic guide

Our first tests of the Zeeman-Sisyphus decelerator were conducted *without* the magnetic guide in place. This complicated the detection scheme because all optical pumping steps occurred in the high-field regime ($\mathcal{B} \gtrsim \gamma_{\rm SR}/\mu_B \approx 40$ Gauss for CaOH), where the states are grouped as WFS or SFS according to the projection of the electron spin on the laboratory field (M_S). On the other hand, detection occurred near zero field, where the states are grouped according to $J'' = 1/2$ or $3/2$ due to the spin-rotation coupling. There is not a one-to-one mapping between the WFS/SFS basis and the J'' basis, i.e., all $J'' = 1/2$ states become SFS at high fields, but some of the $J'' = 3/2$ states become WFS while others become SFS. This can be seen in Fig. 7.5, which plots the Zeeman tuning of relevant CaOH energy levels. Because all $J'' = 1/2$ levels are SFS, by depleting the $J'' = 3/2$ levels we were able to selectively detect purely SFS states.[6] It was found that essentially 100% depletion of the $J'' = 3/2$ population could be achieved efficiently by driving the $\tilde{A}(020)\,\mu\,^2\Pi_{1/2}(J' = 5/2) \leftarrow \tilde{X}\,^2\Sigma^+(000, N'' = 1)$ transition at 601 nm.

By detecting molecules exiting the decelerator in SFS states, we were able to test the performance of individual pumping regions. For example, pumping from WFS to SFS in regions D1 or D3 should enhance the detected fluorescence. We used this scheme to track the WFS→SFS optical pumping features in D1 and D3 as the magnets were energized (see Fig. 7.7). The data in Fig. 7.7(b) show how the optical pumping feature in D1 tunes with magnetic field when only the upstream magnet is energized. The data verify the expectation that the $P(1)$-branch transition tunes at a rate of approximately 14 GHz/T, dominated by the $1\mu_B$ tuning of the $\tilde{X}\,^2\Sigma^+$ state. Also as expected, the excited state showed only a very small magnetic tuning that will be described below.

[6] Note that one of the $J'' = 3/2$ states does become SFS at high fields, so this scheme necessarily depletes some of the SFS population. However, it *fully* depletes WFS population, so it is still the case that following depletion we detect only molecules that exited the Zeeman-Sisyphus magnets in a SFS state.

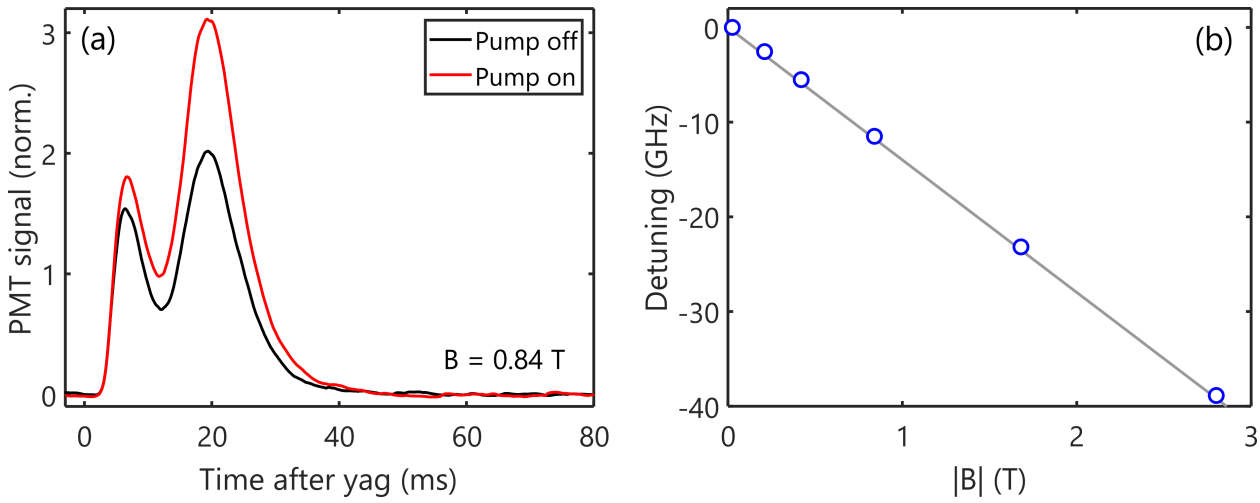

Figure 7.7: Zeeman tuning of optical pumping features with pumping light applied in region D1. (a) Enhancement of $J'' = 1/2$ population observed when pumping light is applied in D1, with $\mathcal{B} = 0.84$ T. (b) Frequencies at which this enhancement is observed as a function of magnetic field in region D1. Blue points represent measured frequencies. The gray line shows the $\mu_B \approx 13.99$ GHz/T slope expected for the Zeeman tuning for a state with magnetic moment $1\mu_B$.

7.2.4 Optical pumping with magnetic guide

We installed the magnetic guide described in Sec. 7.5.3 after collecting initial slowing data. However, for continuity of presentation we will describe the optical pumping measurements performed with the guide in place before moving on to the deceleration measurements. Only WFS states can be transmitted through the magnetic guide, but molecules ideally exit the slower in a SFS state. Thus, we also had to introduce the state-preparation optical pumping region S2 in order to drive any SFS population back into the WFS states just after the downstream magnet. From the measured and calculated magnetic field profiles (see Sec. 7.5), the field in the S2 pumping region was expected to be between 400 and 600 Gauss. We located the resonance by pumping all population into the SFS manifold in D3 while simultaneously applying light in S2 and looking for a revival feature when population returned to the WFS manifold. A resonance was located at the expected position, and with about 100 mW of laser light in S2 we achieved about 80% repumping efficiency (see Fig. 7.8). The spectrum indicated a double-peaked structure, the origin of which is not well understood. For the data presented below, we parked at the higher frequency peak.

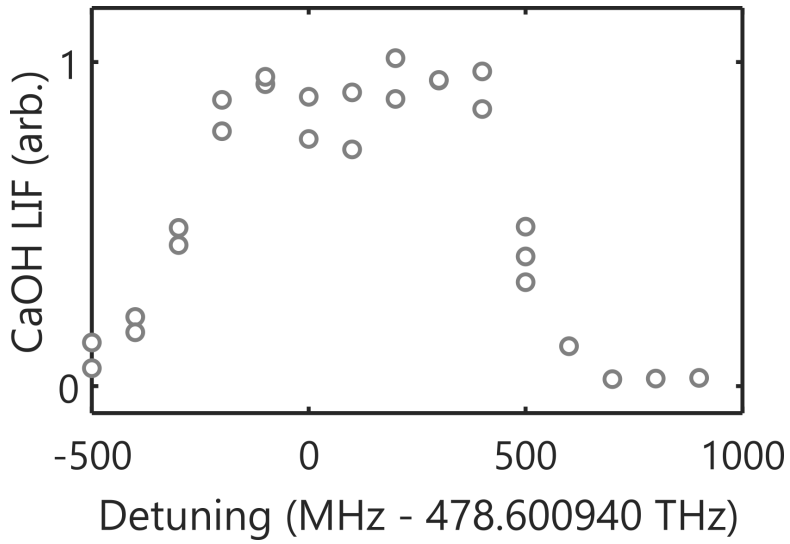

Figure 7.8: Scan over SFS→WFS resonance for state-preparation to enter the magnetic guide. Depletion light was applied continuously in pumping region D3 to establish a depleted baseline. A laser was scanned in region S2 to revive the signal.

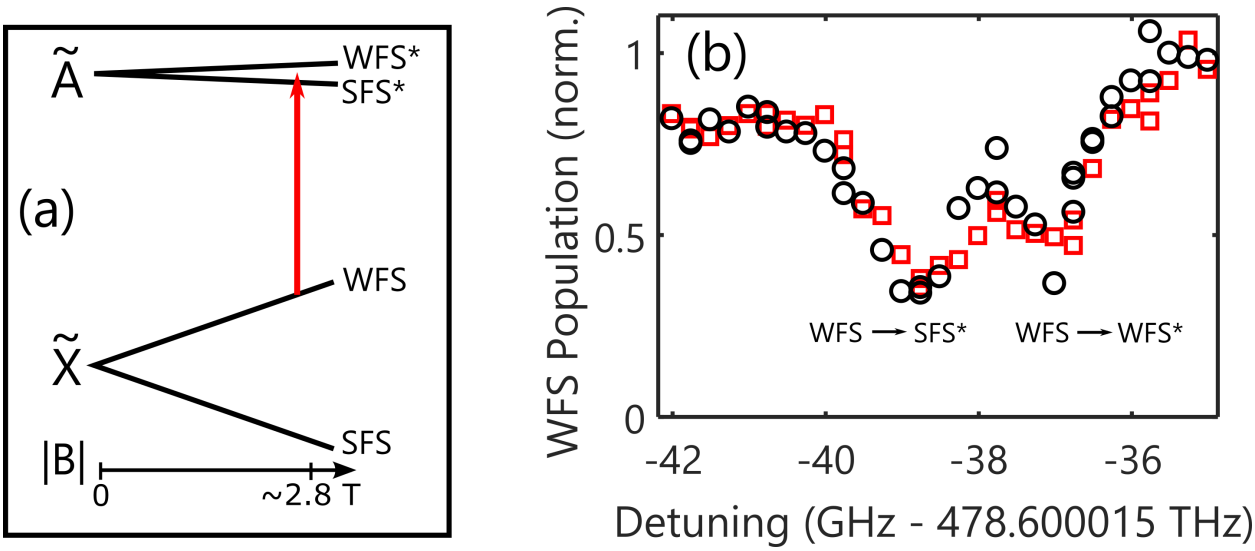

Figure 7.9: Optical pumping measurements in the high-field pumping regions, D1 and D3. (a) Transitions addressed in order to pump WFS population into the SFS manifold. (b) WFS state population measured downstream as a function of laser frequency applied in D1 (black circles) or D3 (red squares), with $\mathcal{B} = 2.8$ T. The observed doublet arises due to Zeeman splitting in the $\tilde{A}\,^2\Pi_{1/2}(000, J' = 1/2)$ level. The offset at lower frequencies is due to asymmetrical Zeeman broadening present in the pumping region. Inset: Level structure giving rise to the observed transitions.

Detecting optical pumping efficiencies was more straightforward after installing the magnetic guide. The guide filters out all SFS population, so even with photon cycling that scrambles J'' in the detection region we can easily infer the population transfer that was realized in the deceleration region. We studied the optical pumping performance by monitoring the population in WFS states downstream while applying various combinations of optical pumping light in D1, D2, and D3. Figure 7.9 shows the optical pumping efficiency from WFS to SFS states when $\mathcal{B}_{\text{max}} \approx 2.8$ T and 150 mW of optical pumping light is applied in D1 or D3. Two optical pumping features are observed due to excited-state Zeeman splitting (specifically the g'_ℓ term described in App. G). Because the same laser is used to drive transitions in both D1 and D3, it was critical that the two coils had identical values of $\mathcal{B}_{\text{max}}$. Tuning the current in each coil with ~ 0.1 A resolution was sufficient to balance the fields well within the width of the optical pumping features. The curvature in $\mathcal{B}$ in regions D1/D3 leads to Zeeman broadening of the observed optical pumping features. Because the field reaches a local minimum and the targeted optical pumping transition occurs at red detuning relative to zero field, we expect to observe asymmetric pumping lineshapes with preferentially higher efficiency at lower frequency (larger red detuning). This is consistent with the observations shown in Fig. 7.9.

Each ground-state Zeeman sublevel couples to a single excited-state sublevel [241], so due to the details of angular momentum selection rules in the fully decoupled regime we must drive both of the observed features simultaneously to achieve full population transfer. To do so, the optical pumping light is passed through a resonant electro-optical modulator tuned to $f_{\text{EOM}} \approx 1.7$ GHz. In Fig. 7.10, we show the optical pumping efficiency when both Zeeman features are addressed in D1. At laser powers above about 200 mW, we observe $>97\%$ optical pumping efficiency. Repeating these measurements in D3 yields identical results.

The results of Fig. 7.10 show that we have efficiently depleted the WFS manifold, but they do *not*

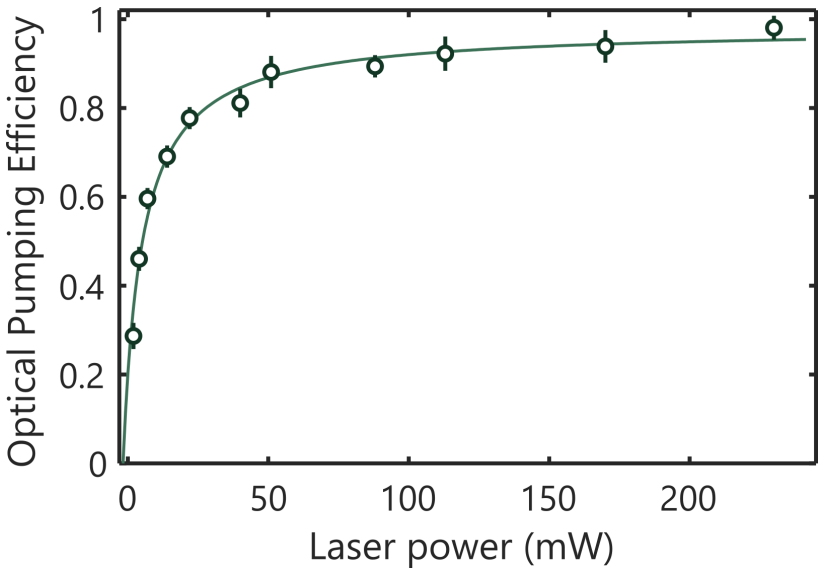

Figure 7.10: Efficiency of pumping from WFS to SFS manifold when both features of the excited-state Zeeman doublet are driven simultaneously in D1. Similar behavior is observed in D3.

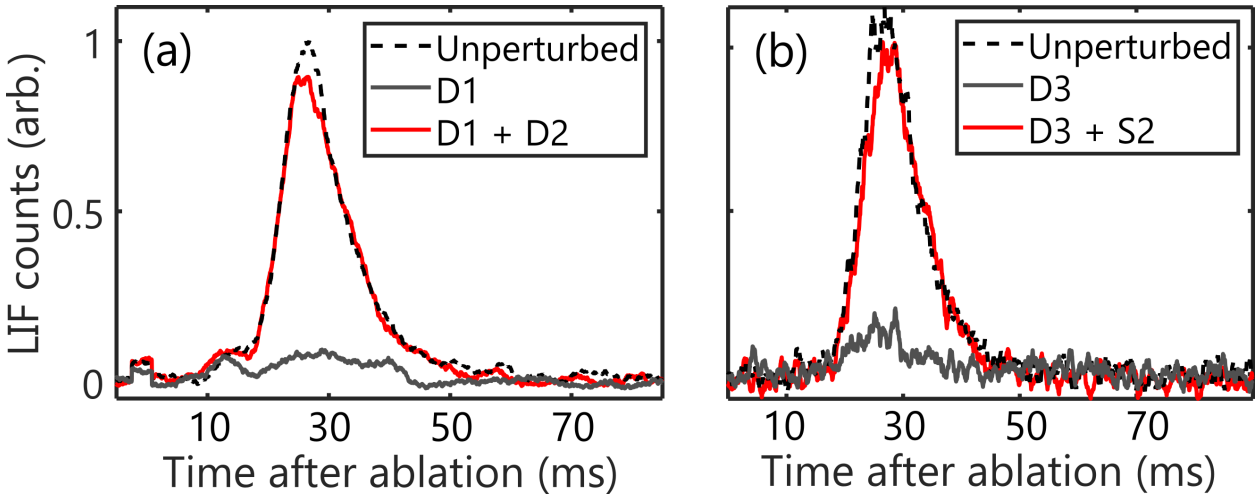

Figure 7.11: Optical pumping and repumping efficiency measurements with $\mathcal{B} = 2.8$ T. (a) Depletion and revival in the first magnet (regions D1 + D2). (b) Depletion and revival in the second magnet (regions D3 + S2). CaOH LIF detected downstream is plotted for an unperturbed beam (black dashed line), a molecular beam pumped in the high-field region only (gray solid line), and a molecular beam pumped in both high- and low-field regions.

prove that we can realize the full optical pumping cycle required to achieve deceleration. That requires showing that we correctly "juggle" population between WFS and SFS manifolds. Figure 7.11 shows the results of pumping WFS→SFS states in one high-field region followed by repumping SFS→WFS states in the subsequent low-field region (using the pairs of pumping regions D1+D2 and D3+S2). In regions D1 and D3 we applied 250 mW of laser power split from an SFG source, we supplied 200 mW from a cw dye laser in region D2, and 150 mW from a separate dye laser in region S2. These powers are typical of the slowing experiments described below. We observed depletion indicating that at least 90% of the initial WFS population was pumped into SFS states in the appropriate high-field region. In D2 and S2, the excited-state Zeeman shifts are unresolved, so full optical pumping can be achieved with a single frequency. We find optical pumping efficiencies $> 95\%$ in D2 with ~ 150 mW of laser power. Similarly, we observe that over 90% of that population is returned to the WFS manifold when the appropriate low-field region is pumped. That the round-trip efficiency is measured to be at least 90% is consistent with the one-way optical pumping measurements of Fig. 7.10 indicating $> 95\%$ efficiency.

Optical pumping in region S1 transfers to the WFS manifold any population that exited the buffer-gas cell in a SFS; this will ideally double the population available for slowing. Having generated the light for state-preparation pumping in region S2, we decided also to apply laser light in region S1 just before the upstream magnet. Because S1 and S2 can be pumped at the same frequency, the dye laser pumping S2 was split and 150 mW of power was sent through S1. Figure 7.12 shows the detected signal with and without the pumping light applied in S1. This data was taken while studying individual velocity classes in order to ensure the interaction time was sufficient to pump all molecules produced by our source. An enhancement of $2.0(1)\times$ is observed at 60 m/s [see Fig. 7.12(a)], consistent with expectations. As shown in Fig. 7.12(b), the enhancement is fit to be $1.9(2)\times$ when considering all velocities between 30 and 90 m/s.

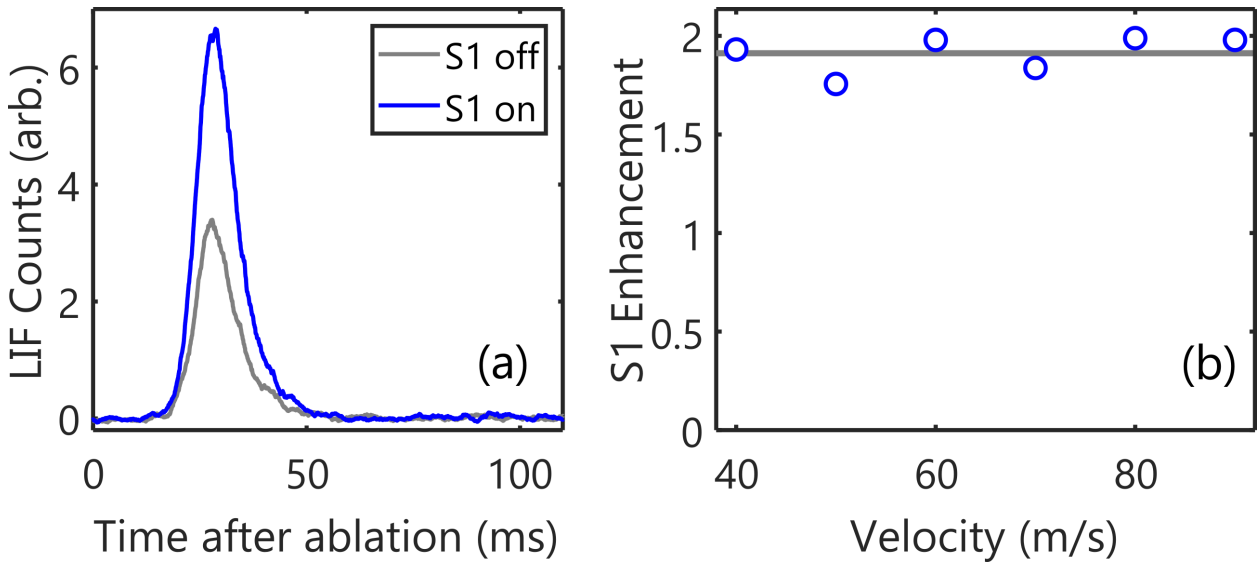

Figure 7.12: Optical pumping in region S1 to prepare all molecules in the WFS manifold. (a) Fluorescence due to molecules at 50 m/s detected downstream with and without pumping light in S1 applied. (b) Ratio of detected signals with and without S1 pumping as a function of velocity. Gray horizontal line shows the average enhancement factor, found to be about $1.9(2)\times$.

7.2.5 Number of photons scattered per pumping step

The natural $\tilde{X}\,^2\Sigma^+\,(100)$ is population is measured to be 12(2)% of the total $\tilde{X}\,^2\Sigma^+\,(000, 100)$ population. Applying light in D1 increases the $\tilde{X}\,^2\Sigma^+\,(100)$ population by a factor of $1.8(1)\times$, implying that about $9(2)\%$ of the $\tilde{X}\,^2\Sigma^+(000)$ population has been transferred to $\tilde{X}\,^2\Sigma^+(100)$ due to pumping in D1. Given the CaOH $\tilde{A}\,^2\Pi_{1/2}(000) \rightarrow \tilde{X}\,^2\Sigma^+(100)$ branching ratio, this is consistent with an average of $1.7(2)$ photons scattered per molecule in the region D1. We have conducted similar measurements in regions D2 and D3 and found an increase in $\tilde{X}\,^2\Sigma^+(100)$ population that implies scattering of about $1.5(2)$ photons per region. This implies that on average molecules scatter about 5 photons in the deceleration regions (D1, D2, and D3), and an additional 3 photons in the state-preparation regions (S1 and S2). Overall, fewer than 10 photon scatters per molecule are required during the slowing steps. With no (100) repumper present in the Zeeman-Sisyphus decelerator, the CaOH branching ratios indicate that more than 65% of the population will remain in the $\tilde{X}\,^2\Sigma^+(000)$ manifold following this number of photon scatters; additional population may accu-

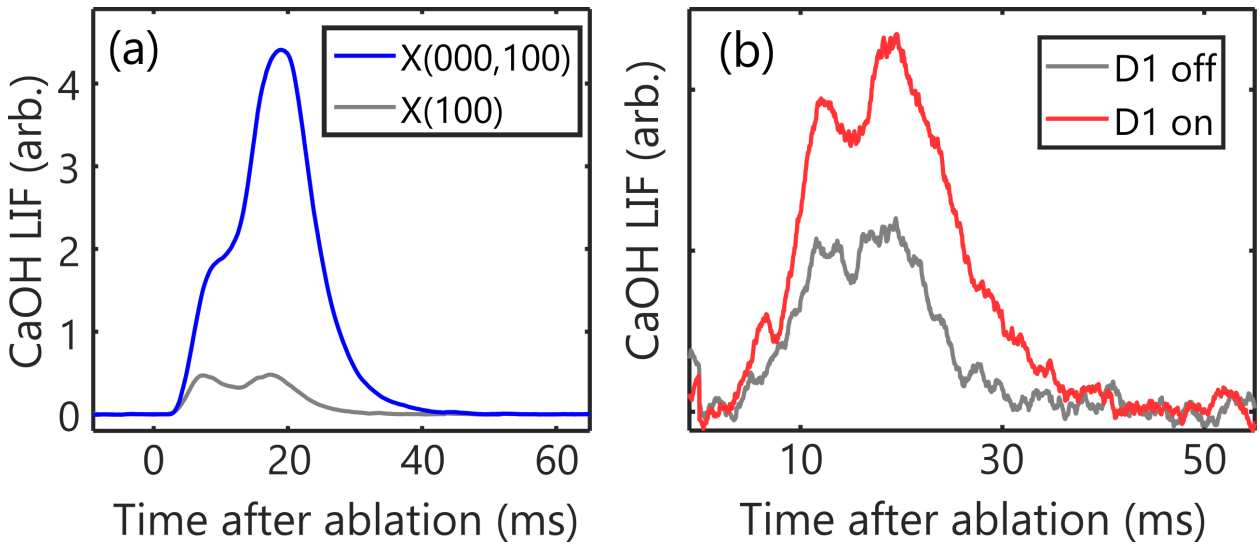

Figure 7.13: Measuring $\tilde{X}\,^2\Sigma^+\,(100)$ population in order to infer the number of photons scattered during an optical pumping step. (a) Unperturbed molecular beams measured with just $\tilde{X}\,^2\Sigma^+(000)$ or both $\tilde{X}\,^2\Sigma^+(000, 100)$ in the detection region. This provides a measure of the natural population in $\tilde{X}\,^2\Sigma^+(100)$. (b) $\tilde{X}\,^2\Sigma^+(100)$ population with and without pumping light applied in region D1. This provides a measure of the population pumped into $\tilde{X}\,^2\Sigma^+(100)$ due to the high-field optical pumping step.

mulate in $\tilde{X}\,^2\Sigma^+(100)$ and experience some, but not all, of the theoretical maximum deceleration. Adding an $\tilde{X}\,^2\Sigma^+(100)$ repumper somewhere in the decelerator could be used to further increase the slowed signal, but we have not taken efforts to do so with CaOH molecules. In the future, when working with molecules that have less favorable branching ratios, adding such a repumper may be warranted.

7.3 CaOH deceleration

The Zeeman-Sisyphus deceleration method is simple in the sense that energy removal is essentially guaranteed once the optical pumping steps are verified to be working correctly. Above, we have described the optical pumping tests and their efficiency. Now, we describe measurements of the velocity distributions that demonstrate deceleration of CaOH molecules. By measuring how the velocity distributions change when optical pumping light is applied in regions D1, D2, and D3 we can study the efficiency of deceleration.

In order to maximize the number of slowed molecules, we used a beam source with the lowest possible output velocity. Following the results of Ch. 3, we used a two-stage cell connected to our ^{3}He pot. The second cell was 40 mm long and separated from the first cell by a 2.5 mm gap. When pumping on the ^{3}He pot, the second cell reaches $0.7 - 0.8$ K. To avoid speedups due to methanol or water "icing" the cell, we chose to ablate pressed targets composed of $Ca(OH)_2$, despite their lower reliability. Typical ^{3}He buffer-gas flow rates of $3 - 5$ sccm were used.

7.3.1 CaOH velocity detection

To detect the CaOH velocity distribution, we kept the $\tilde{X}\,^2\Sigma^+(000) \rightarrow \tilde{A}\,^2\Pi_{1/2}(000)$ detection laser transverse to the molecular beam and moved the $\tilde{X}\,^2\Sigma^+(100) \rightarrow \tilde{A}\,^2\Pi_{1/2}(000)$ laser to a Doppler-sensitive direction (either counter-propagating against the molecular beam or directed at 45° relative to the molecular beam). The detuning from transverse resonance at which the Doppler-shifted resonance occurs is then converted to an inferred velocity using the relativistic Doppler shift formula. The natural linewidth of the CaOH $\tilde{A}\,^2\Pi_{1/2}(000)$ state is $\Gamma = 2\pi \times 6.4$ MHz, which sets the velocity resolution to around 3 m/s. We had to eliminate a number of systematic effects related to velocity detection in order to extract clean velocity distributions. These included carefully compensation the fringing magnetic field from the Zeeman-Sisyphus magnets in the detection region, reducing the detection laser powers used, and detecting with a single spin-rotation sideband on the $\tilde{X}\,^2\Sigma^+(100)$ detection laser beam.

Even after zeroing out the detection region magnetic field, we still observed spurious signals due to off-resonant scattering from one of the sidebands present in the detection region. While we found some success in suppressing these off-resonant signals by reducing the detection power (typically less than 5 mW of $\tilde{X}\,^2\Sigma^+(100)$ power was used), the most reliable way to eliminate them was to perform velocity detection with just a single sideband on the $\tilde{X}\,^2\Sigma^+(100)$ laser beam and

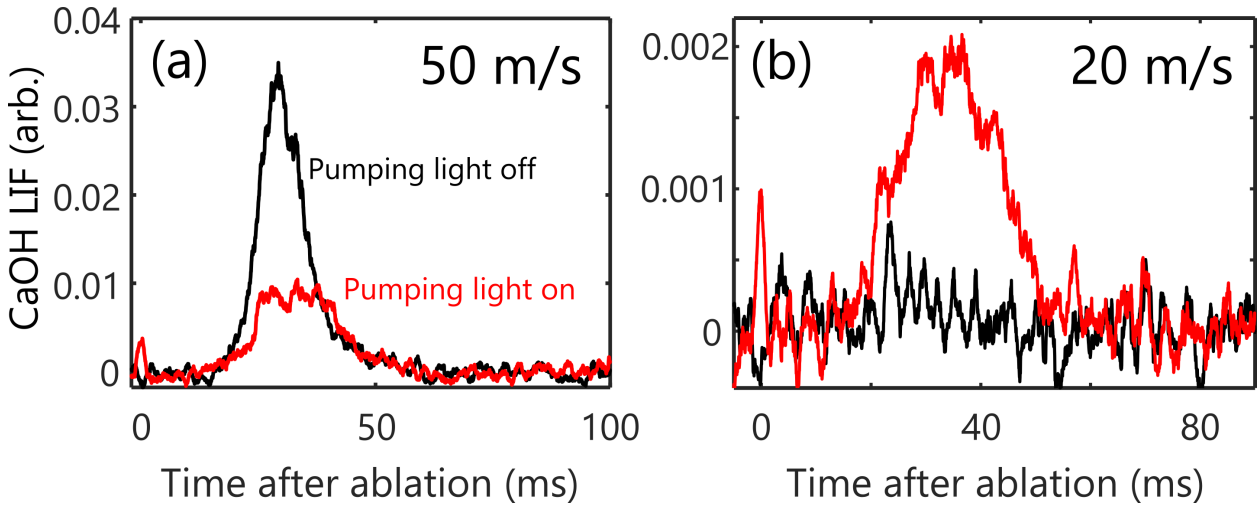

Figure 7.14: Timetraces providing evidence of deceleration through depletion of high velocity classes and enhancement of signal at low velocities. (a) 50 m/s velocity class and (b) 20 m/s velocity class. The magnets are always on, but optical pumping light is off (on) for the black (red) traces.

measure velocities relative to the bluest ($J'' = 1/2$) transition component. Finally, off-resonance signals can be reduced further by integrating the fluorescence signal only at times *after* the earliest possible time-of-arrival for a given velocity class. The earliest possible time can be determined based on simple kinematics considering the velocity at which population is detected and the distance between source and detection regions.

7.3.2 CaOH deceleration results

The initial deceleration data was taken without a magnetic guide installed and without state-preparation optical pumping (regions S1 and S2). After verifying all optical pumping steps in regions D1, D2, and D3, we conducted velocity-sensitive measurements of the CaOH beams. Some early results are shown in Fig. 7.14. The optical pumping light leads to a significant reduction in number of molecules detected at 50 m/s [Fig. 7.14(a)]. Meanwhile, there is a marked increase in signal detected at 20 m/s, as seen in Fig. 7.14(b). This transfer of population from high to low velocities was the first sign of deceleration. However, the absolute signal at 20 m/s was relatively low and it was difficult to discern any signal at lower velocities. Simulations of the deceleration process sug-

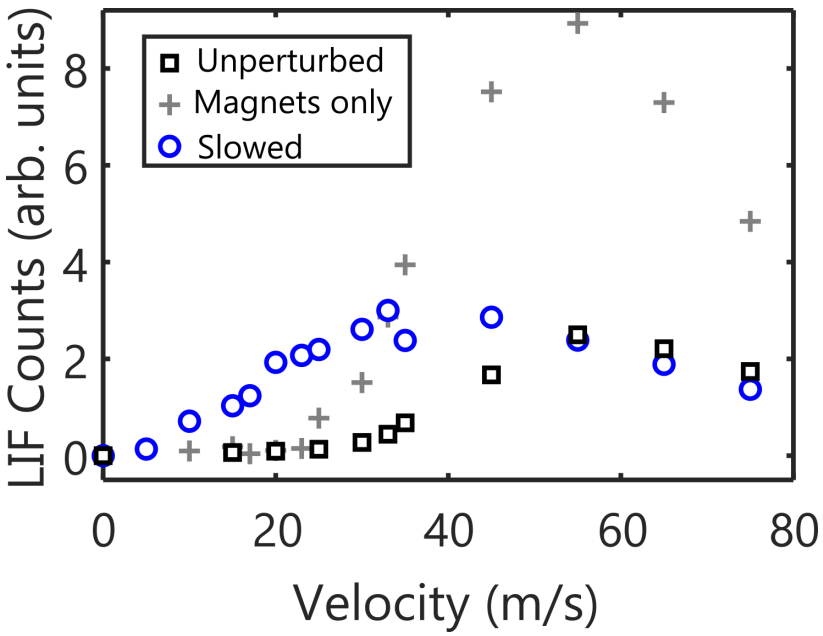

Figure 7.15: CaOH velocity distributions for an unperturbed beam, an unslowed beam passing through magnets energized at 40 A, and a slowed molecular beam (*without* state-preparation pumping in region S1).

gested that nearly all of the slowed population was lost while propagating the ~ 40 cm between decelerator output and detection region.

Adding a magnetic guide was predicted to increase the slow molecule flux arriving in the detection region by at least a factor of $5\times$. The guide described in Sec. 7.5.3 was installed in order to realize these gains. In Fig. 7.15 we plot the measured velocity distributions with various combinations of laser light and/or slowing magnetic fields applied: "unperturbed" (magnets and pumping light off), "magnets only" (coils energized to 40 A, no pumping light), and "slowed" (coils energized to 40 A and pumping light applied). In all cases, there is no state-preparation pumping applied in region S1, but pumping in region S2 is applied in order for molecules exiting the decelerator in SFS states to be transmitted through the magnetic guide. Based on independent calibration of the fluorescence detection system, we estimate that, to within a factor of two, the full molecular beam contains 1.5×10^5 molecules per pulse in the detection region. In the unperturbed molecular beam, the population with velocities below 20 m/s is consistent with zero; we estimate an upper bound

of 0.2% of the population in this range. Fewer than 0.02% of the molecules have velocities below 10 m/s. Note that simply energizing the coils increases the detected molecule number by a factor of about $3\times$, an effect that is understood to be due to order-of-unity focusing effects caused by the transverse field distribution within the Zeeman-Sisyphus coils. Our numerical simulations of the slowing process, which include the three-dimensional field distribution, capture this effect accurately. Applying the optical pumping light then produces a dramatic shift in the low-velocity tail of the distribution, producing a large fraction of molecules with velocities below 20 m/s. For the slowed beam, the fractions of molecules (relative to the unperturbed population) below 20 m/s and 10 m/s increase to $9(2)\%$ and $1.5(3)\%$, respectively.

The number of slow molecules can be increased by applying state-preparation pumping light in region S1. When this is done, the number of molecules increases by nearly a factor of $2\times$, as was discussed previously. The results of slowing measurements that include optical pumping in region S1 are shown in Fig. 7.16. When this is done, the fraction of slow molecules rises to $24(3)\%$ below 20 m/s and $3.5(5)\%$ below 10 m/s. The fraction of slow molecules is therefore enhanced by at least two orders of magnitude following deceleration. Based on the calibration of the fluorescence collection and the estimated number of molecules in the unperturbed beam, this means that approximately 3×10^4 molecules per pulse are found in velocity classes capturable by long-lived traps (e.g., MOT or magnetic). Figure 7.16 also shows the results of Monte Carlo simulations that take as input experimentally measured laser parameters and accurate, three-dimensional magnetic field profiles for both the superconducting coils and the magnetic guide. We find excellent agreement between the simulations and experimental results, indicating that the details of the slowing process are modeled accurately. Note that fewer than 10 photon scatters are used in the optical pumping steps to decelerate a CaOH molecule near the peak of the distribution by $\Delta v_f \approx 35$ m/s. By contrast, the radiative force due to 10 scattered photons would slow a CaOH molecule by just

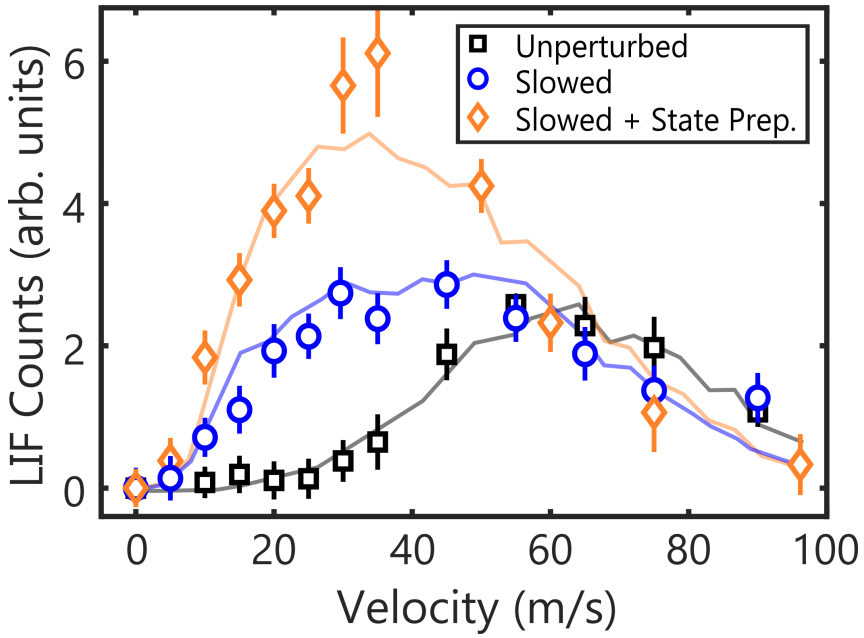

Figure 7.16: CaOH velocity distributions with (blue circles) and without (black squares) Zeeman-Sisyphus deceleration applied. Also shown (orange diamonds) is the velocity distribution when all molecules are pumped into WFS states in region S1 as they enter the decelerator. Solid lines are the results of Monte Carlo trajectory simulations that take into account the three-dimensional field profile inside the decelerator.

$\Delta v_f \approx 0.1$ m/s.

In order to gain additional confidence that we understand the decelerator's performance, we can look at the time-of-arrival distributions of individual velocity classes. Figure 7.17 shows the time-dependent laser-induced fluorescence resulting from molecules with forward velocity in the range $13 - 17$ m/s. Without the Zeeman-Sisyphus slowing applied, there is no detectable population in this velocity class. When the slowing light *is* applied, a large accumulation of population is observed in this velocity range. The peak laser-induced fluorescence occurs at $\Delta t_{\text{max}} \approx 42$ ms after ablation, well before the earliest possible arrival time for molecules produced at such velocities by the beam source ($\Delta t_{\text{natural}} \approx 75$ ms). This provides additional confirmation of deceleration: the molecules *detected* at 15 m/s must have originally been traveling faster in order to arrive in the detection region as early as they do. The observed time of arrival agrees well with the results of our numerical simulations, which predict that molecules produced near 50 m/s are slowed to around

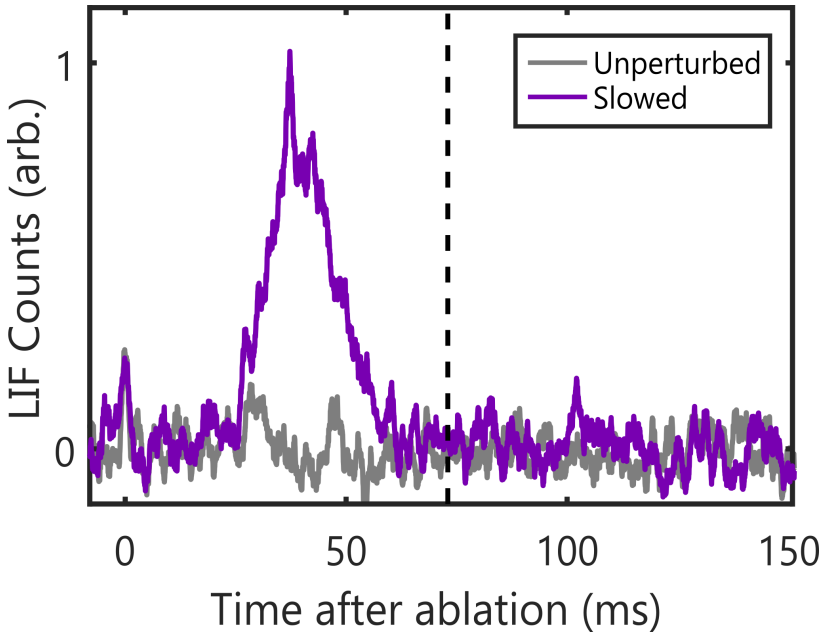

Figure 7.17: Laser-induced fluorescence due to molecules in the 15 m/s velocity class without (gray) and with (purple) the optical pumping lasers applied. The dashed vertical line indicates the earliest possible time of arrival for any molecules produced by the buffer-gas beam source at 15 m/s.

15 m/s and arrive in the detection region 40 ms after the ablation pulse.

7.4 Progress toward Zeeman-Sisyphus deceleration of YbOH

We are currently working to extend Zeeman-Sisyphus deceleration to YbOH. This is, in principle, a simple task: we must simply replace the lasers addressing CaOH transitions with a set tuned to the YbOH $\tilde{A}\,^2\Pi_{1/2}(000) \leftarrow \tilde{X}\,^2\Sigma^+(000)$ transition. The main challenge arises due to the complicated excited-state Zeeman structure in YbOH. Zeeman spectroscopy of YbOH $\tilde{A}\,^2\Pi_{1/2}(000) \leftarrow \tilde{X}\,^2\Sigma^+(000)$ band has previously been reported [173] and analysis of the ${}^OP_{12}(3)$ line indicated a Landé g-factor of $g_J \approx 0.26$. This is reasonably consistent with the parity-dependent g-factor predicted by a Curl-type relationship of approximately $g'_\ell \approx -0.865$ (see App. G for more details on the Zeeman structure and g-factors).[7] This is over an order of magnitude larger than the value mea-

[7]The relationship between g_J and g'_ℓ is derived in Ref. [173] and is $g_J = g'_\ell \frac{(J+1/2)}{2J(J+1)}$. For $J = 3/2$ this means $g_J = g'_\ell \times (4/15)$.

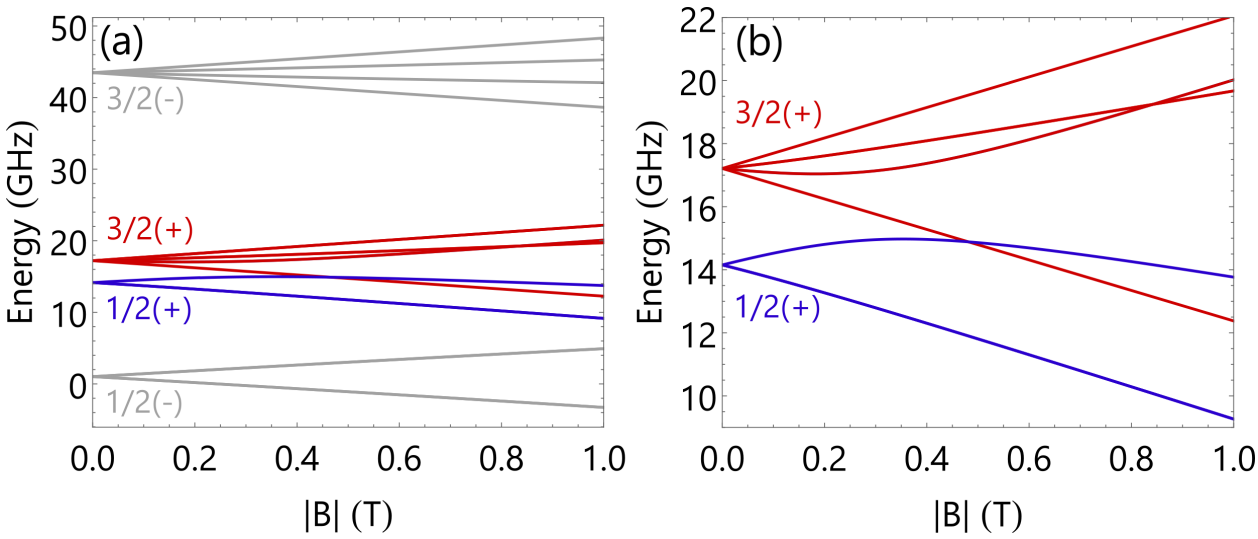

Figure 7.18: Zeeman structure of the YbOH $\tilde{A}\,^2\Pi_{1/2}(000)$ levels with $J' \leq 3/2$, plotted up to 1 T. States are labeled according to their zero-field quantum numbers $J(p)$, where p is the parity. States with the same parity as the $N'' = 1$ state are shown in gray. Levels that correlate with $J' = 1/2$ at $\mathcal{B} = 0$ are shown in blue and those that correlate with $J' = 3/2$ are shown in red. (a) All $J' = 1/2$ and $3/2$ levels. (b) The $J' = 1/2$ and $3/2$ levels with positive parity.

sured for CaOH. A plot of the YbOH $\tilde{A}\,^2\Pi_{1/2}(000)$ Zeeman tuning showing all states with $J' \leq 3/2$ is presented in Fig. 7.18.

The large g'_ℓ in combination with the large Λ-type doubling of the YbOH $\tilde{A}\,^2\Pi_{1/2}(000)$ state implies significant mixing between $J' = 1/2$ and $J' = 3/2$ states will occur and that the Zeeman shifts will become nonlinear at fields as low as about 0.2 T (as is observed in Fig. 7.18). This J-mixing is likely to destroy the rotational closure that is typically assumed to hold when driving the $P(1)$ line. While this, on its own, does not rule out Zeeman-Sisyphus deceleration of YbOH, it does potentially mean that additional rotational repumping lasers will be required to slow without accumulating population in the $N'' = 3, J'' = 5/2$ state.[8]

Following a similar procedure to that used for CaOH (see Sec. 7.2), we have performed initial YbOH optical pumping tests by monitoring the population transmitted through the magnetic guide while applying pumping light in region D1. The signal being monitored comes from pumping *away* from the detected states and therefore cannot confirm that we are correctly pumping from

[8]Decays to the $N'' = 3, J'' = 7/2$ spin-rotation component are excluded by the $\Delta J = \pm 1$ selection rule.

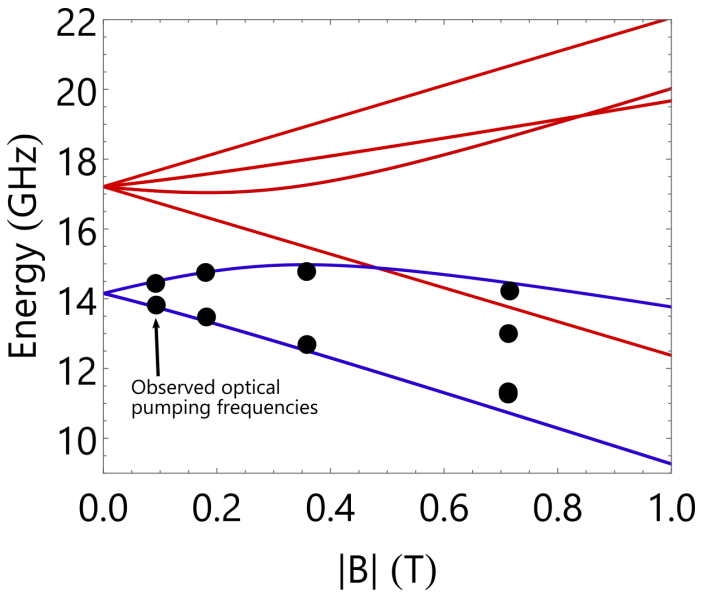

Figure 7.19: Spin-flip optical pumipng transitions in YbOH. Theoretical Zeeman energies for the excited state are plotted as colored lines. The value of $g'_\ell\,(=-0.865)$ used to generate these curves comes from a Curl-type prediction. The black dots indicate the excited state energies inferred from optical pumping measurements in the D1 high-field region (i.e., transition frequencies after subtracting out the $1\mu_B$ ground-state Zeeman shift.

WFS to SFS manifolds. Nonetheless, monitoring depletion of the WFS states gives a reliable way to map out the excited-state Zeeman shifts in detail. By subtracting off the nearly-linear ground-state Zeeman shifts, we can extract the approximate excited-state energies as a function of $\mathcal{B}$. These are plotted in Fig. 7.19 and we find reasonable agreement with theoretical predictions using the g'_ℓ derived from a Curl-type relationship (see App. G).

7.5 Zeeman-Sisyphus apparatus

In this section, we describe the design and construction of the superconducting magnets that make up our Zeeman-Sisyphus decelerator. After describing the magnets themselves, we provide a summary of the cryogenic chamber that was built to house the magnets. Finally, we discuss the magnetic guide that was installed to help increase the number of molecules that are ultimately detected in the downstream UHV chamber.

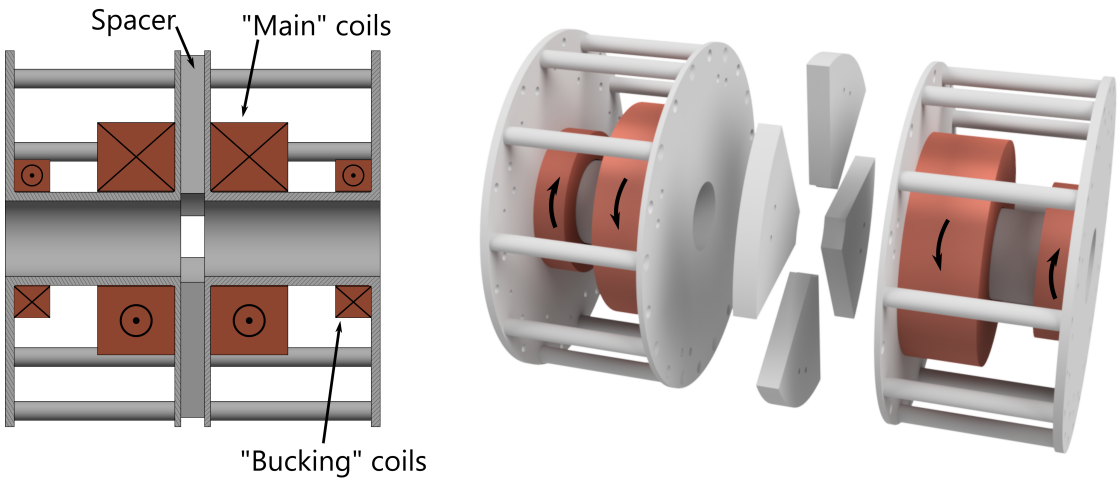

Figure 7.20: Mechanical drawing (left) and exploded view (right) of a single stage of the Zeeman-Sisyphus decelerator. The central bore has a 2.54 cm diameter and the overall length of the coil unit is approximately 12.5 cm.

7.5.1 Magnet design

The magnet assembly used for Zeeman-Sisyphus deceleration consists of two compensated Helmholtz units (CHUs). Mechanical drawings of a CHU are presented in Fig. 7.20. A single CHU (overall length 12.6 cm) comprises a set of "main" coils run in near-Helmholtz configuration and a pair of "bucking" coils with current running in opposite direction. The bucking coils make possible a shorter overall beamline, both by allowing CHUs to be placed in closer proximity to one another and by reducing the fringing field from the decelerator at the location of any downstream detection and/or trapping regions.

Each main/bucking coil pair is wound onto a bobbin (5.9 cm long, 2.54 cm diameter inner bore) machined from Al6061. Al6061 was chosen due to its relatively good thermal conductivity, and based on the differential thermal contraction between the coils and the bobbin. We want the bobbin to shrink more than the coils upon cooling to 4 K. This ensures that the coils cannot move, and potentially initiate a quench, as they are energized. Thus, for our purposes Al6061 is a better choice than a titanium alloy. In addition, the rods near the outer radius of each bobbin are used to pre-stress the assembly in anticipation of outward forces from the energized magnets.

Two bobbins are combined with a set of spacers (8 mm width) to produce a complete CHU. The spacers are designed to maintain transverse optical access over an 8 mm wide and 1.5 cm tall region at the center of each CHU (regions D1 and D3 in Fig. 7.2). When two CHUs are mounted next to each other for Zeeman-Sisyphus deceleration, a 2.5 cm gap between the CHUs provides similar access in the low-field region (D2 in Fig. 7.2). The coil forms experience forces both due to the attraction between the two main coils and repulsion between the main and bucking coils. Due to the spacer, attraction between the main Helmholtz coils compresses nearly solid metal. Because the spacer can take up this compression between the two halves of the bobbin, the "inner" face of each bobbin is only 2 mm thick. We used COMSOL to study the bending of this face and found that all stresses remained well below the yield strength of ~ 40 ksi. On the other hand, when the system is fully energized, each bucking coil is repelled from the nearest main coil by approximately 1300 N (300 lb). The "outer" face of each bobbin is therefore thicker (~ 3 mm) and a fillet of radius 0.79 mm is included to prevent stress concentration. Numerical simulations in COMSOL showed that this radius maintains stress at the outer corner below about 10 ksi, safely below the yield strength of ~ 40 ksi.

Coils made of NbTi wire were wound on these bobbins by American Magnetics Inc. (AMI). AMI reports a measured inductance of 0.5 H and a field-to-current ratio of around 0.698 kG/A.The peak on-axis field of each solenoid can be tuned to a maximum of 2.8 T when driven at a current of 40 A. This peak magnetic field was chosen in order to maximize energy removal without surpassing the field at which the WFS $N'' = 1$ and SFS $N'' = 3$ levels cross in YbOH. A photograph of the coils installed in the cryogenic system is shown in Fig. 7.21.

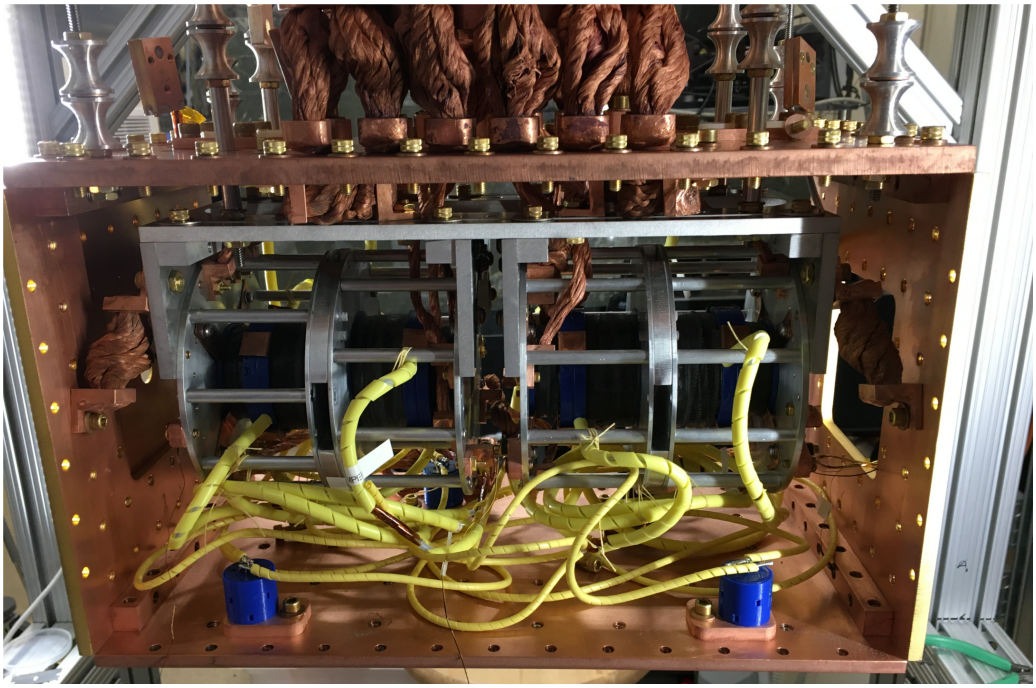

Figure 7.21: Photograph of Zeeman-Sisyphus magnets installed in 4 K shield. Heat links connecting the coil bobbin to the 4 K stage are visible. Two quench protection diodes (blue, bolted to the bottom fo the 4 K shield) are visible.

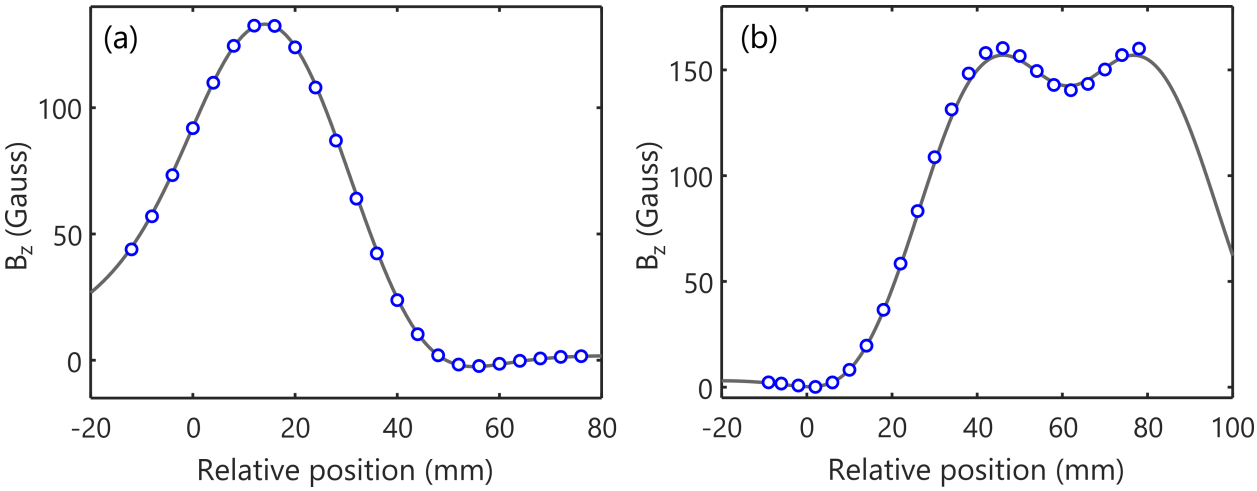

Figure 7.22: Comparison of measured and simulated magnetic fields along the central axis of a Helmholtz unit when 0.2 A is run through (a) a single bobbin ("main"/"bucking" coil pair) or (b) a complete CHU. The simulation is scaled up by 2% in order to optimize agreement on the peak heights.

Magnetic field profile

As an initial test of the magnets, we measured at room temperature the longitudinal field produced along the center of the coils when run at a current $I_{\text{test}} = 0.2$ A (see Fig. 7.22). We performed these measurements for both a single bobbin (one "main" and one "bucking" coil) as well as for a complete CHU. These tests allowed us to verify that the magnetic field profile was as designed and, importantly, to ensure that the magnetic field never crosses through zero along the length of the decelerator.[9] Note that while the coils wound on a *single* bobbin due produce a field that crosses through zero [Fig. 7.22(a)], a fully assembled CHU does not suffer from this problem [Fig. 7.22(b)]. The measured values were found to be approximately 2% larger than the simulated values. This disagreement could arise for a number of reasons, including slight inaccuracies in the test setup (e.g., probe or current calibration) or in the numerical model of the coils (AMI did not provide us with the exact wire diameter or number of windings used in each coil). It is not of major concern, as the disagreement corresponds to $\lesssim 0.05$ T at 2.8 T peak when the coils are fully energized.

In the final decelerator, two CHUs are placed sequentially along the beam line and run with their fields oriented in the same direction. The simulated field magnitude along the decelerator's central axis is plotted in Fig. 7.23. Figure 7.23(a) shows the full field profile along with the locations of optical pumping transitions used for deceleration (indicated as red boxes). The magnetic field reaches a local minimum at $z \approx 13.5$ cm. Figure 7.23(b) shows an expanded view in the vicinity of this minimum, demonstrating that $|\mathcal{B}| \geq 0.01$ T for all z. A contour plot of the magnetic field magnitude along the deceleration beam line is shown in Fig. 7.24. Note that the field increases with radius away from the central axis, a fact that leads to order-of-unity focusing effects for molecules

[9] Points where the magnetic field crosses through zero are dangerous because they could lead to loss of spin polarization.

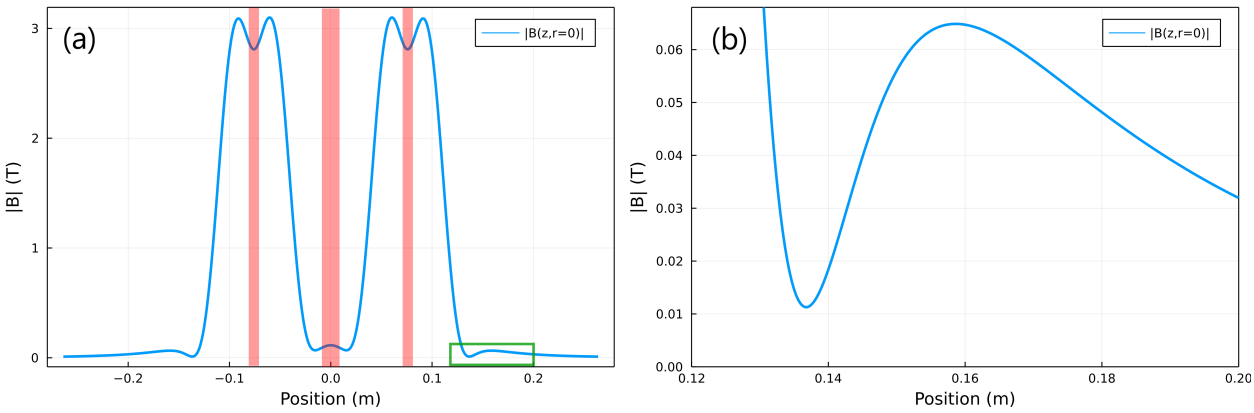

Figure 7.23: Magnetic field magnitude along the central axis of the superconducting coils. (a) Computed value of $|B(z, r = 0)|$ as a function of position. The locations of optical pumping transitions used for deceleration (D1, D2, D3) are indicated as red shaded regions. The region enclosed by a green rectangle is shown in more detail in (b). (b) Expanded view near the local minimum following the second superconducting coil. It is important to note that the magnetic field never crosses through zero, remaining always above approximately 0.015 T.

traversing the decelerator.

7.5.2 Cryogenic system

The magnets are cooled by a pulse tube refrigerator (Cryomech PT420) in a dedicated vacuum chamber. While this adds some experimental complexity, principally in the need to use an additional pulse tube and associated radiation shields, it is beneficial to cool the magnets separately from the beam source in order to obtain the lowest base temperatures and to allow independent thermal cycling of the magnet and beam source chambers.

An overview of the magnet cryostat is shown in Fig. 7.25. The cryostat is enclosed in an aluminum vacuum chamber that had previously been used as a molecular beam source in our group. Two sets of radiation shields, one held at 40 K and one at 4 K, enclose and support the magnet assembly. The shields are cooled by a PT420 pulse tube with integrated damping pot.[10] In an effort to avoid pressure buildup due to small conductance between the shields, no superinsulation was used on the upstream or downstream faces of the shields. The 4 K upstream and downstream

[10]For our application the damping pot is not particularly necessary.

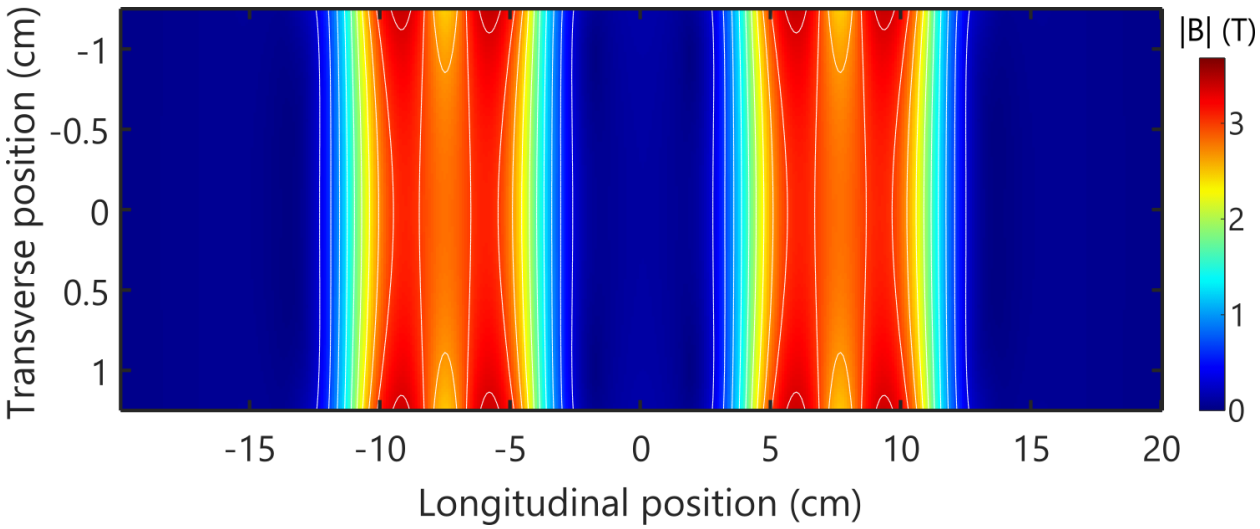

Figure 7.24: Contour plot of the magnetic field inside of the Zeeman-Sisyphus decelerator. The vertical extents span the inner bore of the coil forms. Optical pumping regions D1 and D3 are located at longitudinal position $\sim \pm 7.5$ cm and region D2 is located at the zero of the longitudinal position axis.

faces were gold plated to lower their emissivities to $\epsilon \sim 0.05$ and prevent oxidation. To ensure the entire magnet assembly reaches the minimum possible temperature, a number of copper heat links were run from the 4 K stage of the PT420 to the magnet bobbins. Seven heat links were bolted to the vertical faces of each magnet bobbin, split between the upstream and downstream faces. Additional heat links were run from the bottom of the 4 K shields. Charcoal sorbs are also bolted around the 4 K shield to provide additional pumping for He buffer gas passing through the chamber. During buffer-gas flow, room temperature ion gauges read a pressure around 3×10^{-8} torr, but the pressure inside the cryogenic region may be lower due to the high-speed cryopumping of the sorbs.

The magnets' current leads consist of three parts: copper resistive leads between 300 K and 40 K, high-T_c superconducting (HTS) leads between 40 K and 4 K, and low-T_c superconducting (LTS) leads between 4 K and the magnets themselves. Four hermetically sealed high-current feedthroughs[11] on the top of the chamber are used to drive the two superconducting coils independently. In the design phase, we considered both copper and brass resistive leads. Brass has a

[11] Accu-Glass part number 112480; fluted ceramic with copper conductor, rated to 150 A.

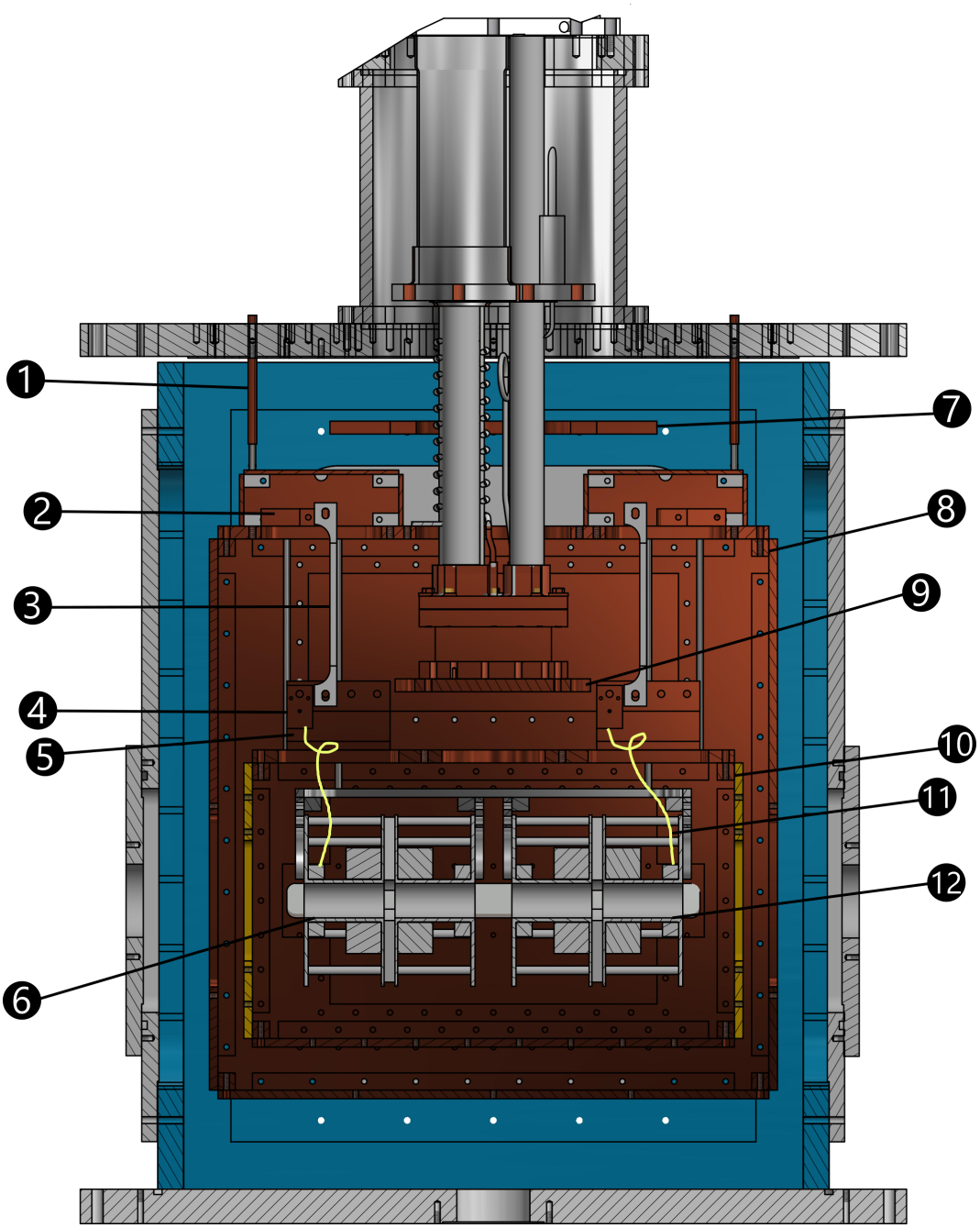

Figure 7.25: Cryogenic chamber housing the Zeeman-Sisyphus coils. This image shows a section view through the chamber midplane. There are additional copies of the current feedthroughs, HTS and LTS leads, that are not shown. Molecular beam propagates from left to right in this image. 1 Current feedthrough. Two are shown, but there are four in total. 2 40 K heat sink and connection to HTS lead. 3 HTS lead. 4 Lug for LTS lead. 5 4 K heatsink block for HTS lead. 6 Upstream magnet bobbin. 7 Pulse tube 40 K stage; attached to 40 K shield via flexible heat links that are not shown. 8 40 K shield. 9 Pulse tube 4 K stage; attached to 4 K shield and magnet bobbins via flexible heat links that are not shown. 10 4 K shield; front and back plates are gold-plated, while the remainder is unplated Cu10100. 11 LTS wire running between heat sink lug and the downstream coil. Two are shown, but there are four in total. 12 Downstream magnet bobbin.

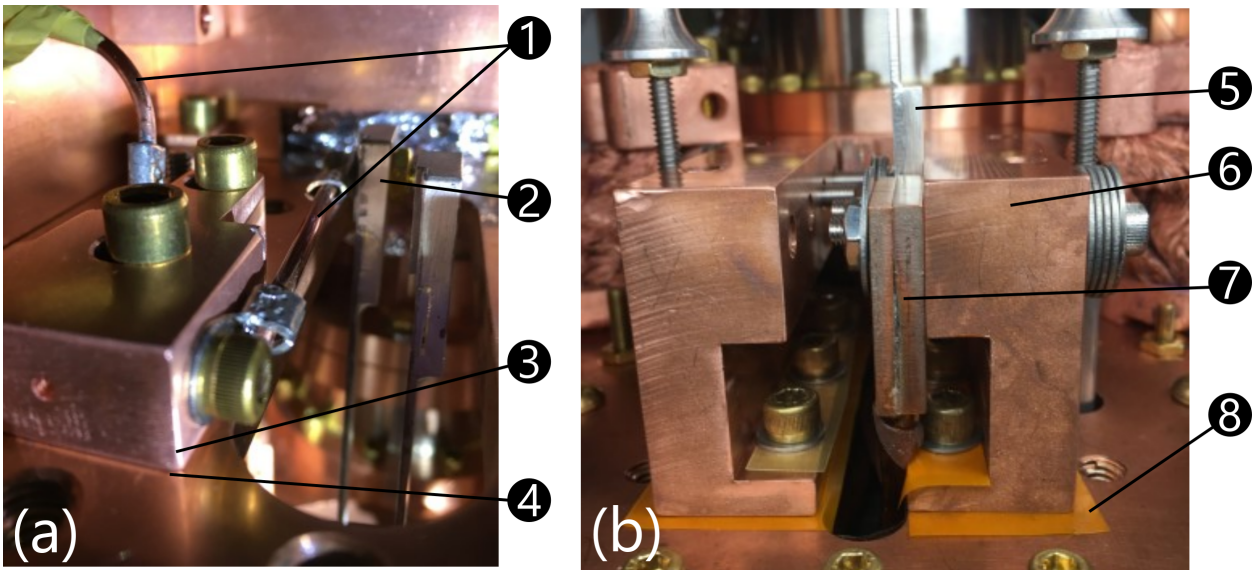

Figure 7.26: Heat sinking and electrical connection for the superconducting coil leads. (a) Connections on the 40 K shield. Components are labeled as: ❶ Resistive copper leads. ❷ Top of HTS lead. ❸ 40 K heat sink block. ❹ Kapton insulation. (b) Connections on the 4 K shield. Components are labeled as: ❺ Bottom of HTS lead. ❻ 4 K heat sink block. ❼ Top of LTS lead. ❽ Kapton insulation.

lower thermal conductivity than copper but also a higher resistivity (both by a factor of about $4\times$ at room temperature). At optimal wire dimensions[12] it was possible to design for resistive leads that would deliver about 3 W per lead to the 40 K stage.[13] The vacuum side of each feedthrough is connected to a set of 2 mm diameter, 10 cm long copper wires that serve as our resistive leads. These are heat sunk at 40 K at the connection to the top of the HTS leads [see Fig. 7.26(a)].

Two sets of HTS leads (four total) are used to carry current between the 40 K and 4 K stages. The leads are customized ballasted[14] HTS-110 leads (GMW Associates). They have an overall length of 150 mm and are rated for a maximum current of 75 A. The conductive heat load per pair of leads is specified by the manufacturer to be at most 72 mW between 64 K and 4 K. The top of each HTS lead is connected to the corresponding resistive lead as was shown in Fig. 7.26(a), and the bottom is connected to the LTS lead as shown in Fig. 7.26(b). Each heat sink is bolted to the

[12]The relevant geometry factor is $G \equiv \text{Area/Length} \approx 2 \times 10^{-5}$ m.

[13]Conductive *cooling* of the atmosphere side of the feedthrough occurs through the resistive lead/feedthrough assembly. We apply a small ~ 1 W heat load to each feedthrough to keep them above the dew point.

[14]The leads have a current shunt incorporated.

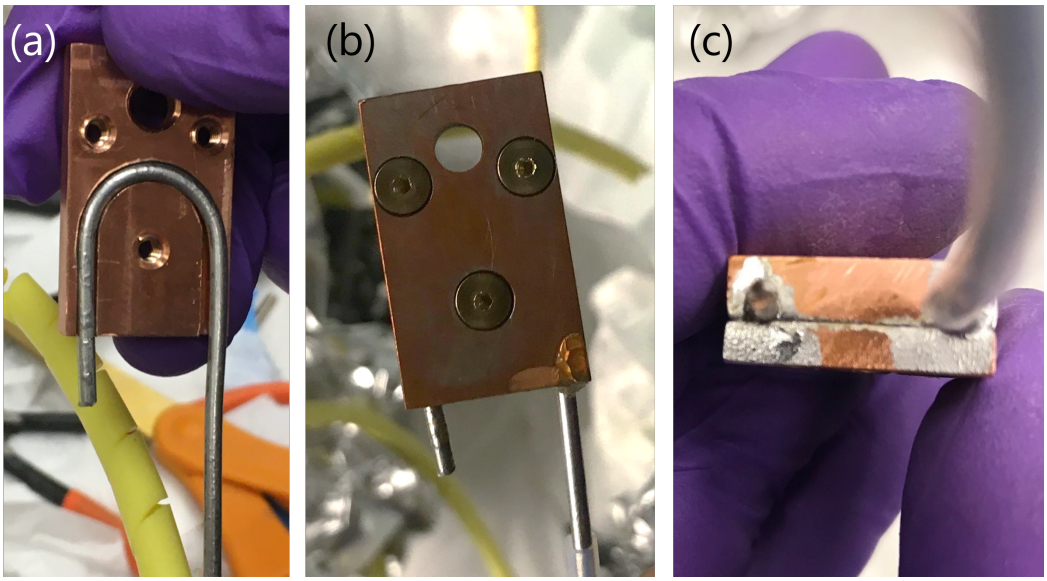

Figure 7.27: Construction of lugs to make electrical connections to the LTS leads. (a) Disassembled lug with LTS lead placed in the groove. (b) Assembled lug after clamping screws are inserted. (c) Bottom of lug following soldering the joint.

appropriate radiation shield with electrical insulation provided by a 0.002 in thick sheet of Kapton. This thickness was chosen to avoid the possibility of breaking through the sheet.

The LTS leads are also attached to 4 K heat sinking blocks shown in Fig. 7.26(b). We machined a custom set of Cu10100 lugs (see Fig. 7.27) to attach the LTS leads. The lugs are made up of two pieces of 3/16" thick copper, each of which has a groove machined in it with width slightly larger than the LTS lead diameter. The LTS leads were carefully bent around a post and inserted into the groove. After insertion of the lead, the other side of the lug was clamped shut by three #4-40 brass screws. Finally, the entire lug was heated by a heat gun and Sn/Pb solder was used to improve electrical contact.

7.5.3 Permanent magnetic guide

Following deceleration, slow molecules must travel from the end of the superconducting coils to a room-temperature detection region further downstream. Due to the constraints of our vacuum

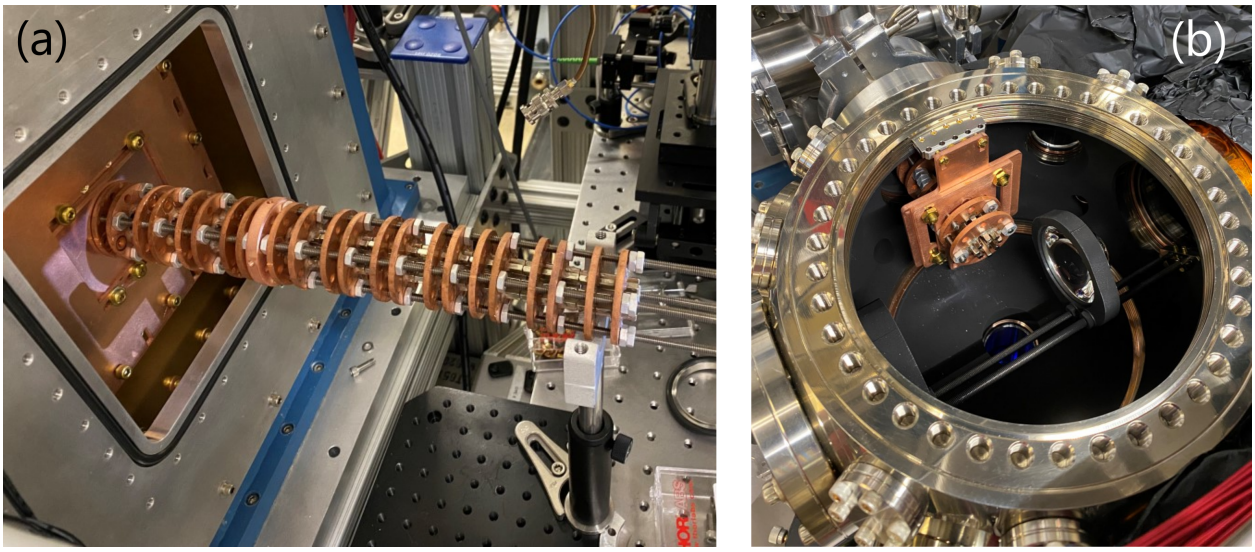

Figure 7.28: Magnetic guide during installation. (a) Guide assembly after being attached to the 4 K and 40 K shield of the magnet chamber. (b) Output of the magnetic guide as it entering the detection chamber. Two axes of adjustment are available to minimize strain on the assembly.

chamber, it is difficult to position this detection region closer than about 25 cm beyond the end of the downstream coil form.[15] Molecules may be lost while traversing this distance, both because of natural divergence and also because of defocusing forces caused by fringing fields at the output of the superconducting coils. Despite these effects, the transverse temperature of molecules exiting the decelerator is not particularly high: Monte Carlo simulations predict a transverse velocity distribution with characteristic speed around 1 m/s ($\sim$5 mK). It is straightforward to construct magnetic guides with depths at least 100 mK, so guiding the molecules to prevent divergence losses is possible.

We constructed a multi-stage octupole magnetic guide spanning the distance between the 4 K shield of the magnet chamber and the MOT chamber used for detection (see Fig. 7.28). Each stage of the guide is built from eight 1 in$\times$1/8 in$\times$1/8 in N42 NdFeB bar magnets magnetized through their thickness (BX022 from K&J Magnetics). The magnets are arranged in an octupole configura-

[15]This limitation is not fundamental, but rather arises because we reused an old vacuum chamber to house the magnets. Future iterations of the magnet design could in principle reduce this distance.

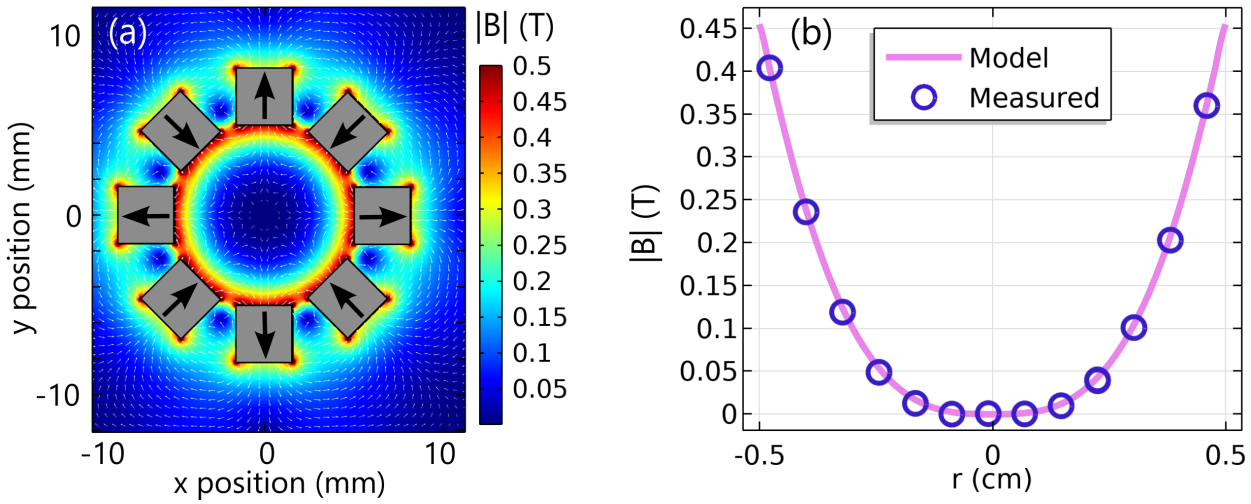

Figure 7.29: Magnetic field distribution in the permanent magnetic guide. (a) Computed $|\mathcal{B}|$ at the center of each magnetic guide stage. Arrows on each magnet indicate the direction of magnetization. (b) $|\mathcal{B}|$ as a function of radial position at the center of each guide stage. The solid line is the output of a COMSOL simulation while the points are measured values. The field magnitude has an approximately cubic dependence on radial position.

tion, as indicated in Fig. 7.29.[16] The stages are arranged along the length of four titanium threaded rods and positioned to achieve minimal gap between consecutive stages. The simulated and measured fields for this magnet assembly are shown in Fig. 7.29. For $^2\Sigma^+$ molecules, the maximum measured field is equivalent to about 270 mK, more than sufficient to confine the transverse velocities typical of our molecular beams.

Molecule-He collisions within the guide would be a potential concern if there is any buildup of He buffer-gas flow inside the guide. The guide has a relatively open structure that should help prevent a pressure rise in the interior. However, in our design the guide fits relatively snugly within a section of KF50 tubing. A turbopump near the middle of the guide was added to improve pumping along the length of the guide. Base pressures around 1×10^{-7} torr are typical with ~ 4 sccm of buffer-gas flow. While we have not observed definitive signs of beam attenuation in the guide, the pressure is borderline acceptable. Future designs should aim to achieve lower base pressures by improving conductance around the guide.

[16] Stycast 2850FT is used for magnets near the cryogenic chamber while Masterbond EP30-2 is used for magnets in the room-temperature regions.

When I looked around I saw and heard none like me. Was I, then, a monster, a blot upon the earth, from which all men fled and whom all men disowned?

Mary Shelley, "Frankenstein"

8

Observation and Spectroscopy of $YbOCH_3$

While the bulk of this thesis has been focused on methods to prepare YbOH molecules for an EDM experiment, it is important to ask whether there are not more favorable species to use for such an experiment. One of the most natural options would be $YbOCH_3$, which essentially results from substituting a methyl group in place of the hydrogen in YbOH. As a symmetric top, $YbOCH_3$ would offer some intrinsic advantages over YbOH because there are easily polarized states that arise from rotation of the hydrogen nuclei about the Yb-O-C axis (called $K'' = 1$ states— see below). Due to their low energy, these states are much longer lived than the YbOH bending mode. While the YbOH $\ell = 1$ bending mode's lifetime is estimated to be about 1 s, the $YbOCH_3$ $K'' = 1$

states could have natural lifetimes $\gg 10$ s. If fully utilized, this would lead to an intrinsic electron EDM sensitivity more than $30\times$ greater than that of YbOH.

Unfortunately, no previous spectroscopy of $YbOCH_3$ has been reported. In this chapter, we describe the first spectroscopic characterization of $YbOCH_3$ molecules.[1] In Sec. 8.1 we motivate the use of symmetric top molecules for precision measurements. Section 8.2 discusses low-resolution spectroscopy of $YbOCH_3$ that was conducted in collaboration with Tim Steimle; we observe several electronic transitions and determine vibrational branching ratios. We also compare these measurements to density functional theory calculations that aided in assignment. In Sec. 8.3 we describe rotationally-resolved, high-resolution spectra collected for the $\tilde{A} \leftarrow \tilde{X}$ origin band and preliminary features of their assignment. We conclude in Sec. 8.4 with some of the next steps that are required to understand $YbOCH_3$ in more detail.

8.1 Why symmetric top molecules?

To the best of our knowledge, $YbOCH_3$ is the highest-Z symmetric top molecule amenable to optical cycling to be experimentally characterized. It is a promising system for precision tests of parity and/or time-reversal symmetry violation. In addition to the high-Z nucleus that leads to a valence electron experiencing strong relativistic effects, the presence of easily polarized, internal co-magnetometer states in the $|K''| \neq 0$ manifolds allow full access to a large internal effective electric field and rejection of potential systematic errors [21, 26]. Consider, for example, laser-cooled and trapped $YbOCH_3$ used for future tests of the electron EDM. Under the reasonable assumptions that the internal effective electric field of $YbOCH_3$ matches that of YbOH ($\mathcal{E}_{\text{eff}} \approx 25\,\text{GV/cm}$) [19, 244, 245] and that achievable experimental lifetimes approach $10-100$ s [246–248], 10^5 trapped $YbOCH_3$ molecules and one week of averaging could provide a statistical sensitivity

[1] Some of this chapter appears in Ref. [146].

to the eEDM four orders of magnitude beyond the current limit [24]. This is about an order of magnitude more sensitive than an equivalent measurement in YbOH.

Even with a much smaller photon budget, transverse laser cooling and high-fidelity readout enabled by rapid photon cycling could lead to new limits on precision tests of CP-violation [249]. Consider an experiment using ^{173}YbOCH$_3$ in a molecular beam to search for a nuclear magnetic quadrupole moment (MQM). Combining the demonstrated production of YbOCH$_3$, enhanced chemical production [194], and transverse laser cooling using <150 photons [250], bright beams with $> 10^7$ molecules per pulse in the science state appear possible. Forward velocities around 50 m/s and laser cooling to < 1 mK in the transverse direction [250, 251] would make coherence times on the order of 10 ms feasible. Under these conditions, a sensitivity on the order of 10 μHz would be achievable with one week of averaging. Assuming (reasonably) that the nuclear MQM sensitivity parameter is similar to that of YbOH, this would be near or below the level required to set new limits on T-violating BSM physics, e.g., the QCD $\bar{\theta}$ parameter or the difference of quark chromo-EDMs [224, 252]. Note that symmetric top molecules offer some intrinsic advantages over linear species for such measurements, including requiring smaller laboratory electric fields for full polarization and that nuclear spin statistics ease the task of state preparation by naturally populating the $|K''| = 1$ science state [26].

YbOCH$_3$ is also an interesting candidate for possible tests of P-violation. Recently, the degenerate bending modes in open-shell linear triatomic molecules have been proposed for tests of nuclear spin-dependent parity violation [253, 254]. Similar searches could be conducted in symmetric top molecules that meet certain structural conditions. One key requirement of such an experiment is that the ground-state parity doubling is not smaller than all spin-rotation/hyperfine structure, such that opposite-parity states with the same total angular momentum may be Zeeman-tuned into near resonance. In ^{171}YbOCH$_3$, we expect that hyperfine and K-doublet splittings will be of the

same order of magnitude, ∼0.3 MHz [255]. The size of the K-doubling increases with N, so that by working in, e.g., the $N'' = 2$ or 3 state it may be possible to tune the parity-doubling to be larger than the hyperfine structure. Future measurements with hyperfine resolution will be required to determine the exact splittings. Alternatively, chiral variants such as YbOCHDT may be useful for studies of parity violation arising from P-odd cosmic fields, e.g., in searches for axion-like particles [38, 39]. Chiral species are predicted to be particularly sensitive to oscillating pseudovector fields that cannot be easily probed in existing spin-precession experiments [38]. Because such effects scale rapidly with Z [39], YbOCHDT may provide orders-of-magnitude increased sensitivity over previously considered chiral probes. Production and characterization of chiral ytterbium monomethyl, YbCHDT, may be especially promising by bringing the heavy nucleus closer to the chiral center.

8.2 Low-resolution excitation and DLIF spectroscopy

Our initial observation of $YbOCH_3$ occurred in the Steimle lab at Arizona State University. Molecular beams of $YbOCH_3$ were produced in a setup similar to that used in recent studies of YbOH [153, 172, 173]. Briefly, a rotating ytterbium rod is ablated at ∼20 Hz with a short pulse of 532 nm radiation ($\sim$ 10 ns, $\sim$ 5 mJ). The ablation plume is entrained in and reacted with a gas mixture of methanol vapor and Ar in a supersonic expansion. The gas mixture is produced by passing Ar at $\sim$ 4000 kPa over room-temperature liquid methanol (CH_3OH; vapor pressure $\sim$ 10 kPa). Typical pulse widths for the molecular beam are $\sim$ 50 μs. We used a number of complementary spectroscopic methods including two-dimensional (2D) spectroscopy, DLIF spectroscopy, radiative decay, and high-resolution excitation spectroscopy to conclusively confirm detection of $YbOCH_3$ and provide initial spectroscopic characterization.

For the 2D spectroscopy [256–258] and DLIF measurements, the free-jet expansion is probed

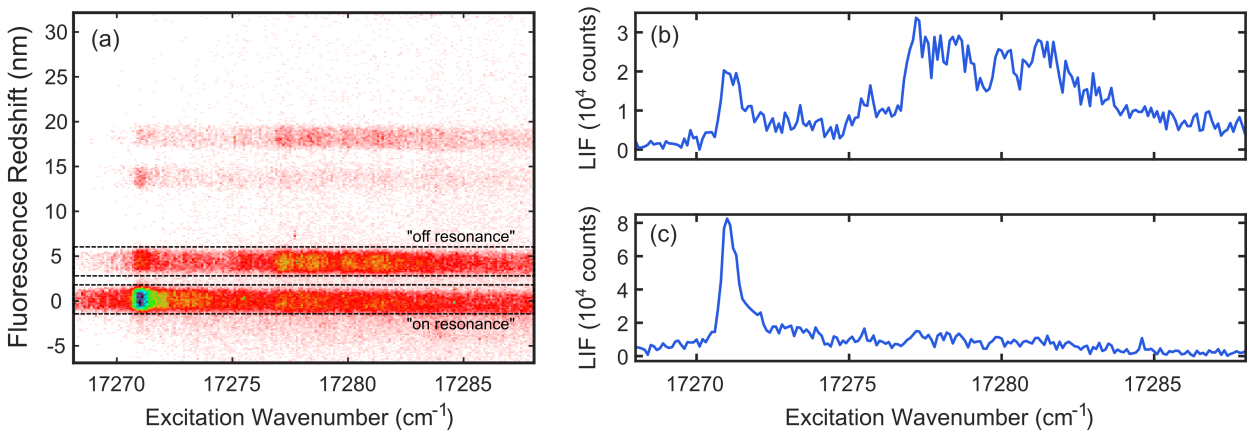

Figure 8.1: (a) Pulsed-dye laser 2D spectrum in the vicinity of the $YbOCH_3$ $\tilde{A}\ ^2E_{1/2} \leftarrow \tilde{X}\ ^2A_1$ bandhead. Integration at fixed fluorescence wavelength can be used to obtain excitation spectra. Color scale indicates number of LIF counts detected. Integration at fixed excitation wavenumber would yield DLIF spectra, but we describe higher resolution DLIF data below. (b) Excitation spectrum obtained by vertical integration in the region labeled "off-resonance." Strong decay to the bending mode is observed from approximately 10 cm^{-1} to the blue of the origin frequency (see text). (c) Excitation spectrum by vertical integration in the region labeled "on-resonance." A strong bandhead associated with the 0_0^0 $\tilde{A}\ ^2E_{1/2} \leftarrow \tilde{X}\ ^2A_1$ vibronic transition is observed, characteristic of a $^2E - ^2A_1$ transition.

approximately 10 cm downstream from the source using radiation from an excimer-pumped, tunable, pulsed dye laser (∼10 ns pulse width, ∼3 cm^{-1} linewidth). The molecular laser-induced fluorescence (LIF) is focused into a 0.67 m, high-efficiency (f-number = 6.0) Czerny-Turner-type monochromator with a low-dispersion grating (300 lines/mm). The DLIF from the grating is imaged on a cooled and temporally gated intensified charge-coupled device (ICCD). The CCD array is binned to produce an array of intensities versus emission wavelength. The ICCD can be gated with resolution $\lesssim$1 ns, which enables temporal separation of the LIF from background light due to the dye laser and ablation plume. The ICCD gate width is typically set to 200 ns and delayed 10 ns after the pulsed laser. The wavelength calibration and relative sensitivity of the spectrometer were calibrated prior to data collection using an argon pen lamp and blackbody source.

8.2.1 2D spectroscopy

Initial survey scans used 2D (excitation vs. DLIF) spectroscopy to search for $YbOCH_3$ fluorescence. A 75 nm-wide fluorescence spectral window was monitored while scanning the excitation laser

Table 8.1: Vibrational normal mode numbering and symmetry labels for $MOCH_3$ molecules under transformations of the C_{3v} point group.

Mode	Symmetry	Description
ν_1	a_1	CH_3 symmetric stretch
ν_2	a_1	CH_3 symmetric bend
ν_3	a_1	O-C stretch
ν_4	a_1	M-O stretch
ν_5	e	CH_3 asymmetric stretch
ν_6	e	CH_3 asymmetric bend
ν_7	e	O-CH_3 wag
ν_8	e	M-O-C bend

wavelength. To facilitate data analysis, this window tracked the excitation laser as it was scanned. The pulsed dye laser was scanned over a range of about 400 cm^{-1} near the YbOH $\tilde{A}\,^2\Pi_{1/2} \leftarrow \tilde{X}\,^2\Sigma^+$ origin band (17323 cm^{-1} [173]). A strong and broad fluorescence signal was observed around 17271 cm^{-1}. The 2D spectrum in the vicinity of this signal is shown in Fig. 8.1(a). The ground state vibrational frequencies observed in emission closely matched those expected of $YbOCH_3$, leading to an initial assignment of this as the $YbOCH_3$ $0_0^0\,\tilde{A}\,^2E_{1/2} \leftarrow \tilde{X}\,^2A_1$ band. (For convenience, we include the vibrational normal mode numbering and symmetry labeling in Tab. 8.1.) Ytterbium monohydroxide is also produced in the ablation reaction, and by comparing the intensities of the two species's origin bands we estimate that we produced about an order of magnitude more $YbOCH_3$ than YbOH.

We obtain the excitation spectra shown in Fig. 8.1(b) by vertically integrating ± 2 nm slices of the off-resonance fluorescence. Similarly, Fig. 8.1(c) is obtained by vertical integration of the on-resonance fluorescence. Horizontal integration at fixed excitation wavenumber can be used to obtain dispersed fluorescence traces, although these have lower resolution than the DLIF measurements described in Sec. 8.2.2.

The on-resonance detected excitation spectrum [Fig. 8.1(c)] exhibits an intense, sharp, blue-degraded band near 17271 cm^{-1} which is assigned as the $0_0^0\,\tilde{A}\,^2E_{1/2} \rightarrow \tilde{X}\,^2A_1$ emission. The

excitation spectrum is quite compact, implying that the geometry changes little upon excitation and that the electronic orbital angular momentum in the $\tilde{A}\,^2E$ state is largely unquenched (i.e., $\zeta_e \approx 1$) [259, 260]. The off-resonance excitation spectrum, shown in Fig. 8.1(b), is obtained by vertical integration over a ± 2 nm range centered $\sim$130 cm^{-1} to the red of the excitation wavelength (i.e., by monitoring the Stokes-shifted emission). The extracted excitation spectrum exhibits both the sharp band near 17271 cm^{-1} and a weaker, broader, and unstructured fluorescence feature near 17281 cm^{-1}. The latter is assigned as excitation from $\tilde{X}\ ^2A_1(v=0)$ to a state of unknown character that we simply designate as [17.28]. The relative intensities of the bands at 17271 cm^{-1} and 17281 cm^{-1} for the on- and off-resonance detection suggest that the bending mode in the [17.28] state is quite active.

Also evident in the 2D spectrum are Stokes-shifted signals centered about 400 cm^{-1} and 535 cm^{-1} to the red of the excitation. These are assigned as $4_1^0\,\tilde{A}\,^2E_{1/2} \rightarrow \tilde{X}\ ^2A_1$ and $4_1^0 8_1^0 \tilde{A}\ ^2E_{1/2} \rightarrow \tilde{X}\ ^2A_1$, respectively (with similar assignments for the [17.28] bands). Again, the relative intensities of these bands suggest higher bending mode activity in the [17.28] state. It is noteworthy that in YbOH there is also an unassigned vibronic state approximately 10 cm^{-1} above the $\tilde{A}\,^2\Pi_{1/2}(000)$ state [153]. A key difference is that in $YbOCH_3$ this higher-energy state couples preferentially to the Yb-O-C bending mode while in YbOH the analogous level exhibits a DLIF spectrum nearly identical to the diagonal origin band.

We also recorded 2D spectra in the vicinity of several bands involving excited vibrational levels in the $\tilde{X}\ ^2A_1$ and $\tilde{A}\ ^2E$ states. A weak feature was observed about 130 cm^{-1} to the red of the origin band near the expected $8_1^0\,\tilde{A}\,^2E_{1/2} \leftarrow \tilde{X}\,^2A_1$ vibronic transition. We observed two bands near the expected position of the $4_0^1\,\tilde{A}\,^2E_{1/2} \leftarrow \tilde{X}\ ^2A_1$ transition, approximately 400 cm^{-1} above the origin band [Fig. 8.2(a)]. These bands, near 17641 cm^{-1} (designated as the [17.64] state) and 17681 cm^{-1} (designated as the [17.68] state), are blue-shifted by 370 cm^{-1} and 410 cm^{-1} relative

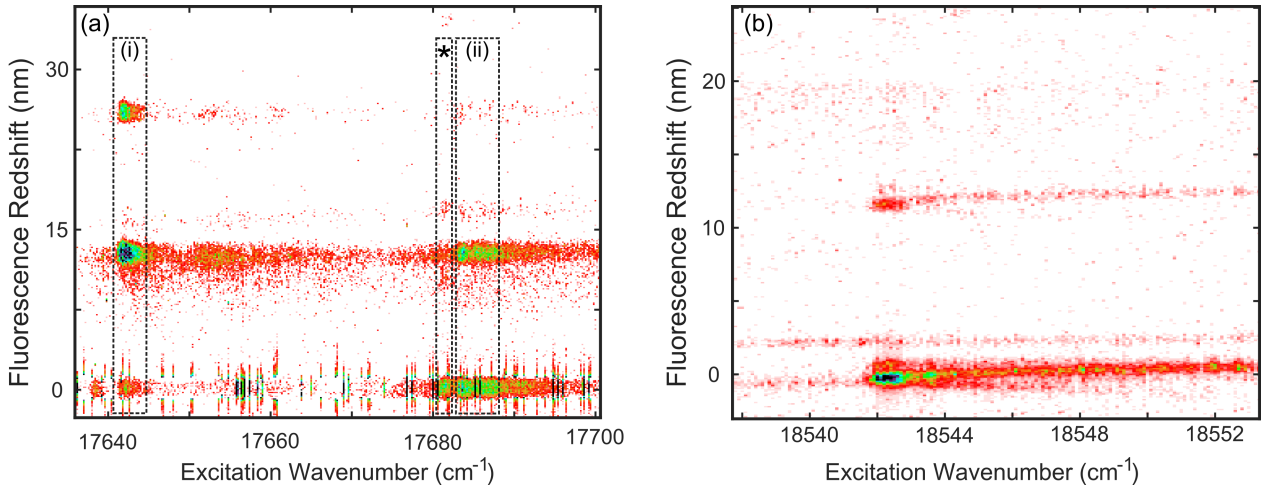

Figure 8.2: (a) Pulsed-dye laser 2D spectrum in the vicinity of the $4_0^1\,\tilde{A}\,^2E_{1/2} \leftarrow \tilde{X}\,^2A_1$ bands. Integration at fixed fluorescence wavelength can be used to obtain excitation spectra. The DLIF features near 17641 cm^{-1} (marked "(i)") and 17683 cm^{-1} (marked "(ii)") are shown in Fig. 8.4. The weak feature marked by an asterisk is due to the YbOH [17.68] band. (b) Pulsed-dye laser 2D spectrum in the vicinity of the $0_0^0\,\tilde{A}\,^2E_{3/2} \leftarrow \tilde{X}\,^2A_1$ band.

to the origin band. Based on the long observed progressions in the Yb-O stretching mode, these levels both appear to have strong $v_4 = 1$ character (see Sec. 8.2.2). This observation is similar to YbF, where two closely-spaced excited states (the [557] and [561] states) have substantial $v = 1$ character [178, 261]. Fluorescence from these states do not show the strong activity in the ν_8 mode that was observed on the origin band.

In addition, we explored a region approximately 1300 cm^{-1} above the origin band, where the $\tilde{A}\,^2E_{3/2} \leftarrow \tilde{X}\,^2A_1$ transition would be expected. As shown in Fig. 8.2(b), a band was observed near 18540 cm^{-1} with weak off-diagonal decays at frequencies matching the $YbOCH_3$ ν_4 and ν_8 modes. This implies an effective spin-orbit constant of $a\zeta_e d \approx$1270 cm^{-1}, similar to that of YbF [262] and YbOH [173], indicating that the spin-orbit interaction is not significantly quenched.

The $\tilde{A}\,^2E_{1/2}(v = 0)$ vibronic state radiative lifetime was measured by fixing the dye laser wavelength to the $0_0^0\,\tilde{A}\,^2E_{1/2} \leftarrow \tilde{X}\,^2A_1$ bandhead and recording the DLIF spectrum at variable time delay after the pulsed laser excitation. The ICCD gate (200 ns wide) was delayed after the pulsed dye laser in steps of $\sim$ 3 ns and the resulting fluorescence fit to an exponential to determine the

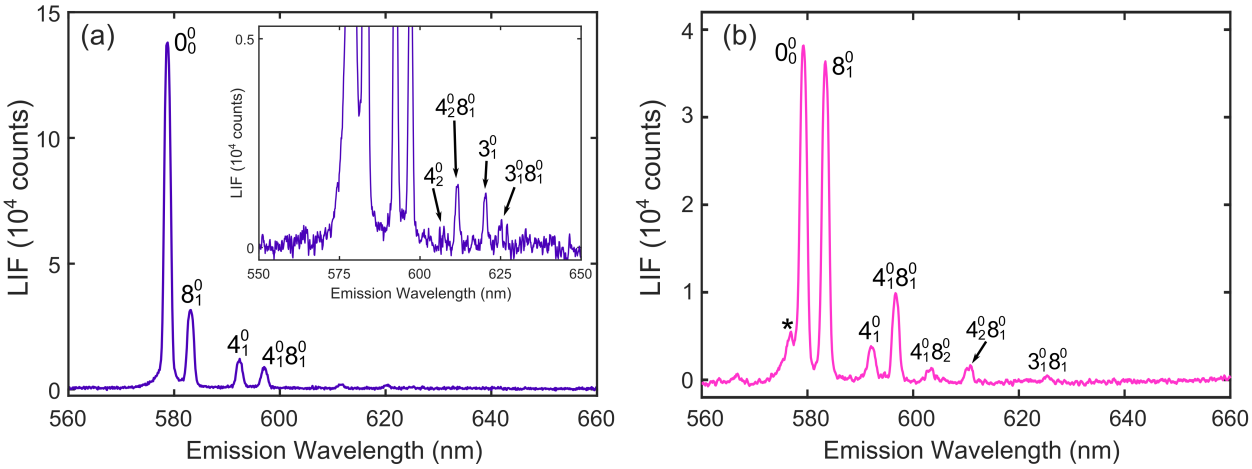

Figure 8.3: DLIF spectrum resulting from excitation of the $0_0^0\,\tilde{A}\,^2E_{1/2} \leftarrow \tilde{X}\,^2A_1$ bandhead. Numbers above each peak indicate transition assignments using the vibrational labeling of Tab. 8.1. (a) $YbOCH_3$, excitation at 17271.1 cm^{-1}. Inset: expanded vertical axis to emphasize the weakest decay features observed. (b) $YbOCD_3$, excitation at 17249.7 cm^{-1}. The small shoulder marked by an asterisk is attributed to impurity YbOH/YbOD.

excited state lifetime. The radiative lifetime of the $\tilde{A}\,^2E_{1/2}(v=0)$ level is determined to be $37(4)$ ns, somewhat longer than the value of $22(2)$ ns for the $\tilde{A}\,^2\Pi_{1/2}(000)$ state of YbOH [153].

8.2.2 Dispersed fluorescence

Higher resolution DLIF spectra were recorded by fixing the excitation laser wavelength and reducing the entrance slit of the monochromator. Typically 5,000 ablation pulses were co-added to achieve sensitive measurement of the vibrational frequencies and FCFs. Background traces were recorded separately to eliminate scattered light due to either the probe or ablation laser.

The DLIF spectrum resulting from pulsed dye laser excitation at the $YbOCH_3$ bandhead ($\sim$17271 cm^{-1}) is shown in Fig. 8.3(a). The measured vibrational intervals are listed in Tab. 8.2 and vibrational frequencies are extracted as discussed in Sec. 8.2.6. The DLIF is consistent with a relatively diagonal FCF matrix, as expected. A short progression in ν_4 (the Yb-O stretching mode) is observed, with relative intensities similar to those of YbOH [153]. We observed prominent decay to ν_8 (Yb-O-C bending mode), which was unexpected because the $8_1^0\,\tilde{A}\,^2E_{1/2} \rightarrow \tilde{X}\,^2A_1$ transition is nominally forbidden by symmetry. Vibronic coupling due to the (pseudo)-Jahn-Teller interaction has previ-

ously been invoked to explain similar decays in $CaOCH_3$ [193]. We do not observe fluorescence at $2\nu_8$, which is symmetry allowed, also similar to observations in $CaOCH_3$ (see Sec. 4.5). Weak features associated with ν_3 (C-O stretch) are also observed, and the frequencies and branching ratios are similar to values observed in $CaOCH_3$ [193, 206].

Isotopic studies aided in the assignment of the ligand-centered vibrations. Figure 8.3(b) displays the DLIF spectrum following excitation in $YbOCD_3$ and vibrational frequencies extracted from these data are listed in Tab. 8.2. The origin band of $YbOCD_3$ was found near 17250 cm^{-1}. This $\approx$ 20 cm^{-1} isotope shift is similar to the shift ($\approx$ 10 cm^{-1}) observed upon deuteration of $CaOCH_3$ [263]. Interestingly, the branching ratios observed for $YbOCD_3$ differ strikingly from those observed in $YbOCH_3$, although the frequencies agree well with the expected isotope shifts.

We have also measured DLIF spectra following excitation to bands near the expected position of the $\tilde{A}\,^2E_{1/2}(v_4 = 1)$ state. As described above, two such states were found near 17641 cm^{-1} and 17683 cm^{-1}, which we call the [17.64] and [17.68] states, respectively. DLIF measurements from these levels are shown in Figs. 8.4(a) and (b). These spectra both show strong decays to a progression in ν_4, confirming large $v_4 = 1$ character of each excited state. Weak features associated with decay to $v_8 = 1$ are also observed, although with significantly lower intensity than observed on the origin band. The presence of two states with significant $v_4 = 1$ character is likely due to mixing of the $\tilde{A}\,^2E_{1/2}(v_4 = 1)$ vibronic level with vibronic levels of states associated with f-orbital vacancies, e.g. $([\mathrm{Xe}]4f^{13}6s^2)_{Yb^+}$, similar to the case of YbF [178, 261]. It is noteworthy that the LIF excitation spectrum of YbOH [153], which is present as an impurity in our sample, also exhibits two relatively weak features at 17643 cm^{-1} and 17681 cm^{-1}. Fortunately, the associated YbOH DLIF spectra are readily distinguishable from those resulting from emission of the [17.64] and [17.68] states of $YbOCH_3$.

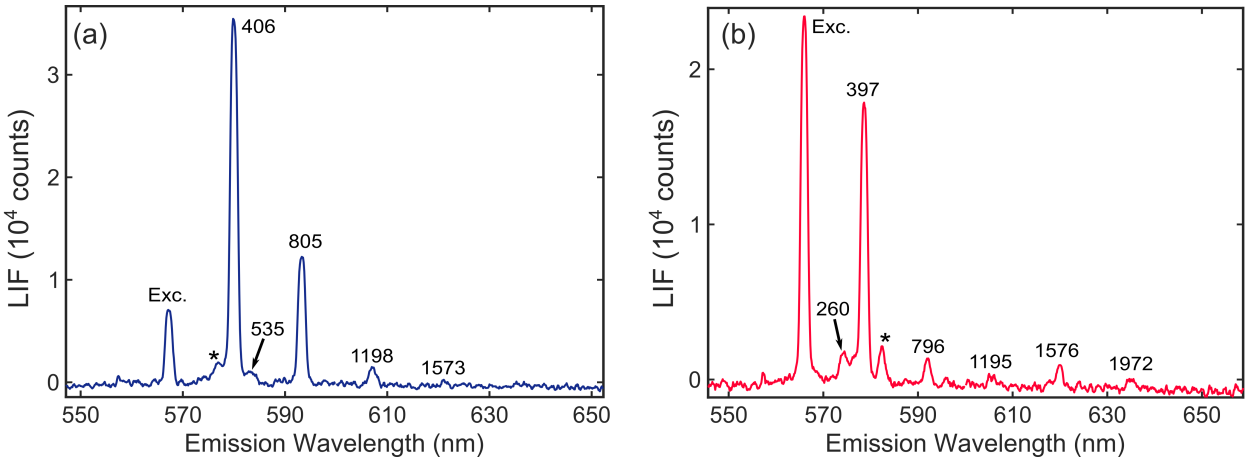

Figure 8.4: DLIF spectrum resulting from excitation at (a) 17641.75 cm^{-1} and (b) 17683.40 cm^{-1}. The numbers above the spectral features are the measured shifts (in cm^{-1}) relative to the excitation wavelength ("Exc."). Features marked by an asterisk are due to YbOH impurity fluorescence, as described in the text.

8.2.3 Analysis of vibrational structure

The wavelength axes of the DLIF spectra were calibrated and linearized prior to data collection. Ground-state vibrational intervals were determined from the DLIF spectra by locally fitting each peak and taking appropriate differences. The measured frequencies and assignments are listed in Table 8.2 along with comparisons to the alkaline-earth monomethoxides $SrOCH_3$ and $CaOCH_3$. The observed ground state vibrational energies were fit to the phenomenological expression [157]

$$E(v) = \sum_i \omega_i \left(v_i + \frac{d_i}{2}\right) + \sum_{i,k} x_{ik} \left(v_i + \frac{d_i}{2}\right)^2, \tag{8.1}$$

where mode i has degeneracy d_i, frequency ω_i, and v_i quanta of excitation. The constants x_{ik} denote the leading anharmonic corrections. Only the observed modes (ν_3, ν_4, and ν_8) were included in the fit. The fit incorporated DLIF traces with pulsed-dye laser excitation to the $\tilde{A}(v = 0)$, [17.64], and [17.68] states. The results of this fit are presented in Sec. 8.2.6.

Table 8.2: Observed and calculated (*ab initio*) vibrational intervals in $\tilde{X}\ ^2A_1$ for $YbOCH_3$ and $YbOCD_3$. Calculated values are in the harmonic approximation. Previously measured values for alkaline-earth monomethoxides are included for comparison. All frequencies are in cm^{-1}. Typical measurement error bars are ± 5 cm^{-1} depending upon signal-to-noise ratio and proximity to argon emission calibration lines.

	$YbOCH_3$		$YbOCD_3$		$SrOCH_3$ [a]	$CaOCH_3$ [b]
Mode	(obs.)	(calc.)	(obs.)	(calc.)	(obs.)	(obs.)
ν_3	1151	1154	-	1085	1138	1156
ν_4	400	390	370	369	405	487
ν_8	130	134	120	124	135	142
$2\nu_8$	260	268	-	248	-	-
$\nu_4+\nu_8$	533	524	500	493	-	625
$2\nu_4$	805	780	-	738	806	973
$2\nu_4+\nu_8$	933	914	880	862	-	-
$\nu_4+2\nu_8$	-	658	680	617	-	-
$\nu_3+\nu_8$	1287	1288	1270	1262	-	-
$3\nu_4$	1197	1170	-	-	-	-
$4\nu_4$	1576	1560	-	-	-	-
$5\nu_4$	1972	1950	-	-	-	-

[a] Measured values from Refs. [264] and [265]
[b] Measured values from Ref. [265]

8.2.4 Vibrational branching ratios

Vibrational branching ratios (VBRs), $b_{v',v''}$, were determined by the ratios of integrated areas under each observed peak. These are related to the FCFs by [192]

$$\begin{aligned} b_{v',v''} &= \frac{I_{iv',fv''}}{\sum_{fv''} I_{iv',fv''}} \\ &\approx \frac{\mathrm{FCF}_{iv',fv''} \times \nu^3_{iv',fv''}}{\sum_{fv''} \mathrm{FCF}_{iv',fv''} \times \nu^3_{iv',fv''}}, \end{aligned} \tag{8.2}$$

where i and f label initial and final states, respectively. Table 8.3 lists the observed vibrational branching ratios and FCFs determined for the $YbOCH_3$ $\tilde{A}\ ^2E_{1/2} - \tilde{X}\ ^2A_1$, [17.64]$-\tilde{X}\ ^2A_1$, and [17.68]$-\tilde{X}\ ^2A_1$ bands. The spectrometer and ICCD relative intensity sensitivities were calibrated prior to data collected. The typical noise level of the DLIF spectra corresponds to $\sim$100 counts per pixel, equivalent to $\sim$1 part in 10^3 relative to the dominant peak. Systematic errors associated

with the calibration lead to ∼5% relative uncertainty in peak height near 580 nm and ∼10% relative uncertainty near 630 nm.

8.2.5 Electronic structure calculations

To aid assignment of the DLIF spectra, *ab initio* calculations were performed for $YbOCH_3$ and $YbOCD_3$ using the ORCA quantum chemistry program [266, 267]. Molecular orbitals, optimized geometries, normal modes, and vibrational frequencies for the ground electronic state were calculated at the level of unrestricted Kohn-Sham (UKS) density-functional theory (DFT) using the B3LYP functional [268, 269]. We carefully studied the accuracy of various basis set and functional choices. Final calculations employed a quadruple-ζ basis set, including two sets of polarization functions and diffuse orbitals on the heavy atoms. A 28-electron small-core pseudopotential was used for the Yb atom [36, 270, 271]. Time-dependent DFT (TD-DFT) was used to model the $\tilde{A}\ ^2E$ state, using the same basis and functional as were used for the ground electronic state. This allowed computation of excitation energies and geometry optimization using analytic Hessians. Vibrational frequencies were determined via numerical differentiation. The theoretical methods were validated by performing test calculations for YbOH and $CaOCH_3$. See Ref. [146] for comparisons between different basis sets, validation against previous measurements, and additional computational outputs.

8.2.6 The $\tilde{X}\ ^2A_1$ state

Assignments of the observed vibrational decays were relatively straightforward using the *ab initio* predictions, isotopic data, and comparison to alkaline-earth monomethoxides. For the origin band, the peaks redshifted by 130 cm^{-1} and 400 cm^{-1} are assigned to 8_1^0 and 4_1^0, respectively. The feature redshifted by 1150 cm^{-1} is near the expected frequency of either ν_3 (1× O-C stretch) or $3\nu_4$ (3×

Table 8.3: Branching ratios and FCFs from the $\tilde{A}\,^2E_{1/2}(v=0)$, [17.64], and [17.68] states of YbOCH$_3$ to the $\tilde{X}\,^2A_1$ levels. Values are determined from the pulsed-dye laser excitation DLIF spectra. After accounting for the detection noise and systematic uncertainties due to calibration, the noise levels of the smallest VBRs are $\pm 0.7 \times 10^{-3}$ for the 0_0^0 band and $\pm 2 \times 10^{-3}$ for the [17.64] and [17.68] bands.

	$\tilde{A}\,^2E_{1/2}(v=0)$		[17.64]		[17.68]	
	VBR	FCF	VBR	FCF	VBR	FCF
0_0	0.729	0.7184	0.132	0.122	0.526	0.504
8_1	0.164	0.1653	-	-	-	-
4_1	0.054	0.0566	0.624	0.617	0.375	0.385
$4_1 8_1$	0.038	0.0413	0.0181	0.0183	0.044	0.046
4_2	9.89×10^{-4}	1.1×10^{-3}	0.201	0.214	0.0268	0.0293
$4_2 8_1$	6.8×10^{-3}	7.9×10^{-3}	-	-	-	-
3_1	5.49×10^{-3}	6.7×10^{-3}	-	-	-	-
$3_1 8_1$	2.13×10^{-3}	2.65×10^{-3}	-	-	-	-
4_3	-	-	0.021	0.0244	5.13×10^{-3}	6.02×10^{-3}
4_4	-	-	3.6×10^{-3}	4.36×10^{-3}	0.015	0.0194
4_5	-	-	-		7.6×10^{-3}	1.0×10^{-2}

Yb-O stretch). Because this decay has a stronger intensity than 4_2^0, we favor the assignment to 3_1^0. Furthermore, the DLIF spectra from the [17.64] and [17.68] states show a feature at slightly higher frequency (≈ 1170 cm^{-1}) that is assigned to $3\nu_4$. The weak feature redshifted by $\sim$1280 cm^{-1} is assigned to the decay $3_1^0 8_1^0$ based on the predicted frequencies for various combination bands. In addition, the intensity of this feature relative to the 3_1^0 peak is roughly consistent with the strengths of other combination bands involving ν_8.

The vibrational frequencies are determined by fitting observed vibrational energy intervals to Eq. 8.1. We find $\omega_3 = 1152(5)$ cm^{-1}, $\omega_4 = 405(3)$ cm^{-1}, $\omega_8 = 130(3)$ cm^{-1}, and $x_{44} = -2.0(6)$ cm^{-1}. These fitted frequencies agree well with the computed harmonic frequencies and with the corresponding values for CaOCH$_3$ and SrOCH$_3$ after accounting for differences in reduced mass [265]. The anharmonic contribution to the Yb-O stretching mode is similar to that observed in YbOH in both magnitude and sign [153]. Finally, the fitted value ω_3 is similar to that predicted for the methoxy anion, consistent with a highly ionic metal-ligand bond [272].

Our *ab initio* calculations predict that the $\tilde{X}\ ^2A_1$ state has a linear Yb-O-C bond and symmetric,

off-axis H atoms with C_{3v} symmetry, just like the alkaline-earth monomethoxides. The calculated values $r_{OC} = 1.39$ Å and $r_{CH} = 1.10$ Å for $YbOCH_3$ are quite similar to those measured in $CaOCH_3$ ($r_{OC} = 1.411(7)$ Å and $r_{CH} = 1.094$ Å) [263], while the calculated value of $r_{YbO} = 2.04$ Å for $YbOCH_3$ is very close to the measured value for YbOH ($r_{YbO} = 2.0397$ Å) [172]. In addition, our *ab initio* calculations predict a molecule-frame dipole moment of $\mu(\tilde{X}) = 2.2$ D in the $\tilde{X}\ ^2A_1$ ground state. This is nearly identical to the ground-state dipole moment of YbOH (1.9(2) D [173]) and comparable to that of $CaOCH_3$ (1.58(8) D [255]). These calculations also report the $\tilde{X}\ ^2A_1$ electronic state arises primarily from Yb-centered $6s\sigma$ (65%) and $6p\sigma$ (15%) orbitals. This is quite similar to YbF where experimental analysis of the hyperfine structure showed that the $X\ ^2\Sigma^+$ state had 57% $6s$ character [273]. The resulting polarization of the valence electron away from the Yb-O bond is consistent with the predicted molecule-frame dipole moment being significantly smaller than that of an electrostatic model with point charges located near the Yb^+ and OCH_3^- moieties [260]. Together, these results help confirm the expectation that $YbOCH_3$ in the $\tilde{X}\ ^2A_1$ ground state conforms to many of the patterns established by previous studies of alkaline-earth monomethoxides. The predicted vibrational frequencies for $YbOCH_3$ and $YbOCD_3$ show excellent agreement with our measurements, as can be seen in Tab. 8.2.

8.2.7 The excited states

We have observed a number of excited states assigned to $YbOCH_3$, associated with bands near 17271 cm^{-1}, 17281 cm^{-1}, 17641 cm^{-1}, 17683 cm^{-1}, and 18542 cm^{-1}. The band at 17271 cm^{-1} is assigned to terminate on the $\tilde{A}\ ^2E_{1/2}(v = 0)$ level. As discussed above, both the [17.64] and [17.68] states seem to have strong $v_4 = 1$ (Yb-O stretching) character, but on the basis of the FCF measurements we tentatively assign the [17.64] state as dominantly $\tilde{A}\ ^2E_{1/2}(v_4 = 1)$, while the [17.68] state appears to be a perturbing state similar to those observed in both YbF [178] and YbOH [153].

The band near 18542 cm^{-1} is tentatively assigned as $0_0^0\ \tilde{A}\,^2E_{3/2} \leftarrow \tilde{X}\ ^2A_1$. This implies an effective spin-orbit splitting $a\zeta_e d \approx 1270$ cm^{-1}, similar to that of YbF [262]. Future high-resolution studies will be useful to provide further confirmation of these assignments.

TD-DFT calculations targeting the $\tilde{A}\ ^2E$ state predict an excitation energy $T_e = 18060$ cm^{-1}. This is in good agreement with the measured value of $T_e \approx 17900$ cm^{-1} (accounting for the spin-orbit coupling). The $\tilde{A}\ ^2E$ state is predicted to have C_{3v} symmetry, with bond lengths/angles $r_{\mathrm{YbO}} = 2.010$ Å, $r_{\mathrm{OC}} = 1.396$ Å, $r_{\mathrm{CH}} = 1.095$ Å, and $\theta_{\mathrm{OCH}} = 111.283°$. The calculations predict a linear Yb-O-C structure. The predicted change in Yb-O bond length is quite similar to that observed for YbOH and consistent with the relatively diagonal branching ratios [173]. The calculation predicts a vibrational frequency $\omega_4 = 410$ cm^{-1}, which is in reasonable agreement with the splitting observed between the $\tilde{A}\ ^2E$ and [17.64]/[17.68] states.

Observation of the relatively intense 8_1^0 feature in the $\tilde{A}\,^2E_{1/2}(v=0)$ DLIF spectrum (Fig. 8.3) was at first unexpected because, assuming both the $\tilde{X}$ and $\tilde{A}$ states have C_{3v} symmetry, the ν_8 mode is of e symmetry and this decay is symmetry-forbidden within the Born-Oppenheimer (BO) approximation. One possible explanation for the strength of this transition is that $YbOCH_3$ possesses a bent geometry (C_s symmetry) in the $\tilde{A}$ state. We disfavor this explanation for several reasons. First, we do *not* observe emission from $\tilde{A}\ ^2E_{1/2}$ to $\tilde{X}\ ^2A_1(v_8 = 2)$, which would be expected if there were significant geometrical change upon electronic excitation. Similarly, we do not observe strong decays to $\tilde{X}\ ^2A_1(v_8 = 1)$ from the [17.64] or [17.68] states. Second, a bent excited state would likely be accompanied by significant quenching of the electronic orbital angular momentum, but the above assignment of the $\tilde{A}\,^2E_{3/2}$ state is consistent with $a\zeta_e d \approx 1270$ cm^{-1}, indicating little quenching. Third, we did not observe rotational bands associated with the K_a structure expected for a bent molecule; the contour of the high-resolution spectra could be well simulated using a symmetric top Hamiltonian.

8.2.8 Spin-orbit-vibronic coupling

Instead, we attribute the relatively strong 8_1^0 signal to spin-orbit vibronic coupling. Following Ref. [206], we consider the possibility of Jahn-Teller coupling within $\tilde{A}\ ^2E$, characterized by parameter k_8, and pseudo-Jahn-Teller coupling between $\tilde{A}\ ^2E$ and nearby states of A_1 symmetry, characterized by parameter λ_8. Here, we assume that ν_8 is the only mode with significant Jahn-Teller activity. Spin-orbit coupling between $\tilde{A}\ ^2E$ and $\tilde{B}\,^2A_1$ can interfere with (pseudo-)Jahn-Teller terms and lead to a second-order, effective coupling between the $\tilde{A}\ ^2E(v_8 = 1)$ and $\tilde{A}\ ^2E(v_8 = 0)$ vibronic levels. Given the intensity of the 8_1^0 feature, we infer an effective matrix element

$$\langle \tilde{A}\ ^2E_{1/2}, v_8 = 1 | H_{JT} | \tilde{A}\ ^2E_{1/2}, v_8 = 0 \rangle \approx 50\ \text{cm}^{-1}.$$

Again following Ref. [206], we may also express this matrix element as $k_8 + 2C_{AB}\lambda_8$. The first term represents direct coupling between $\tilde{A}\ ^2E(v_8 = 0, 1)$ while the second term represents the spin-orbit vibronic coupling via an intermediate $^2A_1$ state. C_{AB} is the mixing induced by spin-orbit coupling between $\tilde{A}\ ^2E$ and $\tilde{B}\,^2A_1$, approximated using the measured spin-orbit parameter of $YbOCH_3$ and the estimated $\tilde{B}\,^2A_1$ energy scaled from YbF. It has been shown for $CaOCH_3$ that the k_8 term is negligible compared to the λ_8 term. Assuming the same holds for $YbOCH_3$, we estimate $\lambda_8 \approx 55\ \text{cm}^{-1}$. This is approximately three times smaller than the value of λ_8 computed by *ab initio* methods for $CaOCH_3$, which is consistent with the expected trend as spin-orbit coupling strength increases [164]. Though preliminary, this estimate shows that the strong 8_1^0 feature can be explained reasonably by the spin-orbit vibronic coupling mechanism.

Recent studies of $CaOCH_3$ by our group lend support to these quantitative estimates. In those measurements, see Sec. 4.5, we observed the analogous vibronically-induced 8_1^0 feature in $CaOCH_3$, albeit with weaker VBR $\approx 3 \times 10^{-3}$. Note that this agrees quite well with the *ab initio* prediction of

Ref. [206], where the decay was predicted but not observed. Applying the same analysis as used above, we determine a linear pseudo-Jahn-Teller coefficient for $CaOCH_3$ of $\lambda_8^{CaOCH_3} \approx 135$ cm^{-1}. This is in good agreement with the *ab initio* value of 150 cm^{-1} [206] and provides a satisfactory check of the estimation methods used above. Nonetheless, *ab initio* treatment of the vibronic coupling problem in $YbOCH_3$ would be highly desirable. In addition, we note that other interpretations are possibly valid, such as the k_8 parameter being nonnegligible or vibronic coupling between $\tilde{A}\ ^2E$ and nearby electronic states arising from excitations of Yb $4f$ electrons. The presence of a strong perturbation makes it very challenging to use standard semi-empirical methods [130, 153, 193] to predict the FCFs in $YbOCH_3$. This reinforces the need for careful experimental studies to guide future experiments with this molecule.

8.3 High-resolution spectroscopy

The high-resolution spectrum recorded near the $0_0^0\ \tilde{A}\ ^2E_{1/2} \leftarrow \tilde{X}\ ^2A_1$ bandhead identified above is shown in Fig. 8.5. The spectrum is quite congested due to the presence of several isotopes of Yb with relatively high natural abundance, including ^{174}Yb (32%), ^{172}Yb (22%), ^{173}Yb (16%), ^{171}Yb (14%), and ^{176}Yb (13%). We have also recorded this spectrum using a cryogenic buffer-gas beam source at Harvard. The lower rotational temperature achieved in that case can help to simplify the spectrum somewhat, but even with this data it remained too complex for easy assignment. We make some qualitative observations here, showing the spectrum is consistent with a $^2E_{1/2} \leftarrow^2 A_1$ transition.

The rotational energy level structure of a $^2A_1$ state is that of an open-shell prolate symmetric top molecule near the Hund's case (b) limit. For an $MOCH_3$ species, the $K_R'' = 1$ stack of levels begins approximately 6 cm^{-1} ($\approx A''$) above the $K_R'' = 0$ stack. The $|K_R''| = 1$ levels obey different nuclear spin statistics and will also be populated significantly and show prominently in the spectrum. The

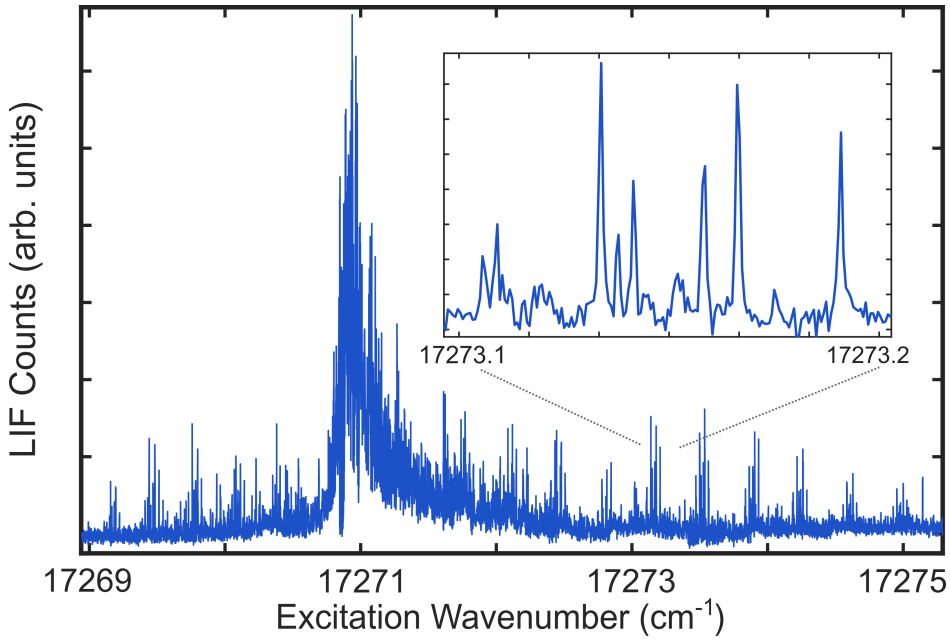

Figure 8.5: High-resolution excitation spectrum near the YbOCH$_3$ 0_0^0 $\tilde{A}\,^2E_{1/2} \leftarrow \tilde{X}\,^2A_1$ bandhead. Features marked by an asterisk were selected for cw-excitation DLIF measurements. Inset: Details of spectrum near 17273.15 cm^{-1}, with isotopic and K-stack structure visible.

energy level pattern of a $^2E_{1/2}$ state is that of an open-shell prolate symmetric top near the Hund's case (a) limit. The parity doubling in the $K'_R = 0, K' = 1$ level is expected to be large and hence the dominant $\tilde{A}\,^2E_{1/2}(K'_R = 0, K' = 1) \leftarrow \tilde{X}\,^2A_1(K''_R = 0)$ band is expected to have the same general appearance as the $\tilde{A}\,^2\Pi_{1/2} \leftarrow \tilde{X}\,^2\Sigma^+$ band of YbOH. Indeed, we observe that the high-resolution spectrum is reminiscent of the $\tilde{A}\,^2\Pi_{1/2} \leftarrow \tilde{X}\,^2\Sigma^+$ origin band of YbOH due to the sharply peaked, blue-degraded bandhead and the widely spaced peaks in the P/R branches [153, 173]. Using the expected YbOCH$_3$ rotational constant, B, determined by either empirically scaling parameters for YbOH or by *ab initio* calculations, we estimate that these peaks are spaced by approximately $4B$. This branch spacing implies an excited state parity doubling $\epsilon_1 - 2h_1 \approx B$ [22].[2] Here, $\epsilon_1 - 2h_1$ plays the role of the usual $p + 2q$ (Λ-type doubling) parameter in a linear $^2\Pi$ state [274]. Note that a similar branch spacing of about $4B$ is observed in the YbOH $\tilde{A}\,^2\Pi_{1/2} \leftarrow \tilde{X}\,^2\Sigma^+$ origin band [173].

[2] In this expression, ϵ_1 is a higher-order spin-rotation parameter and h_1 is a Jahn-Teller parameter [263].

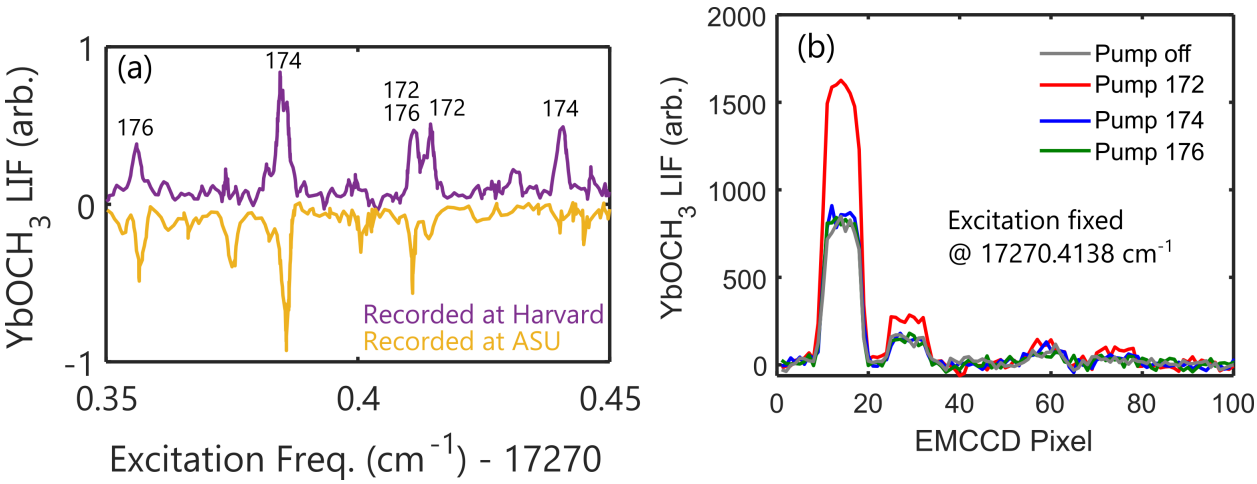

Figure 8.6: Chemical enhancement for $YbOCH_3$ spectral assignments. (a) Portion of the $YbOCH_3$ spectrum showing data from both ASU and Harvard. The different relative peak heights originate from different rotational temperatures of the source (~ 4 K at Harvard and ~ 10 K at ASU). (b) DLIF traces recorded at fixed excitation frequency with the enhancement laser tuned to address the ^{172}Yb, ^{174}Yb, and ^{176}Yb intercombination lines. Only one isotope shows enhancement, in this case indicating that the selected peak originates from $^{172}YbOCH_3$ molecules.

8.3.1 Chemical enhancement for spectral assignment

One of the challenges to understanding the high-resolution spectrum is the presence of many isotopologues of $YbOCH_3$ with high natural abundance. This complexity is also present in the spectra of YbOH molecules. It has recently been shown [275] that using chemically enhanced production one can simplify the observed spectra by isolating single isotopologues. In Sec. 5.1.2, we showed that ^{174}YbOH production is increased by around an order of magnitude when the ^{174}Yb $^1S_0 \rightarrow ^3P_1$ transition is driven inside the cell. Because only a single Yb isotope is excited to the metastable $^3P_1$ state, this provides isotope-selective enhancement. Any lines that show an enhancement effect in a recorded spectrum are known to originate from the isotope whose intercombination line was driven inside the cell.

We have applied this tool to $YbOCH_3$ by monitoring a few spectral features recorded in the Harvard CBGB apparatus while pumping different Yb isotopes to the $^3P_1$ state. Figure 8.6(a) shows a small portion of the $YbOCH_3$ $\tilde{A} \leftarrow \tilde{X}$ origin band spectrum with spectral features labeled by their Yb isotopic assignment. In Fig. 8.6(b) we show an example of how these assignments were

deduced, i.e. a set of DLIF spectra collected with the excitation laser locked to the spectral feature in question and the enhancement laser tuned to drive one Yb isotope at a time to the $^3P_1$ state. In the example shown, the peak is found to originate from the $^{172}YbOCH_3$. This sort of "tagging" was repeated for each peak in Fig. 8.6(a). Using this method, it should be possible to determine a spectrum for each $YbOCH_3$ isotope, easing the task of parameter determination.

8.4 Conclusion

We have presented the first observation and characterization of $YbOCH_3$ molecules. We have produced this molecule in both a pulsed supersonic beam source and a cryogenic buffer-gas beam source. Our measurements indicate that the FCFs of this molecule are relatively diagonal, although less favorable for photon cycling and laser cooling than those of YbOH. Despite having stronger off-diagonal decays than the isoelectronic species YbF and YbOH, the vibrational branching ratios in $YbOCH_3$ converge rapidly enough to permit efficient laser cooling. Even in the absence of full 3D laser cooling, $YbOCH_3$ would allow optical cycling of $\sim$150 photons with about 3 vibrational repumping lasers. This scale enables efficient state preparation, transverse cooling, and/or unit-efficiency readout for precision measurements in a molecular beam.

Further data are needed to sharpen the developing picture of the $\tilde{A}\ ^2E_{1/2} - \tilde{X}\ ^2A_1$ band. The $\tilde{A}\,^2\Pi$ states in YbF and YbOH are quite complex due to a series of perturbing states nearby in energy [153, 178], and it appears that analogous states exist in $YbOCH_3$. Careful studies of the $\tilde{A}$ state and nearby perturbing levels will be necessary to develop a laser cooling scheme capable of scattering $\gg 10^3$ photons with $YbOCH_3$. Finally, vibronic interactions with matrix elements off-diagonal in K may lead to leakage from the optical cycle at rates high enough to require repumping. Characterizing these effects using high-resolution spectroscopy will also be important prior to laser cooling $YbOCH_3$.

An important step to continue the study of $YbOCH_3$ molecules is to assign the high-resolution spectrum. This task should be greatly simplified by our demonstration of chemical enhancement to determine the isotopic identities of spectral features. In addition, optical Stark spectra could be used to unambiguously identify the K assignment of each line. Using these two tools, it should be possible to unravel the complicated high-resolution spectrum and determine the rotationally closed cycling transitions. Once this is completed, one could begin to demonstrate photon cycling following the steps establishing in Ch. 5. This process would then need to be repeated for each vibrational state requiring repumping before laser cooling can be attempted.

Nevertheless, it is important to remember that polyatomic molecules give us life and reasons to live...

Peter van der Straten and Harold Metcalf, in "Atoms and Molecules Interacting with Light"

9

Asymmetric Top Molecules for Laser Cooling

In this chapter, we propose methods and candidate species for direct laser cooling experiments focused on asymmetric top molecules (ATMs).[1] Previous laser cooling experiments have relied on high molecular symmetry to greatly restrict losses from the optical cycle [78, 276]. Extension to *asymmetric* molecules necessarily involves removing these restrictions. While Isaev and Berger

[1] Some of the results described in this chapter were published in Ref. [130]. The theoretical work was conducted in collaboration with the Zelevinsky group at Columbia University, and Ivan Kozyryev conducted the *ab initio* calculations. Experimental measurements were performed in collaboration with Tim Steimle at Arizona State University.

previously performed *ab initio* estimates of the vibrational branching ratios for the chiral ATM MgCHDT [36], to date there has been no complete description of general methods to directly laser cool and trap ATMs. It has not previously been clear how the reduced symmetry of ATMs would affect optical cycling, or even if full laser cooling of asymmetric species would be possible.

In ATMs, all three principal axes have distinct moments of inertia. These molecules can have at most twofold rotational symmetry and, formally, there can be no orbitally degenerate states.[2] The reduced symmetry has several important consequences for laser cooling. First, mixing between electronic manifolds— especially among the closely-spaced electronically excited states $\tilde{A}$, $\tilde{B}$, and $\tilde{C}$— may lead to perturbations that severely limit photon cycling. Second, vibronic selection rules that are present in the case of linear or symmetric top molecules break down. Third, the reduced symmetry requires careful consideration of how, and whether, a rotationally-closed cycling transition can be constructed.

Despite these structural complexities, we have found that a general class of ATMs is amenable to optical cycling. We follow the motifs of other molecules explored in this thesis and focus on species of the form M-L, comprising an alkaline-earth atom (M) that is ionically and monovalently bonded to an electronegative ligand (L), as described in Ch. 2. We present calculations of the vibrational branching ratios in these molecules, demonstrating that with only a few repumping lasers one may scatter enough photons to achieve sub-Doppler cooling similar to that achieved for YbOH (see Ch. 6). Crucially, we describe how, despite the complex rotational structure in these asymmetric tops, a simple laser cooling scheme may be constructed that limits rotational branching to an easily repumped manifold of states.

We consider here a very large class of molecules that has fortunately been the focus of considerable spectroscopic attention (making practical application in the laboratory much easier). We

[2] Point groups C_1, C_i, C_s, C_2, D_2, C_{2h}, D_{2h}, and C_{2v}.

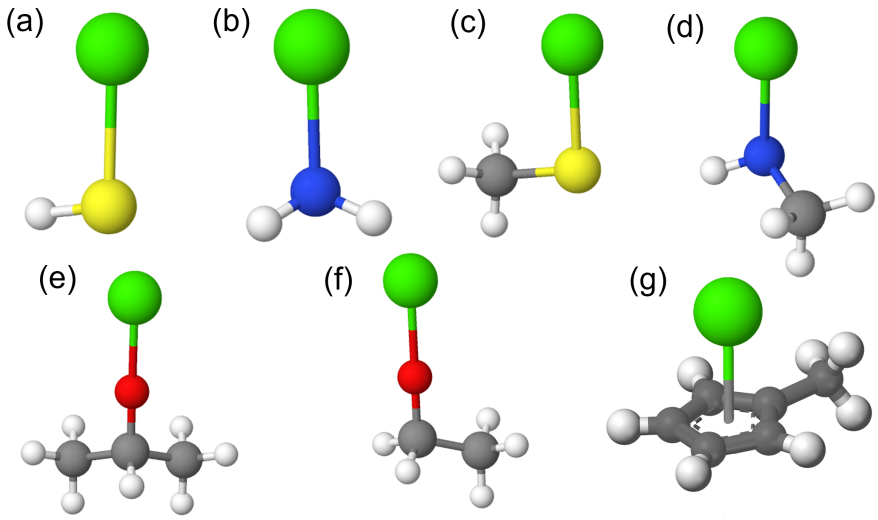

Figure 9.1: Model geometries for several of the species proposed in this work. (a) MSH, (b) MNH_2, (c) $MSCH_3$, (d) $MNHCH_3$, (e) $MOCH(CH_3)_2$, (f) MOC_2H_5, (g) $MC_5H_4CH_3$, where M represents an alkaline-earth metal atom. Atomic species are colored according to green: alkaline-earth metal, yellow: sulfur, blue: nitrogen, red: oxygen, gray: carbon, white: hydrogen. Structures were generated using MolView [299].

have limited ourselves almost exclusively to molecules which have actually been produced and observed in the laboratory. Such species include (see Fig. 9.1): AE hydrosulfides (MSH) [277–281], monoamides (MNH_2) [282–289], methanethiols ($MSCH_3$) [290], alkylamides ($MNHCH_3$) [291], isopropoxides ($MOCH(CH_3)_2$) [265], monoethoxides (MOC_2H_5) [292], pyrollyls (MC_4H_4N) [293], and methylpentadienyls ($MC_5H_4CH_3$) [293–295], where M = Mg, Ca, Sr, or Ba.[3] Chiral-substituted AE-methyls (MCHDT) [296–298] and AE-methoxides (MOCHDT) [264] are also considered. The wealth of spectroscopic data available for these species is essential to providing quantitative examples for the general approach to laser cooling ATMs.

9.1 Electronic transitions

The structure of the low-lying electronic states of the ATMs considered here is best understood through their correlations with linear AE monohalides [143, 285]. A schematic energy level dia-

[3] Yb-containing ATMs are interesting targets due to the high-Z nucleus, but have not yet been studied.

gram is shown in Fig. 9.2 (see also Fig. 9.2). As the AE-metal atom, M, approaches the ligand, L, one of the ns^2 valence electrons is transferred from M to L. The electron remaining localized around M^+ is polarized away from the bond via orbital mixing with excited np and nd orbitals [143]. In the linear limit, the ground state, $\tilde{X}$, is of $^2\Sigma^+$ symmetry while the two lowest electronically excited states are $\tilde{A}\,^2\Pi$ and $\tilde{B}\,^2\Sigma^+$. As the cylindrical symmetry of the molecule is broken, the degeneracy between orbitals directed along the b- and c-axes is lifted and the $\tilde{A}\,^2\Pi$ state splits in two.

In general there will be four low-lying states of interest to laser cooling experiments, $\tilde{X}\,^2A'$, $\tilde{A}\,^2A'$, $\tilde{B}\,^2A''$, and $\tilde{C}\,^2A'$.[4] For molecules of C_{2v} symmetry, the principal axes of the molecule coincide with the axes along which the electronic orbitals are aligned. For molecules of lower symmetry, there will be a misalignment between the M-L bond and the primary axis along which the electronic orbitals are oriented. As will be discussed below, this angle determines to what extent the nominal rotational selection rules will hold. For the species considered here, the lowest three electronically excited states can be addressed by convenient laser wavelengths between 570 nm and 730 nm and have short lifetimes $\sim 20 - 40$ ns. Both features are crucial for exerting large optical forces.

9.1.1 Ab initio calculations

To understand the detailed electronic structure of laser-coolable ATMs, we have performed *ab initio* molecular structure calculations for four prototypical species: CaOH ($C_{\infty v}$ symmetry), $CaCH_3$ (C_{3v} symmetry), $CaNH_2$ (C_{2v} symmetry) and CaSH (C_s symmetry). Figure 9.3 provides a comparison of the singly occupied molecular orbital (SOMO) and the lowest unoccupied molecular orbital (LUMO) as the symmetry of the ML molecule is reduced (column $1 \rightarrow 4$). Despite significant differences in structural symmetry, for the SOMO, LUMO and LUMO+1 (rows 1-3) the

[4] The symmetry labeling will differ depending on the point group, but the overall structure will be similar.

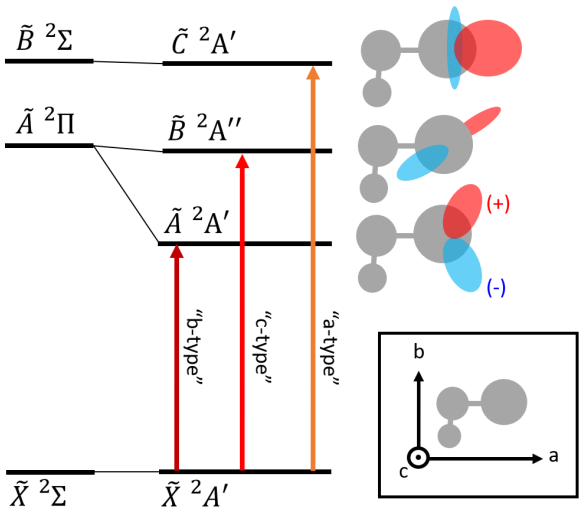

Figure 9.2: Energy level diagram for species of C_s symmetry relevant to the present work, including correlations between linear (left) and asymmetric top (right) states. The asymmetry of the molecule leads to a splitting of the $^2\,\Pi$ potential, lifting the degeneracy of the in-plane and out-of-plane orbitals. The diagram is essentially the same, aside from symmetry labeling, for other highly ionic doublet species. Optical transitions are labeled by the dominant transition dipole moment component. Schematic drawings of the orientation of the electron density are included to rationalize these assignments. Red and blue label phase of the electronic wavefunction. Inset: Principal axis system for the example species.

molecular orbitals are essentially unchanged as the molecule distorts. The orbitals are only slightly distorted for LUMO+2 (row 4). Quantitatively, both ionic bonding and heavy valence electron localization on the metal atom are described by the Mulliken charge and spin population analyses. As the ligand is changed from OH ($C_{\infty v}$) to CH_3 (C_{3v}) to NH_2 (C_{2v}) and SH (C_s), the Mulliken charge on the Ca atom goes from $+0.58$ to $+0.58$ to $+0.55$ and $+0.51$ while the spin population changes from 0.999 to 0.908 to 0.982 and 0.963, respectively. This is in qualitative agreement with the electron affinities determined for these anion ligands [300]. The similar electronic structure in these molecules suggests that laser cooling of ATMs can proceed similarly to cooling linear species.

Losses due to purely electronic transitions are not expected to affect photon cycling in these molecules. One potential loss channel involves radiative "cascade" decay through electronic states intermediate to the photon cycling states [116]. For the molecules considered here, no electronic states between the $\tilde{A}$ and $\tilde{X}$ states have been observed. When optical cycling with the excited $\tilde{B}$ or $\tilde{C}$ states, radiative cascades through the lower-lying states are suppressed by a factor of $(\Delta\omega/\omega)^{-3} \sim$

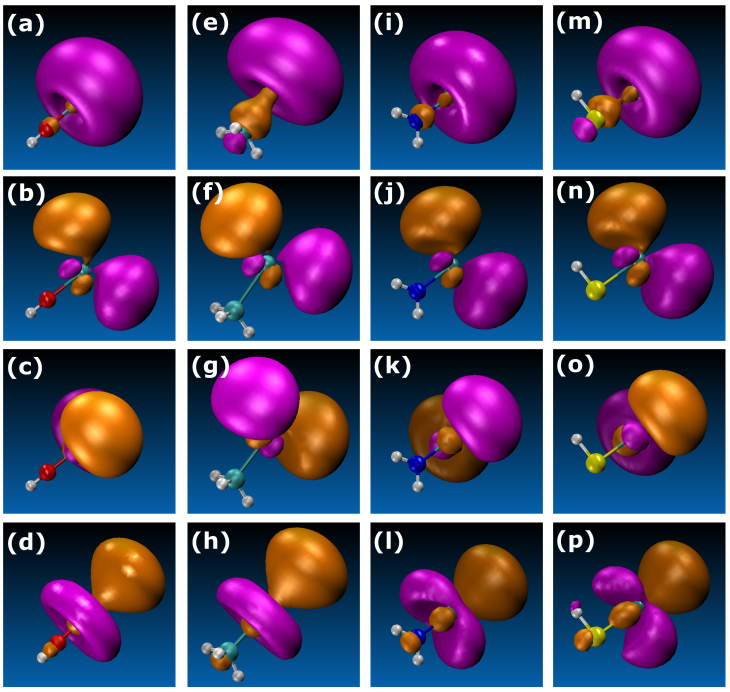

Figure 9.3: Comparison of molecular orbitals for electronic transitions employed in the proposed laser cooling scheme for four ML molecules with different symmetries: CaOH (a-d), $CaCH_3$ (e-h), $CaNH_2$ (i-l), and CaSH (m-p). Molecular geometries are plotted for the ground electronic state; rows 1 through 4 correspond to SOMO, LUMO, LUMO+1, and LUMO+2 configurations, respectively. Molecular symmetry is incrementally reduced from column 1 to column 4: $C_{\infty v}$, C_{3v}, C_{2v}, and C_s. All isosurfaces are plotted for the isovalue of 0.03 with magenta (orange) representing positive (negative) values.

10^4 due to the small energy spacings. This is similar to rates observed already in experiments cooling diatomic species [117], which do not present any challenges to such experiments. A second potential source of loss involves higher-order multipole transitions, e.g. M1 and E2 transitions, that would remove molecules from the optical cycle by populating opposite-parity rovibrational states. Such rates will be similar to those observed in previously cooled diatomic species, where loss due to M1 or E2 transitions have been found to be negligible until $\gg 10^5$ photons have been scattered [78, 276, 301].

9.2 Vibrational branching: theory

Accurate values of the vibrational branching ratios during an electronic decay are of utmost importance to molecular laser cooling. To provide information relevant to laser cooling, these measurements would ideally use cw excitation to a low-J rotational state, be free from state-changing collisions, include careful calibration of detection efficiency over a wide range of wavelengths, and have sensitivities at the $< 10^{-3}$ level. These restrictions severely limit the number of useful direct FCF measurements in the literature. By contrast (and fortunately), high-quality spectroscopic data including bond lengths and angles for many molecules of interest is plentiful. As such, we use a semi-empirical method to compute FCFs for a large set of ATMs expected to be favorable for laser cooling. When accurate high-resolution spectroscopic measurements are available, the computational methods described below can provide vibrational branching ratios in excellent agreement with observations, and with accuracy better than purely *ab initio* predictions [192, 193]. The accuracy of these calculations depends entirely on the accuracy of the measured molecular geometries. In the absence of such experimental data, *ab initio* calculations enable unique insights into identification of favorable ligands for laser cooling [128] and estimation of the vibrational branching ratios [142].

During a generic electronic decay, both the electronic and vibrational coordinates can vary. In many cases, one may neglect the dependence of the electronic transition moment on the nuclear coordinates [135]. For the molecules considered here, this approximation is justified by the excellent agreement between calculation and experiment (see Tab. 9.1 and Refs. [192, 193]). In this approximation, the FCFs are computed by evaluating the overlap integral between excited and ground vibrational wavefunctions:

$$q_{v',v''} = \left| \int \psi_{v'}(\mathbf{Q}')\psi_{v''}(\mathbf{Q}'')\, d\mathbf{Q} \right|^2, \tag{9.1}$$

where $\mathbf{Q}''$ represent the vibrational normal modes of the ground state and $\mathbf{Q}'$ the vibrational normal modes of the excited state. We compute these integrals within the harmonic approximation, as anharmonic contributions are $\sim 5 \times 10^{-2}$ for the molecules considered here [290].

We follow standard methods to calculate the FCFs [302]. In brief, we first perform a **GF**-matrix analysis [149] to determine the normal modes in each electronic manifold. Experimentally measured vibrational frequencies are used to fit the elements of the **F** matrix. We include a Duschinsky transformation between ground and excited normal coordinates to account for normal mode mixing (see Fig. 9.4). We then follow the method of Sharp and Rosenstock [154, 303] which uses generating functions and a linear transformation between the normal coordinates of ground and excited states to define analytic expressions for the FCFs [154, 304]. This model allows one to predict vibrational branching ratios for all vibrational modes within the harmonic approximation. It has been validated for many linear and non-linear polyatomic species [192, 193, 213] with excellent agreement between theory and experiment. The computed FCFs depend strongly on the changes in molecular geometry upon electronic excitation and more weakly on changes in vibrational frequencies. High-resolution spectroscopy confirms that the molecular geometries change minimally upon electronic excitation [282, 284, 285].

We benchmark our multidimensional FCF calculations by comparing to experimental measurements. FCFs for $SrNH_2$ have been previously measured [284] on the $\tilde{C}\,^2A_1 \rightarrow \tilde{X}\,^2A_1$ and $\tilde{A}\,^2B_2 \rightarrow \tilde{X}\,^2A_1$ bands. Table 9.1 reports the calculated and measured vibrational branching ratios for $SrNH_2$. We find excellent agreement between theory and experiment. The small discrepancies, which occur in vibrations of the ligand, may arise from the fact that the spectroscopy was typically

Transition	Decay to	Calculated	Measured[a]
$\tilde{A} \rightarrow \tilde{X}$	0_0	0.960	0.959
	1x Sr-N stretch	0.039	0.04
	2x Sr-N stretch	1×10^{-3}	$\sim 1.6 \times 10^{-3}$
	1x NH_2 bend	3×10^{-5}	2×10^{-5}
	1x N-H sym. stretch	8×10^{-6}	4×10^{-5}
$\tilde{C} \rightarrow \tilde{X}$	0_0	0.976	-
	1x Sr-N stretch	0.011	0.01
	2x Sr-N stretch	1×10^{-4}	-
	1x NH_2 bend	0.010	overlapped
	1x N-H sym. stretch	6×10^{-6}	8×10^{-6}

[a]From Ref. [284]

Table 9.1: Comparison of measured and calculated vibrational branching ratios for $SrNH_2$. Because decay to the NH_2 bending mode is overlapped in the $\tilde{C} \rightarrow \tilde{X}$ band, we are not able to sum experimental FCFs in this case. The molecular geometry and vibrational frequencies used in the calculations are taken from Refs. [284, 286, 305].

unable to fully determine the ligand geometry, so systematic errors affecting the calculations are possible. These calculations indicate that for $SrNH_2$, photon cycling of $\sim 10^4$ photons should be possible with just three vibrational repumping lasers. There also exist measurements of vibrational branching ratios in $CaOC_2H_5$ [292], predicting a decay to the Ca-O stretching mode of ~ 0.1, in good agreement with our calculation below.[5] Besides these few cases, vibrational branching ratios for nonlinear, laser-coolable species are rarely reported. Clearly, there is need for new, accurate measurements of vibrational branching ratios in AE-containing ATMs.

Calculated multidimensional FCFs for $CaNH_2$, CaSH, and SrSH are reported in Tab. 9.2. Although there are no published FCF measurements for these species, high-resolution studies have noted that off-diagonal decays were either unobservably small or highly suppressed, in agreement with our predictions [290]. For these molecules, our calculations indicate that 3-5 repumping lasers will be required to scatter $> 10^4$ photons. Vibrational normal modes of MSH species are shown in

[5]These measurements were taken with pulsed-laser excitation and the data shows signs of collisional excitation which could present systematic errors in their interpretation.

	$CaNH_2$		
	$\tilde{A} \to \tilde{X}$	$\tilde{B} \to \tilde{X}$	$\tilde{C} \to \tilde{X}$
0_0^0	0.963	0.993	0.979
1x Ca-N stretch	0.034	2×10^{-3}	0.019
1x NH_2 bend	2×10^{-3}	1×10^{-3}	8.8×10^{-4}
2x Ca-N stretch	1.6×10^{-4}	5×10^{-5}	3.6×10^{-6}
1x N-H sym. stretch	3.1×10^{-7}	3×10^{-6}	3.3×10^{-7}
	CaSH		
	$\tilde{A} \to \tilde{X}$	$\tilde{B} \to \tilde{X}$	$\tilde{C} \to \tilde{X}$
0_0^0	0.820	0.952	0.999
1x Ca-S stretch	0.163	0.0276	3.3×10^{-4}
1x Ca-S-H bend	0.016	0.0199	3.5×10^{-6}
2x Ca-S stretch	1.6×10^{-4}	4×10^{-4}	$< 10^{-6}$
1x S-H stretch	1×10^{-6}	1×10^{-6}	1×10^{-6}
	SrSH		
	$\tilde{A} \to \tilde{X}$	$\tilde{B} \to \tilde{X}$	$\tilde{C} \to \tilde{X}$
0_0^0	0.828	0.953	0.976
1x Sr-S stretch	0.170	0.046	0.023
1x Sr-S-H bend	0.0014	4×10^{-4}	2×10^{-4}
2x Sr-S stretch	1×10^{-4}	$< 10^{-5}$	$< 10^{-4}$
1x S-H stretch	1×10^{-6}	1×10^{-6}	1×10^{-6}

Table 9.2: Calculated multidimensional FCFs for $CaNH_2$, CaSH, and SrSH. The molecular geometry and vibrational frequencies used in the calculations are as reported in Refs. [277–279, 282, 283, 285, 290].

Fig. 9.4, depicting a strong mixing between the bending and M-S stretching motions; this mixing is included in our calculations. Dynamic visualizations of all vibrational normal modes for $CaNH_2$ are provided in the media Supplemental Materials. Proper accounting of the differences between ground state and excited state normal modes is included in the calculations of Tabs. 9.1 and 9.2. Comparison of the methods also shows that while the individual FCFs may differ slightly, the sum of the dominant few FCFs is consistent.

The computations above require the complete molecular geometry and vibrational frequencies

for all vibrational modes, which have not been experimentally determined for many species. Often, only the metal-ligand bond lengths have been determined. Experience with the monohydroxides shows that the metal-ligand stretching mode is typically the dominant decay channel. Table 9.3 presents metal-ligand stretching mode FCFs for a wide variety of species using the simple model of Ref. [306]. We have relied almost exclusively on experimental inputs and there is limited previous spectroscopy of the $\tilde{C}$ states in these species. Thus, in many cases it is only possible to compute FCFs for the $\tilde{A}$ and/or $\tilde{B}$ states.

The FCFs for the ATMs in Tab. 9.3 are highly diagonal due to the small changes in potential energy surface shapes upon decay. We estimate the relative error in our calculations by using the same model for compute FCFs for isoelectronic diatomic and linear triatomic species; for the diagonal FCFs, the relative error is expected to be $< 3\%$. Note that perturbations in the excited electronic state can introduce unexpectedly strong off-diagonal decays [193], and for any particular species the dominant uncertainty in the FCFs will likely be due to these perturbative couplings. These will become more prevalent especially with increasing complexity and decreasing symmetry of the ligand. In addition, higher-lying excited states such as the $\tilde{C}$ states are very likely to suffer from perturbations even in smaller molecules. We will see evidence of this in CaSH and $CaNH_2$ in Sec. 9.3.

We have also conducted a set of *ab initio* calculations to understand these species (see Supplemental Materials). Normal modes and vibrational frequencies were computed at optimized geometries using the ORCA Quantum Chemistry Software [266] and wavefunction overlap integrals were computed numerically using the ezSpectrum software [308]. The calculations are benchmarked by testing the predictions for CaOH against experimentally determined FCFs [193]. For the lowest excited electronic transition $\tilde{A} \rightarrow \tilde{X}$, the FCF for the fundamental 0_0^0 transition changed from 0.988 (CaOH) to 0.870 (CaSH) to 0.989 ($CaNH_2$). The dominant vibrational loss channel was to the

Molecule	Transition	q_{00}	q_{01}	λ_{00} (nm)	λ_{01} (nm)
CaSH	$\tilde{A} \rightarrow \tilde{X}$	0.826	0.157	650	664
	$\tilde{B} \rightarrow \tilde{X}$	0.983	0.016	630	643
	$\tilde{C} \rightarrow \tilde{X}$	0.999	0.0003	622	634
SrSH	$\tilde{A} \rightarrow \tilde{X}$	0.850	0.137	700	713
	$\tilde{B} \rightarrow \tilde{X}$	0.962	0.037	675	687
	$\tilde{C} \rightarrow \tilde{X}$	0.981	0.0184	666	678
$MgNH_2$ [a]	$\tilde{A} \rightarrow \tilde{X}$	0.933	0.065	~410[b]	~420[b]
$CaNH_2$	$\tilde{A} \rightarrow \tilde{X}$	0.964	0.035	640	662
	$\tilde{B} \rightarrow \tilde{X}$	0.997	0.0002	633	654
	$\tilde{C} \rightarrow \tilde{X}$	0.976	0.022	576	593
$SrNH_2$	$\tilde{A} \rightarrow \tilde{X}$	0.957	0.039	700	723
	$\tilde{B} \rightarrow \tilde{X}$	0.971	0.028	679	700
	$\tilde{C} \rightarrow \tilde{X}$	0.956	0.013	630	648
$BaNH_2$ [c]	$\tilde{A} \rightarrow \tilde{X}$	0.916	0.081	~895[b]	~925[b]
	$\tilde{C} \rightarrow \tilde{X}$	0.851	0.137	~760[b]	~780[b]
MgCHDT	$\tilde{A} \rightarrow \tilde{X}$	0.936	0.062	499	526
CaCHDT	$\tilde{A} \rightarrow \tilde{X}$	0.997	0.002	680	700
CaOCHDT	$\tilde{A} \rightarrow \tilde{X}$	0.951	0.048	628	648
	$\tilde{B} \rightarrow \tilde{X}$	0.946	0.046	565	586
SrOCHDT	$\tilde{A} \rightarrow \tilde{X}$	0.945	0.046	689	709
$CaSCH_3$	$\tilde{A} \rightarrow \tilde{X}$	0.809	0.171	645	658
	$\tilde{B} \rightarrow \tilde{X}$	0.981	0.018	633	645
$SrSCH_3$	$\tilde{A} \rightarrow \tilde{X}$	0.832	0.153	694	706
	$\tilde{B} \rightarrow \tilde{X}$	0.978	0.021	676	688
	$\tilde{C} \rightarrow \tilde{X}$	0.957	0.042	647	657
$CaNHCH_3$	$\tilde{A} \rightarrow \tilde{X}$	0.953	0.046	652	673
$SrNHCH_3$	$\tilde{A} \rightarrow \tilde{X}$	0.944	0.054	706	726
$CaOC_2H_5$	$\tilde{A} \rightarrow \tilde{X}$	0.892	0.102	631	647
$CaOCH(CH_3)_2$	$\tilde{A} \rightarrow \tilde{X}$	0.956	0.043	632	645
$SrOCH(CH_3)_2$	$\tilde{A} \rightarrow \tilde{X}$	0.943	0.056	690	704
$CaC_5H_4CH_3$ [d]	$\tilde{A} \rightarrow \tilde{X}$	0.825	0.094	691	706
	$\tilde{B} \rightarrow \tilde{X}$	0.86	0.078	686	701

[a] Mg-N bond lengths inferred from Refs. [287, 288, 307].
[b] Excitation wavelengths not measured at high resolution.
[c] Ba-N bond lengths inferred from Refs. [128, 289].
[d] Dispersed fluorescence measured in Ref. [294].

Table 9.3: Franck-Condon factors calculated for decay to 0 quanta (q_{00}) and 1 quantum (q_{01}) of the metal-ligand stretching mode. λ_{00} and λ_{01} are the main cycling and first repumping transition wavelengths in nm. Experimentally measured geometries and frequencies come from Refs. [277–280, 280, 281, 281–287, 287, 288, 288, 289, 289–293, 293–295, 297, 298].

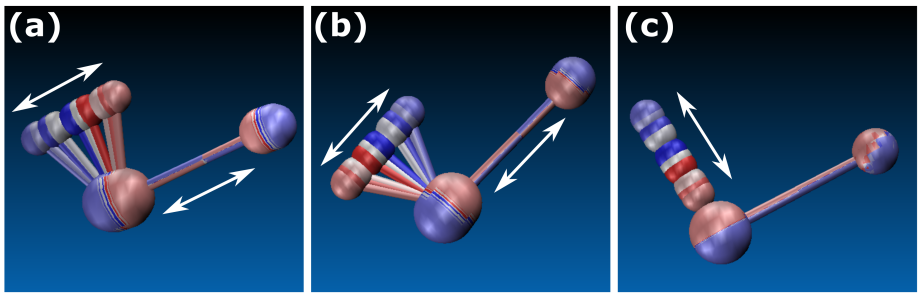

Figure 9.4: Normal modes for CaSH corresponding to (a) 316 cm^{-1}, (b) 360 cm^{-1} and (c) 2640 cm^{-1} vibrational frequencies. The beginning of the trajectory is indicated in red, the middle in white, and the end in blue. Note the strong mixing between the bending motion and Ca-S stretching vibration.

Ca-ligand stretching mode for all three molecules with decay fractions 0.01 (CaOH), 0.10 (CaSH) and 0.01 ($CaNH_2$) to this mode. The Duschinsky transformation [309] of the normal modes was used for all three molecules to account for the change in normal coordinates in each electronic state. In the case of CaSH, we observed strong mixing between the stretching and bending motions (see Fig. 9.4). While the CaSH 0_0^0 vibronic FCF is predicted to be < 0.9, the sum of the three dominant vibrational loss channels is $\gtrsim 0.99$. Previous work [142] has indicated that only the sum of the three dominant FCFs should be considered stable for predictive purposes when purely *ab initio* methods are being used.

Based on these calculations and their agreement with experiment, ATMs are strong candidates for optical cycling and laser cooling. For species of the form MSH and MNH_2 (M=Mg, Ca, Sr), the calculations indicate that at least one electronic transition in several of the species considered can scatter $> 10^3$ photons with only a single repumping laser. The calculations predict that the number of photon scatters per molecule is increased to $> 10^4$ per molecule— the typical number required to slow a molecular beam and capture into a MOT— with three repumping lasers. Indeed, the calculated FCFs are comparable to those of isoelectronic diatomic species which have already been successfully laser-cooled [113, 117]. For the larger species, at least 100 photons can be scattered with just two lasers. It is remarkable that even in species as complex as calcium methylcyclopentadienyl

[$CaC_5H_4CH_3$, Fig. 9.1(g)], with 36 vibrational normal modes, the FCFs converge to $\gtrsim 0.95$ with just one or two repumping lasers [294]. This is sufficient for high-fidelity detection, preparation of single quantum states, or transverse laser cooling in order to enhance interrogation times in a molecular beam [126, 217].

9.3 Vibrational branching: measurements

In collaboration with the Steimle group, we have studied two of the proposed ATMs, calcium hydrosulfide (CaSH) and calcium monoamide ($CaNH_2$). CaSH and $CaNH_2$ are prototypical examples of molecules with, respectively, C_s and C_{2v} point group symmetry. These measurements served to validate the theoretical computations presented above and to systematically study the effect of lowering the molecular symmetry. As has been noted, the Bernath group has previously reported dispersed fluorescence measurements of $SrNH_2$ recorded with a Broida oven source [284]. These measurements appeared to achieve sensitivity below the 10^{-4} level, but it is unclear what systematic errors could be caused by the high pressures and temperatures of the Broida oven. For example, collisional relaxation and non-resonant emission are evident in the data of Ref. [284].

9.3.1 Experimental setup and analysis

A detailed overview of the experimental setup has been described previously [153, 193]. In brief, a pulsed supersonic molecular beam is used as a source of internally cold molecules ($T_{\text{rot}} \sim 10$ K). A continuously rotating calcium rod is ablated with with a pulse of 532 nm radiation generated by a frequency doubled Nd:YAG laser (~ 10 ns duration, ~10 mJ pulse energy) operating at 10 Hz. The ablation plume is entrained in a supersonic expansion gas mixture of Ar at a typical backing pressure ~4000 kPa. The Ar is mixed with approximately 4% of either hydrogen sulfide or ammonia

to produce CaSH or $CaNH_2$, respectively. Similar yields of both CaSH and $CaNH_2$ were observed, both approximately a factor of 3-5 smaller than the yield of CaOH in the same setup [193].

The free-jet expansion is probed approximately 10 cm downstream from the pulsed valve via laser excitation from a single frequency cw-dye laser. The resulting fluorescence is collected and focused into a 0.67 m, high-efficiency Czerny-Turner-type monochromator with a low-dispersion grating (300 lines/mm). The dispersed laser-induced fluorescence (DLIF) over a 75 nm wide spectral window is detected on a gated intensified charge-coupled device (ICCD). The CCD pixels are binned vertically to produce a one-dimensional array of intensities versus emission wavelength. The wavelength calibration of the spectrometer was performed separately using an argon lamp, and a blackbody source was used to calibrate the relative intensity sensitivity as a function of wavelength. The $\sim$1 MHz resolution of the cw-dye laser allowed rotationally-resolved measurements. A wavemeter with accuracy $\lesssim 1$ GHz enabled coarse wavelength tuning while a separate, skimmed molecular beam was continuously monitored to allow unambiguous identification of individual rotational lines. The rotational resolution and absence of state-changing collisions in the molecular beam were important to eliminate potential systematic errors in the measurements [193, 292].

A typical DLIF measurement comprises the average of $\sim 5 \times 10^4$ shots. In each case, several datasets were recorded: (i) a "signal" with the Nd:YAG and cw-dye laser on, (ii) a "background" with excitation laser blocked by the Nd:YAG on, and (iii) an "off-resonance" trace with the Nd:YAG on and the probe laser tuned off resonance from all molecular transitions. Decay of the metastable $Ca^*\ ^3P_1$ level, which is partially populated by the ablation process, is apparent in measurements covering the region near 657 nm. The off-resonance background traces are important for removing most of this effect, although in almost all cases the Ca^* emission does not fall near a possible vibrational decay and therefore has no effect on the measurements. Analysis of the DLIF spectra to extract VBRs is conducted as described in Sec. 8.2.3.

Table 9.4: Vibrational normal mode numbering and symmetry labels for $CaNH_2$ under transformations of the C_{2v} point group. The listed frequencies are approximate and come from *ab initio* computations.

Mode	Symmetry	Frequency (cm^{-1})	Description
ν_1	a_1	3500	N-H symmetric stretch
ν_2	a_1	1570	NH_2 in-plane symmetric bend
ν_3	a_1	550	Ca-N stretch
ν_4	b_1	3580	N-H asymmetric stretch
ν_5	b_1	300	NH_2 in-plane asymmetric bend
ν_6	b_2	470	NH_2 out-of-plane bend

Radiative lifetime measurements were performed by tuning a Nd:YAG-pumped pulsed-dye laser to intense bandheads and monitoring the DLIF spectrum with a 1 μs ICCD detection window. The ICCD gate delay relative to dye laser excitation was then increased in 5-10 ns increments. The resulting fluorescence decay curves were fit to a first order exponential to determine the excited state fluorescence lifetime, τ.

9.3.2 Calcium monoamide

As a planar molecule with C_{2v} symmetry, $CaNH_2$ represents a natural step in symmetry descent from symmetric top molecules. We measured vibrational branching ratios for the electronically excited states $\tilde{A}\ ^2B_2$, $\tilde{B}\ ^2B_1$, and $\tilde{C}\ ^2A_1$, all in the 0^0 vibrational levels. Table 9.4 enumerates the six vibrational normal modes of $CaNH_2$.

$CaNH_2$ $\tilde{A}\ ^2B_2\ (v = 0)$ state

Figure 9.5 shows the observed DLIF trace following excitation of the $CaNH_2$ $0_0^0\tilde{A}\ ^2B_2 \leftarrow \tilde{X}\ ^2A_1$ band near 647 nm. We drove the excitation at 15451.599 cm^{-1}, which according to previously reported spectroscopy corresponds to a Q branch transition originating from the $\tilde{X}\ ^2A_1(3_{13})$ rotational state. The dominant off-diagonal molecular fluorescence is associated with the ν_3 (Ca-N stretch) mode, redshifted by 540 cm^{-1}. Additional weaker features that we assign to the ν_5 (in-

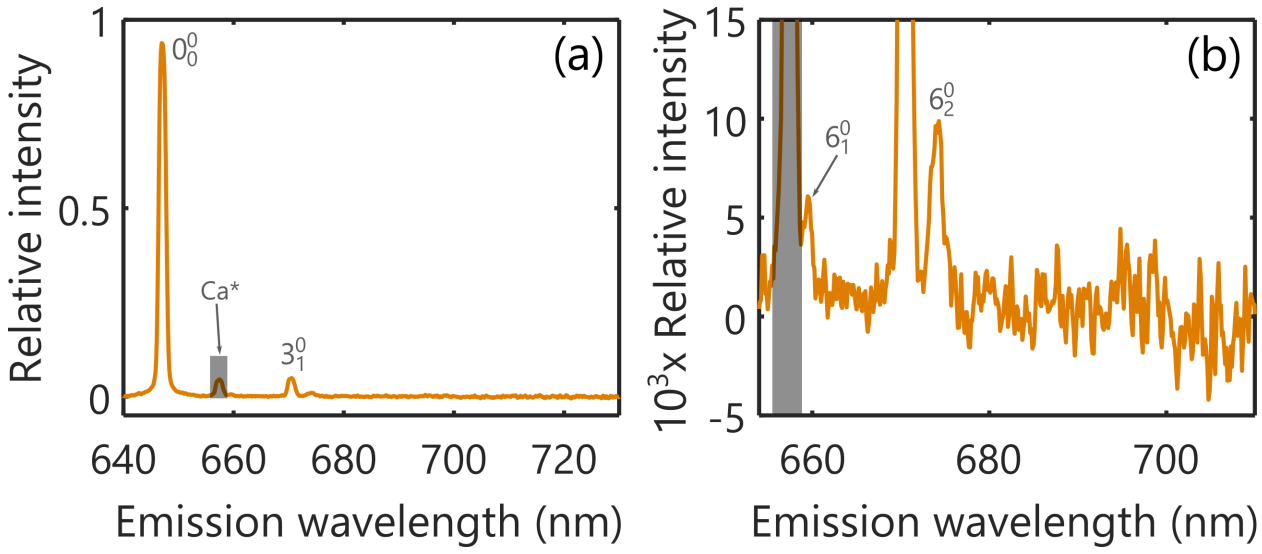

Figure 9.5: DLIF spectrum following excitation of $CaNH_2$ molecules to the $\tilde{A}\ ^2B_2\ (v=0)$ state at 15451.599 cm^{-1}. Gray numbers above each peak indicate the vibronic decay label. (a) Full range of recorded intensities. (b) Detail near the noise floor, indicating that relative intensity sensitivity around the 0.5% level is achieved. Gray shaded bands cover the spectral artifact due to atomic Ca emission.

plane asymmetric bend) mode are also evident. The vibrational assignments should be taken as tentative. These features are observed to occur with fluorescence redshifts of about 300 cm^{-1} and 620 cm^{-1}. Decay assigned to $1\nu_5$ is about 2-3$\times$ weaker than that to $2\nu_5$. Emission due to impurity Ca* atoms is evident at 657 nm ($^3P_1 \rightarrow^1 S_0$ band). Because the Ca* emission potentially obscures molecular LIF with redshift $\sim$300 cm^{-1} we have also used pulsed-laser excitation to measure the $\tilde{A}\ ^2B_2 \rightarrow \tilde{X}\ ^2A_1$ DLIF. This method effectively eliminates the atomic emission relative to the molecular LIF due to fast gating of the ICCD. No additional decays overlapping the atomic fluorescence were observed in such measurements. Based on the observed signal-to-noise ratio, any unobserved decays have branching ratios $< 0.3\%$. The inferred branching ratios are collected in Tab. 9.5. These imply that at least a few hundred photon scatters per molecule should be possible with three vibrational repumpers, roughly similar to the complexity required for photon cycling in YbOH.

Table 9.5: Vibrational intervals (in cm^{-1}) and branching ratios (in %) determined following excitation to the $CaNH_2$ $\tilde{A}\ ^2B_2(v=0)$ state. The noise level for the smallest observed VBRs is around 0.2%.

Redshift (cm^{-1})	Assignment	Relative intensity (%)
0	0_0^0	93.6(5)
300	5_1^0	0.5(2)
540	3_1^0	4.8(2)
620	5_2^0	0.9(2)

$CaNH_2$ $\tilde{B}\ ^2B_1$ $(v=0)$ state

Figure 9.6 shows the observed DLIF following excitation of the $CaNH_2$ $0_0^0\tilde{B}\ ^2B_1(4_{04}) \leftarrow \tilde{X}\ ^2A_1(4_{13})$ band near 630 nm. In this case, we observe decays that we assign to ν_3, ν_5, and ν_6. As expected, the ν_3 feature associated with Ca-N stretching vibration is dominant. A small amount of in-plane bending (ν_5) is excited upon decay. The feature around 440 cm^{-1} is assigned to ν_6, the NH_2 out-of-plane bending mode. It is interesting to note that decay to ν_6 is observed in decay from the $\tilde{B}\ ^2B_1$ state, which has electronic orbitals that are directed *out* of the molecular plane, but not from the $\tilde{A}\ ^2B_2$ state, which has orbital lobes *in* the plane. The noise level is limited to about 0.2%, and must be improved in order to determine the repumping lines required to scatter more than about 500 photons per molecule. The extracted intensities indicate that the $\tilde{B} \rightarrow \tilde{X}$ band also exhibits a highly diagonal FCF matrix. This is encouraging because the $\tilde{B}\ ^2B_1(v=0)$ level is embedded among excited vibrational levels of the $\tilde{A}\ ^2B_2$ state. Nonetheless, perturbations between these states appears negligible at the level of $\gtrsim 0.1\%$, as would have been expected based on the symmetry species. In this case, about four vibrational repumping lasers appear sufficient to scatter an average of about 500 photons per molecule.

$CaNH_2$ $\tilde{C}\ ^2A_1$ $(v=0)$ state

Finally, we investigated the $CaNH_2$ $0_0^0\tilde{C}\ ^2A_1 \leftarrow \tilde{X}\ ^2A_1$ band near 575 nm. The resulting DLIF spectrum is shown in Fig. 9.7. Significant off-diagonal fluorescence is observed in this spectrum. While

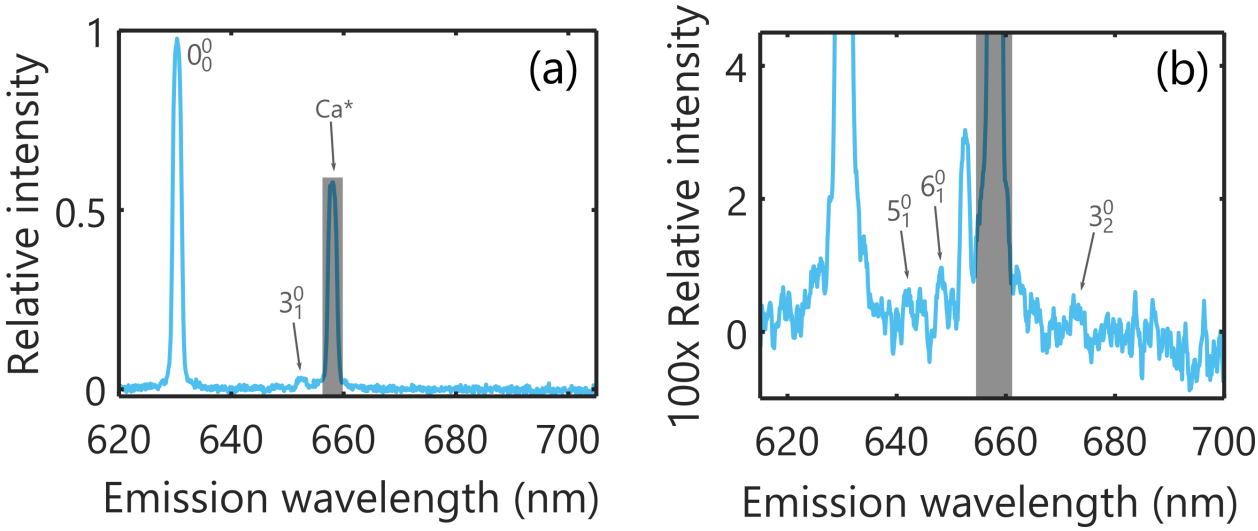

Figure 9.6: DLIF spectrum following excitation of $CaNH_2$ molecules to the $\tilde{B}\ ^2B_1\ (v = 0)$ state at 15872.595 cm^{-1}. Gray numbers above each peak indicate the vibronic decay label. (a) Full range of recorded intensities. (b) Detail near the noise floor, indicating that relative intensity sensitivity around the 0.2% level is achieved. Gray shaded bands cover the spectral artifact due to atomic Ca emission.

Table 9.6: Vibrational intervals (in cm^{-1}) and branching ratios (in %) determined following excitation to the $CaNH_2$ $\tilde{B}\ ^2B_1(v = 0)$ state. The noise level for the smallest observed VBRs is around 0.2%.

Redshift (cm^{-1})	Assignment	Relative intensity (%)
0	0_0^0	95.7(8)
345	5_1^0	0.38(2)
435	6_1^0	0.96(2)
540	3_1^0	2.7(2)
1020	3_2^0	0.2(1)

some features are readily assigned on the basis of previously determined vibrational frequencies, we are unable to assign a number of relatively strong features. As can be seen in Fig. 9.7(b), some unassigned peaks appear as doublets separated by about 50 cm^{-1}. This value is close to the spin-orbit coupling constant in many Ca-containing molecules, but that does not appear to be a relevant scale here because, as an ATM, $CaNH_2$ would be expected to have quenched orbital angular momentum and because the $\tilde{C}\ ^2A_1$ state correlates to a $^2\Sigma^+$ state in linear molecules. The 50 cm^{-1} splittings could also arise due to nonradiative population transfer among the excited states following ablation, but none of our other spectra showed signs of this effect. In investigating the many decay pathways in more detail, we recorded DLIF traces for three rotational levels in $\tilde{C}\ ^2A_1$, and

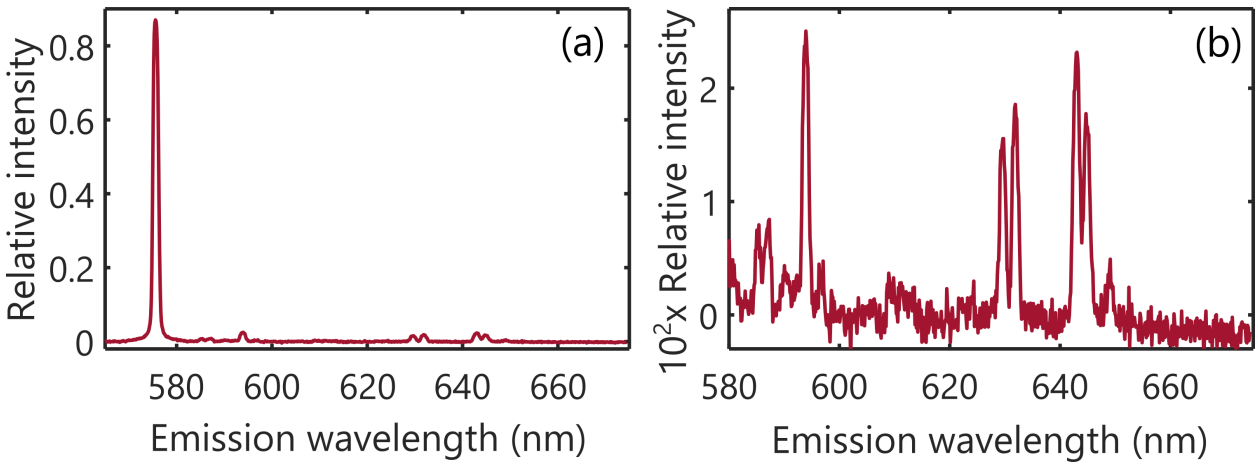

Figure 9.7: DLIF spectrum following excitation of $CaNH_2$ molecules to the $\tilde{C}\ ^2A_1\ (v = 0)$ state. This spectrum shows the average of three excitation pathways: 17373.900 cm^{-1}, 17373.919 cm^{-1}, and 17376.273 cm^{-1}. (a) Full range of recorded intensities. (b) Detail near the noise floor, indicating that relative intensity sensitivity around the 0.2% level is achieved.

all showed the same features.

9.3.3 Calcium hydrosulfide

CaSH is a bent triatomic molecule with C_s symmetry. The electronically excited states $\tilde{A}\ ^2A'$, $\tilde{B}\ ^2A''$, and $\tilde{C}\ ^2A'$ have each been considered as potentially promising for optical cycling. However, theoretical calculations showed that the $\tilde{A} \rightarrow \tilde{X}$ band was expected to be the least diagonal of these transitions [130]. Moreover, the Ca* atomic emission strongly overlaps the dominant off-diagonal molecular fluorescence from this excited state. For this reason, we limited the investigations in CaSH to the $\tilde{B}\ ^2A''$ and $\tilde{C}\ ^2A'$ levels. CaSH possesses three vibrational modes summarized in Tab. 9.8. Unlike in *linear* triatomic species, decays to both even and odd quanta of excitation of the bending mode are allowed.

CaSH $\tilde{B}\ ^2A''\ (v = 0)$ state

The CaSH $\tilde{B}\ ^2A''$ state was probed by exciting on the $0_0^0\tilde{B}\ ^2A'' \leftarrow \tilde{X}\ ^2A'(K_a = 0 - 1)$ subband at 158479.770 cm^{-1}. Based on previous high-resolution spectroscopy, this corresponds to exciting

Table 9.7: Vibrational branching ratios determined for the $CaNH_2$ $\tilde{C}\ ^2A_1 \rightarrow \tilde{X}\ ^2A_1$ band. Question marks indicate features that could not be assigned but were repeatedly observed for decays from $\tilde{C}\ ^2A_1$.

Redshift (cm^{-1})	Assignment	Relative intensity
0	0_0^0	86.8(10)
290	4_1^0	0.9(2)
340	??	0.82(2)
430	6_1^0	0.38(2)
540	3_1^0	2.5(3)
615	??	0.4(2)
975	$3_1^0 6_1^0$	0.4(2)
1020	3_2^0	0.3(2)
1490	$3_2^0 6_1^0$	1.5(3)
1550	2_1^0	1.8(3)
1820	$2_1^0 4_1^0$	2.3(4)
1870	??	1.6(3)
1970	$2_1^0 6_1^0$	0.3(1)

Table 9.8: Vibrational normal mode numbering and symmetry labels for CaSH under transformations of the C_s point group. The listed frequencies are approximate and come from *ab initio* computations.

Mode	Symmetry	Frequency (cm^{-1})	Description
ν_1	a'	2680	S-H stretch
ν_2	a'	360	Ca-S-H bend
ν_3	a'	310	Ca-S stretch

molecules in the $N'' = 4$ state [76]. The DLIF spectrum recorded for this excitation is shown in Fig. 9.8 and the extracted VBRs are presented in Tab. 9.9. We observe decays to both ν_1 and ν_2 with roughly equal intensity. It was expected that decays to the Ca-S-H bending mode could have high intensity because there are no selection rules to prevent this. In addition, both the Ca-S stretching and Ca-S-H bending modes would be expected to be relatively strongly affected by electronic excitation on the Ca atom. We do not observe decays to any other vibrational modes, but unfortunately the Ca^* feature could obscure low-intensity decays near the 1_2^0 or 2_2^0 frequencies. Future DLIF studies are required that have higher sensitivity and show less contamination from the Ca^* signal.

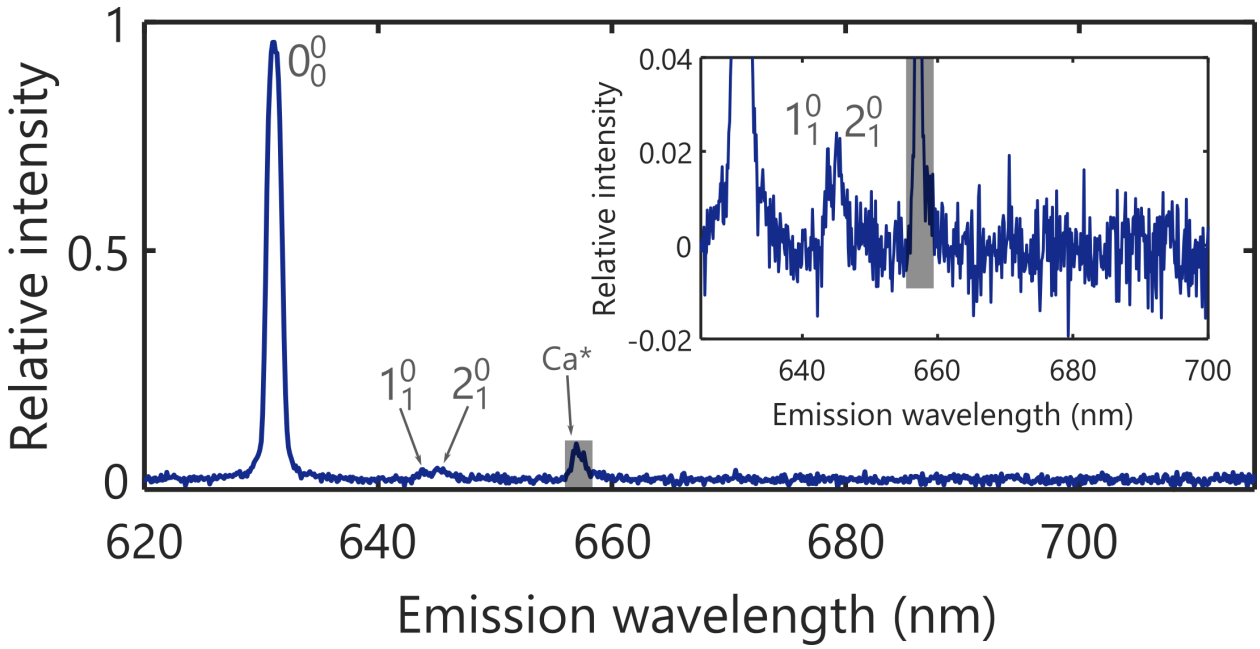

Figure 9.8: DLIF spectrum following excitation of CaSH molecules to the $\tilde{B}\ ^2A''$ state at 15849.770 cm^{-1}. Gray numbers near each peak indicate the vibronic decay label. Inset: details near the noise floor, indicating that relative intensity sensitivity around the 1% level is achieved.

Table 9.9: Vibrational intervals (in cm^{-1}) and branching ratios (in %) determined following excitation to the CaSH $\tilde{B}\ ^2A''(v=0)$ state. The noise level for the smallest observed VBRs is around 0.1%.

Redshift (cm^{-1})	Assignment	Relative intensity (%)
0	0_0^0	96.0(8)
311	3_1^0	1.8(2)
350	2_1^0	2.1(2)

CaSH $\tilde{C}\ ^2A'\ (v=0)$ state

We collected DLIF spectra from the CaSH $\tilde{C}\ ^2A'(v=0)$ level by exciting at 16076.842 cm^{-1}. The resulting DLIF spectrum is shown in Fig. 9.9 and the VBRs extracted from this data in reported in Tab. 9.10. In this spectrum, we observe quite strong off-diagonal decay to the ν_2 and ν_3 fundamentals. This was especially surprising (and disappointing) because the calculations presented in Sec. 9.2 suggested that this band should have extremely diagonal VBRs. The GF matrix calculations that led to this expectation were based on a molecular geometry assigned in Ref. [278], but subsequent *ab initio* calculations conducted by Lan Cheng suggest that the reported geometry could be

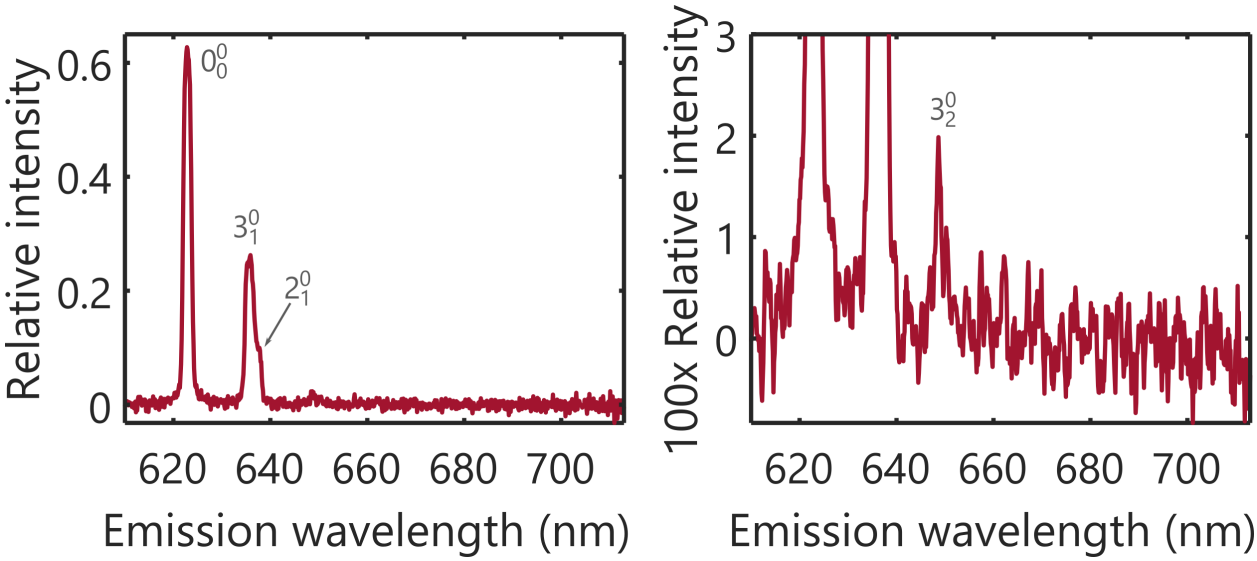

Figure 9.9: DLIF spectrum following excitation of CaSH molecules to the $\tilde{C}\ ^2A'$ state at 16076.842 cm^{-1}. Gray numbers near each peak indicate the vibronic decay label. Inset: details near the noise floor, indicating that relative intensity sensitivity around the 1% level is achieved.

Table 9.10: Vibrational intervals (in cm^{-1}) and branching ratios (in %) determined following excitation to the CaSH $\tilde{C}\ ^2A'(v=0)$ state. The noise level for the smallest observed VBRs is around 0.1%.

Redshift (cm^{-1})	Assignment	Relative intensity (%)
0	0_0^0	62.8(10)
320	3_1^0	25.9(5)
370	2_1^0	9(2)
640	3_2^0	1.9(5)

in error. These computations indicated that the Ca-S bond length experiences significant change upon electronic excitation, from 2.596 Å to 2.545 Å, and that the Ca-S-H bond angle changes significantly from $90.2°$ to $84.6°$. The calculations also indicated that the decay to ν_2 (Ca-S-H bend) that appears as a shoulder near 640 nm is due to vibronic coupling between the $\tilde{A}\ ^2A'$ and $\tilde{C}\ ^2A'$ states. While these measurements imply that the $\tilde{C}\ ^2A'$ state is not particularly useful as a "main" excited for optical cycling, the strong coupling excited vibrational states in $\tilde{X}\ ^2A'$ could still be useful as a repumping pathway. Future studies of vibronic coupling among the electronically excited states could be of interest for physical chemistry applications.

	ΔK_a	ΔK_c	Exceptions
a-type	0	± 1	$\Delta N \neq 0$ for $K_a' \to K_a'' = 0$
b-type	± 1	± 1	
c-type	± 1	0	$\Delta N \neq 0$ for $K_c' \to K_c'' = 0$

Table 9.11: Selection rules in the dipole approximation for the proposed ATM laser-cooling transitions. Higher order decays ($\Delta K_c = \pm 2$, etc.) are suppressed, but may be induced by perturbations. There is an additional restriction due to the fact that $K_a + K_c = N$ or $N + 1$ [157, 311].

9.4 Rotational branching

The rotational structure of ATMs can be extremely complex and a good overview of the theory can be found in textbooks such as Refs. [133, 139, 310]. Following standard convention, we label the rotational states by $N_{K_a K_c}$. N is the total angular momentum excluding electron and nuclear spins. The principal rotational constants are labeled A, B, and C, where $A > B > C$. K_a and K_c are not rigorous quantum numbers, but are defined as the projection of N onto the hypothetical symmetry axis formed by distorting the molecule to prolate (a-axis) and oblate limits (c-axis), respectively. The unpaired electron spin can couple weakly to rotation and $J = N + S$ is the total angular momentum excluding nuclear spin. Hyperfine structure is typically unresolved ($<$ 1 MHz). Losses to dark states throughout the complicated rotational ladder are a potential concern during photon cycling. Here we show that rotational and parity selection rules can eliminate or mitigate these potential problems.

In a generic ATM, the transition dipole moment, $\hat{\mu}$, can have components along any of the three principal axes. The transition dipole moment components are labeled $\hat{\mu}_a$, $\hat{\mu}_b$, and $\hat{\mu}_c$ to indicate their projection along the principal axes of the molecule. The transitions are then labeled a-type, b-type, or c-type according to which component of the transition dipole moment they couple. The selection rules for each type of transition are summarized in Tab. 9.11. There are additional restrictions due to the fact that $K_a + K_c = N$ or $N + 1$ [157, 311].

Using the selection rules enumerated in Tab. 9.11 we find that it is possible to construct closed

cycling schemes for transitions coupling to any component of $\hat{\mu}$. Some representative photon cycling schemes are presented in Fig. 9.10. Dashed lines indicate rotational branches which may be induced by spin-rotation mixings in some cases. In well-behaved cases, the dashed lines may not require repumping. An a-type band, expected for the $\tilde{C} \leftarrow \tilde{X}$ transitions, is shown in Fig. 9.10(a). The rotational structure is reminiscent of a $(b)^2\Sigma^+ \leftarrow (b)^2\Sigma^+$ transition in linear molecules, where the first letter indicates the appropriate Hund's case.[6] In this case, a combination of parity and angular momentum selection rules guarantee rotational closure when driving the ${}^{Q}Q_{12}(0, 1, 0.5)$ and ${}^{Q}P_{11}(0, 1, 1.5)$ lines.[7] A single rf-sideband, easily generated using an electro-optic modulator (EOM) or acousto-optic modulator (AOM), must be added to the excitation laser. Figure 9.10(b) shows a scheme for rotational closure on a b-type band, typical of $\tilde{A} \leftarrow \tilde{X}$ transitions. Here, excitation out of the $K_a'' = 1$ sublevel is convenient because it allows one to target the lowest level of the excited electronic state. In this case, we drive the ${}^{P}Q_{12}(1, 1, 0.5)$ and ${}^{P}P_{11}(1, 1, 1.5)$ lines. Figure 9.10(c) shows how to achieve rotational closure on a c-type band, applicable to the $\tilde{B} \leftarrow \tilde{X}$ transitions. The b- and c-type bands shown here are similar to a $(b)^2\Sigma^{\pm} \leftarrow (b)^2\Pi$ transition in linear species.[8] Here, we choose to drive the ${}^{P}Q_{12}(1, 0, 0.5)$ and ${}^{P}P_{11}(1, 0, 1.5)$ lines. Similar to the a-type band, an rf sideband is required to address the two spin-rotation components of the $N'' = 1$ manifold for either b-type or c-type bands. Note that the $K_a'' = 1$ state, which is convenient for optical cycling, provides a suitable ground state because it is metastable with lifetimes $\gg 10$ s for the species considered here.

The cycling schemes in Fig. 9.10 provide a basis for rotational closure in realistic molecules. For the near-prolate ATMs that we primarily consider, $\tilde{A} \rightarrow \tilde{X}$ decays approximately follow b-type selection rules, $\tilde{B} \rightarrow \tilde{X}$ decays approximately obey c-type selection rules, and $\tilde{C} \rightarrow \tilde{X}$ decays

[6] Such a transition is used for laser slowing of CaF molecules [117] and laser cooling of SrOH molecules [126].

[7] We use the branch designation ${}^{\Delta K_a}\Delta J_{F_n' F_n''}(K_a'', K_c'', J'')$, where F_n labels the spin-rotation component.

[8] Such a transition is proposed for laser cooling the CH radical [312].

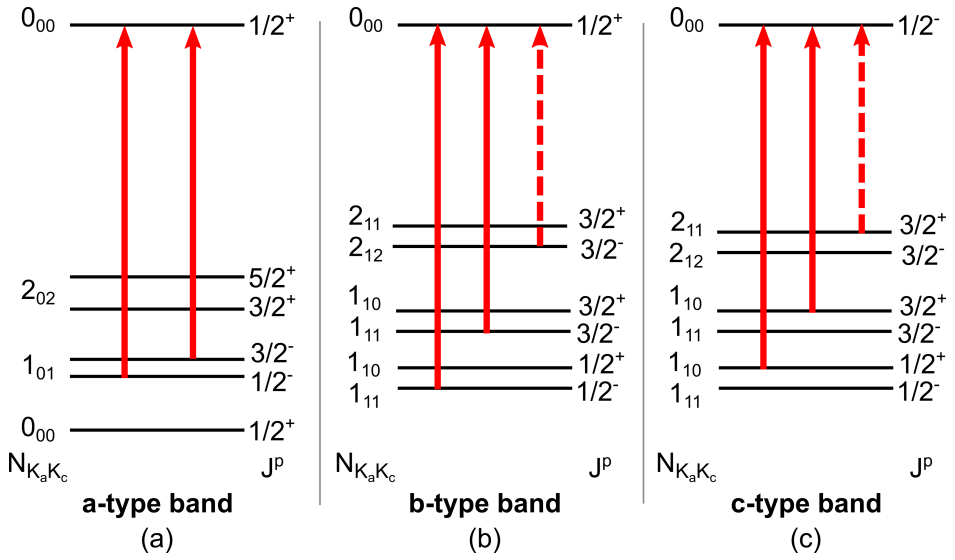

Figure 9.10: Schemes to achieve rotationally-closed photon cycling for pure (a) a-type transitions, (b) b-type transitions, and (c) c-type transitions. Dashed lines indicate transitions which will need to be repumped in special cases, as described in the text. In the $K_a = 1$ levels, the spin-rotation and asymmetry doubling are approximately the same size. These level diagrams assume a near-prolate ATM, but analogous results apply for near-oblate tops.

approximately obey a-type selection rules. As the molecule becomes more asymmetric these patterns will break down and a given excited state may decay via one of several components of $\hat{\mu}$. For example, hybrid ab-type band will commonly occur for molecules with C_s symmetry due to the misalignment of the principal axes from the electronic orbitals [see Fig. 9.3(m-p)]. One additional decay must be repumped, in essence combining the schemes in Fig. 9.10(a) and (b). Alternatively, microwave remixing within the ground manifold can return population to the optical cycle. These decay and repumping pathways are similar to the rotational branch features that can appear in diatomic molecules with $\Lambda'' \geq 1$ [183].

The degree of asymmetry will determine the relative strengths of different components of $\hat{\mu}$. For example, because $\hat{\mu}_a \gg \hat{\mu}_c$ when photon cycling on the $\tilde{C} \leftarrow \tilde{X}$ band of hydrosulfide species, these can likely scatter $\sim 10^4$ photons using the scheme of Fig. 9.10(a) before repumping of the $K_a'' = 1$ state is required. For hybrid bc-type decays, which may occur in molecules with symmetry lower than C_s or due to perturbations, repumping is easily achieved by combining the schemes of Fig. 9.10(b) and (c). A single laser with sidebands imposed by EOMs or AOMs can bridge

the full spin-rotation/asymmetry doubling structure. Finally, for species with near-C_{3v} symmetry (e.g. MOCHDT or MCHDT), where the $\tilde{A}\,^2A'$ and $\tilde{B}\,^2A''$ states have essentially coalesced into the $\tilde{A}\,^2E$ level, an additional decay to the $2_{1K_c}(J'' = 3/2)$ state will appear. Again, this state can be remixed using either microwaves or a single additional laser frequency, as shown by dashed lines in Fig. 9.10. The effects of perturbations, though not expected to significantly alter the results presented above, are discussed in Ref. [130]. Overall we see that, despite the complex ATM rotational structure, application of one or two lasers (depending on the molecular species) with appropriate rf sidebands leads to rotational closure sufficient for scattering $\gtrsim 10^4$ photons. An important next step is to attempt optical cycling with a molecule of low symmetry, such as CaSH, to confirm these predictions.

'And remember, also,' added the Princess of Sweet Rhyme, 'that many places you would like to see are just off the map and many things you want to know are just out of sight or a little beyond your reach. But someday you'll reach them all, for what you learn today, for no reason at all, will help you discover all the wonderful secrets of tomorrow.'

Norton Juster, "The Phantom Tollbooth"

10

Conclusion and Outlook

Initially, the goal of this thesis was to demonstrate methods to laser cool and trap YbOH molecules for an electron EDM measurement. One of the great joys— and surprises— of conducting that research was that it led to additional discoveries with wide-ranging impact toward the laser cooling and trapping of increasingly complex polyatomic molecules. In hindsight, the step from YbOH to complex polyatomic molecules is not particularly surprising. Technologically, working with such a heavy and complex molecular as YbOH required the development of tools like very slow buffer-gas beams and few-photon slowing that were described in Ch. 3 and 7, respectively. Approaching the problem of cooling and trapping from this point of view naturally lends itself to tackling problems that must *also* be solved if one wishes to trap larger polyatomic molecules that are capable of limited

(but not excessive) photon cycling. In addition, the tools developed for high-sensitivity branching ratio spectroscopy (Ch. 4) can be adapted to study increasingly complex polyatomic molecules. In this concluding chapter, we will briefly remark on some ideas that these developments have sparked and that appear to be promising avenues for future research.

10.1 Microwave Zeeman-Sisyphus decelerator

One of the motivations for developing the Zeeman-Sisyphus decelerator described in Ch. 7 was its wide applicability to molecules with magnetic ground states. However, the technique took advantage of the ability to drive electron spin-flip transitions via an excited state with large spin-orbit coupling. There is no guarantee that such a state will always be available. For example, nonlinear molecules often have quenched electronic orbital angular momentum.[1] How could we drive the spin-flip transitions in cases like these?

One possibility is to drive the spin flip directly in the ground electronic state via a microwave field; this is electron spin resonance, dressed up as a method for molecular beam deceleration. There are two distinct advantages of using microwave transitions. First, the reliance on "well-behaved" electronically excited states is removed, vastly increasingly the number of molecules that can be slowed with the same apparatus. Second, because all $1\mu_B$ species have the same Zeeman tuning (aside from the details of residual spin-rotation/hyperfine splittings at zero-field), the same apparatus could be used to slow all such molecules essentially without changing any experimental parameter. Enticingly, one could even be consider slowing multiple different species *simultaneously*.

[1] Here, again, is a case where YbOH and nonlinear molecules force us to confront the same problems.

10.2 Microwave-Optical Stark-Sisyphus deceleration

We have also developed theoretically an alternative deceleration technique that uses electric, rather than magnetic, fields to remove kinetic energy from polar molecules. Notably, this would extend few-photon slowing techniques to nonmagnetic species. An overview of the decelerator is shown in Fig. 10.1. The decelerator consists of a series of stages producing alternately high ($\lesssim$30 kV/cm) and low ($\sim$1 kV/cm) electric fields. Molecules produced by a CBGB are prepared in a low-field-seeking (LFS) state and are incident on a high-field region. The molecules decelerate as they enter the field. Near its peak, the electric field is shaped to have a shallow slope. Microwaves in this region are tuned near resonance for a transition from the LFS state to a high-field-seeking (HFS) state. The changing DC electric field tunes the molecular energy levels across the resonance, driving an adiabatic rapid passage from LFS to HFS states. The trailing edge of the high-field region's electric field has a very steep slope, which ensures that the adiabaticity condition is only satisfied once in each high-field region. In this way, molecules will remain in a HFS state as they exit the high-field region and continue to decelerate. Next, the molecules continue into a low-field region. In the center of this region, they are optically pumped back into a LFS state.

This sequence of microwave and optical transitions is repeated until molecules have been slowed to a desired velocity. Velocity-sensitive optical pumping beams in each low-field region can be added to pump sufficiently slow molecules to a state with significantly smaller dipole moment, after which these molecules are insensitive to the microwave and optical pumping fields and follow approximately ballistic trajectories. The proposed decelerator bears some resemblance to previously proposed deceleration techniques for diatomic molecules [313] and to methods used for cooling, but not slowing, of polyatomic molecules [314].

This deceleration scheme relies on the presence of both HFS and LFS states in the electrostatic field. Low-lying rotational or vibrational modes in polyatomic molecules offer convenient, long-

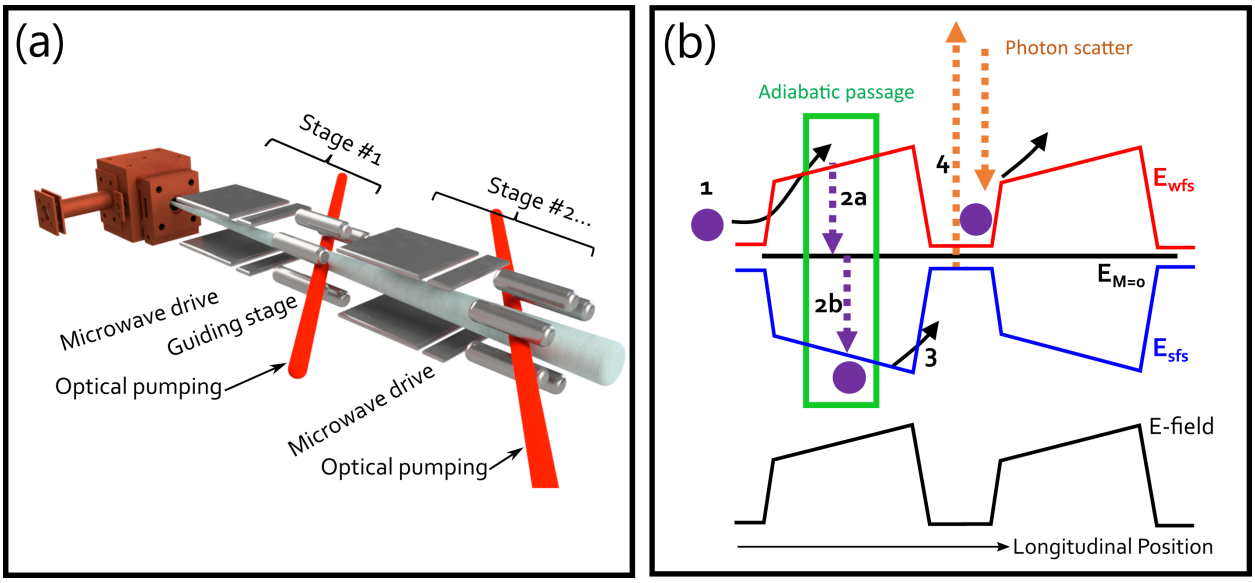

Figure 10.1: Schematic layout of the proposed microwave-optical Stark-Sisyphus slower. (a) Rendering of the proposed layout. (b) Overview of the deceleration process. Steps are as follows: (1) Molecules enter an asymmetric, periodic electric field in a WFS. (2a,2b) As they near the peak field, a microwave field drives an adiabatic rapid passage to the SFS states. (3) The field has a sharp falling slope so that evolution as molecules leave the high-field region is diabatic. (4) In a low-field region, molecules are optically pumped back to WFS states and the process can be repeated.

lived parity doublets with both HFS and LFS sublevels. Figure 10.2 shows the structure of a typical $K = 1$ parity doublet in the presence of an electric field.[2] For electric field strengths greater than about 100 V/cm, all spin-rotation/hyperfine structure is decoupled and the levels are split according to M_N, the projection of angular momentum onto the external field. Because $N = 1$ is the lowest rotational state of a $K = 1$ parity doublet, M_N can take on the values $+1$, 0, or -1. Initially, the three levels tune approximately linearly in the electric field strength. Eventually, level repulsion with the $N = 2$ manifold causes all of the $N = 1$ sublevels to become high-field seeking. There is thus an optimal value at which to operate the high-field stages, above which the energy removal is not significantly increased. Note that the deceleration scheme depends on the presence of angular momentum about the internuclear axis, which is generically present in the polyatomic molecules we are considering.

[2]We denote by K the projection of angular momentum onto the molecule's symmetry axis. For linear molecules this is often labeled by ℓ, and for near-prolate asymmetric tops K_a. We use K to maintain consistency among linear, symmetric, and asymmetric top species.

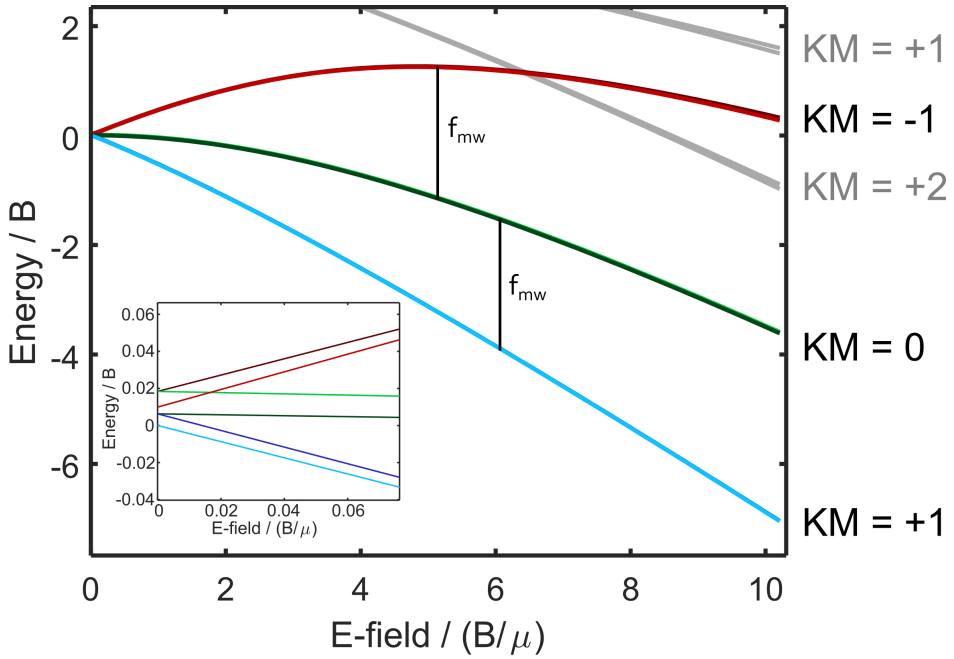

Figure 10.2: Energy levels relevant to microwave-optical Stark-Sisyphus deceleration. While the low-field details are species dependent, at fields sufficiently large to decouple the spin-rotation/hyperfine structure, this level structure is accurate for all effective $K = 1$ states. Vertical lines mark the fields at which a single-frequency microwave field can drive transitions.

Based on this energy level pattern, we can establish a simple estimate of the energy removal per deceleration stage. Figure 10.3 shows the results of this analysis for many molecules that have been proposed for direct laser cooling experiments, including linear, symmetric top, and asymmetric top species. Using previously determined rotational constants and dipole moments, we find that between 1 and 2 K of energy removal per stage is possible for over a dozen molecular species. (Note that many additional species are likely viable candidates, but either rotational constants or dipole moments were not available in the literature.) Optimized buffer-gas molecular beam sources offer forward velocities equivalent to about 8 K [99, 243], requiring between 4 and 16 deceleration stages to slow to rest any of the molecules included in Fig. 10.3.

This Stark-Sisyphus deceleration method has several technical advantages over previously proposed and demonstrated decelerators. First, the decelerator can slow either pulsed or continuous molecular beams. While some previously proposed methods work for continuous (or long-pulse)

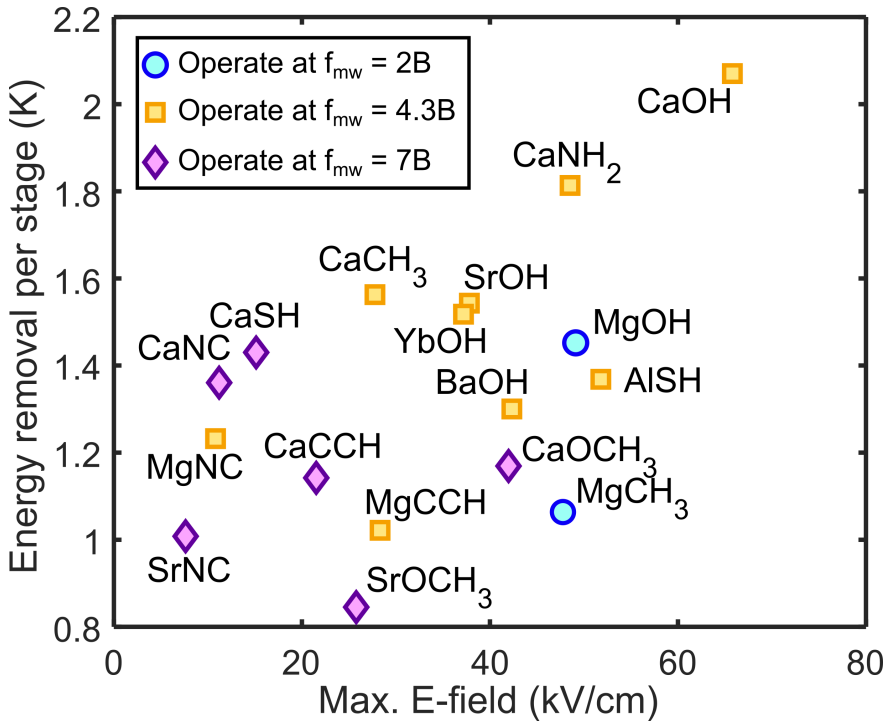

Figure 10.3: Energy removal per stage of Stark-Sisyphus deceleration for many laser-coolable molecules. Depending on the species' rotational constants, it can be convenient to operate the decelerator at different microwave frequencies, as indicated for three exemplary choices. In all cases shown, at least 0.8 K can be removed per stage.

beams [241, 313, 315], most slowing methods currently used for molecular beam deceleration are inherently pulsed [117, 232–237]. Our proposed decelerator can be switched off on timescales orders of magnitude faster than those associated with trapping or cooling, eliminating any deleterious effects of the decelerator on trapped molecules. Second, the method can be applied to any molecular species with a low-lying degenerate state. This includes some diatomic molecules (with Π, Δ, etc. electronic ground states) and essentially all polyatomic molecules (with either ℓ- or K-doublets due to vibrational and/or rotational angular momentum). It is equally applicable to molecules of any spin multiplicity. Third, it appears possible to turn *off* the deceleration force once a certain critical velocity is achieved simply by driving a velocity-dependent transition to a field-insensitive state. This will provide an effective cooling force and prevent over-slowing of certain molecules, leading to higher flux at the decelerator output. No such field-insensitive states can be found in $^2\Sigma^+$ molecules in a *magnetic* decelerator. Other technical advantages include the relatively open

geometry of the decelerator array, eliminating concerns about collisions with remnant buffer-gas atoms and allowing mode-matching to a molecular beam with large transverse extent (as is typical of CBGBs).

10.3 Large molecules

Although not discussed in this thesis, over the past few years we have also explored the possibility of optical cycling in large, complex polyatomic molecules— including molecules containing polycyclic aromatic rings. In collaboration with the groups of Wes Campbell and Eric Hudson, we have adapted the apparatus described in Ch. 4 to produce and detect these molecules, measuring their vibrational structure and the vibrational branching ratios of several electronically excited states per species. These results [316], largely supported theoretical work led by the Anastassia Alexandrova that proposed these species for optical cycling [230, 231], are very promising. Excitingly, molecules containing nearly two dozen atoms were found to have vibrational branching ratios sufficiently diagonal to permit some laser cooling and/or Zeeman-Sisyphus deceleration.

Figure 10.4 compares the DLIF spectra for three Ca-containing molecules of increasing complexity: CaOH, $CaOCH_3$, and $CaOC_{10}H_7$. Despite the fact that $CaOC_{10}H_7$ contains over an order of magnitude more vibrational modes than CaOH, the gross structure of their DLIF spectra is largely similar. In all cases, the Ca-O stretching mode is the dominant off-diagonal decay channel. $CaOC_{10}H_7$ shows some activity in a handful of additional modes at the $\sim 0.1 - 1\%$ level, indicating that achieving optical cycling will be more challenging— but not necessary prohibitive. These results are not unique to $CaOC_{10}H_7$. As proposed in Refs. [230, 231], there are dozens of species that can be formed via targeted substitution around the carbon rings. Optical cycling functionalization of aromatic compounds, including large arenes, appears to be a viable path toward useful molecules for quantum science and ultracold (organic) chemistry.

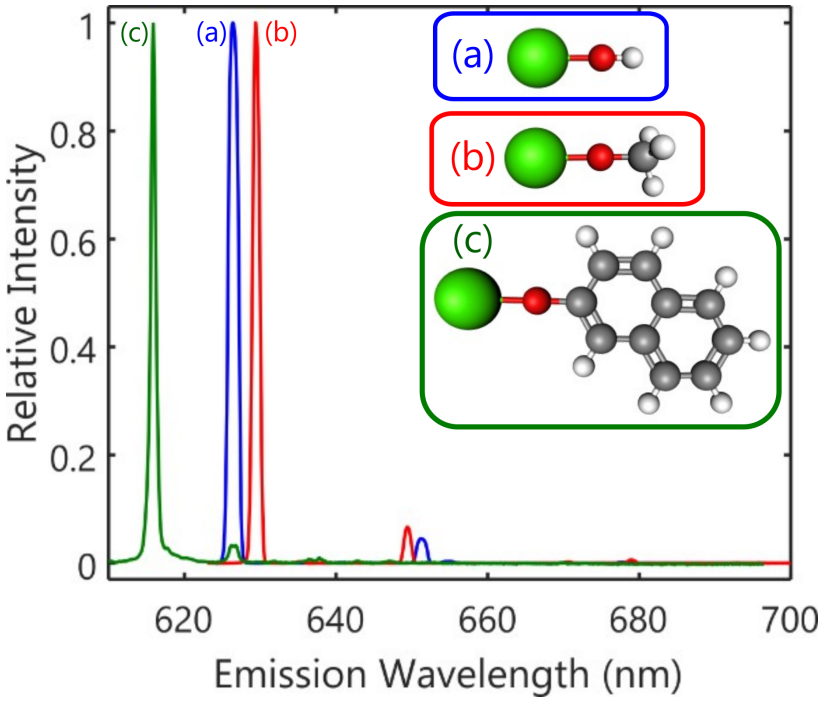

Figure 10.4: Comparison of DLIF spectra following excitation of (a) CaOH, (b) $CaOCH_3$, and (c) $CaOC_{10}H_7$ to the $\tilde{A}$ excited state. Spectra (a) and (b) were recorded using fluorescence from a molecular beam, and spectrum (c) was recorded by collecting fluorescence from inside a buffer-gas cell. The diagonal fluorescence features are normalized to unity.

As optical cycling is brought to larger species, the rotational constants of the molecules used will decrease. It is interesting to think about what problems (and opportunities) arise as the rotational constants become comparable to or smaller than the excited state linewidth.[3] Led by Wes Campbell, we have begun to explore this regime theoretically; a detailed overview can be found in Ref. [317]. In brief, we have found that in the regime of unresolved rotational structure, cooling of the rotational degrees of freedom proceeds analogously to translational Doppler cooling. These results indicate that the reach of optical cycling and laser cooling of molecules may be extremely broad. Molecules, such as those discussed in the body of this thesis, that are "complex" due to their high mass, low symmetry, or large number of atomic constituents all appear amenable to optical cycling and some degree of laser cooling.

[3] An alternative, but similar, regime is one in which the rotational constants are much smaller than the linewidth of a pulsed laser, e.g. mode-locked ps laser, used for excitation.

A

Stark Shifts, Parity Doubling, and eEDM Sensitivity

In this appendix we discuss the Stark level structure for diatomic molecules (without parity doublets) and polyatomic molecules. We will emphasize the physics underlying the Stark structure for these molecules and the similarities between Stark shifts of different polyatomic molecules. We will also discuss the origin of splittings between opposite-parity states in different types of molecules. An important consequence of these parity-doublet splittings is that molecules do not have permanent laboratory-frame dipole moments at zero field.

The interaction between an applied electric field, $\boldsymbol{\mathcal{E}}$, and an electric dipole moment, $\boldsymbol{\mu}_{\mathrm{el}}$, is given

in spherical tensor notation as [132]

$$H_S = -T^1(\boldsymbol{\mu}_{\text{el}}) \cdot T^1(\boldsymbol{\mathcal{E}}). \tag{A.1}$$

In what follows, we will assume the electric field defines the laboratory Z axis so that $\boldsymbol{\mathcal{E}} = \mathcal{E}\hat{Z}$. In spherical tensor notation [131], this defines the space-fixed $p = 0$ direction. To proceed further, we need to construct the matrix representation of this Hamiltonian and diagonalize it.

A.1 Diatomic molecules without parity doublets

For a diatomic molecule, the dipole moment points along the (molecule-fixed) $q = 0$ direction, i.e. the internuclear axis. Following the standard recipe [131], we can evaluate the Stark Hamiltonian A.1 as

$$\begin{aligned} H_S &= -T^1(\boldsymbol{\mu}_{\text{el}}) \cdot T^1(\boldsymbol{\mathcal{E}}) \\ &= -T^1_{p=0}(\boldsymbol{\mu}_{\text{el}}) T^1_{p=0}(\boldsymbol{\mathcal{E}}) \\ &= -\mathcal{E} \sum_q \mathcal{D}^{(1)}_{0q}(\omega)^* T^1_q(\boldsymbol{\mu}_{\text{el}}) \\ &= -\mu_{\text{el}} \mathcal{D}^{(1)}_{00}(\omega)^* \mathcal{E}. \end{aligned} \tag{A.2}$$

The matrix elements of H_S have thus been simplified to matrix elements of the Wigner-$\mathcal{D}$ matrices, which are well known [131].

The Stark shifts of the levels with $N = 0$ through $N = 3$ are plotted in Fig. A.1(a). Here we have chosen parameters representative of YbOH molecules in the (000) vibrational level. The level shifts can be understood quite easily from the ideas that coupled levels will repel one another and that only levels with $\Delta N = \pm 1, \Delta M = 0$ are coupled due to cylindrical symmetry about the field

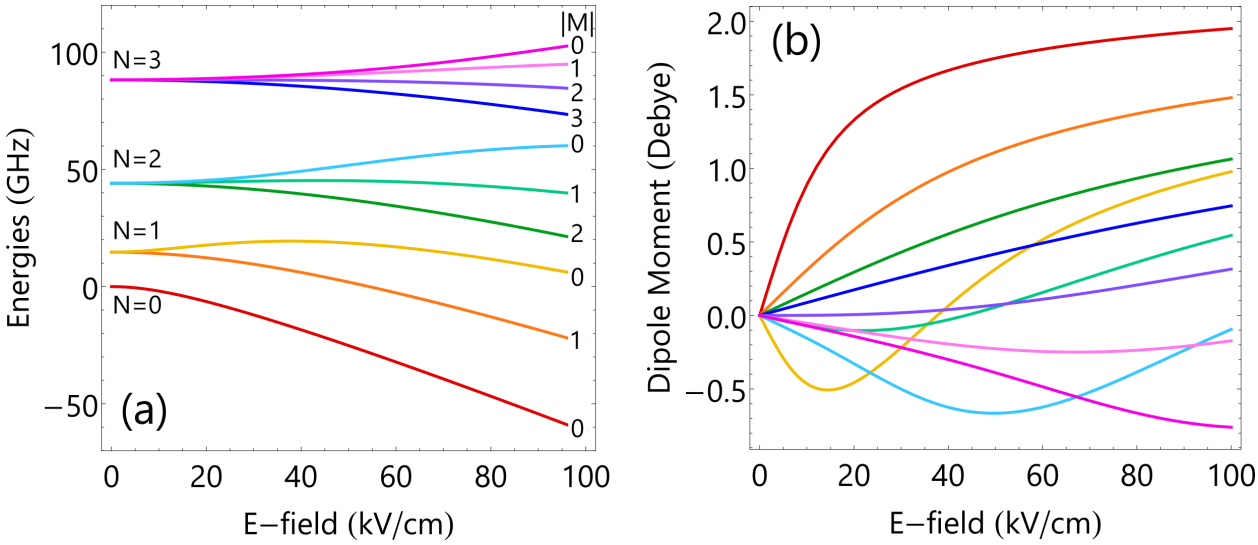

Figure A.1: (a) Stark shifts and (b) dipole moments for diatomic molecule without parity doublets. Parameters are chosen to match YbOH in the $\tilde{X}\,^2\Sigma^+(000)$ level.

axis. For example, the $N = 0, M = 0$ level is repelled from all other $M = 0$ levels and shifts strongly downward. The $N = 1, M = 0$ level is repelled from below by the $N = 0, M = 0$ level and from above by all higher-lying $M = 0$ levels; because the $N = 0$ state is the closest to $N = 1$, it first shifts upward before turning over. At sufficiently high fields, *all* levels become strong-field seeking. To shift any level by an appreciable amount requires fields on the order of 10 kV/cm or larger.

Figure A.1(b) shows the lab-frame dipole moment for each rotational state as a function of applied electric field. The dipole moments are calculated as $\mu_{\rm el}(\mathcal{E}) = -dE/d\mathcal{E}_Z$. No state shows significant polarization until fields larger than about 5-10 kV/cm are applied. While some states anti-align with the applied field at intermediate electric field values, eventually all states tend to align with the field.

A.2 Molecules with parity doublets

While in the diatomic molecules discussed above the parity alternated with rotational quanta as $(-1)^N$, there are other molecules for which each rotational level consists of a closely-spaced pair of

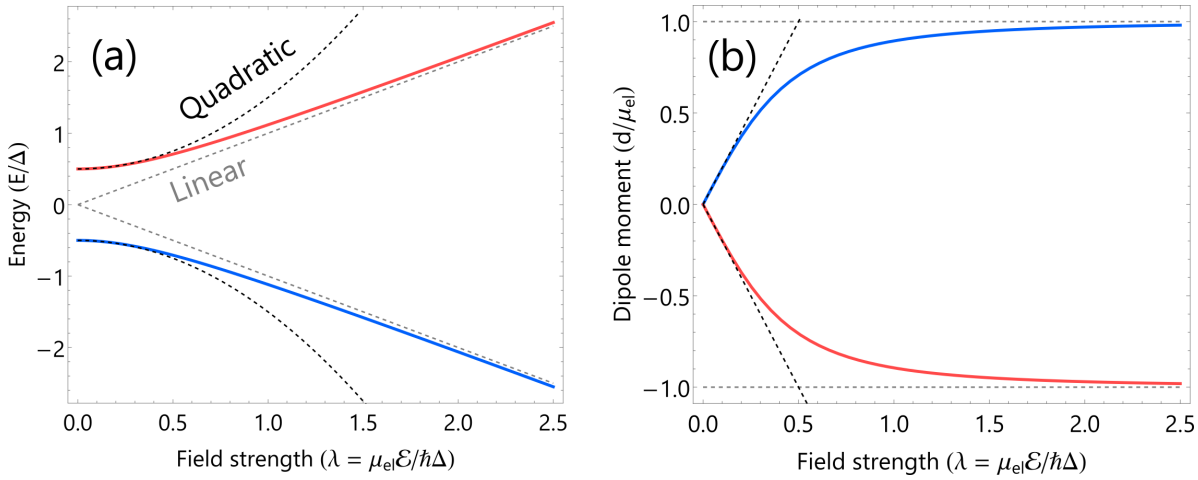

Figure A.2: (a) Stark shifts and (b) lab-frame dipole moments in a two-level model. Also indicated are the quadratic (black dashed lines) and linear (gray dashed lines) Stark shifts appropriate at low and high fields, respectively. Figure modeled after Ref. [21].

levels with opposite parity. An electric field can directly mix these states and polarize the molecules at fields much smaller than those required to mix states that differ in N. We will describe the *sources* of these "parity doublets" in Sec. A.2.1, but first discuss the *behavior* of parity-doubled levels in applied electric fields.

The essential physics is demonstrated by a simple two-level model [21]. Consider two states of opposite parity that are split by an energy Δ and coupled by an electric field $\mathcal{E}$. The system is described by a Hamiltonian

$$H = \begin{pmatrix} \hbar\Delta/2 & -\mu_{\rm el}\mathcal{E} \\ -\mu_{\rm el}\mathcal{E} & -\hbar\Delta/2 \end{pmatrix}. \tag{A.3}$$

This has energies $E_\pm = \pm\frac{\hbar\Delta}{2}\sqrt{1+4\lambda^2}$, where $\lambda \equiv |\mu_{\rm el}\mathcal{E}|/\hbar\Delta$ [21]. These energies are plotted in Fig. A.2(a). At low fields ($\mu_{\rm el}\mathcal{E} \ll \hbar\Delta$) the Stark shifts are quadratic, and at high fields ($\mu_{\rm el}\mathcal{E} \gg \hbar\Delta$) the Stark shifts are linear. The crossover from low to high fields is set by the field at which the electric dipole interaction energy roughly matches the zero-field energy splitting.

This behavior can be thought of in terms of an induced dipole with dipole moment

$$d = \left| \frac{\partial E_{\pm}}{\partial \mathcal{E}} \right| = \frac{2\mu_{\mathrm{el}}\lambda}{\sqrt{1+4\lambda^2}}, \tag{A.4}$$

see Fig. A.2(b). At low fields, the electric field must mix the opposite-parity states in order to start to align the molecule in the laboratory frame. While this mixing is incomplete, the Stark shifts are quadratic because the molecular dipole moment is growing with field and being aligned at the same time. Once the opposite-parity states are fully mixed, the laboratory-frame dipole moment is approximately saturated and the Stark shifts become linear as the electric field interacts with the fully available molecular dipole moment.

A.2.1 Sources of parity doubling

In any molecular structure that has angular momentum about the internuclear axis, states with equal but opposite projection of this angular momentum may be naively expected to be degenerate. In reality, exact degeneracy of such states is not permitted and there will always be some interaction which lifts the degeneracy and splits the states into separated levels of opposite parity [318]. Examples include Λ-doubling (due to electron orbital angular momentum), ℓ-doubling (due to nuclear orbital angular momentum in vibrational bending modes), and K-doubling (due to rigid body rotation of a symmetric top about the symmetry axis). Depending on the physical cause, the parity splitting in molecules discussed in this thesis can range from $\sim$GHz (e.g., Λ-doublets) to $\sim$100 kHz (e.g., K-doublets in symmetric top molecules).

For an example of the way that parity doubling arises, consider a linear triatomic molecule in a vibrational bending mode with one unit of angular momentum about the internuclear axis (an

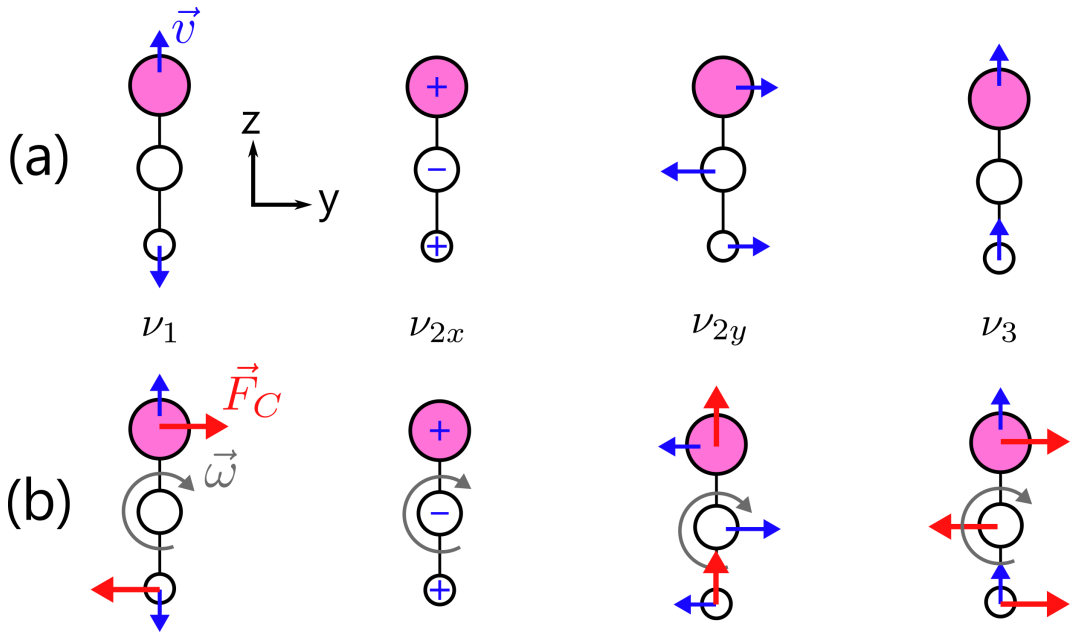

Figure A.3: Origin of ℓ-doubling due to Coriolis coupling between bending and stretching vibrations. (a) Vibrational modes in the non-rotating molecule with nuclear velocities indicated in blue. (b) Vibrational modes in the rotating molecule, including Coriolis forces indicated in red. Note that mode ν_{2y} and the stretching modes can be coupled due to the Coriolis interaction, but ν_{2x} experiences no such interaction.

$\ell = 1$ state).[1] There are three normal vibrations: the symmetric stretch (ν_1), the doubly degenerate bend (ν_2), and the antisymmetric stretch (ν_3). These are illustrated in Fig. A.3(a) as would occur for a rotationless molecule. Bending vibrations in-plane (ν_{2y}) and out-of-plane (ν_{2x}) relative to the plane of rotation are equivalent and degenerate in the non-rotating case. If the molecule is rotating with angular velocity $\boldsymbol{\omega}$, the vibrating atoms experience a Coriolis force, $\boldsymbol{F}_C = 2m\,\boldsymbol{\omega} \times \boldsymbol{v}$, due to their motion in a rotating frame. The magnitude of the force depends on the vibrational mode. $\boldsymbol{F}_C$ for the out-of-plane bending vibrations vanishes, whereas $\boldsymbol{F}_C$ for the in-plane bending vibrations excites motion along the stretching vibrations [see Fig. A.3(b)]. Similarly, the motions of nuclei executing stretching vibrations acquire some off-axis components along the bending mode. Thus, there can be coupling between ν_{2y} and ν_1/ν_3, but ν_{2x} does not couple with either of these. The nominally degenerate ν_2 components can be split because they experience different perturbations.

[1]The reasoning outlined here draws heavily from Refs. [136, 319].

The parameter that characterizes the magnitude of this ℓ-doublet splitting is [320]

$$|q_v| = \frac{2B^2}{\omega_2}\left(1 + 4\sum_{k=1,3}\frac{\zeta_{2k}^2\omega_2^2}{\omega_k^2 - \omega_2^2}\right), \tag{A.5}$$

where ω_k the vibrational frequency of mode ν_k, and ζ_{2k} the Coriolis coupling constant between modes ν_2 and ν_k. This formula expresses that the ℓ-doubling is related to Coriolis interactions with distant states and that the strength of that interaction is set by the ease with which rotation couples the modes (ζ_{2k}). Typical values for molecules like CaOH are $q_v \approx -20$ MHz [212].

In other molecules, the parity doubling arises from different effects. For example, in the ground vibrational state of C_{3v} symmetric top molecules like YbOCH$_3$, the $K = \pm 1$ levels are nominally degenerate with equal but opposite rotation of the CH$_3$ group about the symmetry axis. These levels are actually split by hyperfine terms that directly couple states with $|\Delta K| = 2$. This arises from the anisotropic dipolar interaction between the three H nuclear spins and the unpaired valence electron [132, 321]. More generally, terms can be found in the Hamiltonian of any species that split nominally degenerate states of opposite parity, as is necessary to ensure that no molecule has a permanent laboratory-frame dipole moment in the limit $\mathcal{E} \to 0$ (which would break parity and time-reversal symmetries) [318].

In *diatomic* molecules, nominally degenerate states can only come from electron orbital angular momentum, since no other motion can produce angular momentum about the internuclear axis. Parity doubling known as either Λ-doubling or Ω-doubling does occur in diatomic molecules, including in electron-EDM-sensitive molecules such as ThO [23, 24] and HfF$^+$ [2, 25]. Because the parity doubling derives from electronic structure, there is no guarantee that these molecules will *also* have an electronic structure that allows for optical cycling and laser cooling. This is the *key point* about working with polyatomic molecules: in polyatomic molecules, the source of laser coolability

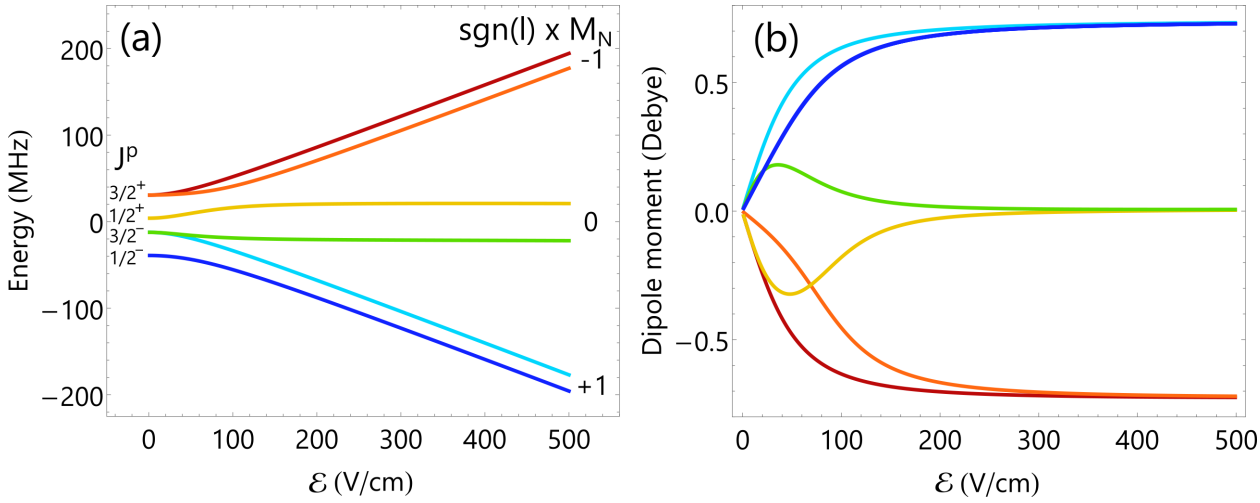

Figure A.4: (a) Stark shifts and (b) dipole moments for a linear molecule $\ell = 1$ bending mode. The parameters used for this calculation come from CaOH: $B \approx 9997$ MHz, $\gamma \approx 35$ MHz, $q_v \approx 21$ MHz, and $\mu_{\rm el} \approx 1.5$ Debye. Hyperfine interactions are included in the computation but not resolved at this scale.

(electronic structure) and the source of parity doubling (nuclear motion) are decoupled [26]. The same is not true for diatomic molecules.

A.3 Stark shifts in a linear molecule $\ell = 1$ state

The Stark shifts and lab-frame dipole moments for a linear triatomic molecule in a ${}^2\Sigma(01^10, N = 1)$ bending mode are plotted in Fig. A.4. We have used molecular parameters for CaOH in constructing this example. The energies are computed by diagonalizing a Hamiltonian

$$H = H_{\rm rot} + H_{\rm SR} + H_{\ell d} + H_{\rm HF} + H_S, \tag{A.6}$$

where the terms are (in order) the rigid-body rotation, the spin-rotation interaction, the ℓ-doubling, hyperfine terms, and the electric field interaction. Matrix elements for $H_{\rm rot}$, $H_{\rm HF}$, and H_S are taken from Ref. [132]. The ℓ-doubling and spin-rotation terms are described in Sec. A.5 and A.6 to provide useful spherical tensor formulas and to clarify some subtleties.

The structure seen in Fig. A.4 is qualitatively different from the diatomic molecule case de-

scribed above. In the bending mode case, there are Stark shifts due to mixing of opposite parity states *within* the $N = 1$ state, whereas for diatomic molecules we required mixing of different N states to achieve any Stark tuning (since parity alternates as $(-1)^N$ in that case). In addition, these shifts become linear at fields as small as a few 100s of V/cm, at which point the lab-frame dipole moment value of $\mu_{\text{el}}/2$ is essentially saturated.[2] Another qualitative difference is the fact that once full polarization is achieved, there are three distinct dipole-moment orientations that can be realized: the molecule can point along, against, or "neutral" relative to the applied electric field.[3] In the laboratory, the molecular orientation can thus be chosen spectroscopically, e.g. via optical pumping or coherent state preparation. These qualitative features are the core reasons polyatomic molecules are useful for a number of experiments.

The structure shown in Fig. A.4 is displayed over a range sufficiently large to mix the ℓ-doublet components of $N = 1$, but sufficiently small to *not* cause mixing between the $N = 1$ and $N = 2$ rotational levels. As the Stark shifts grow and become similar to (or larger than) intervals between rotational energy levels, interactions between states with different N will cause the Stark shifts to deviate from (quasi-)linear. A level structure shown in Fig. 10.2 arises and the dipole moments behave as shown in Fig. 1.2. Thus, in the limit of large $\mathcal{E}$, the Stark shifts and dipole moments begin to resemble those of diatomic molecules without parity doubling.

A.4 Electron spin projection

For electron EDM measurements, the EDM energy shift is determined by the degree of electron-spin alignment along $\vec{\mathcal{E}}_{\text{eff}}$, i.e. $\langle\Sigma\rangle$ in the molecule frame. This is quite different from the degree of molecular alignment in the laboratory frame, which is given by $\langle\hat{n}\rangle$ (proportional to the lab-frame

[2]The asymptotic value is less than μ_{el} because we computed for an $\ell = 1$ state. Higher ℓ states allow access to a larger fraction of μ_{el}.

[3]There are *three* saturated values because we computed for an $N = 1$ state. In general, there will be $2N+1$ asymptotic dipole moment projections, one for each value of $\text{sgn}(\ell) \times M_N$.

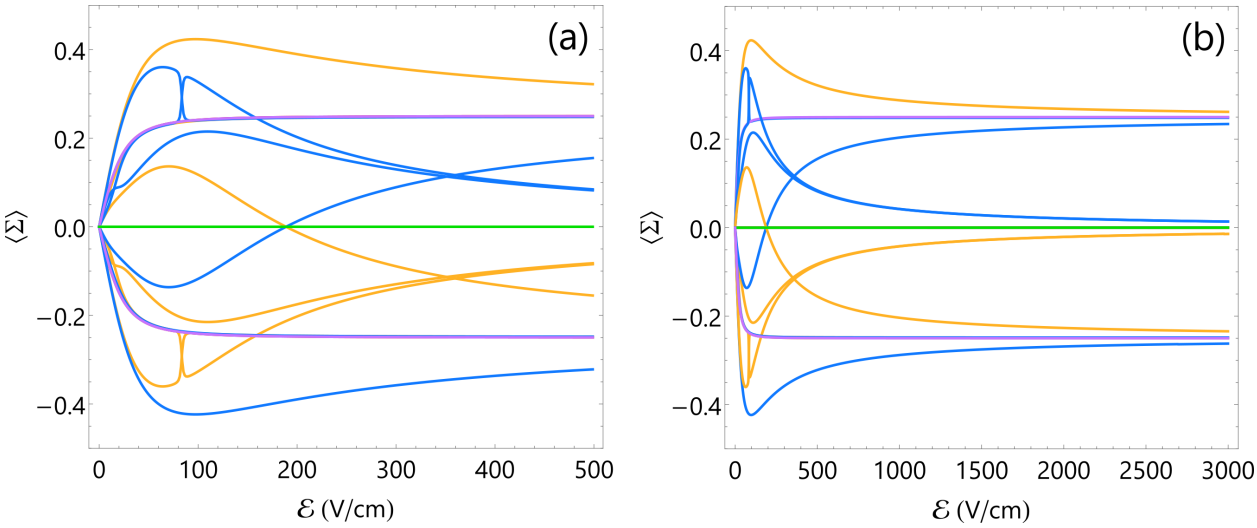

Figure A.5: $\langle\Sigma\rangle$ as a function of electric field for the YbOH (01^10), $N = 1$ state. Lines are color coded according to the value of M_F. (a) At low to intermediate fields, certain sublevels approach the maximum possible value $\langle\Sigma\rangle = \pm 0.5$. (b) At large fields, the projection in YbOH approaches $\langle\Sigma\rangle = 0, \pm 0.25$ indicating that the electron spin is not fully aligned to the molecule axis.

dipole moments computed for Fig. A.4). To compute $\langle\Sigma\rangle$ as a function of applied electric field, we construct an operator representing the molecule-frame value of Σ (conveniently done in a Hund's case (a) basis set) and then compute the expectation value of this operator using the eigenstates of Hamiltonian A.6 at each field value. The results are plotted in Fig. A.5, where we have used the parameters for YbOH $\tilde{X}\,^2\Sigma^+(000)$ [19, 173] and assumed $q_v \approx -13$ MHz [322].

A fully aligned electron spin would have $\langle\Sigma\rangle = \pm 1/2$, but we see that in the limit of large $\mathcal{E}$ the $\ell = 1$ bending modes of YbOH saturated to $\langle\Sigma\rangle = \pm 1/4$, half the maximum value. This differs markedly from the case of, e.g., ThO in the $^3\Delta_1$ state, for which the limit value does approach $\langle\Sigma\rangle = \pm 1/2$. The differences arises from the fact that in ThO a strong spin-orbit coupling effect "locks" the electron spin relative to the internuclear axis, essentially correlating Σ and Λ. This spin-orbit coupling is absent in YbOH $\tilde{X}\,^2\Sigma^+(01^10)$. Nonetheless, at intermediate field values (around 100 V/cm in Fig. A.5), there are states that attain about 85% of the maximum possible spin alignment. It is important to take this into account when estimating the electron EDM sensitivity achievable in YbOH (and related species, such as $YbOCH_3$). Note that the calculation shown in Fig. A.5

should be considered approximate because the molecular constants for the YbOH $\tilde{X}\,^2\Sigma^+(01^10)$ state have yet to be measured.

A.5 The ℓ-doubling matrix elements

The rotational structure of linear molecules in bending modes is discussed in Ref. [320], although these authors unfortunately do not use a spherical tensor formalism. Here, we recast the ℓ-doubling Hamiltonian into a spherical tensor form that is convenient for numerical computations. The relevant Hamiltonian terms are [320]

$$H_{\ell d} = q_{v1}\left(J_+ S_+ G_-^2 + J_- S_- G_+^2\right) + q_{v2}\left(J_+^2 G_-^2 + J_-^2 G_+^2\right), \tag{A.7}$$

where $G_\pm$ are the ladder operators for vibrational angular momentum, and q_{v1} and q_{v2} are ℓ-doubling parameters whose identities will be developed more below. In spherical tensor notation, this Hamiltonian can be written [131]

$$H_{\ell d} = \sum_{q=\pm1} T^2_{-2q}(\boldsymbol{G},\boldsymbol{G})\left[2q_{v1}\,T^2_{2q}(\boldsymbol{J},\boldsymbol{S}) + 2q_{v2}\,T^2_{2q}(\boldsymbol{J},\boldsymbol{J})\right]. \tag{A.8}$$

This can be compared to the Λ-doubling Hamiltonian that is familiar from the theory of diatomic molecules in $^2\Pi$ states, e.g. Eq. (9.65) in Ref. [131]:

$$H_{\Lambda d} = \sum_{q=\pm1} e^{-2iq\phi}\left[(p_v + 2q_v)\,T^2_{2q}(\boldsymbol{J},\boldsymbol{S}) - q_v\,T^2_{2q}(\boldsymbol{J},\boldsymbol{J})\right], \tag{A.9}$$

where the $e^{-2iq\phi}$ factor acts as a ladder operator on the electronic orbital angular momentum. Hamiltonian A.9 has well-known matrix elements [131] that can be mapped onto the ℓ-doubling case. We identify terms in Hamiltonians A.8 and A.9 as $2q_{v1} \leftrightarrow p_v + 2q_v$ and $2q_{v2} \leftrightarrow -q_v$. For

an ℓ-doublet in a $^2\Sigma^+$ electronic state, we would expect $p_v \to 0$. With these substitutions, the ℓ-doubling Hamiltonian matrix elements can be evaluated using standard spherical tensor methods and a Hund's case (a) basis set, $|N, J, F, M_F; v_2, \ell; S, \Sigma\rangle$:

$$\begin{aligned}\langle N, J, F, M_F; v_2, \ell; S, \Sigma | H_{\ell d} | N, J, F, M_F; v_2, \ell'; S, \Sigma' \rangle = \\ \sum_{q=\pm 1} \delta_{\ell', \ell \mp 2} \Bigg\{ \delta_{\Sigma,\Sigma'} \left(\frac{1}{2\sqrt{6}}\right) q_v (-1)^{J-\ell-\Sigma} \begin{pmatrix} J & 2 & J \\ -\ell-\Sigma & -2q & \ell'+\Sigma' \end{pmatrix} \\ \times \sqrt{(2J-1)(2J)(2J+1)(2J+2)(2J+3)} \\ + 2 q_v (-1)^{J-\ell-2\Sigma+S} \begin{pmatrix} J & 1 & J \\ -\ell-\Sigma & -q & \ell'+\Sigma' \end{pmatrix} \\ \times \begin{pmatrix} S & 1 & S \\ -\Sigma & q & \Sigma' \end{pmatrix} \sqrt{J(J+1)(2J+1)S(S+1)(2S+1)} \Bigg\}. \quad \text{(A.10)}\end{aligned}$$

Note that there is a phase factor that differs in this equation as compared to the Λ-doubling case. This can apparently be traced back to the phase conventions for $|\Lambda\rangle$ and $|\ell\rangle$ eigenkets (see Eqs.(2.4.19)-(2.4.22) in Ref. [132]).

A.6 Spin-rotation matrix elements

For the calculations displayed in Fig. A.4, the dominant sources of zero-field structure within a rotational state are the parity doubling and the spin-rotation interaction. It is worth pointing out a subtlety of the spin-rotation Hamiltonian, namely the reduction in spin-rotation splitting that occurs in bending modes.[4] The relevant Hamiltonian and ma-

[4]Thanks to Zack Lasner for pointing out that Eq. 18 of Ref. [320] does not seem to handle this correctly. The spherical tensor formulas in Ref. [132] do take it into account by default.

trix elements of $H_{\rm SR}$ are given in Eq. (2.3.35) of Ref. [132]. When adapted to the case of a linear molecule the Hamiltonian becomes $H_{\rm SR} = \gamma(\boldsymbol{N}\cdot\boldsymbol{S} - N_z S_z)$. We can evaluate the matrix elements to be

$$\begin{aligned}\langle N',\ell', S, J', M_J'|H_{\rm SR}|N,\ell,S,J,M_J\rangle = \\ \delta_{N',N}\,\delta_{\ell',\ell}\,\delta_{J',J}\,\delta_{F',F}\,\delta_{M_F',M_F}\,\left[\frac{J(J+1)-N(N+1)-S(S+1)}{2}\right. \\ \left.-\ell(2N+1)\sqrt{S(S+1)(2S+1)}(-1)^{N+J+S}(-1)^{N-\ell}\begin{Bmatrix} S & N & J \\ N & S & 1\end{Bmatrix}\begin{pmatrix} N & 1 & N \\ -\ell & 0 & \ell\end{pmatrix}\right].\end{aligned} \tag{A.11}$$

For $S = 1/2$, these diagonal matrix elements can be evaluated analytically and yield two spin-rotation states (neglecting the overall rotational and ℓ-doubling terms):

$$F_2(J = N+S) = \frac{\gamma}{2}\left(1 - \frac{\ell^2}{N(N+1)}\right)N, \tag{A.12}$$

$$F_1(J = N-S) = -\frac{\gamma}{2}\left(1 - \frac{\ell^2}{N(N+1)}\right)(N+1). \tag{A.13}$$

Note that these terms show that the spin-rotation splitting is reduced when $\ell \neq 0$, indicating the quenching of spin-rotation interaction due to vibrational angular momentum. In particular, the spin-rotation splitting for $N = 1, \ell = 1$ is only $3\gamma/4$, half the magnitude of that in an $N = 1, \ell = 0$ state. This is analogous to the reduced spin-rotation splitting in $K = 1$ states of symmetric top molecules like $CaOCH_3$.

B

Labeling Vibrational States and Transitions

In this appendix we describe a vibrational labeling scheme useful to describe branch features in complex polyatomic molecules. For linear triatomic molecules, it is common to label the vibrational levels by a scheme such as $(v_1 v_2^{\ell} v_3)$, where v_1 denotes the quanta of excitation in the symmetric stretching mode (mode ν_1), v_2 denotes the number of quanta in the bending mode (mode ν_2), and v_3 denotes the number of quanta in the antisymmetric stretching mode (mode ν_3). Finally, the superscript ℓ labels the amount of vibrational angular momentum present. Transitions are labeled by specifying the vibrational state of both the ground and excited state, e.g. $(v_1' v_2'^{\ell'} v_3') \leftarrow (v_1'' v_2''^{\ell''} v_3'')$. Clearly this scheme will be-

come very tedious to use for larger polyatomic molecules that have correspondingly more vibrational modes.

An alternative labeling scheme is as follows. If a molecule makes a transitions from a (ground) state with v'' vibrational quanta in the n^{th} normal mode to a (excited) state with v' vibrational quanta in the n^{th} normal mode, we write:

$$n_{v''}^{v'} \equiv (0, 0, \ldots, v', \ldots, 0) \leftarrow (0, 0, \ldots, v'', \ldots, 0). \tag{B.1}$$

For example, the transition $\tilde{A}(001) \rightarrow \tilde{X}(002)$ in a linear triatomic molecule is written as $3_2^1\tilde{A} \rightarrow \tilde{X}$. As a special case, the origin band transition, $\tilde{A}(000) \rightarrow \tilde{X}(000)$, is written $0_0^0\tilde{A} \rightarrow \tilde{X}$.

This notation is extended to combination bands in a reasonably obvious way. That is, a transition from a (ground) state with v_n'' vibrational quanta in the n^{th} normal mode *and* v_m'' vibrational quanta in the m^{th} normal mode to a (excited) state with v_n' vibrational quanta in the n^{th} normal mode *and* v_m' vibrational quanta in the m^{th} normal mode is denoted by:

$$n_{v_n''}^{v_n'}\, m_{v_m''}^{v_m'} \equiv (0, 0, \ldots, v_n', \ldots, v_m', \ldots, 0) \leftarrow (0, 0, \ldots, v_n'', \ldots, v_m'', \ldots, 0). \tag{B.2}$$

As an example, the transition $\tilde{A}(102) \leftarrow \tilde{X}(001)$ is written as $1_0^1 3_1^2\tilde{A} \leftarrow \tilde{X}$.

Clearly this notation requires some rule for enumerating the vibrational modes. Unfortunately, there is not a strictly followed convention, but a very common one is the following. First, group the vibrational modes by their point group symmetry labels. (The totally symmetric modes are listed first, then the other singly degenerate modes, followed by degenerate modes.) Next, for each irreducible representation, order the modes from highest

Table B.1: Vibrational normal mode numbering and symmetry labels for $MOCH_3$ molecules under transformations of the C_{3v} point group.

Mode	Symmetry	Description
ν_1	a_1	CH_3 symmetric stretch
ν_2	a_1	CH_3 symmetric bend
ν_3	a_1	O-C stretch
ν_4	a_1	M-O stretch
ν_5	e	CH_3 asymmetric stretch
ν_6	e	CH_3 asymmetric bend
ν_7	e	O-CH_3 wag
ν_8	e	M-O-C bend

to lowest frequency. Finally, number the modes accordingly. Applying this scheme to the $MOCH_3$ molecules with C_{3v} symmetry yields the ordering listed in Tab. B.1. Note that for linear triatomics (discussed at the beginning of this appendix) we do not follow this convention.

C

^{3}He Gas Handling System

Figure C.1 shows a schematic of the gas handling system constructed to control the ^{3}He pot loading and pumping cycle. The pump used is a multistage Roots pump (Adixen ACP40).

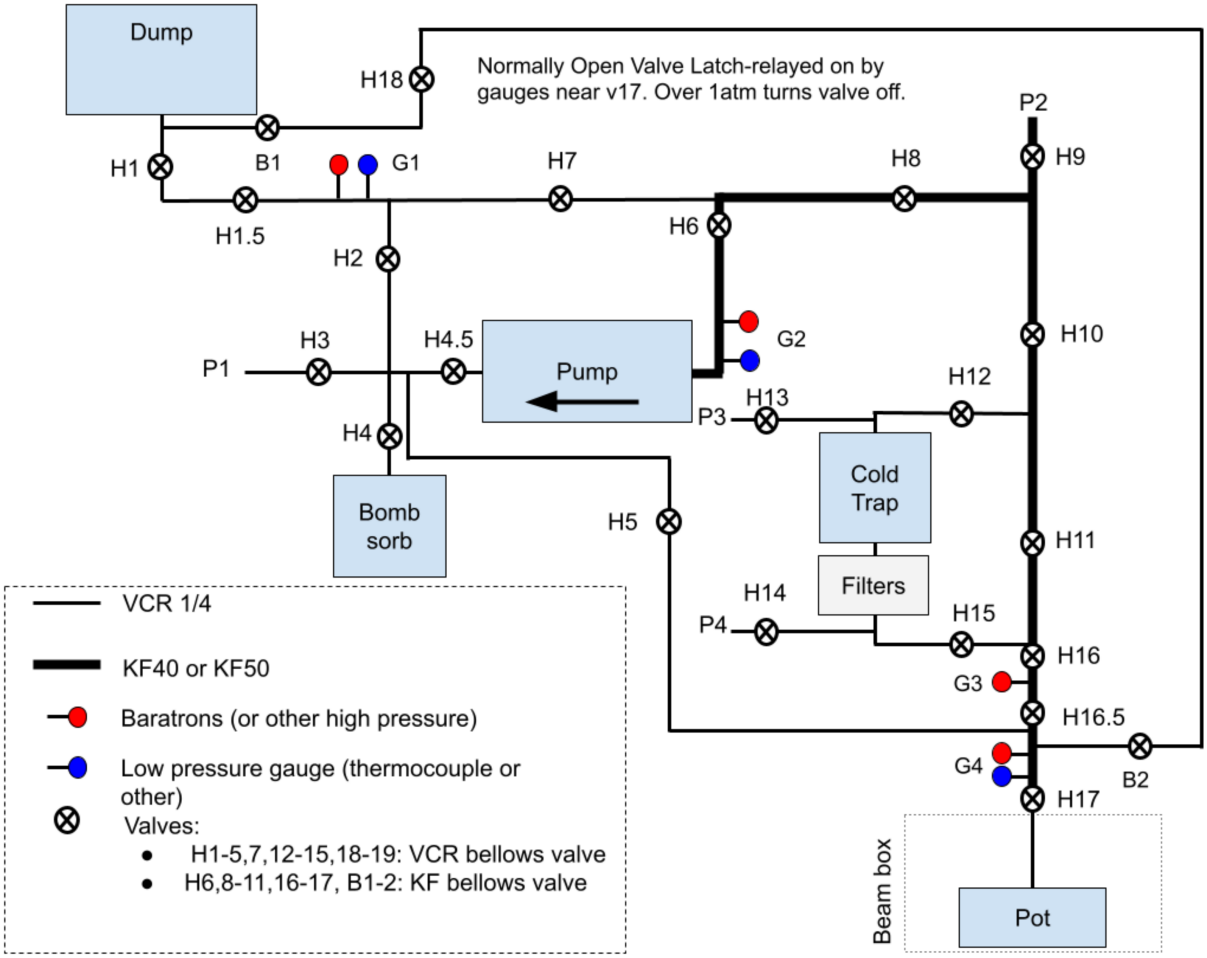

Figure C.1: Block diagram of the ^{3}He fridge gas-handling system.

D

Franck-Condon Factor Calculations

Here we derive an analytical formula for the calculation of FCFs of the form $\langle v_1 v_2 | v_1' v_2' \rangle$. Such an intensity formula is particularly applicable to linear triatomic molecules, where v_1 and v_2 represent the two σ-symmetry stretching modes.[1] Previous predictions of multidimensional FCFs for laser-coolable molecules [125, 193] have used the procedure of Sharp and Rosenstock [154]. Here, alternative closed-form formulas for two-dimensional FCFs are provided. The analytical formulas have some advantages because they are relatively

[1] This derivation appears in Ref. [153], where it was used to predict the branching ratios measured for YbOH molecules.

easy to code, and are exact and free from convergence problems.

Below, we derive a generalized version of the calculation by Chang [156], who considered the special case of FCFs of the form $\langle v_1 v_2 | 00 \rangle$. The method is easily extended to calculations with more than two vibrational modes; general formulas may be found in Ref. [155].

D.1 Analytical formula for two modes

The wavefunction of an n-dimensional harmonic oscillator can be expressed as

$$|v_1 v_2 \cdots v_n\rangle = \prod_{i=1}^{n} N_{v_i} H_{v_i} \left(\sqrt{\alpha_i} Q_i\right) \exp\left(-\frac{1}{2}\alpha_i Q_i^2\right), \tag{D.1}$$

where the normalization constant is given by

$$N_{v_i} = \left(\frac{\sqrt{\alpha_i}}{2^{v_i} v_i! \sqrt{\pi}}\right)^{1/2}, \tag{D.2}$$

$H_{v_i}(x)$ is the Hermite polynomial of order v_i, and $\alpha_i = \omega_i/\hbar$ with ω_i the angular frequency of the ith normal mode.

The vibrational overlap integral is, in general, $\langle v_1' v_2' \cdots v_n' | v_1 v_2 \cdots v_n \rangle$. For a linear, triatomic molecule we know that there will be two vibrational modes with σ symmetry and one (degenerate) mode with π symmetry. For simplicity, we neglect mixing between these modes, which should be weak. The vibrational overlap integral therefore factors into the product of a two-dimensional overlap integral due to the stretching modes and a one-dimensional overlap integral due to the bending mode. Our problem has simplified to

the evaluation of $\langle v_1' v_3' | v_1 v_3 \rangle \langle v_2' | v_2 \rangle$.

Chang [156] has given analytical formulas for the special case of the form $\langle 00 | v_1 v_2 \rangle$. Here we derive a generalization of the formula that applies to the case $\langle v_1' v_2' | v_1 v_2 \rangle$. This requires evaluation of the integral given by

$$\langle v_1' v_2' | v_1 v_2 \rangle = N' \iiiint H_{v_1}\left(\sqrt{\alpha_1} Q_1\right) H_{v_2}\left(\sqrt{\alpha_2} Q_2\right) H_{v_1'}\left(\sqrt{\alpha_1'} Q_1'\right) H_{v_2'}\left(\sqrt{\alpha_2'} Q_2'\right) \times \exp\left(-\frac{1}{2}\alpha_1 Q_1^2 - \frac{1}{2}\alpha_2 Q_2^2 - \frac{1}{2}\alpha_1' Q_1'^2 - \frac{1}{2}\alpha_2' Q_2'^2\right) dQ_1 dQ_2 dQ_1' dQ_2', \quad \text{(D.3)}$$

where

$$N' = \frac{1}{\pi}\left(\frac{\sqrt{\alpha_1 \alpha_3 \alpha_1' \alpha_3'}}{2^{v_1+v_3+v_1'+v_3'} v_1! v_3! v_1'! v_3'!}\right)^{1/2}. \quad \text{(D.4)}$$

We begin by simplifying the integrand. From the Duschinsky transformation, we can relate the normal coordinates of the ground and excited states,

$$Q_1' = J_{11} Q_1 + J_{12} Q_2 + D_1 \quad \text{(D.5)}$$

$$Q_2' = J_{21} Q_1 + J_{22} Q_2 + D_2. \quad \text{(D.6)}$$

Following Chang, we also define the useful auxiliary variables

$$x = Q_1 + B_1 Q_2 + C_1 \tag{D.7}$$

$$y = Q_2 + C_2. \tag{D.8}$$

These definitions allow us to express the normal coordinates in terms of the auxiliary variables x and y:

$$\sqrt{\alpha_1} Q_1 = a_1 x + a_2 y + b_1 \tag{D.9}$$

$$\sqrt{\alpha_2} Q_2 = a_3 y + b_2 \tag{D.10}$$

$$\sqrt{\alpha'_1} Q'_1 = a_4 x + a_5 y + b_3 \tag{D.11}$$

$$\sqrt{\alpha'_2} Q'_2 = a_6 y + b_4, \tag{D.12}$$

where

$$a_1 = \sqrt{\alpha_1} \tag{D.13}$$

$$a_2 = -\sqrt{\alpha_1} B_1 \tag{D.14}$$

$$b_1 = \sqrt{\alpha_1} \left(B_1 C_2 - C_1 \right) \tag{D.15}$$

$$a_3 = \sqrt{\alpha_2} \tag{D.16}$$

$$b_2 = -\sqrt{\alpha_2} C_2 \tag{D.17}$$

$$a_4 = \sqrt{\alpha'_1} J_{11} \tag{D.18}$$

$$a_5 = \sqrt{\alpha'_1} \left(-B_1 J_{11} + J_{12} \right) \tag{D.19}$$

$$b_3 = \sqrt{\alpha'_1} \left(B_1 C_2 J_{11} - C_1 J_{11} - C_2 J_{12} + D_1 \right) \tag{D.20}$$

$$a_6 = \sqrt{\alpha'_2} J_{21} \tag{D.21}$$

$$a_7 = \sqrt{\alpha'_2} \left(-B_1 J_{21} + J_{22} \right) \tag{D.22}$$

$$b_4 = \sqrt{\alpha'_2} \left(B_1 C_2 J_{21} - C_1 J_{21} - C_2 J_{22} + D_2 \right). \tag{D.23}$$

The B_i, C_i, and D_i values will be defined below. First, we also simplify the argument of the exponential to take the form

$$\exp\left(-\frac{1}{2}\alpha_1 Q_1^2 - \frac{1}{2}\alpha_2 Q_2^2 - \frac{1}{2}\alpha'_1 Q_1'^2 - \frac{1}{2}\alpha'_2 Q_2'^2 \right) = E \exp\left(-A_1 x^2 - A_2 y^2 \right). \tag{D.24}$$

The constants A_i, B_i, C_i, and D_i are defined as:

$$A_1 = \frac{1}{2}\left(\alpha_1 + \alpha_1' J_{11}^2 + \alpha_2' J_{21}^2\right) \tag{D.25}$$

$$B_1 = \frac{1}{2A_1}\left(\alpha_1' J_{11} J_{12} + \alpha_2' J_{21} J_{22}\right) \tag{D.26}$$

$$C_1 = \frac{1}{2A_1}\left(\alpha_1' J_{11} D_1 + \alpha_2' J_{21} D_2\right) \tag{D.27}$$

$$A_2 = \frac{1}{2}\left(\alpha_2 + \alpha_1' J_{12}^2 + \alpha_2' J_{22}^2\right) - A_1 B_1^2 \tag{D.28}$$

$$C_2 = \frac{1}{2A_2}\left(\alpha_1' J_{12} D_1 + \alpha_2' J_{22} D_2 - 2A_1 B_1 C_1\right) \tag{D.29}$$

$$E = \exp\left(-\frac{1}{2}\alpha_1' D_1^2 - \frac{1}{2}\alpha_2' D_2^2 + A_1 C_1^2 + A_2 C_2^2\right). \tag{D.30}$$

We have now transformed Eq. D.3 to the form

$$\begin{aligned}\langle v_1' v_2' | v_1 v_2 \rangle = N' E \iint & H_{v_1}\left(a_1 x + a_2 y + b_1\right) H_{v_2}\left(a_3 y + b_2\right) \\ & \times H_{v_1'}\left(a_4 x + a_5 y + b_3\right) H_{v_2'}\left(a_6 x + a_7 y + b_4\right) \\ & \times \exp\left(-A_1 x^2 - A_2 y^2\right) dx\, dy,\end{aligned} \tag{D.31}$$

which can be further simplified using the properties of Hermite polynomials. In particular, note that

$$H_n(x+y) = \sum_{k=0}^{n} \binom{n}{k} H_{n-k}(x)(2y)^k, \tag{D.32}$$

so that the product of Hermite polynomials can be given as a sum of Hermite polynomials evaluated at constant values:

$$H_{v_1}\left(a_1x+a_2y+b_1\right)H_{v_2}\left(a_3y+b_2\right)H_{v_1'}\left(a_4x+a_5y+b_3\right)H_{v_2'}\left(a_6x+a_7y+b_4\right)=$$

$$\sum_{k_1=0}^{v_1}\sum_{k_2=0}^{v_1-k_1}\sum_{k_3=0}^{v_2}\sum_{k_4=0}^{v_1'}\sum_{k_5=0}^{v_1'-k_4}\sum_{k_6=0}^{v_2'}\sum_{k_7=0}^{v_2'-k_6}\binom{v_1}{k_1}\binom{v_1-k_1}{k_2}\binom{v_2}{k_3}\binom{v_1'}{k_4}\binom{v_1'-k_4}{k_5}\binom{v_2'}{k_6}\binom{v_2'-k_6}{k_7}$$

$$\times H_{v_1-k_1-k_2}(b_1)H_{v_2-k_3}(b_2)H_{v_1'k_4-k_5}(b_3)$$

$$\times (2a_1)^{k_1}(2a_2)^{k_2}(2a_3)^{k_3}(2a_4)^{k_4}(2a_5)^{k_5}(2a_6)^{k_6}(2a_7)^{k_7}$$

$$\times x^{k_1+k_4+k_6}y^{k_2+k_3+k_5+k_7}. \quad \text{(D.33)}$$

The Gaussian integral formula,

$$\int_{-\infty}^{\infty}x^{2n}e^{-ax^2}dx=\frac{(2n-1)!!}{(2a)^n}\left(\frac{\pi}{a}\right)^{1/2}, \quad \text{(D.34)}$$

can now be used to evaluate the integral of Eq. D.31 with the substitutions of Eq. D.33. We find that the integral overlap is

$$\langle v_1'v_2'|v_1v_2\rangle = N_{v_1v_2;v_1'v_2'}EH_{v_1v_2;v_1'v_2'}, \quad \text{(D.35)}$$

where E has been defined above,

$$N_{v_1v_2;v_1'v_2'} = \left(\frac{\sqrt{\alpha_1\alpha_2\alpha_1'\alpha_2'}}{2^{v_1+v_2+v_1'+v_2'}v_1!v_2!v_1'!v_2'!A_1A_2}\right)^{1/2}, \quad \text{(D.36)}$$

$$H_{v_1v_2;v_1'v_2'} = \sum_{k_1=0}^{v_1}\sum_{k_2=0}^{v_1-k_1}\sum_{k_3=0}^{v_2}\sum_{k_4=0}^{v_1'}\sum_{k_5=0}^{v_1'-k_4}\sum_{k_6=0}^{v_2'}\sum_{k_7=0}^{v_2'-k_6}\binom{v_1}{k_1}\binom{v_1-k_1}{k_2}\binom{v_2}{k_3}$$
$$\times\binom{v_1'}{k_4}\binom{v_1'-k_4}{k_5}\binom{v_2'}{k_6}\binom{v_2'-k_6}{k_7}$$
$$\times H_{v_1-k_1-k_2}(b_1)H_{v_2-k_3}(b_2)H_{v_1'k_4-k_5}(b_3)$$
$$\times F_1^{k_1}F_2^{k_2}F_3^{k_3}F_4^{k_4}F_5^{k_5}F_6^{k_6}F_7^{k_7}$$
$$\times (k_1+k_4+k_6-1)!!(k_2+k_3+k_5+k_7-1)!!, \quad \text{(D.37)}$$

with $k_1+k_4+k_6$ even and $k_2+k_3+k_5+k_7$ even, and

$$F_1 = \left(\frac{2}{A_1}\right)^{1/2}a_1, \quad F_2 = \left(\frac{2}{A_2}\right)^{1/2}a_2, \quad F_3 = \left(\frac{2}{A_2}\right)^{1/2}a_3, \quad \text{(D.38)}$$

$$F_4 = \left(\frac{2}{A_1}\right)^{1/2}a_4, \quad F_5 = \left(\frac{2}{A_2}\right)^{1/2}a_5, \quad F_6 = \left(\frac{2}{A_1}\right)^{1/2}a_6 \quad \text{(D.39)}$$

$$F_7 = \left(\frac{2}{A_2}\right)^{1/2}a_7. \quad \text{(D.40)}$$

Using these formulas, the multidimensional FCFs can be computed as

$$|\langle v_1'v_2'|v_1v_2\rangle|^2 = (N_{v_1v_2;v_1'v_2'}EH_{v_1v_2;v_1'v_2'})^2. \quad \text{(D.41)}$$

	$\tilde{A}(000)$	$\tilde{A}(100)$
$\tilde{X}(000)$	0.862	0.133
$\tilde{X}(100)$	0.120	0.624
$\tilde{X}(200)$	0.015	0.195
$\tilde{X}(300)$	0.0017	0.039
$\tilde{X}(001)$	1.7×10^{-5}	7×10^{-6}
$\tilde{X}(101)$	5×10^{-7}	1.2×10^{-5}

Table D.1: Calculated FCFs using the two-dimensional model of Eq. D.41. The computed values do not include the effects of perturbations or anharmonicity.

D.2 Application to YbOH

We can apply these equations to calculate FCFs for the $\tilde{A}(000)$ and $\tilde{A}(100)$ states of YbOH. In our two-dimensional model, v_1 and v_2 represent the symmetric and antisymmetric stretching modes, respectively. In this case, the vibrational frequencies are $\omega_1 = 529.0\,\text{cm}^{-1}$, $\omega_2 = 3766$ cm^{-1}, $\omega_1' = 585.0$ cm^{-1}, and $\omega_2 = 3766$ cm^{-1}. The bond lengths are determined from the measured rotational constants, assuming that $r_{\text{OH}} = 0.922$ Å is fixed to the BaOH value. We assume $r_{\text{YbO}}(\tilde{X}(000)) = 2.0397$ Å, $r_{\text{YbO}}(\tilde{A}(000)) = 2.0070$ Å, and $r_{\text{YbO}}(\tilde{A}(100)) = 2.0057$ Å. The computed FCFs are shown in Tab. D.1. These do not include the effect of bending mode FCFs, which can be calculated using a one-dimensional model for distorted (but non-displaced) harmonic oscillators.

E

YbOH Lines

This appendix summarizes the rotationally-resolved YbOH transitions found during the course of this work. A graphical overview is shown in Fig. E.1 and transition frequencies are compiled in Tab. E.1. The frequencies listed in Tab. E.1 are as determined by our wavemeter (High Finesse WS7) which is referenced to a continuously monitored transition in atomic Li. We have not taken additional efforts to correct these frequencies for absolute drifts or offsets, but have empirically found that they agree with measurements performed by the Steimle group to an accuracy of around 200 MHz.

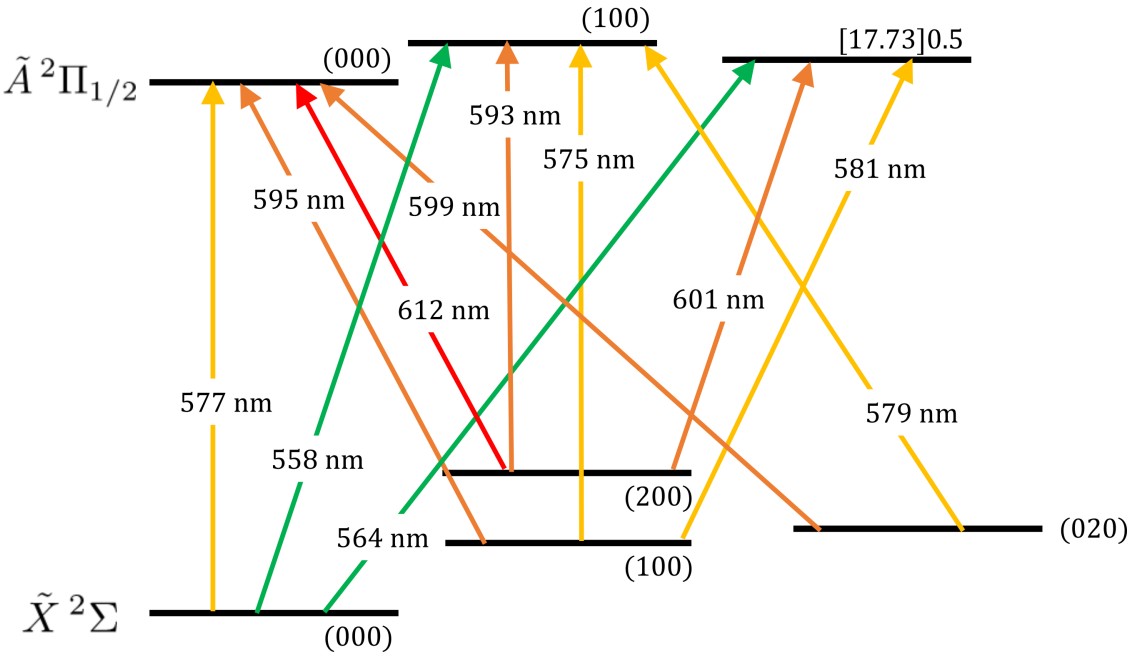

Figure E.1: Summary of transitions observed at high resolution in YbOH.

Table E.1: List of YbOH transitions that have been observed at high resolution. Frequencies are measured by a commercial wavemeter and nominally controlled against long term drifts, but have not been corrected relative to an absolute frequency standard. All transitions in this table originate from the $N'' = 1$ state, but in cases where the spin-rotation structure was not clearly resolved, the "Line" label is left empty.

Ground State	Excited State	Line	Frequency (THz)	Frequency (cm^{-1})
$\tilde{X}(000)$	$\tilde{A}(000)$	${}^{p}Q_{12}(N''=1)$	519.347495	17323.5677
		$P_1(N''=1)$	519.347615	17323.5717
	$\tilde{A}(100)$		536.865480	17907.9048
	[17.73]	${}^{p}Q_{12}(N''=1)$	531.576050	17731.4684
		$P_1(N''=1)$	531.576170	17731.4724
$\tilde{X}(100)$	$\tilde{A}(000)$	${}^{p}Q_{12}(N''=1)$	503.478740	16794.2430
		$P_1(N''=1)$	503.478890	16794.2480
	$\tilde{A}(100)$		520.996725	17378.5801
	[17.73]	${}^{p}Q_{12}(N''=1)$	515.707130	17202.1382
		$P_1(N''=1)$	515.707285	17202.1489
$\tilde{X}(200)$	$\tilde{A}(000)$	${}^{p}Q_{12}(N''=1)$	487.781480	16270.6388
		$P_1(N''=1)$	487.781700	16270.6461
	$\tilde{A}(100)$	${}^{p}Q_{12}(N''=1)$	505.299310	16854.9707
		$P_1(N''=1)$	505.299530	16854.9781
	[17.73]		500.010150	16678.5433
$\tilde{X}(02^{0}0)$	$\tilde{A}(000)$	${}^{p}Q_{12}(N''=1)$	500.632100	16699.2893
		$P_1(N''=1)$	500.632250	16699.2943
	$\tilde{A}(100)$		518.148810	17283.5836
	[17.73]		512.859686	17107.1577

F

Coherent 699 Ring Dye Laser

Continuous-wave dye lasers are an invaluable tool to the spectroscopist. The work in this thesis made extensive use of Coherent 899 ring dye lasers, and also saw the reintroduction of a Coherent 699 dye laser to the Doyle group. In this Appendix, we compile some useful information related to both of these dye laser systems. For general background on cw dye lasers, one should consult Ref. [323]. The best practical reference for dye laser operation is surely the Coherent 899 manual [324].

Table F.1: Mirror sets needed for operation with various laser dyes. For each dye, the top row lists the mirror specified in the 699 manual while the bottom row lists the same taken from the 899 manual.

Dye	P1	M1	Tweeter	M4	M5
Rhodamine 110	0406-619-01	0406-453-04	0406-605-04	0406-669-00	0406-454-04
	0406-619-01	0158-789-06	0158-785-06	0406-669-00	0158-790-06
Rhodamine 6G	0406-619-01	0406-453-05	0406-605-05	0406-663-00	0406-454-05
	0406-619-01	0158-789-07	0158-785-07	0406-663-00	0158-790-07
Rhodamine 640	0406-619-01	0406-453-06	0406-605-06	0406-670-00	0406-454-06
	0406-619-01	0158-789-08	0158-785-08	0406-670-00	0158-790-08

F.1 Useful part numbers

We set up the Coherent 699 ring laser by retrofitting it with a modern nozzle (RDSN-02 from Radiant Dyes Laser & Acc. GmbH) and dye circulator (CW-2000, also from Radiant Dyes). Filter changes make use of the model RDF11 filter from Radiant Dyes. We also replaced the previously installed mirror set with optics appropriate for operation with Rhodamine 6G. Because information on the required optics can be difficult to find, Tab. F.1 lists the mirror sets needed for a few laser dyes covering a large portion of the visible spectrum. We include the part numbers specified for both 699 and 899 ring laser models.

F.2 Observed output powers

Figure F.1 plots some optimized output powers I have recorded at various wavelengths while operating the 699 dye laser. These were all recorded with 10 W of pump laser power at 532 nm and a circulator running at about 9 bar. Substructure observed in the curves is simply due to how much effort was put into optimization at the time. Generally speaking, it is easy to obtain output powers about 70-80% of what can be achieved with an 899 dye laser, but because the 699 alignment is a little more finicky it can be tricky to optimize to

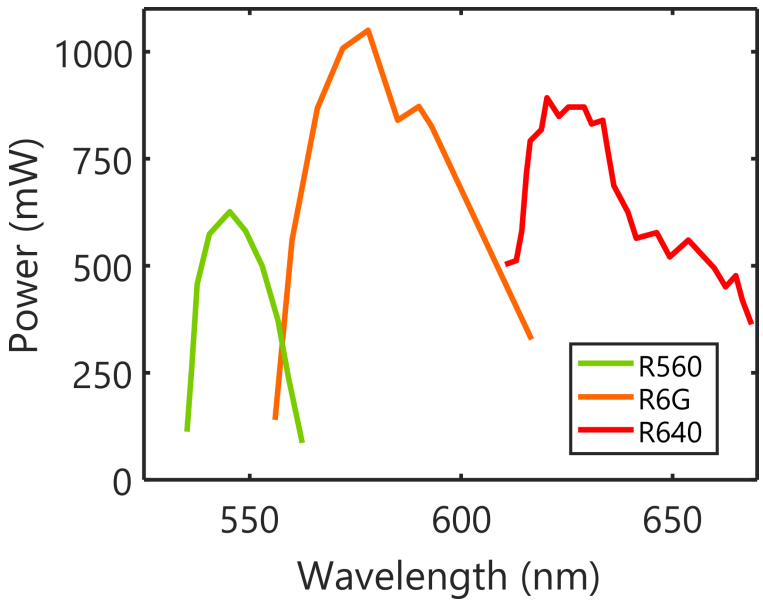

Figure F.1: Observed output powers from Coherent 699 dye laser using different laser dyes. For all curves, we use a 10 W pump at 523 nm.

fully match the 899 performance.

F.3 Alignment tricks

The 699 cavity is slightly more difficult to align than the cavity of an 899, primarily because the focuses of the upper fold mirror and the tweeter are adjusted by manually sliding the optic along an invar bar. Here are a few tips that can make alignment quicker. First, set the pump focus to occur just before the light enters the dye jet. The pump focus is extremely hysteretic, so this step requires patience. A way to check for when the focus is nearly set is to look for the pump light transmitted through the dye jet and set the mirror position so the transmitted beam just begins to distort. Once this is set, check the sizes of the reflections off the fold mirrors. Loosen the mounts and adjust the mirror positions along their mounting rods such that the reflections off of M5 and M3 are about 4 mm and 2.5 mm, respectively, in front of the magnet stack. My experience has been that a slightly smaller reflection

off of M5 is preferable, especially for the 699 cavity. Lasing should be readily established by overlapping the cavity peaks and the output mode should be close to TEM00. Now, iteratively adjust the focuses of M3 and M5. Moving a mirror inevitably stops the cavity from lasing, but applying a small amount of pressure to the invar bar usually establishes oscillation and gives an idea of what adjustments must be made to maintain lasing.

The 899 manual gives a useful guide to how the beam quality changes as various mirrors move: (1) moving the pump mirror towards the jet will flatten the mode and moving P1 away from the jet will vertically elongate the mode; (2) moving M3 or M5 toward the jet horizontally elongates the mode and increases beam diameter; (3) moving M3 or M5 away from the jet vertically elongates the mode and decreases beam diameter. Keeping these effects in mind is especially useful for the 699 since hysteresis can make tuning mirror positions very tedious. Observing the beam shape and trying to optimize toward a clean TEM00 mode following these expected behaviors has proven to be a useful way to quickly optimize the cavity and also peak up power.

G

Excited-State Zeeman Structure and g'_ℓ

Here, we provide further insight into the excited-state Zeeman Hamiltonian for the $\tilde{A}\,^2\Pi_{1/2}$ states. This is relevant to the excited states used for Zeeman-Sisyphus deceleration. We will see that a parity-dependent term characterized by the parameter g'_ℓ sets the dominant Zeeman tuning for the excited state of CaOH. To the best of our knowledge, a measurement of g'_ℓ for CaOH has not been previously reported in the literature. Our optical pumping measurements during preparation for Zeeman-Sisyphus deceleration allow us to determine its value.

G.1 Zeeman Hamiltonian and matrix elements

To a first approximation, the $\tilde{A}\,^2\Pi_{1/2}$ state is expected to show negligible Zeeman shifts because the electron orbital and spin magnetic moments approximately cancel. In actuality, the $\tilde{A}\,^2\Pi_{1/2}$ state will typically mix with nearby $^2\Sigma$ states due to rotational or spin-orbit interactions, and this mixing can give rise to additional terms in the Zeeman Hamiltonian. In particular, a parity-dependent g-factor, denoted g'_ℓ, is the dominant tuning term for the molecules we consider in this thesis. The relevant Zeeman terms to describe the $\tilde{A}\,^2\Pi_{1/2}$ state are given in Ref. [325] as

$$H_Z = g_S\mu_B\mathbf{S}\cdot\mathcal{B} + g'_L\mu_B\mathbf{L}\cdot\mathcal{B} + g_\ell\mu_B\left(S_x\mathcal{B}_x + S_y\mathcal{B}_y\right) + g'_\ell\mu_B\left(e^{-2i\phi}S_+\mathcal{B}_+ + e^{+2i\phi}S_-\mathcal{B}_-\right). \quad \text{(G.1)}$$

Here, g_S is the electron spin g-factor, g'_L is the electron orbital g-factor (corrected for second-order effects), and g_ℓ and g'_ℓ are anisotropic g-factors (parity independent and parity dependent, respectively). For a $^2\Pi_{1/2}$ state, the g_S and g'_L terms approximately cancel.[1] This leaves the anisotropic terms, of which only g'_ℓ has matrix elements within the $\tilde{A}\,^2\Pi_{1/2}$ manifold. In a coupled, non-parity basis set that includes nuclear spin, these matrix elements are derived to be

[1] The degree to which they do *not* cancel is approximately $(g_S - 2)/2 \approx 10^{-3}$. As we will see, this is more than an order of magnitude smaller than the value for g'_ℓ determined for CaOH.

$$\begin{aligned}
&\langle \Lambda; S\Sigma; J\Omega I F M_F | H'_Z | \Lambda'; S\Sigma'; J'\Omega' I F' M'_F \rangle \\
&\quad = -g'_\ell \mu_B \mathcal{B}_Z (-1)^{F-M_F+S-\Sigma+J-\Omega} (-1)^{F'+J+I+1} \sqrt{S(S+1)(2S+1)} \\
&\qquad \times \sqrt{(2F+1)(2F'+1)(2J+1)(2J'+1)} \begin{pmatrix} F & 1 & F' \\ -M_F & 0 & M'_F \end{pmatrix} \begin{Bmatrix} J' & F' & I \\ F & J & 1 \end{Bmatrix} \\
&\qquad \times \sum_{q=\pm 1} \begin{pmatrix} S & 1 & S \\ -\Sigma & -q & \Sigma' \end{pmatrix} \begin{pmatrix} J & 1 & J' \\ -\Omega & q & \Omega' \end{pmatrix} \delta_{\Lambda', \Lambda \mp 2}.
\end{aligned} \tag{G.2}$$

If we specialize to the case of $\tilde{A}\,^2\Pi_{1/2}$ for MOH molecules (where M is an alkaline-earth atom with no nuclear spin), the relevant quantum numbers are $S = 1/2$, $I = 1/2$, $\Lambda = -\Lambda' = +1$, $\Sigma = -\Sigma' = -1/2$, $\Omega = -\Omega' = +1/2$ and the matrix element G.2 simplifies to

$$\begin{aligned}
&\langle +1; S, -1/2; J, +1/2, IFM_F | H'_Z | -1; S, +1/2; J, -1/2, IFM_F \rangle \\
&\qquad = g'_\ell \mu_B \mathcal{B}_Z \frac{(2J+1)(4F(F+1)+4J(J+1)-3)}{32F(F+1)J(J+1)} M_F.
\end{aligned} \tag{G.3}$$

Upon conversion to a parity-conserving basis, this leads to diagonal matrix elements of the form

$$\langle J, F, M_F; \pm | H'_Z | J, F, M_F; \pm \rangle = \pm g_F \mu_B \mathcal{B}_Z M_F, \tag{G.4}$$

where

$$g_F = g'_\ell \frac{(2J+1)(4F(F+1)+4J(J+1)-3)}{32F(F+1)J(J+1)}. \tag{G.5}$$

In this thesis, we are specifically interested in the $J = 1/2, p = +$ state. In that case,

we find $g_F = g'_\ell/3$, so that in the linear regime the levels tune as $\Delta E = \frac{1}{3} g'_\ell \mu_B M_F \mathcal{B}_Z$. This matches the result quoted in Ref. [326]. We can also compare to the results of Ref. [173], which neglected the nuclear spin and found a magnetic tuning $\Delta E_\pm = g_J \mu_B \mathcal{B}_Z M_J$ with $g_J = \pm g'_\ell \frac{(J+1/2)}{2J(J+1)}$. For $J = 1/2, p = +$, this gives a tuning $\Delta E = \frac{2}{3}\mu_B \mathcal{B}_Z M_J$, i.e. the stretched states tune as $\Delta E = \pm\frac{1}{3} g'_\ell \mu_B \mathcal{B}_Z$. This tuning matches the stretched state in the hyperfine basis ($F = 1, M_F = \pm 1$), which also tune as $\Delta E = \pm\frac{1}{3} g'_\ell \mu_B \mathcal{B}_Z$, showing that these results are consistent once nuclear hyperfine structure has decoupled (which happens at fields of just a few tens of Gauss).

G.2 Curl-type relationships and the meaning of g'_ℓ

The matrix elements of the g'_ℓ term were derived above, but without much explanation of the origin of that term in the Hamiltonian. This section attempts to provide some physical insight.

To begin, focus on the g_ℓ (unprimed) term and consider a $^2\Sigma^+$ (not a $^2\Pi$ state). To lowest order, one would expect that in a $^2\Sigma^+$ state the Zeeman effect is isotropic (because the spin is not strongly coupled to the internuclear axis) and dominated by the g_S term. The form of the g_ℓ term implies that this term is related to the portion of the electron spin that is perpendicular to the internuclear axis. Any nonzero value of g_ℓ should originate from the fact that Σ is partially resolved along the internuclear axis, for example due to mixing of the $^2\Sigma^+$ state of interest and any nearby $^2\Pi$ states— these lead to anisotropy. It is known that the spin-rotation constant (γ) of $^2\Sigma^+$ states *also* arises from mixing with nearby $^2\Pi$ states, so it would be reasonable to expect these two effects to be related. Curl

has derived a reasonably accurate way to estimate the correction is [327]

$$g \approx g_e - \gamma/2B \tag{G.6}$$

and we can interpret the correction and providing the g_ℓ term as [328]

$$g_\ell \approx -\gamma/2B. \tag{G.7}$$

Because both g_ℓ and γ gain most of their magnitude from second-order contributions due to the $^2\Sigma^+ - ^2\Pi$ interaction, it is not too surprising that they are related in this way.

Now we can explain the g'_ℓ term in an analogous way. Just as the $^2\Pi$ state has some effect on the parameters of nearby $^2\Sigma^+$ states, so too should the reverse occur. The g'_ℓ term is one of the results that the $^2\Sigma^+ - ^2\Pi$ interaction has on the $^2\Pi$ state. The Λ-doubling in $^2\Pi$ states also arises from this interaction, so an analogy to the Curl relationship G.7 is the so-called Curl-type relationship [173, 326, 329]

$$g'_\ell \approx p/2B. \tag{G.8}$$

The Hamiltonian term associated with this g-factor is also of anisotropic nature and is parity-dependent, belying its relationship to the Λ-doubling parameter p. There are additional Curl-type relationships that can be understood in a similar fashion [326, 329].

How large of an effect does the g'_ℓ term have? Plugging the previously measured values of p (≈ -0.043 cm^{-1}) and B (≈ 0.341 cm^{-1}) for CaOH [180] into the Curl relationship of Eq. G.8 predicts $g'_\ell \approx -0.063$. In the next section this will be shown to agree extremely

well with measurements. The value of g'_ℓ for YbOH is significantly larger due to the larger Λ-doubling interaction. For that molecule, $p \approx -0.438\,\mathrm{cm}^{-1}$ and $B \approx 0.253\,\mathrm{cm}^{-1}$, yielding a Curl-type relationship prediction of $g'_\ell \approx -0.865$.

G.2.1 Second-Order Expressions for g_ℓ and g'_ℓ

The second-order expressions that lead to g_ℓ and g'_ℓ in the effective Zeeman Hamiltonian can shed further light on the connection between these factors and the Λ-doubling terms. In particular, Ref. [329] derives

$$g_\ell = -\left(g_L + g_r^N\right) \sum_{q=\pm1} \sum_{\eta'\,\Lambda'} \frac{\langle \eta\Lambda | T^1_q(\boldsymbol{L}) | \eta'\Lambda' \rangle \langle \eta'\Lambda' | A T^1_{-q}(\boldsymbol{L}) | \eta\Lambda \rangle}{E^0_{\eta\Lambda} - E^0_{\eta'\Lambda'}}, \tag{G.9}$$

$$g'_\ell = -2\left(g_L + g_r^N\right) \sum_{\eta'} (-1)^s \frac{\langle \eta\Lambda | T^1_1(\boldsymbol{L}) | \eta'\Lambda' \rangle \langle \eta'\Lambda' | A T^1_{-1}(\boldsymbol{L}) | \eta\Lambda \rangle}{E^0_{\eta\Lambda} - E^0_{\eta'\Lambda'}}. \tag{G.10}$$

The sums are taken over states of Σ and Δ symmetry. These forms indicates that g_ℓ and g'_ℓ will have similar magnitude. The effect of g_ℓ on the energies of the $^2\Pi_{1/2}$ levels is small because the matrix elements of the g_ℓ term are negligible within this state. Note that these formulas also demonstrate the connection between g'_ℓ and the Λ-doubling parameter, which can also be written as a second-order expression involving the production of L_+ and AL_- operators.

G.3 Measurement of g'_ℓ for CaOH

This g'_ℓ term in the Zeeman Hamiltonian is what gives rise to the two optical pumping features observed in Fig. 7.9. To the best of our knowledge, the value of g'_ℓ for CaOH ($\tilde{A}\,^2\Pi_{1/2}$)

has not been previously reported; we can use our optical pumping measurements to determine this parameter. At 2.8 T, the observed splitting between the excited-states WFS and SFS levels is found to be $\Delta f = 1700(100)$ MHz. According to Eq. G.2, the Zeeman tuning of the stretched states in the $\tilde{A}\,^2\Pi_{1/2}(J' = 1/2)$ level will be given by $\Delta E_Z = \frac{1}{3} g'_\ell \mu_B \mathcal{B}_Z M_F$, implying a splitting $\Delta f = \frac{2}{3} g'_\ell \mu_B \mathcal{B}_Z$ between the two observed optical pumping features. This leads to $g'_\ell = -0.065(4)$. The parameter g'_ℓ has been previously measured for CaF and was found to be $-0.0611(37)$ [325]. The values determined for CaF and CaOH are thus quite similar, which is to be expected. In addition, the measured CaOH value ($g'_\ell = -0.065(4)$) agrees well with the value predicted above from the Curl-type relationship ($g'_\ell \approx -0.063$).

References

[1] D. DeMille, "Diatomic molecules, a window onto fundamental physics," Physics Today **68**, 34 (2015).

[2] W. B. Cairncross and J. Ye, "Atoms and molecules in the search for time-reversal symmetry violation," Nat. Rev. Phys. **1**, 510 (2019).

[3] R. H. Parker, C. Yu, W. Zhong, B. Estey, and H. Müller, "Measurement of the fine-structure constant as a test of the standard model," Science **360**, 191 (2018).

[4] M. S. Safronova, D. Budker, D. DeMille, D. F. J. Kimball, A. Derevianko, and C. W. Clark, "Search for new physics with atoms and molecules," Rev. Mod. Phys. **90**, 025008 (2018).

[5] W. D. Phillips, "Nobel Lecture: Laser cooling and trapping of neutral atoms," Rev. Mod. Phys. **70**, 721 (1998).

[6] S. Chu, "The manipulation of neutral particles," Rev. Mod. Phys. **70**, 685 (1998).

[7] F. Schäfer, T. Fukuhara, S. Sugawa, Y. Takasu, and Y. Takahashi, "Tools for quantum simulation with ultracold atoms in optical lattices," Nat. Rev. Phys. **2**, 411 (2020).

[8] L. Canetti, M. Drewes, and M. Shaposhnikov, "Matter and antimatter in the universe," New J. Phys. **14**, 095012 (2012).

[9] A. D. Sakharov, "Violation of CP Invariance, C asymmetry, and baryon asymmetry of the universe," Pisma Zh. Eksp. Teor. Fiz. **5**, 32 (1967).

[10] M. Dine and A. Kusenko, "Origin of the matter-antimatter asymmetry," Rev. Mod. Phys. **76**, 1 (2004).

[11] J. L. Feng, "Naturalness and the status of supersymmetry," Annual Review of Nuclear and Particle Science **63**, 351 (2013).

[12] S. Barr, "A Review of CP Violation in Atoms," International Journal of Modern Physics A **08**, 209 (1993).

[13] M. Pospelov and A. Ritz, "Electric dipole moments as probes of new physics," Ann. Phys. **318**, 119 (2005).

[14] E. Petrik West, *A Thermochemical Cryogenic Buffer Gas Beam Source of ThO for Measuring the Electric Dipole Moment of the Electron*, Ph.D. thesis, Harvard University (2017).

[15] N. Fortson, P. Sandars, and S. Barr, "The search for a permanent electric dipole moment," Physics Today **56**, 33 (2003).

[16] E. D. Commins and D. DeMille, "The electric dipole moment of the electron," in *Lepton Dipole Moments* (2009) pp. 519–581.

[17] C. Cesarotti, Q. Lu, Y. Nakai, A. Parikh, and M. Reece, "Interpreting the electron EDM constraint," J. High Energ. Phys. **2019:59** (2019).

[18] I. B. Khriplovich and S. Lamoreaux, *CP Violation Without Strangeness: Electric Dipole Moments of Particles, Atoms, and Molecules* (Springer-Verlag, 1997).

[19] V. S. Prasannaa, N. Shitara, A. Sakurai, M. Abe, and B. P. Das, "Enhanced sensitivity of the electron electric dipole moment from YbOH: The role of theory," Phys. Rev. A **99**, 062502 (2019).

[20] L. V. Skripnikov, A. N. Petrov, and A. V. Titov, "Communication: Theoretical study of ThO for the electron electric dipole moment search," J. Chem. Phys. **139**, 221103 (2013).

[21] N. R. Hutzler, "Polyatomic molecules as quantum sensors for fundamental physics," Quantum Sci. Technol. **5**, 044011 (2020).

[22] G. Herzberg, *Molecular Spectra and Molecular Structure: Spectra of Diatomic Molecules*, Vol. 1 (Van Nostrand, 1966).

[23] ACME Collaboration, "Order of magnitude smaller limit on the electric dipole moment of the electron," Science **343**, 269 (2014).

[24] ACME Collaboration, "Improved limit on the electric dipole moment of the electron," Nature **562**, 355 (2018).

[25] W. B. Cairncross, D. N. Gresh, M. Grau, K. C. Cossel, T. S. Roussy, Y. Ni, Y. Zhou, J. Ye, and E. A. Cornell, "Precision measurement of the electron's electric dipole moment using trapped molecular ions," Phys. Rev. Lett. **119**, 153001 (2017).

[26] I. Kozyryev and N. R. Hutzler, "Precision measurement of time-reversal symmetry violation with laser-cooled polyatomic molecules," Phys. Rev. Lett. **119**, 133002 (2017).

[27] I. Kozyryev, Z. Lasner, and J. M. Doyle, "Enhanced sensitivity to ultralight bosonic dark matter in the spectra of the linear radical SrOH," Phys. Rev. A **103**, 043313 (2021).

[28] P. Jansen, H. L. Bethlem, and W. Ubachs, "Tipping the scales: Search for drifting constants from molecular spectra," J. Chem. Phys. **140**, 010901 (2014).

[29] M. G. Kozlov and S. A. Levshakov, "Microwave and submillimeter molecular transitions and their dependence on fundamental constants," Ann. Phys. (Berl.) **525**, 452 (2013).

[30] P. Jansen, I. Kleiner, C. Meng, R. M. Lees, M. H. M. Janssen, W. Ubachs, and H. L. Bethlem, "Prospects for high-resolution microwave spectroscopy of methanol in a Stark-deflected molecular beam," Mol. Phys. **111**, 1923 (2013).

[31] P. Jansen, L.-H. Xu, I. Kleiner, H. L. Bethlem, and W. Ubachs, "Methyl mercaptan (CH_3SH) as a probe for variation of the proton-to-electron mass ratio," Phys. Rev. A **87**, 052509 (2013).

[32] M. G. Kozlov, "Linear polyatomic molecules with $^2\Pi$ ground state: Sensitivity to variation of the fundamental constants," Phys. Rev. A **87**, 032104 (2013).

[33] M. Quack, "How important is parity violation for molecular and biomolecular chirality?" Angew. Chem. **41**, 4618 (2002).

[34] D. G. Blackmond, "The origin of biological homochirality," Philos. Trans. R. Soc. B **366**, 2878 (2011).

[35] S. Eibenberger, J. Doyle, and D. Patterson, "Enantiomer-specific state transfer of chiral molecules," Phys. Rev. Lett. **118**, 123002 (2017).

[36] T. A. Isaev and R. Berger, "Polyatomic candidates for cooling of molecules with lasers from simple theoretical concepts," Phys. Rev. Lett. **116**, 063006 (2016).

[37] A. C. et al., "A new experiment to test parity symmetry in cold chiral molecules using vibrational spectroscopy," Quantum Electron. **49**, 288 (2019).

[38] K. Gaul, M. G. Kozlov, T. A. Isaev, and R. Berger, "Chiral Molecules as Sensitive Probes for Direct Detection of P-Odd Cosmic Fields," Phys. Rev. Lett. **125**, 123004 (2020).

[39] K. Gaul, M. G. Kozlov, T. A. Isaev, and R. Berger, "Parity-nonconserving interactions of electrons in chiral molecules with cosmic fields," Phys. Rev. A **102**, 032816 (2020).

[40] S. Stellmer, B. Pasquiou, R. Grimm, and F. Schreck, "Laser cooling to quantum degeneracy," Phys. Rev. Lett. **110**, 263003 (2013).

[41] A. Urvoy, Z. Vendeiro, J. Ramette, A. Adiyatullin, and V. Vuletić, "Direct Laser Cooling to Bose-Einstein Condensation in a Dipole Trap," Phys. Rev. Lett. **122**, 203202 (2019).

[42] P. Wójcik, T. Korona, and M. Tomza, "Interactions of benzene, naphthalene, and azulene with alkali-metal and alkaline-earth-metal atoms for ultracold studies," The Journal of Chemical Physics **150**, 234106 (2019).

[43] T. Tscherbul and R. Krems, "Controlling electronic spin relaxation of cold molecules with electric fields," Phys. Rev. Lett. **97**, 083201 (2006).

[44] T. Tscherbul, Y. V. Suleimanov, V. Aquilanti, and R. Krems, "Magnetic field modification of ultracold molecule-molecule collisions," New J. Phys. **11**, 055021 (2009).

[45] T. Tscherbul, H.-G. Yu, and A. Dalgarno, "Sympathetic cooling of polyatomic molecules with S-state atoms in a magnetic trap," Phys. Rev. Lett. **106**, 073201 (2011).

[46] Z. Li, R. V. Krems, and E. J. Heller, "Collision dynamics of polyatomic molecules containing carbon rings at low temperatures," J. Chem. Phys. **141**, 104317 (2014).

[47] G. Quéméner and J. L. Bohn, "Shielding $^2\Sigma$ ultracold dipolar molecular collisions with electric fields," Phys. Rev. A **93**, 012704 (2016).

[48] F. Richter, D. Becker, C. Bény, T. A. Schulze, S. Ospelkaus, and T. J. Osborne, "Ultracold chemistry and its reaction kinetics," New J. Phys. **17**, 055005 (2015).

[49] K.-K. Ni, S. Ospelkaus, D. Wang, G. Quéméner, B. Neyenhuis, M. H. G. de Miranda, J. Bohn, J. Ye, and D. Jin, "Dipolar collisions of polar molecules in the quantum regime," Nature **464**, 1324 (2010).

[50] S. Ospelkaus, K.-K. Ni, D. Wang, M. H. G. de Miranda, B. Neyenhuis, G. Quéméner, P. Julienne, J. Bohn, D. Jin, and J. Ye, "Quantum-state controlled chemical reactions of ultracold potassium-rubidium molecules," Science **327**, 853 (2010).

[51] R. J. Pattillo, R. Cieszewski, P. C. Stancil, R. C. Forrey, J. F. Babb, J. F. McCann, and B. M. McLaughlin, "Photodissociation of CS from excited rovibrational levels," Astrophys. J. **858**, 10 (2018).

[52] E. Herbst and E. F. van Dishoeck, "Complex organic interstellar molecules," Annu. Rev. Astron. Astrophys **47**, 427 (2009).

[53] S. Kwok, "Complex organics in space from Solar System to distant galaxies," Astron. Astrophys. Rev. **24**, 8 (2016).

[54] R. V. Krems, "Cold controlled chemistry," Phys. Chem. Chem. Phys. **10**, 4079 (2008).

[55] M. T. Hummon, T. V. T. an J. Kłos, H.-I. Lu, E. Tsikata, W. C. Campbell, A. Dalgarno, and J. M. Doyle, "Cold N-NH collisions in a magnetic trap," Phys. Rev. Lett. **106**, 053201 (2011).

[56] T. Tscherbul, J. Kłos, and A. Buchachenko, "Ultracold spin-polarized mixtures of $^2\Sigma$ molecules with S-state atoms: Collisional stability and implications for sympathetic cooling," Phys. Rev. A **84**, 040701 (2011).

[57] A. Micheli, G. K. Brennen, and P. Zoller, "A toolbox for lattice-spin models with polar molecules," Nat. Phys. **2**, 341 (2006).

[58] A. Micheli, G. Pupillo, H. P. Büchler, and P. Zoller, "Cold polar molecules in two-dimensional traps: Tailoring interactions with external fields for novel quantum phases," Phys. Rev. A **76**, 043604 (2007).

[59] A. V. Gorshkov, S. R. Manmana, G. Chen, J. Ye, E. Demler, M. D. Lukin, and A. M. Rey, "Tunable superfluidity and quantum magnetism with ultracold polar molecules," Phys. Rev. Lett. **107**, 115301 (2011).

[60] M. L. Wall, K. Maeda, and L. D. Carr, "Simulating quantum magnets with symmetric top molecules," Ann. Phys. (Berl.) **525**, 845 (2013).

[61] M. L. Wall, K. Maeda, and L. D. Carr, "Realizing unconventional quantum magnetism with symmetric top molecules," New J. Phys. **17**, 025001 (2015).

[62] J. A. Blackmore, L. Caldwell, P. D. Gregory, E. M. Bridge, R. Sawant, J. Aldegunde, J. Mur-Petit, D. Jaksch, J. M. Hutson, B. E. Sauer, M. R. Tarbutt, and S. L. Cornish, "Ultracold molecules for quantum simulation: rotational coherences in CaF and RbCs," Quantum Sci. Technol. **4**, 014010 (2018).

[63] D. DeMille, "Quantum computation with trapped polar molecules," Phys. Rev. Lett. **88**, 067901 (2002).

[64] S. F. Yelin, K. Kirby, and R. Côté, "Schemes for robust quantum computation with polar molecules," Phys. Rev. A **74**, 050301(R) (2006).

[65] E. R. Hudson and W. C. Campbell, "Dipolar quantum logic for freely rotating trapped molecular ions," Phys. Rev. A **98**, 040302(R) (2018).

[66] K.-K. Ni, T. Rosenband, and D. D. Grimes, "Dipolar exchange quantum logic gate with polar molecules," Chem. Sci. **9**, 6830 (2018).

[67] P. Yu, L. W. Cheuk, I. Kozyryev, and J. M. Doyle, "A scalable quantum computing platform using symmetric-top molecules," New J. Phys. **21**, 093049 (2019).

[68] Q. Wei, S. Kais, B. Friedrich, and D. Herschbach, "Entanglement of polar symmetric top molecules as candidate qubits," J. Chem. Phys. **135**, 154102 (2011).

[69] M. Wall, K. Hazzard, and A. M. Rey, "Quantum magnetism with ultracold molecules," in *From Atomic To Mesoscale: The Role of Quantum Coherence in Systems of Various Complexities* (World Scientific, 2015) pp. 3–37.

[70] V. V. Albert, J. P. Covey, and J. Preskill, "Robust encoding of a qubit in a molecule," Phys. Rev. X **10**, 031050 (2020).

[71] R. Sawant, J. A. Blackmore, P. D. Gregory, J. Mur-Petit, D. Jaksch, J. Aldegunde, J. M. Hutson, M. R. Tarbutt, and S. L. Cornish, "Ultracold polar molecules as qudits," New J. Phys. **22**, 013027 (2019).

[72] Z. Zilic and K. Radecka, "Scaling and Better Approximating Quantum Fourier Transform by Higher Radices," IEEE Transactions on Computers **56**, 202 (2007).

[73] V. Parasa and M. Perkowski, "Quantum phase estimation using multivalued logic," in *2011 41st IEEE International Symposium on Multiple-Valued Logic* (IEEE, 2011).

[74] E. T. Campbell, H. Anwar, and D. E. Browne, "Magic-state distillation in all prime dimensions using quantum Reed-Muller codes," Phys. Rev. X **2**, 041021 (2012).

[75] A. Krishna and J.-P. Tillich, "Towards low overhead magic state distillation," Phys. Rev. Lett. **123**, 070507 (2019).

[76] C. T. Scurlock, T. Henderson, S. Bosely, K. Y. Jung, and T. C. Steimle, "Molecular beam optical stark spectroscopy of CaSH," J. Chem. Phys. **100**, 5481 (1994).

[77] T. C. Steimle, D. A. Fletcher, K. Y. Jung, and C. T. Scurlock, "A supersonic molecular beam optical Stark study of CaOH and SrOH," J. Chem. Phys. **96**, 2556 (1992).

[78] D. McCarron, "Laser cooling and trapping molecules," J. Phys. B **51**, 212001 (2018).

[79] K.-K. Ni, S. Ospelkaus, M. H. G. de Miranda, A. Pe'er, B. Neyenhuis, J. J. Zirbel, S. Kotochigova, P. S. Julienne, D. S. Jin, and J. Ye, "A high phase-space-density gas of polar molecules," Science **322**, 231 (2008).

[80] P. K. Molony, P. D. Gregory, Z. Ji, B. Lu, M. P. Köppinger, C. R. Le Sueur, C. L. Blackley, J. M. Hutson, and S. L. Cornish, "Creation of ultracold ^{87}Rb^{133}Cs molecules in the rovibrational ground state," Phys. Rev. Lett. **113**, 255301 (2014).

[81] J. W. Park, S. A. Will, and M. W. Zwierlein, "Ultracold dipolar gas of fermionic ^{23}Na^{40}K molecules in their absolute ground state," Phys. Rev. Lett. **114**, 205302 (2015).

[82] M. Guo, B. Zhu, B. Lu, X. Ye, F. Wang, R. Vexiau, N. Bouloufa-Maafa, G. Quéméner, O. Dulieu, and D. Wang, "Creation of an ultracold gas of ground-state dipolar ^{23}Na^{87}Rb molecules," Phys. Rev. Lett. **116**, 205303 (2016).

[83] T. M. Rvachov, H. Son, A. T. Sommer, S. Ebadi, J. J. Park, M. W. Zwierlein, W. Ketterle, and A. O. Jamison, "Long-lived ultracold molecules with electric and magnetic dipole moments," Phys. Rev. Lett. **119**, 143001 (2017).

[84] W. B. Cairncross, J. T. Zhang, L. R. B. Picard, Y. Yu, K. Wang, and K.-K. Ni, "Assembly of a rovibrational ground state molecule in an optical tweezer," Phys. Rev. Lett. **126**, 123402 (2021).

[85] H. Yang, X.-Y. Wang, Z. Su, J. Cao, D.-C. Zhang, J. Rui, B. Zhao, C.-L. Bai, and J.-W. Pan, "Evidence for association of triatomic molecule in ultracold ^{23}Na^{40}K and ^{40}K mixture," (2021), arXiv:2104.11424 .

[86] M. Zeppenfeld, B. G. U. Englert, R. Glöckner, A. Prehn, M. Mielenz, C. Sommer, L. D. van Buuren, M. Motsch, and G. Rempe, "Sisyphus cooling of electrically trapped polyatomic molecules," Nature **491**, 570 (2012).

[87] A. Prehn, M. Ibrügger, R. Glöckner, G. Rempe, and M. Zeppenfeld, "Optoelectrical cooling of polar molecules to submillikelvin temperatures," Phys. Rev. Lett. **116**, 063005 (2016).

[88] W. C. Campbell and J. M. Doyle, *Cooling, trap loading, and beam production using a cryogenic helium buffer gas* (2009).

[89] N. R. Hutzler, H.-I. Lu, and J. M. Doyle, "The buffer gas beam: An intense, cold, and slow source for atoms and molecules," Chem. Rev. **112**, 4803 (2012).

[90] J. F. Barry, E. S. Shuman, and D. DeMille, "A bright, slow cryogenic molecular beam source for free radicals," Phys. Chem. Chem. Phys. **13**, 18936 (2011).

[91] J. K. Messer and F. C. De Lucia, "Measurement of Pressure-Broadening Parameters for the CO-He System at 4 K," Phys. Rev. Lett. **53**, 2555 (1984).

[92] D. R. Willey, R. L. Crownover, D. N. Bittner, and F. C. De Lucia, "Very low temperature spectroscopy: The pressure broadening coefficients for CH_3F between 4.2 and 1.9 K," J. Chem. Phys. **89**, 6147 (1988).

[93] M. Mengel and F. C. De Lucia, "Helium and hydrogen induced rotational relaxation of H_2CO observed at temperatures of the interstellar medium," The Astrophysical Journal **543**, 271 (2000).

[94] J. M. Doyle, B. Friedrich, J. Kim, and D. Patterson, "Buffer-gas loading of atoms and molecules into a magnetic trap," Phys. Rev. A **52**, R2515 (1995).

[95] J. D. Weinstein, R. deCarvalho, T. Guillet, B. Friedrich, and J. M. Doyle, "Magnetic trapping of calcium monohydride molecules at millikelvin temperatures," Nature **395**, 148 (1998).

[96] W. C. Campbell, E. Tsikata, H.-I. Lu, L. D. van Buuren, and J. M. Doyle, "Magnetic Trapping and Zeeman Relaxation of NH ($X\ ^3\Sigma^-$)," Phys. Rev. Lett. **98**, 213001 (2007).

[97] S. C. Doret, C. B. Connolly, W. Ketterle, and J. M. Doyle, "Buffer-gas cooled bose-einstein condensate," Phys. Rev. Lett. **103**, 103005 (2009).

[98] S. E. Maxwell, N. Brahms, R. deCarvalho, D. R. Glenn, J. S. Helton, S. V. Nguyen, D. Patterson, J. Petricka, D. DeMille, and J. M. Doyle, "High-flux beam source for cold, slow atoms or molecules," Phys. Rev. Lett. **95**, 173201 (2005).

[99] D. Patterson and J. M. Doyle, "Bright, guided molecular beam with hydrodynamic enhancement," J. Chem. Phys. **126**, 154307 (2007).

[100] H. J. Metcalf and P. van der Straten, *Laser Cooling and Trapping* (Springer-Verlag, 1999).

[101] E. A. Cornell and C. E. Wieman, "Nobel Lecture: Bose-Einstein condensation in a dilute gas, the first 70 years and some recent experiments," Rev. Mod. Phys. **74**, 875 (2002).

[102] J. J. García-Ripoll, P. Zoller, and J. I. Cirac, "Quantum information processing with cold atoms and trapped ions," J. Phys. B **38**, S567 (2005).

[103] M. Endres, H. Bernien, A. Keesling, H. Levine, E. R. Anschuetz, A. Krajenbrink, C. Senko, V. Vuletic, M. Greiner, and M. D. Lukin, "Atom-by-atom assembly of defect-free one-dimensional cold atom arrays," Science **354**, 1024 (2016).

[104] D. Barredo, S. de Léséleuc, V. Lienhard, T. Lahaye, and A. Browaeys, "An atom-by-atom assembler of defect-free arbitrary two-dimensional atomic arrays," Science **354**, 1021 (2016).

[105] P. Hamilton, M. Jaffe, P. Haslinger, Q. Simmons, H. Müller, and J. Khoury, "Atom-interferometry constraints on dark energy," Science **349**, 849 (2015).

[106] S. M. Dickerson, J. M. Hogan, A. Sugarbaker, D. M. Johnson, and M. A. Kasevich, "Multi-axis inertial sensing with long-time point source atom interferometry," Phys. Rev. Lett. **111**, 083001 (2013).

[107] M. Di Rosa, "Laser-cooling molecules," Eur. Phys. J. D **31**, 395 (2004).

[108] B. K. Stuhl, B. C. Sawyer, D. Wang, and J. Ye, "Magneto-optical trap for polar molecules," Phys. Rev. Lett. **101**, 243002 (2008).

[109] E. S. Shuman, J. F. Barry, D. R. Glenn, and D. DeMille, "Radiative force from optical cycling on a diatomic molecule," Phys. Rev. Lett. **103**, 223001 (2009).

[110] E. S. Shuman, J. F. Barry, and D. DeMille, "Laser cooling of a diatomic molecule," Nature **467**, 820 (2010).

[111] J. F. Barry, E. S. Shuman, E. B. Norrgard, and D. DeMille, "Laser radiation pressure slowing of a molecular beam," Phys. Rev. Lett. **108**, 103002 (2012).

[112] J. Barry, D. McCarron, E. Norrgard, M. Steinecker, and D. DeMille, "Magneto-optical trapping of a diatomic molecule," Nature **512**, 286 (2014).

[113] E. B. Norrgard, D. J. McCarron, M. H. Steinecker, M. R. Tarbutt, and D. DeMille, "Submillikelvin dipolar molecules in a radio-frequency magneto-optical trap," Phys. Rev. Lett. **116**, 063004 (2016).

[114] S. Truppe, H. J. Williams, M. Hambach, L. Caldwell, N. J. Fitch, E. A. Hinds, B. E. Sauer, and M. R. Tarbutt, "Molecules cooled below the Doppler limit," Nat. Phys. (2017).

[115] L. Anderegg, B. L. Augenbraun, E. Chae, B. Hemmerling, N. R. Hutzler, A. Ravi, A. L. Collopy, J. Ye, W. Ketterle, and J. M. Doyle, "Radio frequency magneto-optical trapping of CaF with high density," Phys. Rev. Lett. **119**, 103201 (2017).

[116] A. L. Collopy, S. Ding, Y. Wu, I. A. Finneran, L. Anderegg, B. L. Augenbraun, J. M. Doyle, and J. Ye, "3-D magneto-optical trap of yttrium monoxide," Phys. Rev. Lett. **121**, 213201 (2018).

[117] S. Truppe, H. J. Williams, N. J. Fitch, M. Hambach, T. E. Wall, E. A. Hinds, B. E. Sauer, and M. R. Tarbutt, "An intense, cold, velocity-controlled molecular beam by frequency-chirped laser slowing," New J. Phys. **19**, 022001 (2017).

[118] B. Hemmerling, E. Chae, A. Ravi, L. Anderegg, G. K. Drayna, N. R. Hutzler, A. L. Collopy, J. Ye, W. Ketterle, and J. M. Doyle, "Laser slowing of CaF molecules to near the capture velocity of a molecular MOT," J. Phys. B **49**, 174001 (2016).

[119] L. Caldwell, J. A. Devlin, H. J. Williams, N. J. Fitch, E. A. Hinds, B. E. Sauer, and M. R. Tarbutt, "Deep laser cooling and efficient magnetic compression of molecules," Phys. Rev. Lett. **123**, 033202 (2019).

[120] L. W. Cheuk, L. Anderegg, B. L. Augenbraun, Y. Bao, S. Burchesky, W. Ketterle, and J. M. Doyle, "Λ-enhanced imaging of molecules in an optical trap," Phys. Rev. Lett. **121**, 083201 (2018).

[121] L. Anderegg, B. L. Augenbraun, Y. Bao, S. Burchesky, L. W. Cheuk, W. Ketterle, and J. M. Doyle, "Laser cooling of optically trapped molecules," Nature Phys. **14**, 890 (2018).

[122] Y. Wu, J. J. Burau, K. Mehling, J. Ye, and S. Ding, "High phase-space density of laser-cooled molecules in an optical lattice," (2021), arXiv:2107.06422 [physics.atom-ph] .

[123] H. J. Williams, L. Caldwell, N. J. Fitch, S. Truppe, J. Rodewald, E. A. Hinds, B. E. Sauer, and M. R. Tarbutt, "Magnetic trapping and coherent control of laser-cooled molecules," Phys. Rev. Lett. **120**, 163201 (2018).

[124] D. J. McCarron, M. H. Steinecker, Y. Zhu, and D. DeMille, "Magnetic trapping of an ultracold gas of polar molecules," Phys. Rev. Lett. **121**, 013202 (2018).

[125] I. Kozyryev, L. Baum, K. Matsuda, and J. M. Doyle, "Proposal for laser cooling of complex polyatomic molecules," ChemPhysChem **17**, 3641 (2016).

[126] I. Kozyryev, L. Baum, K. Matsuda, B. L. Augenbraun, L. Anderegg, A. P. Sedlack, and J. M. Doyle, "Sisyphus laser cooling of a polyatomic molecule," Phys. Rev. Lett. **118**, 173201 (2017).

[127] M. Li, J. Kłos, A. Petrov, and S. Kotochigova, "Emulating optical cycling centers in polyatomic molecules," Commun. Phys. **2** (2019), 10.1038/s42005-019-0245-2.

[128] M. V. Ivanov, F. H. Bangerter, and A. I. Krylov, "Towards a rational design of laser-coolable molecules: insights from equation-of-motion coupled-cluster calculations," Phys. Chem. Chem. Phys. **21**, 19447 (2019).

[129] T. C. Melville and J. A. Coxon, "The visible laser excitation spectrum of YbOH: The $\tilde{A}\,^2\Pi - \tilde{X}\,^2\Sigma^+$ transition," J. Chem. Phys. **115**, 6974 (2001).

[130] B. L. Augenbraun, J. M. Doyle, T. Zelevinsky, and I. Kozyryev, "Molecular asymmetry and optical cycling: Laser cooling asymmetric top molecules," Phys. Rev. X **10** (2020).

[131] J. M. Brown and A. Carrington, *Rotational spectroscopy of diatomic molecules* (Cambridge Univ. Press, 2003).

[132] E. Hirota, *High-Resolution Spectroscopy of Transient Molecules* (Springer Berlin Heidelberg, 1985).

[133] W. Gordy and R. L. Cook, *Microwave Molecular Spectra* (John Wiley and Sons, 1984).

[134] D. Papoušek and M. R. Aliev, *Molecular vibrational-rotational spectra : theory and applications of high resolution infrared, microwave, and Raman spectroscopy of polyatomic molecules* (Elsevier Scientific Pub. Co., New York, 1982).

[135] P. F. Bernath, *Spectra of Atoms and Molecules* (OUP, 2017).

[136] W. Demtröder, *Molecular Physics: Theoretical Principles and Experimental Methods* (Weinheim: Wiley-VCH Verlag, 2003).

[137] C. H. Townes and A. L. Schawlow, *Microwave spectroscopy* (New York: Dover Publications, 1975).

[138] S. Califano, *Vibrational States* (John Wilye & Sons, Ltd., 1976).

[139] P. R. Bunker and P. Jensen, *Molecular symmetry and spectroscopy* (NRC Research Press, 2006).

[140] G. Fischer, *Vibronic Coupling: The Interaction between the Electronic and Nuclear Motions* (Academic Press, 1984).

[141] T. Azumi and K. Matsuzaki, "What does the term "vibronic coupling" mean?" Photochemistry and Photobiology **25**, 315 (1977).

[142] T. A. Isaev, A. V. Zaitsevskii, and E. Eliav, "Laser-coolable polyatomic molecules with heavy nuclei," J. Phys. B **50**, 225101 (2017).

[143] A. M. Ellis, "Main group metal-ligand interactions in small molecules: New insights from laser spectroscopy," Int. Rev. Phys. Chem. **20**, 551 (2001).

[144] S. F. Rice, H. Martin, and R. W. Field, "The electronic structure of the calcium monohalides. a ligand field approach," J. Chem. Phys. **82**, 5023 (1985).

[145] A. Allouche, G. Wannous, and M. Aubert-Frécon, "A ligand-field approach for the low-lying states of Ca, Sr and Ba monohalides," Chemical Physics **170**, 11 (1993).

[146] B. L. Augenbraun, Z. D. Lasner, A. Frenett, H. Sawaoka, A. T. Le, J. M. Doyle, and T. C. Steimle, "Observation and laser spectroscopy of ytterbium monomethoxide, YbOCH3," Phys. Rev. A **103**, 022814 (2021).

[147] M. J. Dick, *Spectroscopy of selected calcium and strontium containing polyatomic molecules*, Ph.D. thesis, University of Waterloo (2007).

[148] I. Kozyryev, *Laser cooling and inelastic collisions of the polyatomic radical SrOH*, Ph.D. thesis, Harvard University (2017).

[149] E. B. Wilson, J. C. Decius, and P. C. Cross, *Molecular Vibrations: The Theory of Infrared and Raman Vibrational Spectra* (Dover, 1980).

[150] D. J. Griffiths, *Introduction to Quantum Mechanics* (Pearson Prentice Hall, 2005).

[151] G. Herzberg, *Molecular Spectra and Molecular Structure: Infrared and Raman Spectra of Polyatomic Molecules*, Vol. 2 (Van Nostrand, 1945).

[152] W. Quapp and B. P. Winnewisser, "What you thought you already knew about the bending motion of triatomic molecules," J. Math. Chem. **14**, 259 (1993).

[153] E. T. Mengesha, A. T. Le, T. C. Steimle, L. Cheng, C. Zhang, B. L. Augenbraun, Z. Lasner, and J. Doyle, "Branching ratios, radiative lifetimes, and transition dipole moments for YbOH," J. Phys. Chem. A **124**, 3135 (2020).

[154] T. E. Sharp and H. M. Rosenstock, "Franck-Condon Factors for Polyatomic Molecules," J. Chem. Phys. **41**, 3453 (1964).

[155] T. Sattasathuchana, R. Murri, and K. K. Baldridge, "An Efficient Analytic Approach for Calculation of Multi-Dimensional Franck–Condon Factors and Associated Photoelectron Spectra," J. Chem. Theo. Comp. **13**, 2147 (2017).

[156] J.-L. Chang, "A new method to calculate Franck-Condon factors of multidimensional harmonic oscillators including the Duschinsky effect," J. Chem. Phys. **128**, 174111 (2008).

[157] G. Herzberg, *Molecular Spectra and Molecular Structure: Electronic Spectra and Electronic Structure of Polyatomic Molecules*, Vol. 3 (Van Nostrand, 1966).

[158] A. Hansson and J. K. Watson, "A comment on Hönl-London factors," J. Mol. Spec. **233**, 169 (2005).

[159] J. T. Hougen, *The Calculation of Rotational Energy Levels and Rotational Line Intensities in Diatomic Molecules* (NBS Monograph 115, U.S. Government Printing Office, Washington, D.C., 1970).

[160] E. E. Whiting and R. W. Nicholls, "Reinvestigation of rotational-line intensity factors in diatomic spectra," Astrophys. J. Suppl. **27**, 1 (1974).

[161] L. T. Earls, "Intensities in $^2\Pi - ^2\Sigma$ Transitions in Diatomic Molecules," Phys. Rev. **48**, 423 (1935).

[162] J. M. Brown, "Rotational energy levels of symmetric top molecules in ^2E states," Mol. Phys. **20**, 817 (1971).

[163] J. M. Brown, "The Renner-Teller Effect: The Effective Hamiltonian Approach," in *Computational Molecular Spectroscopy*, edited by P. Jensen and P. R. Bunker (Wiley & Sons Ltd., 2000) Chap. 16, pp. 517–537.

[164] T. A. Barckholtz and T. A. Miller, "Quantitative insights about molecules exhibiting Jahn-Teller and related effects," Int. Rev. Phys. Chem. **17**, 435 (1998).

[165] J. Aarts, "The Renner effect in $^2\Pi$ electronic states of linear triatomic molecules," Mol. Phys. **35**, 1785 (1978).

[166] J. M. Brown and F. Jorgensen, "Vibronic energy levels of a linear triatomic molecule in a degenerate electronic state: a unified treatment of the Renner-Teller effect," in *Advances in Chemical Physics, Volume LII*, edited by I. Prigogine and S. A. Rice (Wiley & Sons Ltd., 1983) pp. 117–180.

[167] P. Jensen, G. Osmann, and P. R. Bunker, "The Renner Effect," in *Computational Molecular Spectroscopy*, edited by P. Jensen and P. R. Bunker (Wiley & Sons Ltd., 2000) Chap. 15, pp. 485–515.

[168] J. M. Brown, "The rotational dependence of the Renner-Teller interaction: a new term in the effective Hamiltonian for linear triatomic molecules in Π electronic states," Mol. Phys. **101**, 3419 (2003).

[169] J. M. Brown, "The effective Hamiltonian for the Renner-Teller effect," J. Mol. Spectrosc. **68**, 412 (1977).

[170] M. Li and J. A. Coxon, "High-resolution analysis of the fundamental bending vibrations in the $\tilde{A}^2\Pi$ and $\tilde{X}^2\Sigma^+$ states of CaOH and CaOD: Deperturbation of Renner-Teller, spin-orbit and K-type resonance interactions," J. Chem. Phys. **102**, 2663 (1995).

[171] M. Li, *High-resolution laser spectroscopy of the $\tilde{A}^2\Pi$- $\tilde{X}^2\Sigma^+$ system of calcium hydroxyl and calcium hydroxyl-d radicals*, Ph.D. thesis, Dalhousie University (1995).

[172] S. Nakhate, T. C. Steimle, N. H. Pilgram, and N. R. Hutzler, "The pure rotational spectrum of YbOH," Chem. Phys. Lett. **715**, 105 (2019).

[173] T. C. Steimle, C. Linton, E. T. Mengesha, X. Bai, and A. T. Le, "Field-free, Stark, and Zeeman spectroscopy of the $\tilde{A}-\tilde{X}$ transition of ytterbium monohydroxide," Phys. Rev. A **100**, 052509 (2019).

[174] C. Scurlock, D. Fletcher, and T. Steimle, "Hyperfine Structure in the $(0,0,0)\tilde{X}\,^2\Sigma^+$ State of CaOH Observed by Pump/Probe Microwave-Optical Double Resonance," J. Mol. Spec. **159**, 350 (1993).

[175] J. F. Barry, *Laser cooling and slowing of a diatomic molecule*, Ph.D. thesis, Yale University (2013).

[176] W. Childs, L. Goodman, and I. Renhorn, "Radio-frequency optical double-resonance spectrum of SrF: The $X\,^2\Sigma^+$ state," J. Mol. Spec. **87**, 522 (1981).

[177] R. C. Hilborn, Z. Qingshi, and D. O. Harris, "Laser spectroscopy of the A-X transitions of CaOH and CaOD," J. Mol. Spec. **97**, 73 (1983).

[178] J. Lim, J. R. Almond, M. R. Tarbutt, D. T. Nguyen, and T. C. Steimle, "The [557]-$X\,^2\Sigma$ and [561]-$X\,^2\Sigma$ bands of ytterbium fluoride, ^{174}YbF," J. Mol. Spec. **338**, 81 (2017).

[179] M. R. Tarbutt and T. C. Steimle, "Modeling magneto-optical trapping of CaF molecules," Phys. Rev. A **92**, 053401 (2015).

[180] M. Li and J. A. Coxon, "Laser spectroscopy of the CaOH $\tilde{A} - \tilde{X}(020)$–$(000)$ band: Deperturbation of the Fermi resonance, Renner-Teller, and spin-orbit interactions," J. Chem. Phys. **97**, 8961 (1992).

[181] M. Yeo, M. T. Hummon, A. L. Collopy, B. Yan, B. Hemmerling, E. Chae, J. M. Doyle, and J. Ye, "Rotational state microwave mixing for laser cooling of complex diatomic molecules," Phys. Rev. Lett. **114**, 223003 (2015).

[182] S. Ding, Y. Wu, I. A. Finneran, J. J. Burau, and J. Ye, "Sub-Doppler Cooling and Compressed Trapping of YO Molecules at μK Temperatures," Phys. Rev. X **10**, 021049 (2020).

[183] N. Fitch and M. Tarbutt, *Laser-cooled molecules*, edited by L. F. Dimauro, H. Perrin, and S. F. Yelin, Advances In Atomic, Molecular, and Optical Physics, Vol. 70 (Academic Press, 2021) pp. 157–262.

[184] D. J. Berkeland and M. G. Boshier, "Destabilization of dark states and optical spectroscopy in Zeeman-degenerate atomic systems," Phys. Rev. A **65**, 033413 (2002).

[185] J. A. Devlin and M. R. Tarbutt, "Laser cooling and magneto-optical trapping of molecules analyzed using optical Bloch equations and the Fokker-Planck-Kramers equation," Phys. Rev. A **98**, 063415 (2018).

[186] H.-I. Lu, *Magnetic trapping of molecules via optical loading and magnetic slowing*, Ph.D. thesis, Harvard University, Cambridge, MA (2014).

[187] L. W. Baum, *Laser cooling and 1D magneto-optical trapping of calcium monohydroxide*, Ph.D. thesis, Harvard University (2020).

[188] T. R. Roberts and S. G. Sydoriak, "Thermodynamic Properties of Liquid Helium Three. I. The Specific Heat and Entropy," Physical Review **98**, 1672 (1955).

[189] F. Pobell, *Matter and Methods at Low Temperatures*, 2nd ed. (Springer-Verlag, 1995).

[190] J. Burton, E. V. Cleve, and P. Taborek, "A continuous ^{3}He cryostat with pulse-tube precooling and optical access," Cryogenics **51**, 209 (2011).

[191] X. Zhuang, A. Le, T. C. Steimle, N. E. Bulleid, I. J. Smallman, R. J. Hendricks, S. M. Skoff, J. J. Hudson, B. E. Sauer, E. A. Hinds, and M. R. Tarbutt, "Franck-Condon factors and radiative lifetime of the $A^2\Pi_{1/2} - X^2\Sigma^+$ transition of ytterbium monofluoride, YbF," Phys. Chem. Chem. Phys. **13**, 19013 (2011).

[192] D.-T. Nguyen, T. C. Steimle, I. Kozyryev, M. Huang, and A. B. McCoy, "Fluorescence branching ratios and magnetic tuning of the visible spectrum of SrOH," J. Mol. Spec. **347**, 7 (2018).

[193] I. Kozyryev, T. C. Steimle, P. Yu, D.-T. Nguyen, and J. M. Doyle, "Determination of CaOH and $CaOCH_3$ vibrational branching ratios for direct laser cooling and trapping," New J. Phys. **21**, 052002 (2019).

[194] A. Jadbabaie, N. H. Pilgram, J. Klos, S. Kotochigova, and N. R. Hutzler, "Enhanced molecular yield from a cryogenic buffer gas beam source via excited state chemistry," New J. Phys. **22**, 022002 (2020).

[195] C. Zhang, B. L. Augenbraun, Z. D. Lasner, N. B. Vilas, J. M. Doyle, and L. Cheng, "Accurate prediction and measurement of vibronic branching ratios for laser cooling linear polyatomic molecules," J. Chem. Phys. **155**, 091101 (2021).

[196] M. Dolg, H. Stoll, and H. Preuss, "*Ab initio* pseudopotential study of YbH and YbF," Chem. Phys. **165**, 21 (1992).

[197] B. E. Sauer, J. Wang, and E. A. Hinds, "Laser-rf double resonance spectroscopy of ^{174}Yb in the $X^2\Sigma$ state: spin-rotation, hyperfine interactions, and the electric dipole moment," J. Chem. Phys. **105**, 7412 (1996).

[198] B. E. Sauer, S. B. Cahn, M. G. Kozlov, G. D. Redgrave, and E. A. Hinds, "Perturbed hyperfine doubling in the $A^2\Pi_{1/2}$ and [18.6]0.5 states of YbF," J. Chem. Phys. **110**, 8424 (1999).

[199] L. Baum, N. B. Vilas, C. Hallas, B. L. Augenbraun, S. Raval, D. Mitra, and J. M. Doyle, "Establishing a nearly closed cycling transition in a polyatomic molecule," Phys. Rev. A **103**, 043111 (2021).

[200] R. Pereira and D. H. Levy, "Observation and spectroscopy of high-lying states of the CaOH radical: Evidence for a bent, covalent state," J. Chem. Phys. **105**, 9733 (1996).

[201] C. Brazier and P. Bernath, "Laser and fourier transform spectroscopy of the $\tilde{A}\,^2\Pi - \tilde{X}\,^2\Sigma^+$ transition of SrOH," J. Mol. Spec. **114**, 163 (1985).

[202] P. I. Presunka and J. A. Coxon, "Laser spectroscopy of the $\tilde{A}\,^2\Pi - \tilde{X}\,^2\Sigma^+$ transition of SrOH: Deperturbation analysis of K-resonance in the $v_2 = 1$ level of the $\tilde{A}\,^2\Pi$ state," J. Chem. Phys. **101**, 201 (1994).

[203] S. Kinsey-Nielsen, C. R. Brazier, and P. F. Bernath, "Rotational analysis of the $\tilde{B}\,^2\Sigma^+ - \tilde{X}^2\Sigma^+$ transition of BaOH and BaOD," J. Chem. Phys. **84**, 698 (1986).

[204] J. A. Coxon, M. G. Li, and P. I. Presunka, "Laser spectroscopy of the $(010)\,^2\Sigma^{(+)}$, $^2\Sigma^{(-)} - (000)^2\Sigma^+$ parallel bands in the $\tilde{A}\,^2\Pi - \tilde{X}\,^2\Sigma^+$ system of CaOH," J. Mol. Spectrosc. **164**, 118 (1994).

[205] M. Li and J. A. Coxon, "Dye laser excitation studies of the $\tilde{A}\,^2\Pi(100)/(020) - \tilde{X}\,^2\Sigma^+(020)/(000)$ bands of CaOD: Analysis of the $\tilde{A}\,^2\Pi(100) \sim (020)$ Fermi resonance," J. Chem. Phys. **104**, 4961 (1996).

[206] A. C. Paul, K. Sharma, M. A. Reza, H. Telfah, T. A. Miller, and J. Liu, "Laser-induced fluorescence and dispersed-fluorescence spectroscopy of the $\tilde{A}\,^2E - \tilde{X}\,^2A_1$ transition of jet-cooled calcium methoxide (CaOCH3) radicals," J. Chem. Phys. **151**, 134303 (2019).

[207] V. G. Solomonik and A. N. Smirnov, "Toward chemical accuracy in ab initio thermochemistry and spectroscopy of lanthanide compounds: Assessing core-valence correlation, second-order spin–orbit coupling, and higher order effects in lanthanide diatomics," J. Chem. Theory Comput. **13**, 5240 (2017).

[208] P. F. Bernath, "Spectroscopy and photochemistry of polyatomic alkaline earth containing molecules," Adv. Photochem. **23**, 1 (1997).

[209] M. D. Oberlander and J. M. Parson, "Laser excited fluorescence study of reactions of excited Ca and Sr with water and alcohols: Product selectivity and energy disposal," The Journal of Chemical Physics **105**, 5806 (1996).

[210] J. Coxon and C. Linton, "Re-analysis of the 000–000 and 000–100 bands in the $\tilde{A}\,^2\Pi_{1/2} - \tilde{X}\,^2\Sigma^+$ system of YbOH: Revised estimates of the ground state spin-rotation splitting parameters," J. Mol. Spec. **367**, 111242 (2020).

[211] J. Lim, J. R. Almond, M. Tarbutt, D. T. Nguyen, and T. C. Steimle, "The [557]-X$^2\Sigma$ and [561]-X$^2\Sigma$ bands of ytterbium fluoride, ^{174}YbF," J. Mol. Spec. **338**, 81 (2017).

[212] L. M. Ziurys, D. A. Fletcher, M. A. Anderson, and J. B. W. L., "Rest Frequencies for Alkaline Earth Hydroxide Radicals $(X^2\Sigma^+)$," Astrophys. J. Supplement Series **102**, 425 (1996).

[213] B. L. Augenbraun, Z. D. Lasner, A. Frenett, H. Sawaoka, C. Miller, T. C. Steimle, and J. M. Doyle, "Laser-cooled polyatomic molecules for improved electron electric dipole moment searches," New J. Phys. **22**, 022003 (2020).

[214] D. J. McCarron, E. B. Norrgard, M. H. Steinecker, and D. DeMille, "Improved magneto–optical trapping of a diatomic molecule," New J. Phys. **17**, 035014 (2015).

[215] M. H. Steinecker, D. J. McCarron, Y. Zhu, and D. DeMille, "Improved radio-frequency magneto-optical trap of SrF molecules," ChemPhysChem **17**, 3664 (2016).

[216] H. J. Williams, S. Truppe, M. Hambach, L. Caldwell, N. J. Fitch, E. A. Hinds, B. E. Sauer, and M. R. Tarbutt, "Characteristics of a magneto-optical trap of molecules," New J. Phys. **19**, 113035 (2017).

[217] J. Lim, J. R. Almond, M. A. Trigatzis, J. A. Devlin, N. J. Fitch, B. E. Sauer, M. R. Tarbutt, and E. A. Hinds, "Laser cooled YbF molecules for measuring the electron's electric dipole moment," Phys. Rev. Lett. **120**, 123201 (2018).

[218] M. T. Hummon, M. Yeo, B. K. Stuhl, A. L. Collopy, Y. Xia, and J. Ye, "2D magneto-optical trapping of diatomic molecules," Phys. Rev. Lett. **110**, 143001 (2013).

[219] I. Kozyryev, L. Baum, K. Matsuda, B. Hemmerling, and J. M. Doyle, "Radiation pressure force from optical cycling on a polyatomic molecule," J. Phys. B **49**, 134002 (2016).

[220] J. A. Devlin and M. R. Tarbutt, "Three-dimensional Doppler, polarization-gradient, and magneto-optical forces for atoms and molecules with dark states," New J. Phys. **18**, 123017 (2016).

[221] O. Emile, R. Kaiser, C. Gerz, H. Wallis, A. Aspect, and C. Cohen-Tannoudji, "Magnetically assisted Sisyphus effect," Journal de Physique II **3**, 1709 (1993).

[222] R. Gupta, S. Padua, C. Xie, H. Batelaan, and H. Metcalf, "Simplest atomic system for sub-Doppler laser cooling," J. Opt. Soc. Am. B **11**, 537 (1994).

[223] M. Plimmer, N. Castagna, G. D. Domenico, P. Thomann, A. V. Taichenachev, and V. I. Yudin, "2D laser collimation of a cold Cs beam induced by a transverse B field," J. Exp. Theor. Phys. **82**, 17 (2005).

[224] D. E. Maison, L. V. Skripnikov, and V. V. Flambaum, "Theoretical study of ^{173}YbOH to search for the nuclear magnetic quadrupole moment," Phys. Rev. A **100**, 032514 (2019).

[225] H. Wang, A. T. Le, T. C. Steimle, E. A. C. Koskelo, G. Aufderheide, R. Mawhorter, and J.-U. Grabow, "Fine and hyperfine interaction in ^{173}YbF," Phys. Rev. A **100**, 022516 (2019).

[226] M. Petzold, P. Kaebert, P. Gersema, M. Siercke, and S. Ospelkaus, "A Zeeman slower for diatomic molecules," New J. Phys. **20**, 042001 (2018).

[227] M. Petzold, P. Kaebert, P. Gersema, T. Poll, N. Reinhardt, M. Siercke, and S. Ospelkaus, "Type-II Zeeman slowing: Characterization and comparison to conventional radiative beam-slowing schemes," Phys. Rev. A **98**, 063408 (2018).

[228] P. Kaebert, M. Stepanova, T. Poll, M. Petzold, S. Xu, M. Siercke, and S. Ospelkaus, "Characterizing the Zeeman slowing force for ^{40}Ca^{19}F molecules," New J. Phys. **23**, 093013 (2021).

[229] L. Baum, N. B. Vilas, C. Hallas, B. L. Augenbraun, S. Raval, D. Mitra, and J. M. Doyle, "1D Magneto-Optical Trap of Polyatomic Molecules," Phys. Rev. Lett. **124**, 133201 (2020).

[230] C. E. Dickerson, H. Guo, A. J. Shin, B. L. Augenbraun, J. R. Caram, W. C. Campbell, and A. N. Alexandrova, "Franck-Condon Tuning of Optical Cycling Centers by Organic Functionalization," Phys. Rev. Lett. **126** (2021).

[231] C. E. Dickerson, H. Guo, G.-Z. Zhu, E. R. Hudson, J. R. Caram, W. C. Campbell, and A. N. Alexandrova, "Optical cycling functionalization of arenes," J. Phys. Chem. Lett. **12**, 3989 (2021).

[232] E. R. Hudson, J. R. Bochinski, H. J. Lewandowski, B. C. Sawyer, and J. Ye, "Efficient stark deceleration of cold polar molecules," Eur. Phys. J. D **31**, 351 (2004).

[233] R. Fulton, A. I. Bishop, and P. F. Barker, "Optical stark decelerator for molecules," Phys. Rev. Lett. **93**, 243004 (2004).

[234] T. E. Wall, J. F. Kanem, J. M. Dyne, J. J. Hudson, B. E. Sauer, E. A. Hinds, and M. R. Tarbutt, "Stark deceleration of CaF molecules in strong- and weak-field seeking states," Phys. Chem. Chem. Phys. **13**, 18991 (2011).

[235] E. Lavert-Ofir, S. Gersten, A. B. Henson, I. Shani, L. David, J. Narevicius, and E. Narevicius, "A moving magnetic trap decelerator: a new source of cold atoms and molecules," New J. Phys. **13**, 103030 (2011).

[236] N. Akerman, M. Karpov, Y. Segev, N. Bibelnik, J. Narevicius, and E. Narevicius, "Trapping of molecular oxygen together with lithium atoms," Phys. Rev. Lett. **119**, 073204 (2017).

[237] Y. Liu, M. Vashishta, P. Djuricanin, S. Zhou, W. Zhong, T. Mittertreiner, D. Carty, and T. Momose, "Magnetic trapping of cold methyl radicals," Phys. Rev. Lett. **118**, 093201 (2017).

[238] S. Chervenkov, X. Wu, J. Bayerl, A. Rohlfes, T. Gantner, M. Zeppenfeld, and G. Rempe, "Continuous centrifuge decelerator for polar molecules," Phys. Rev. Lett. **112** (2014).

[239] X. Wu, T. Gantner, M. Koller, M. Zeppenfeld, S. Chervenkov, and G. Rempe, "A cryofuge for cold-collision experiments with slow polar molecules," Science **358**, 645 (2017).

[240] B. L. Augenbraun, A. Frenett, H. Sawaoka, C. Hallas, N. B. Vilas, A. Nasir, Z. D. Lasner, and J. M. Doyle, "Zeeman-sisyphus deceleration of molecular beams," Phys. Rev. Lett. **127**, 263002 (2021).

[241] N. J. Fitch and M. R. Tarbutt, "Principles and Design of a Zeeman-Sisyphus Decelerator for Molecular Beams," ChemPhysChem **17**, 3609 (2016).

[242] D. Comparat, "Molecular cooling via Sisyphus processes," Phys. Rev. A **89**, 043410 (2014).

[243] H.-I. Lu, I. Kozyryev, B. Hemmerling, J. Piskorski, and J. M. Doyle, "Magnetic trapping of molecules via optical loading and magnetic slowing," Phys. Rev. Lett. **112**, 113006 (2014).

[244] M. Denis, P. A. B. Haase, R. G. E. Timmermans, E. Eliav, N. R. Hutzler, and A. Borschevsky, "Enhancement factor for the electric dipole moment of the electron in the BaOH and YbOH molecules," Phys. Rev. A **99**, 042512 (2019).

[245] K. Gaul and R. Berger, "*Ab initio* study of parity and time-reversal violation in laser-coolable triatomic molecules," Phys. Rev. A **101**, 012508 (2020).

[246] K. M. O'Hara, S. R. Granade, M. E. Gehm, T. A. Savard, S. Bali, C. Freed, and J. E. Thomas, "Ultrastable CO_2 Laser Trapping of Lithium Fermions," Phys. Rev. Lett. **82**, 4204 (1999).

[247] S. Bernon, H. Hattermann, D. Bothner, M. Knufinke, P. Weiss, F. Jessen, D. Cano, M. Kemmler, R. Kleiner, D. Koelle, and J. Fortagh, "Manipulation and coherence of ultra-cold atoms on a superconducting atom chip," Nat. Commun. **4** (2013).

[248] Y. Wang, M. Um, J. Zhang, S. An, M. Lyu, J.-N. Zhang, L.-M. Duan, D. Yum, and K. Kim, "Single-qubit quantum memory exceeding ten-minute coherence time," Nat. Photonics **12**, 185 (2018).

[249] C. J. Ho, J. A. Devlin, I. M. Rabey, P. Yzombard, J. Lim, S. C. Wright, N. J. Fitch, E. A. Hinds, M. R. Tarbutt, and B. E. Sauer, "New techniques for a measurement of the electron's electric dipole moment," New J. Phys. **22**, 053031 (2020).

[250] D. Mitra, N. B. Vilas, C. Hallas, L. Anderegg, B. L. Augenbraun, L. Baum, C. Miller, S. Raval, and J. M. Doyle, "Direct laser cooling of a symmetric top molecule," Science **369**, 1366 (2020).

[251] B. L. Augenbraun, Z. D. Lasner, A. Frenett, H. Sawaoka, C. Miller, T. C. Steimle, and J. M. Doyle, "Laser-cooled polyatomic molecules for improved electron electric dipole moment searches," New J. Phys. **22**, 022003 (2020).

[252] M. Denis, Y. Hao, E. Eliav, N. R. Hutzler, M. K. Nayak, R. G. E. Timmermans, and A. Borschesvky, "Enhanced P, T-violating nuclear magnetic quadrupole moment effects in laser-coolable molecules," J. Chem. Phys. **152**, 084303 (2020).

[253] E. B. Norrgard, D. S. Barker, S. Eckel, J. A. Fedchak, N. N. Klimov, and J. Scherschligt, "Nuclear-spin dependent parity violation in optically trapped polyatomic molecules," Communications Physics **2** (2019).

[254] Y. Hao, P. Navrátil, E. B. Norrgard, M. Iliaš, E. Eliav, R. G. E. Timmermans, V. V. Flambaum, and A. Borschevsky, "Nuclear spin-dependent parity-violating effects in light polyatomic molecules," Phys. Rev. A **102**, 052828 (2020).

[255] K. Namiki, J. Robinson, and T. Steimle, "A spectroscopic study of $CaOCH_3$ using the pump/probe microwave and the molecular beam/optical Stark techniques," J. Chem. Phys. **109**, 5283 (1998).

[256] N. J. Reilly, T. W. Schmidt, and S. H. Kable, "Two-dimensional fluorescence (excitation/emission) spectroscopy as a probe of complex chemical environments," J. Phys. Chem. A **110**, 12355 (2006).

[257] J. R. Gascooke, U. N. Alexander, and W. D. Lawrance, "Two dimensional laser induced fluorescence spectroscopy: A powerful technique for elucidating rovibronic structure in electronic transitions of polyatomic molecules," J. Chem. Phys. **134**, 184301 (2011).

[258] D. L. Kokkin, T. C. Steimle, and D. DeMille, "Branching ratios and radiative lifetimes of the U, L, and I states of thorium oxide," Phys. Rev. A **90**, 062503 (2014).

[259] C. R. Brazier and P. F. Bernath, "The $\tilde{A}\,^2E - \tilde{X}\,^2A_1$ transition of monomethyl calcium: A rotational analysis," J. Chem. Phys. **91**, 4548 (1989).

[260] A. J. Marr, F. Grieman, and T. C. Steimle, "A molecular beam optical/stark study of calcium monomethyl," J. Chem. Phys. **105**, 3930 (1996).

[261] I. J. Smallman, F. Wang, T. C. Steimle, M. R. Tarbutt, and E. A. Hinds, "Radiative branching ratios for excited states of ^{174}YbF: Application to laser cooling," J. Mol. Spec. **300**, 3 (2014).

[262] K. L. Dunfield, C. Linton, T. E. Clarke, J. McBride, A. G. Adam, and J. R. D. Peers, "Laser Spectroscopy of the Lanthanide Monofluorides: Analysis of the $\tilde{A}\,^2\Pi - \tilde{X}\Sigma^+$ Transition of Ytterbium Monofluoride," J. Mol. Spec. **174**, 433 (1995).

[263] P. Crozet, A. J. Ross, C. Linton, A. G. Adam, W. S. Hopkins, and R. J. L. Roy, "Geometry of the $CaOCH_3$ radical from isotope effects in the transition," J. Mol. Spec. **229**, 224 (2005).

[264] L. C. O'Brien, C. R. Brazier, and P. F. Bernath, "High-resolution laser spectroscopy of strontium monomethoxide, $SrOCH_3$," J. Mol. Spec. **130**, 33 (1988).

[265] C. R. Brazier, L. C. Ellingboe, S. Kinsey-Nielsen, and P. F. Bernath, "Laser spectroscopy of alkaline earth monoalkoxide free radicals," J. Am. Chem. Soc. **108**, 2126 (1986).

[266] F. Neese, "The ORCA program system," Wiley Interdiscip. Rev. Comput. Mol. Sci. **2**, 73 (2012).

[267] F. Neese, F. Wennmohs, U. Becker, and C. Riplinger, "The ORCA quantum chemistry program package," J. Chem. Phys. **152**, 224108 (2020).

[268] D. Bykov, T. Petrenko, R. Izsák, S. Kossmann, U. Becker, E. Valeev, and F. Neese, "Efficient implementation of the analytic second derivatives of Hartree-Fock and hybrid DFT energies: a detailed analysis of different approximations," Mol. Phys. **113**, 1961 (2015).

[269] P. J. Stephens, F. J. Devlin, C. F. Chabalowski, and M. J. Frisch, "*Ab Initio* Calculation of Vibrational Absorption and Circular Dichroism Spectra Using Density Functional Force Fields," J. Phys. Chem. **98**, 11623 (1994).

[270] M. Dolg, H. Stoll, and H. Preuss, "Energy-adjusted *ab intio* pseudopotentials for the rare earth elements," J. Chem. Phys. **90**, 1730 (1989).

[271] M. J. O'Rourke and N. R. Hutzler, "Hypermetallic polar molecules for precision measurements," Phys. Rev. A **100**, 022502 (2019).

[272] D. A. Weil and D. A. Dixon, "Gas-phase isotope fractionation factor for proton-bound dimers of methoxide anions," J. Am. Chem. Soc. **107**, 6859 (1985).

[273] T. C. Steimle, T. Ma, and C. Linton, "The hyperfine interaction in the $A\,^2\Pi_{1/2}$ and $X\,^2\Sigma^+$ states of ytterbium monofluoride," J. Chem. Phys. **127**, 234316 (2007).

[274] M. J. Dick, P. M. Sheridan, J.-G. Wang, and P. F. Bernath, "High-resolution laser excitation spectroscopy of the $\tilde{A}\,^2E - \tilde{X}\,^2A_1$ transition of $SrCH_3$," J. Chem. Phys. **124**, 174309 (2006).

[275] N. H. Pilgram, A. Jadbabaie, Y. Zeng, N. R. Hutzler, and T. C. Steimle, "Fine and hyperfine interactions in ^{171}YbOH and ^{173}YbOH," J. Chem. Phys. **154**, 244309 (2021).

[276] M. R. Tarbutt, "Laser cooling of molecules," Contemp. Phys. **59**, 356 (2018).

[277] C. N. Jarman and P. F. Bernath, "A high-resolution analysis of the $\tilde{A}\,^2A' - \tilde{X}\,^2A'$ transition of CaSH by laser excitation spectroscopy," J. Chem. Phys. **98**, 6697 (1993).

[278] P. M. Sheridan, M. J. Dick, J.-G. Wang, P. F. Bernath, and P. M. Sheridan, "High-resolution investigation of the excited electronic states of CaSH and SrSH by laser excitation spectroscopy," Mol. Phys. **105**, 569 (2007).

[279] J. Shirley, C. Scurlock, T. Steimle, B. Simard, M. Vasseur, and P. A. Hackett, "Molecular beam optical Stark spectroscopy of CaSH," J. Chem. Phys. **93**, 8580 (1990).

[280] A. Taleb-Bendiab and D. Chomiak, "Millimeter-wave spectrum of MgSH," Chem. Phys. Lett. **334**, 195 (2001).

[281] A. Janczyk and L. M. Ziurys, "Studies of metal hydrosulfides III: The millimeter/submillimeter spectrum of BaSH ($\tilde{X}\,^2A'$)," J. Chem. Phys. **119**, 10702 (2003).

[282] A. J. Marr, M. Tanimoto, D. Goodridge, and T. C. Steimle, "A study of the $\tilde{A}^2B_2$ - $\tilde{X}^2A_1$ band system of $CaNH_2$ employing molecular beam optical Stark spectroscopy," J. Chem. Phys. **103**, 4466 (1995).

[283] Z. Morbi, C. Zhao, J. W. Hepburn, and P. F. Bernath, "High-resolution visible laser spectroscopy of the $\tilde{B}\,^2B_1 - \tilde{X}\,^2A_1$ transition of $CaNH_2$," J. of Chem. Phys. **108**, 8891 (1998).

[284] C. R. Brazier and P. F. Bernath, "High-Resolution Laser Spectroscopy of the $\tilde{A}\,^2B_2 - \tilde{X}\,^2A_1$ and $\tilde{B}\,^2B_1 - \tilde{X}\,^2A_1$ Systems of $SrNH_2$," J. Mol. Spec. **201**, 116 (2000).

[285] Z. Morbi, C. Zhao, and P. F. Bernath, "A high-resolution analysis of the $\tilde{C}\,^2A_1 - \tilde{X}\,^2A_1$ transition of $CaNH_2$: Pure precession in polyatomic molecules," J. Chem. Phys. **106**, 4860 (1997).

[286] P. M. Sheridan, M. J. Dick, J.-G. Wang, and P. F. Bernath, "Rotational analysis of the $\tilde{C}\,^2A_1\tilde{X}\,^22A_1$ transition of $SrNH_2$," J. Mol. Spec. **233**, 269 (2005).

[287] P. M. Sheridan and L. M. Ziurys, "Laboratory Detection of the $MgNH_2$ Radical ($\tilde{X}\,^2A_1$)," Astrophys. J. **540**, L61 (2000).

[288] P. M. Sheridan and L. M. Ziurys, "Trends in the alkaline-earth amide series: The millimetre-wave spectrum of $MgNH_2$ and $MgND_2$ ($^2A_1$)," Can. J. Phys. **79**, 409 (2001).

[289] R. F. Wormsbecher, M. Trkula, C. Martner, R. E. Penn, and D. O. Harris, "Chemiluminescent reactions of alkaline-earth metals with water and hydrazine," J. Mol. Spec. **97**, 29 (1983).

[290] W. T. M. L. Fernando, R. S. Ram, L. C. O'Brien, and P. F. Bernath, "Gas-phase inorganic chemistry: laser spectroscopy of calcium and strontium monothiolates and monohydrosulfides," J. Phys. Chem. **95**, 2665 (1991).

[291] A. M. R. P. Bopegedera, C. R. Brazier, and P. F. Bernath, "Laser spectroscopy of strontium and calcium monoalkylamides," J. Phys. Chem. **91**, 2779 (1987).

[292] A. C. Paul, M. A. Reza, and J. Liu, "Dispersed-fluorescence spectroscopy of jet-cooled calcium ethoxide radical ($CaOC_2H_5$)," J. Mol. Spec. **330**, 142 (2016).

[293] A. M. R. P. Bopegedera, W. T. M. L. Fernando, and P. F. Bernath, "Gas-phase inorganic chemistry: laser spectroscopy of calcium and strontium monopyrrolate molecules," J. Phys. Chem. **94**, 4476 (1990).

[294] E. S. J. Robles, A. M. Ellis, and T. A. Miller, "Electronic spectroscopy of jet-cooled half-sandwich organometallic complexes CaC_5H_5, $CaC_5H_4CH_3$, and CaC_4H_4N," J. Am. Chem. Soc. **114**, 7171 (1992).

[295] T. M. Cerny, J. M. Williamson, and T. A. Miller, "Rotationally resolved electronic spectra of the "half-sandwich" organometallic radical, CaC_5H_5," J. Chem. Phys. **102**, 2372 (1995).

[296] P. M. Sheridan, M. J. Dick, J.-G. Wang, and P. F. Bernath, "High-resolution spectroscopic investigation of the $\tilde{B}\,^2A_1 - \tilde{X}\,^2A_1$ transitions of $CaCH_3$ and $SrCH_3$," J. Phys. Chem. A **109**, 10547 (2005).

[297] A. P. Salzberg, B. E. Applegate, and T. A. Miller, "Rovibronic Spectroscopy of $MgCH_3$ $\tilde{A}\,^2E \leftarrow \tilde{X}\,^2A_1$ Transition," J. Mol. Spec. **193**, 434 (1999).

[298] R. Rubino, J. M. Williamson, and T. A. Miller, "High resolution electronic spectroscopy of $MgCH_3$," J. Chem. Phys. **103**, 5964 (1995).

[299] MolView, http://www.molview.org (2019).

[300] B. S. D. R. Vamhindi and M. Nsangou, "Accurate *ab initio* potential energy curves and spectroscopic properties of the low-lying electronic states of OH-and SH-molecular anions," Mol. Phys. **114**, 2204 (2016).

[301] E. Chae, *Laser slowing of CaF molecules and progress towards a dual-MOT for Li and CaF*, Ph.D. thesis, Harvard University, Cambridge, MA (2015).

[302] P. Chen, "Photoelectron spectroscopy of reactive intermdiates," in *Unimolecular and Biomolecular Reaction Dynamics*, edited by C. Y. Ng, T. Baer, and I. Powis (Wiley, New York, 1994).

[303] M. D. Oberlander, *Laser excited fluorescence studies of reactions of group 2 metals with oxygen containing molecules and of heavy group 15 clusters with fluorine: Reactivities, product state distributions, and spectroscopy of the BiF $A0^+$ - $X0^+$ transition*, Ph.D. thesis, The Ohio State University (1995).

[304] J. Weber and G. Hohlneicher, "Franck-Condon factors for polyatomic molecules," Mol. Phys. **101**, 2125 (2003).

[305] J. M. Thompsen, P. M. Sheridan, and L. M. Ziurys, "Rotational spectroscopy of the $SrNH_2$ and $SrND_2$ radicals ($\tilde{X}\,^2A_1$)," Chem. Phys. Lett. **330**, 373 (2000).

[306] R. W. Nicholls, "Franck-Condon factor formulae for astrophysical and other molecules," Astrophys. J. Supplement Series **47**, 279 (1981).

[307] R. R. Wright and T. A. Miller, "High-resolution, rotationally resolved electronic spectroscopy of the MgNC radical," J. Mol. Spec. **194**, 219 (1999).

[308] V. A. Mozhayskiy and A. I. Krylov, "ezspectrum 3.0," iopenshell.usc.edu/downloads/ezspectrum/. (2009).

[309] H. Kupka and P. H. Cribb, "Multidimensional Franck-Condon integrals and Duschinsky mixing effects," J. Chem. Phys. **85**, 1303 (1986).

[310] D. Papousek and M. R. Aliev, *Molecular Vibrational-rotational Spectra: Theory and Applications of High Resolution Infrared, Microwave, and Raman Spectroscopy of Polyatomic Molecules* (Elsevier Scientific Publishing Company, 1982).

[311] P. C. Cross, R. M. Hainer, and G. W. King, "The asymmetric rotor II. calculation of dipole intensities and line classification," J. Chem. Phys. **12**, 210 (1944).

[312] N. Wells and I. C. Lane, "Prospects for ultracold carbon via charge exchange reactions and laser cooled carbides," Phys. Chem. Chem. Phys. **13**, 19036 (2011).

[313] E. R. Hudson, "Deceleration of continuous molecular beams," Phys. Rev. A **79**, 061407 (2009).

[314] A. Prehn, M. Ibrügger, R. Glöckner, G. Rempe, and M. Zeppenfeld, "Optoelectrical cooling of polar molecules to submillikelvin temperatures," Phys. Rev. Lett. **116**, 063005 (2016).

[315] A. M. Jayich, A. C. Vutha, M. T. Hummon, J. V. Porto, and W. C. Campbell, "Continuous all-optical deceleration and single-photon cooling of molecular beams," Phys. Rev. A **89**, 023425 (2014).

[316] G. Z. Zhu, B. L. Augenbraun, C. Dickerson, Z. D. Lasner, D. Mitra, A. Alexandrova, W. C. Campbell, J. Caram, J. M. Doyle, and E. R. Hudson, "Functionalizing aromatic compounds with optical cycling centers," In preparation (2021).

[317] W. C. Campbell and B. L. Augenbraun, "Photon spin molasses for laser cooling molecular rotation," arXiv:2111.03763 (2021).

[318] W. Klemperer, K. K. Lehmann, J. K. G. Watson, and S. C. Wofsy, "Can molecules have permanent electric dipole moments?" J. Phys. Chem. **97**, 2413 (1993).

[319] J. E. Wollrab, *Rotational Spectra and Molecular Structure* (Academic Press (New York and London), 1967).

[320] A. J. Merer and J. M. Allegretti, "Rotational energies of linear polyatomic molecules in vibrationally degenerate levels of electronic $^2\Sigma$ and $^3\Sigma$ states," Can. J. Phys. **49**, 2859 (1971).

[321] G. R. Gunther-Mohr, C. H. Townes, and J. H. Van Vleck, "Hyperfine Structure in the Spectrum of $N^{14}H_3$. II. Theoretical Discussion," Phys. Rev. **94**, 1191 (1954).

[322] A. Zakharova, I. Kurchavov, and A. Petrov, "Rovibrational structure of the ytterbium monohydroxide molecule and the P,T-violation searches," J. Chem. Phys. **155**, 164301 (2021).

[323] *Dye laser principles, with applications*, Quantum electronics–principles and applications (Academic Press, Boston, 1990).

[324] Coherent 899-21 Operator's Manual. Accessible on Doyle group website .

[325] J. Devlin, M. Tarbutt, D. Kokkin, and T. Steimle, "Measurements of the Zeeman effect in the $A\,^2\Pi$ and $B\,^2\Sigma^+$ states of calcium fluoride," J. Mol. Spec. **317**, 1 (2015).

[326] M. R. Tarbutt, "Magneto-optical trapping forces for atoms and molecules with complex level structures," New J. Phys. **17**, 015007 (2015).

[327] R. F. Curl, "The relationship between electron spin rotation coupling constants and g-tensor components," Mol. Phys. **9**, 585 (1965).

[328] J. Chen, J. Gengler, T. C. Steimle, and J. M. Brown, "Optical Zeeman spectroscopy of calcium monohydride," Phys. Rev. A **73**, 012502 (2006).

[329] J. Brown, M. Kaise, C. Kerr, and D. Milton, "A determination of fundamental Zeeman parameters for the OH radical," Mol. Phys. **36**, 553 (1978)